Mechanical Evolution, Fluid Pressure Generation, and Shallow Slow Slip in Subduction Zones

Harold R. Leah

a thesis submitted for the degree of

Doctor of Philosophy

at Cardiff University

April 2021

Abstract

The shallow plate interface (< 20 km depth) of subduction zones can host complex slip behaviours including earthquakes, slow slip events, steady aseismic creep, and tremor. Factors controlling the spatiotemporal distribution of these behaviours are unclear, and a clearer view of subduction plate interface shear zone deformation and evolution is required.

This thesis investigates processes governing shallow plate interface deformation at the Hikurangi margin, New Zealand, and in the Gwna Complex, Anglesey. At the Hikurangi margin, mixed brittle and ductile deformation structures in calcareous-pelagic input sediments suggest frictional-viscous deformation will dominate if they deform at the plate interface. Down-dip, receiver functions from the NZ3D seismometer array delineate splay faults soling towards a geometrically rough plate interface at 12-15 km depth. The lower plate comprises fluid-rich, variably-altered volcaniclastics atop the > 10 km thick crust of the oceanic Hikurangi Plateau.

In the Gwna Complex, thin mélange-bearing shear zones bound lenticular slices of ocean plate stratigraphy. Structures in shear zones include foliated phyllosilicates and variably-deformed quartz/calcite veins, suggesting creep at 260±10 °C was cyclically punctuated by transient, localised fluid pulses. Stress-dependent strain rates in modelled shear zones vary depending on pore fluid pressure; models predict slow slip velocities at pore fluid pressures greater than hydrostatic but less than lithostatic. Shear zones localised within carbonate veins in the Gwna Complex underwent viscous creep at temperatures cooler than those predicted from calcite deformation experiments, inferred to result from vein-wall rock chemical variations and small grains sizes pinned by second phase inclusions.

Overall, shallow plate interface deformation is controlled by fluid-pressure-dependent localisation within structures pre-existing from earlier deposition or deformation. As inherited structures and fluid pressure distribution control subduction interface shear zone rheology, diverse lithological inputs and fluid pressures at shallow depths likely lead to complex slip behaviours.

Acknowledgements

The main person to thank for the existence of this thesis is my PhD supervisor, Åke Fagereng. As well as obtaining funding for the research, Åke has guided me throughout this PhD. He has been more understanding and flexible to my plans and problems than I could have ever hoped, encouraging me to attend conferences and take leave in far-off places. He has read, with infinite patience, what feels like thousands of overly long, meandering, drafts accompanied by whole booklets of figures. Thank you Åke for your patience and help over the last four years; one day I'll write something short, I promise. This PhD was supported by European Research Council Starting Grant 715836 (MICA).

I wouldn't have even considered undertaking a PhD if it weren't for the enthusiastic guidance of Giulio di Toro and Michele Fondriest during my master's research project. Thank you, guys, for teaching me during my earliest research experiences and supporting my application for this PhD. Many other academics and friends helped me on this journey, I'd like to thank: Rebecca Bell for being a wonderfully caring mentor and including me in varied experiences both in New Zealand and at home, Dave Thompson for teaching me the fundamentals of receiver function analysis and setting me off on the most tangential chapter of this PhD, Duncan Muir for lovely chats, lots of patient help with the SEM, and being the lord of The Bobble, Ian Bastow for patiently guiding me further through the maze of receiver function analysis, David Buchs for being a source of enlightening discussion and humorous field companion, and Tom Blenkinsop for kind and helpful discussions on pressure solution, vorticity, deformation mechanisms and grain shape and size. I'd also like to thank Anthony Oldroyd for patiently preparing and polishing boxes and boxes of thin sections. Following my *viva* I would like to thank Tiago Alves and Zoe Shipton for being excellent and kind examiners.

When I moved to Cardiff for this PhD, I was ready for many things, but I wasn't expecting to meet my partner Alex. Our relationship started right at the beginning of this PhD and she's been there as I've grown and changed over the last four years while carrying out this research. She's been my biggest fan in the good times, my most important ally in the bad, and a constant source of love, reassurance, and reality checks.

From the bottom of my heart, thank you for everything. I wouldn't be who I am today without you.

I have had two ever-present companions throughout my time at Cardiff University; their names are Chris and Sophie. Thank you for the last few years of support, discussions, distractions, coffee, and pastries. Without you two, this whole experience would have been a lot more difficult and lonelier; I am eternally grateful for your company. Christian has also been a great friend, providing sage wisdom and reassurance to me during difficult times. I would also like to thank Adam, Jack, and Sara for their company and friendship. I'll fondly remember our evenings at the Pen and Wig and coffees in the park. Outside the research group, my friends in Cardiff have been brilliant over the last four years, and I'd like to thank them all for many happy memories. Among many others I'm sure I'll forget to include (sorry!), I'd like to thank: Aidan for talking so excitedly about books and time series analysis, Liam for always being up for cooking up a storm and a good time, Panton for providing the boardgames and a many laughs, Max for teaching me about Marx and how good long hair can look, Phil for always being keen for a ride and long chats, Jaz for wonderful acoustic evenings and discussions on Ariana Grande, Niall for being a great field buddy and goalkeeper, and Will for being the real captain of Expected Toulouse. I'd also like to thank everyone at Brodie's for the exceptional coffee; long live the Brodie Bunch.

While life in Cardiff has been a long way from The North, I'm grateful to my family for being frequent visitors and a great source of love and support. Your visits were a welcome break, our virtual weekly chats got me through the harder weeks of lockdown. Thanks, Mum, Dad, Jen, and Tom, you all mean more to me than I can put into words.

Completing this PhD has not been easy, but for many others doing a PhD is much more difficult. As a straight, white, able-bodied, cisgender, middle-class man I have had probably the easiest possible path up to this point. I would like to take this opportunity to acknowledge those whose journey has been harder than mine, or hasn't even begun, because they don't look like me, and pledge solidarity in fighting systematic bias in society which favours people like myself.

Published papers related to this thesis

- Leah, H., Fagereng, Å., Meneghini, F., Morgan, J.K., Savage, H.M., Wang, M., Bell, R. and Ikari, M.J. (2020) Mixed brittle and viscous strain localization in pelagic sediments seaward of the Hikurangi Margin, New Zealand. Tectonics, 39(8), p.e2019TC005965.

Contents

List of Tables

List of Figures

Chapter 1

Introduction

Subduction zones host the largest slip events on Earth within discrete plate interface shear zones, as illustrated by the 2011 M_w 9.0 Tohoku-Oki earthquake (e.g. Chester *et al.*, 2013; Sun *et al.*, 2017). Slip in these shear zones can occur at variable rates by many different mechanisms (Peng and Gomberg, 2010; Rowe *et al.*, 2011), but to understand how and why various slip types occur where they do, a clearer understanding of deformation on the plate interface is required. Studies of subduction zone plate interfaces, and plate interface shear zones in general, often lead to simplified models and interpretations to address specific processes within an inherently complex system (Bekins and Dreiss, 1992; Dahlen, 1990; Oleskevich *et al.*, 1999). Recent work, has begun to recognise the role of this complexity in influencing slip style (Barnes *et al.*, 2020; Beall *et al.*, 2019; Wang and Bilek, 2014). Whether compositional, topographic, or rheological, this complexity is often broadly referred to as heterogeneity. Subduction zone heterogeneity can occur anywhere in the system, from contrasting input materials in the down-going plate down to the final melt fraction released from a subducted slab in the mantle. In this thesis the focus is on this heterogeneity and its effect on deformation at < 20 km depth, approximately corresponding to temperatures < 300 °C (Syracuse *et al.*, 2010).

1.1 Thesis outline

Relative to continental faults, subduction-related shear zones are inaccessible and difficult for structural geologists to study. From near-seafloor sediments at deep ocean trenches (e.g. Byrne *et al.*, 1993; Fagereng *et al.*, 2019; Maltman, 1998) the plate interface deepens landward beneath the forearc crust, becoming increasingly difficult to study directly. A more indirect approach is therefore required to characterise plate interface deformation at depth. After a brief introduction to subduction zone slip and deformation, this thesis uses a wide variety of methods to characterise deformation in modern and ancient subduction zone systems in three main parts (I - III).

Part I characterises a modern subduction zone, the northern Hikurangi margin, New Zealand. After a short introduction to the margin (Chapter 2), ocean drilling data and samples are used to study deformation in calcareous-pelagic sedimentary units immediately seaward of the prism toe (Chapter 3). This is followed by imaging and analysis of the forearc, including the gently-dipping plate interface between 12 and 15 km depth, using receiver functions from the NZ3D array (Chapter 4).

Part II characterises structures from ancient subduction in the Gwna Complex in Anglesey, UK, and relates them to deformation at depth on the plate interfaces of modern subduction zone margins. This part also comprises three chapters; these introduce the Gwna Complex (Chapter 5), use field and microstructural data to investigate shear zone rheology (Chapter 6) and the deformation of carbonates at seismogenic depths (Chapter 7). Finally, Part III reflects on the main research questions in relation to the presented research in the synthesis (Chapter 8) and summarises the conclusions and suggested future work (Chapter 9).

1.2 Recognising the slip continuum

Slip on the plate interface of subduction zones has traditionally been regarded to occur rapidly during earthquakes or very slowly as stable creep (Scholz, 1998). Though other controls (such as geometry and material properties) were thought to exert a second-order control on slip style, the main controlling factor was believed to be

temperature (e.g. Hyndman *et al.*, 1997). At shallow depths near the trench, stable sliding occurs in smectite clays; these clays dehydrate to form stronger products at 100-150 °C, thought to define the upper limit of the 'seismogenic zone', the depth range where earthquakes can nucleate (Fig. 1.1; Moore and Saffer, 2001; Oleskevich *et al.*, 1999). Down-dip, at temperatures > 350 °C, thermally-activated stable sliding was believed to dominate because of the aseismic sliding that occurs there (Hyndman and Wang, 1993). Plate interface depths modelled to deform between these temperatures host the greatest concentration of earthquake hypocentres, suggesting a clear depth segregation in slip modes across the forearc. This is illustrated in Fig. 1.1 in the form of red patches hosting transient slip. It has since become apparent that the acceleration of slip to seismic rates is controlled by the strength response of the materials involved at initial slip velocities (Dieterich, 1979). This velocity-strength response is a property of material on the fault surface and is not just reliant on temperature but also normal stress, mineralogy, rock cohesion, fault surface texture (Scholz, 1998).

In the last two decades, detailed analysis of broadband seismic data (0.001-100 Hz) has revealed several new phenomena associated with plate interface deformation in subduction zones: low frequency earthquakes (LFEs), very low frequency earthquakes (VLFEs), migrating microseismicity, and tremor (Beroza and Ide, 2011; Delahaye *et al.*, 2009; Kato *et al.*, 2012; Obara, 2002; Obara *et al.*, 2004; Obara and Kato, 2016; Rogers and Dragert, 2003). These seismic phenomena, along with geodetically-detected periods of slip at rates between creep and seismogenic (Dragert, 2001; Larson *et al.*, 2004; Wallace and Beavan, 2006), led to the recognition of slow slip. Slow slip events (SSEs) typically last from days to weeks, have small stress drops (< 0.1 MPa), and rupture over areas equivalent to seismic wave-generating earthquakes of moment magnitude 6-7.2 (Bürgmann, 2018; Wallace, 2020a). SSEs tend to occur immediately up-dip or down-dip of the seismogenic zone (Fig. 1.1), and have been shown to also occur at temperatures of 450-550 °C (Behr and Bürgmann, 2021) or at shallow depths where they can propagate almost to the trench (Wallace, 2020b). This thesis focuses on plate interface deformation at depths throughout, and shallower than, the seismogenic zone.

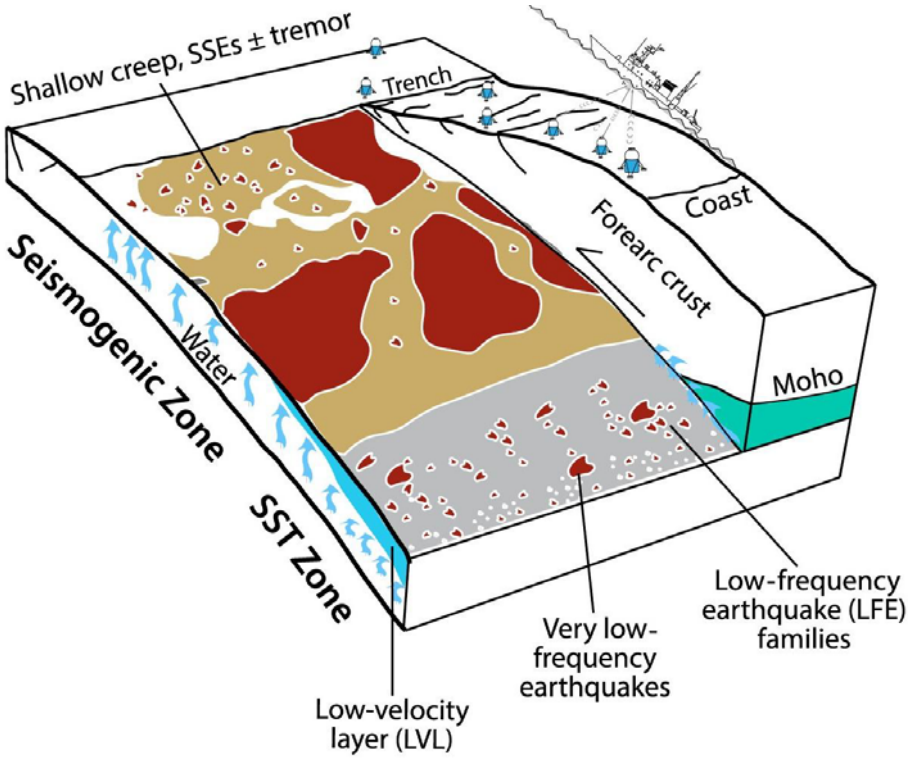

Figure 1.1: Schematic of slip in subduction zones, adapted from Bürgmann (2018). SST = slow slip and tremor.

The discovery of slow slip led to the realisation that a continuum of slip rates on fault surfaces exist between aseismic creep ($\sim 10^{-9}$ to 10^{-12} m s^{-1}) and coseismic slip ($\sim$1 m s^{-1}) (Fig. 1.2; Gomberg *et al.*, 2016; Peng and Gomberg, 2010; Schwartz and Rokosky, 2007). The apparent triggering of slow slip by earthquakes (Wallace *et al.*, 2017), and spatial overlap between earthquakes and slow slip (Ito *et al.*, 2013; Kato *et al.*, 2012; Sun *et al.*, 2017), further asserted this slip rate continuum. It is now clear that transient slip occurs throughout the entire depth range of subduction zone plate interfaces and other sliding surfaces (Fig. 1.2 Gomberg *et al.*, 2016; Leeman *et al.*, 2016; Peng and Gomberg, 2010), suggesting the occurrence and rate of transient slip and creep are determined by additional factors to those inferred from thermally-controlled models (Hyndman and Wang, 1993; Oleskevich *et al.*, 1999).

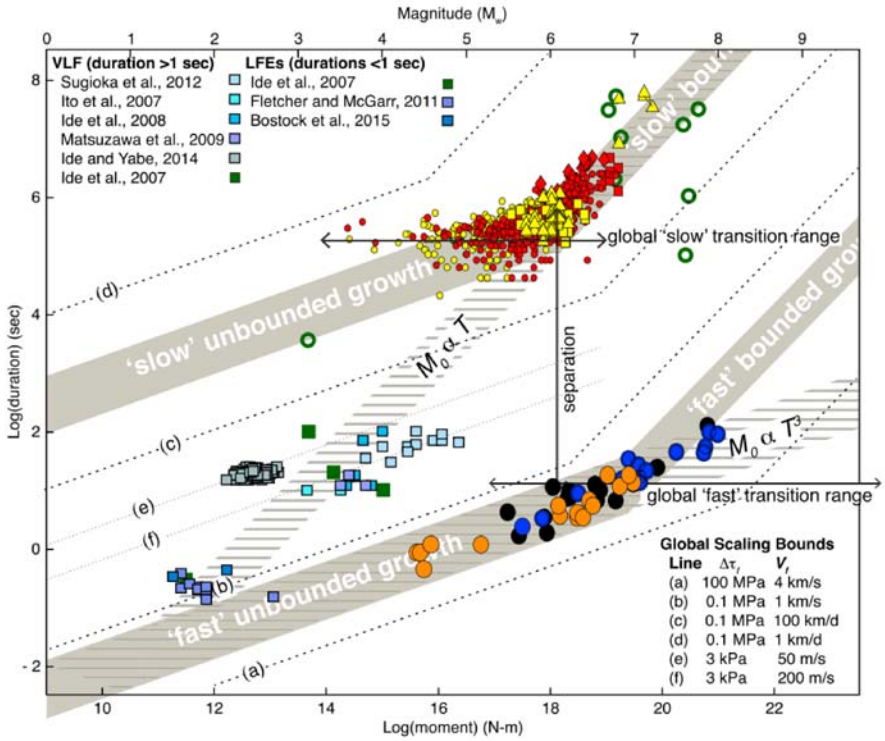

Figure 1.2: Seismic moment (M_0) - duration (t) scaling relationships for a variety of slip events, from Gomberg *et al.* (2016). Shaded areas highlighted interpreted scaling relationships for a rectangular fault transitioning from unbounded to bounded growth, for details see Gomberg *et al.* (2016). Earthquakes shown as filled circles by geographic regions California (black), Japan (orange), other (blue). Slow slip events are shown as smaller squares, triangles, diamonds, and circles. Yellow and red symbols are from analysis by Gomberg *et al.* (2016) in Japan and Cascadia, respectively.

1.3 Stress regimes in subduction zones

Stress in actively deforming subduction zones is difficult to constrain, especially so without direct measurements at depth. Stress is the force per unit area, denoted by σ with units in Pa (or kg m^{-1} s^{-2}). In geological materials, and this thesis, compressive stresses are positive and usually in MPa. In three dimensions the stress tensor is expressed by three perpendicular axes corresponding to the maximum or principal (σ_1), intermediate (σ_2), and minimum (σ_3) principal stresses. In this section a review of methods used to determine stress magnitude and orientation in

subduction zones is presented with a view to show how these methods can provide possible constraints to stress orientations, magnitudes, and distribution along active convergent margins.

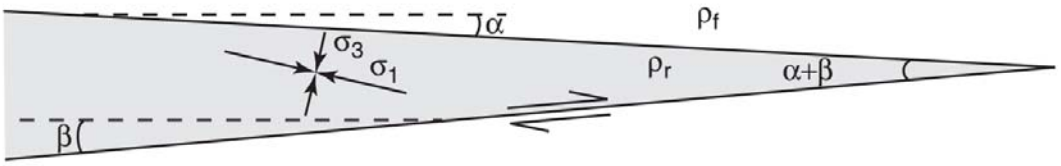

Figure 1.3: Schematic figure illustrating the considered shape of a Coulomb wedge and the variables used in a Coulomb wedge calculation. From Fagereng (2011c).

The Coulomb wedge model describes the steady-state shape of a wedge of unconsolidated material (Figure 1.3) with a material input rate as it is pushed along a surface dipping at a shallow angle (<15°) in terms of the angle between the upper surface of the wedge and the basal surface(Davis *et al.*, 1984). Under constant conditions, and greater displacement from the pushing surface, the shape of the wedge should remain constant but the size of the wedge will grow (Dahlen, 1990). The critical taper angle is dependent on the shear stress and pore fluid pressure at the base of the wedge, and the internal strength of the material comprising the wedge. Coulomb wedges, sometimes called critical Coulomb wedges, are steady-state models constantly on the edge of failure and represent well upper plate wedge geometries over many seismic cycles (Wang and Hu, 2006). Wedges with low friction on the base relative to within the prism, can not maintain a steep wedge upper surface, and deform to a small taper angle. A wedge with a larger taper angle can only occur above a stronger basal shear zone, able to support higher basal shear stresses and leading to the imbrication of thrusts and stacking of associated (folded) strata (Dahlen, 1990). Erosion or deposition of material on the upper surface of a wedge will cause internal reorganisation (by thrust or fold stacking of strata in an upper plate wedge) of the material within the wedge to regain the critical taper angle. A recently-deformed wedge, or one that has been blanketed by sediment, will also 'freeze' until stresses are accumulated and released (Dahlen, 1990). Analysis using the Coulomb wedge theory and remotely or experimentally-derived estimates of

variables can therefore calculate values of effective basal friction. Reasonable values of effective basal friction, which tend to be in the range 0.3-1, can be used in experimental or modelling work on the subduction interface. Analysis of submarine wedges globally indicates interface friction commonly appears to be low, either due to low friction material or high pore fluid pressures (Dahlen, 1990; Davis *et al.*, 1984; Fagereng, 2011c).

Modelling of stress orientations on the interface of subduction zones has been attempted using orientations of principal stresses derived from subduction earthquake focal mechanisms (Hardebeck, 2015). Derived maximum compressive stress orientations plunge systematically trench-ward (opposite to the subduction interface dip direction) at between 10° and 50°, indicating minimum compressive stresses are not vertical as is commonly assumed in Andersonian fault mechanics. This deflected orientation may be due to overburden of the upper plate increasing the vertical stress component of the stress tensor. Regardless, the approximately-optimal angle ($20 - 60°$) of the active shallow subduction interface to the principal compressive stress (σ_1) indicates that the subduction interface is not particularly weak relative to the surrounding material, and low stresses are probably prevalent across weak material throughout the interface and surrounding volumes (Hardebeck, 2015). Low stresses may be maintained across these materials by the subduction and incorporation of a 'lubricant' such as sediment into the fault zone (Lamb, 2006). The inclusion of greater volumes of sediment could lead to low stresses through the alteration of shear zone rheology by inclusion of greater volumes of weak material (Fagereng and Sibson, 2010), increased pore fluid pressure through introducing fluid or reducing permeability (Hubbert and Rubey, 1961; Saffer and Tobin, 2011), via changes or variations in plate roughness and interface complexity (Lamb, 2006; Ruff, 1989; Wang and Bilek, 2014). A weak seismogenic interface only capable of supporting low interface stresses is consistent with weak basal shear strength values modelled from taper angles by Coulomb wedge calculations (Dahlen, 1990; Davis *et al.*, 1984; Fagereng, 2011c).

Measured stress orientations at depth from borehole break-outs within the accretionary wedge of the Nankai margin indicate that maximum horizontal stress

orientations (σ_H) are perpendicular to the margin seaward of, and at the trench, but are parallel to the margin in the upper part of the overriding plate (Chang *et al.*, 2010). A maximum horizontal stress orientation parallel to the margin may indicate a strike-slip regime is dominant in the upper part of the overriding plate, or that σ_1 is subvertical and σ_2 is σ_H (Chang *et al.*, 2010; Chang and Song, 2016). Differential stress on a horizontal plane in the Nankai wedge, at depths of 1800 mbsf, is around 6 MPa (σ_H=55 MPa, σ_h=49 MPa; Chang and Song, 2016). Later, deeper drilling into the same wedge showed that horizontal stress magnitudes diverge at greater depth, suggesting trench-normal horizontal stresses in the wedge increase in magnitude with depth (Kitajima *et al.*, 2017). Near the Japan Trench, Lin *et al.* (2013) showed the Andersonian stress state favouring thrust faulting in the lower part of the upper prism reverted to a stress state favouring normal faulting after the 2011 Tohoku-Oki $M_w = 9.0$ earthquake. The orientation of σ_H at the Japan Trench is thought to be parallel to the plate convergence direction, but has been calculated to be lower than σ_v due to the almost total stress drop associated with coseismic slip upon the plate interface greatly reducing differential stresses (Lin *et al.*, 2013).

1.3.1 The role of fluids on stress and fault stability

Fluids present within the pore spaces of a rock exist within a stress field applied to the bulk rock and are therefore also at pressure within the pore spaces. Fluid pressure (P_f) acts directly against all normal stresses, including the principal stresses (σ_1, σ_2, and σ_3), resulting in effective stress (σ') calculated as

$$\sigma' = \sigma - P_f. \tag{1.1}$$

If pore fluid pressure, which is homogeneous in three dimensions, becomes larger than the least principal stress then $\sigma'_3 < 0$ and the stress becomes tensile in that orientation. Tensile stresses lead to tensile extensional mode I fractures (i.e. a fracture with displacement normal to the fracture plane), but fractures may also open in modes II (shear displacement parallel to the fracture plane and normal to the fracture edge) and III (shear displacement parallel to both fracture plane and

fracture edge) depending on the prevalent stress regime (Irwin, 1957). In subduction zones the two dominant modes are extensional fractures, away from zones of localised shear, and shear fractures near zones of localised shear strain (Fagereng, 2011b).

For fluid pressure to induce extensional fractures at depth, P_f must be greater than the sum of the minimum compressive stress (σ_3) and the tensile strength of the rock (Secor, 1965). Differential stresses in the rock volumes in question must also be low enough to allow the opening of new fractures rather than the reactivation of pre-existing faults. Extensional fractures form perpendicular to the σ_3 direction and open parallel to it. Assuming continuous connected porosity throughout the overlying rocks, fluids at depth are generally at lower hydrostatic pressures resulting from the weight of overlying water. If fluids are not part of an interconnected pore network throughout the thickness of the rock column, P_f is likely to be higher than hydrostatic pressure due to the weight of overlying rock, termed overpressure. If P_f is equal to the pressure from the weight of the overlying rock, this is termed lithostatic pressure. Lithostatic and hydrostatic pressure are calculated using Equation 1.2, where $P_{l/h}$ is lithostatic or hydrostatic pressure, l or h respectively, g is acceleration due to gravity, h is the thickness of material (water or rock) above the measured point, and ρ is the density of the material (rock or water).

$$P_{l/h} = ghp \tag{1.2}$$

Fluid pressure is often reported as the normalised pore pressure ratio (λ^*). Normalised pore pressure ratio is calculated using $\lambda^* = (P_f - P_h)/(P_l - P_h)$ where P_f is pore fluid pressure, P_h is hydrostatic pressure, and P_l is lithostatic pressure. Typical values of λ^* vary between 0 for hydrostatically-pressured conditions and 1 for lithostatic pore pressure (Bassett *et al.*, 2014; Ellis *et al.*, 2015; Saffer and Wallace, 2015).

Aside from direct fluid overpressure within bulk rock volumes, fluids also influence conditions on pre-existing fractures. The activation of sliding on pre-existing fractures is subject to Amontons' Law ($\tau_f = \sigma'_n \mu$). This states that shear stress required for frictional sliding (τ_f) is directly proportional the product of effective normal stress on the sliding surface (σ'_n) and a dimensionless constant which is

independent of the sliding velocity and area, termed the coefficient of friction (μ; Amontons, 1699). Differential stresses at which frictional sliding and tensile failure occur are dictated by the Mohr-Coulomb envelope for the material. Lower differential stresses allow tensile failure, whereas higher differential stresses lead to sliding on pre-existing fractures due to reduced effective normal stress (Sibson, 1998).

Through its effect on σ'_n, Pf has an effect on the likelihood of seismic slip on a surface through calculated values of fault stiffness (Kodaira *et al.*, 2004). Fault stiffness describes the response of the fault to relaxation (i.e. the release of force), and is analogous to the stiffness of a spring (Paterson and Wong, 2005). The frictional stability of slip on a fault is controlled by the relative values of stiffness (k) and critical stiffness (k_{cr}) of the fault, calculated using effective normal stress (σ'_n), critical slip distance (D_c), and velocity dependence of steady-state friction ($a - b$):

$$k_{cr} = \frac{-(a-b)\sigma'_n}{D_c}. \tag{1.3}$$

Velocity strengthening materials (where $a - b$ is positive) will undergo stable slip if $k_{cr} < 0$ (or k) while velocity weakening materials (where $a - b$ is negative) will undergo unstable slip if $k_{cr} > k$ (Scholz, 1998). When $k_{cr} \approx k$, quasi-static oscillations of episodic sliding occur. Indeed, even if k is slightly larger than k_{cr} stick-slip instability may occur if the system is perturbed (Kodaira *et al.*, 2004). By influencing the effective normal stress, pore fluid pressure exerts a control on k_{cr} and consequent fault stability.

1.4 Subduction zone permeability and fluid pressure

Fluid flow in a subduction zone is controlled by the permeability of rocks throughout the forearc wedge. Permeability distribution within a subduction zone controls the locations of fluid flow; high permeability contrasts lead to localised fluid flow and low permeability contrasts lead to distributed fluid flow (Figure 1.4; Saffer and Tobin, 2011). Here, permeability values and fluid pathway distribution are outlined for the

plate interface, and lower and upper plates, and the effect of permeability structure on fluid flow in subduction zones is briefly discussed.

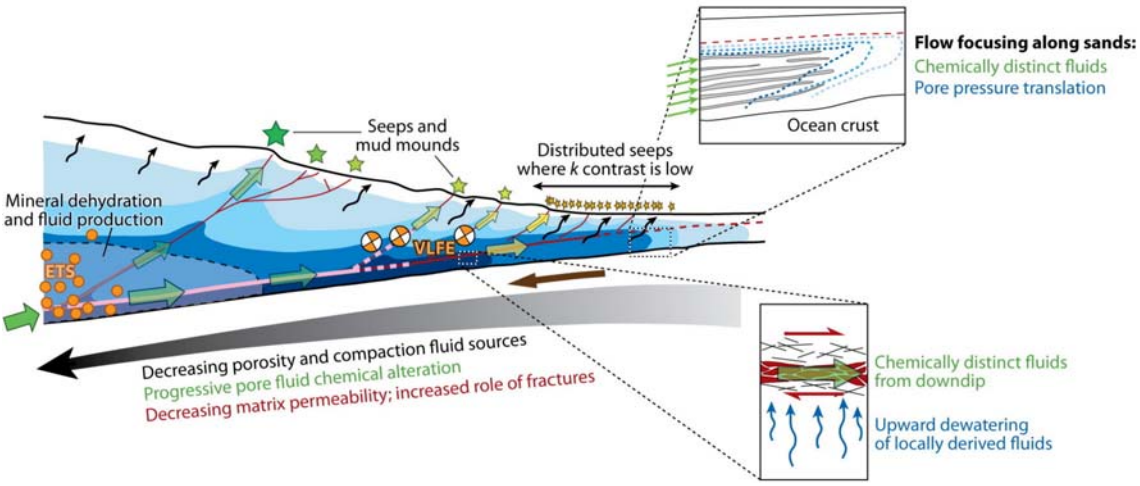

Figure 1.4: Schematic illustration of permeability structure and association with seismic events in the interface and upper plate of a subduction zone, from Saffer and Tobin (2011).

Models utilising laboratory measurements of underthrust and accretionary wedge sediments suggest fault zone permeability is higher than in the variably-consolidated sediment comprising the wedge (Skarbek and Saffer, 2009), so fluid flow there is likely to be directed upward along the fault (Saffer, 2016; Saffer and Tobin, 2011). The upper plate commonly hosts multiple subsidiary thrust faults splaying from the plate interface (Mountjoy and Barnes, 2011; Plaza-Faverola *et al.*, 2016; Rowe *et al.*, 2013). The permeability of these faults is thought to be between 10^{-16} to 10^{-12} m^2 (Lauer and Saffer, 2012; Saffer and Tobin, 2011), two orders of magnitude higher than $\leq 10^{-18}$ m^2 estimated for consolidated sediment at similar depths (Ikari and Saffer, 2012). Incoming sediment at the trench is likely to be poorly consolidated (dependent on depth; Spinelli and Underwood, 2004) and become more consolidated as it is subducted and the pore water is squeezed out (Fagereng *et al.*, 2018; Saffer and Tobin, 2011). The less consolidated sediment near the trench has a higher permeability, leading to a lower permeability contrast with faults than further landward, and more distributed fluid flow throughout the outer wedge (Figure 1.4 Ikari and Saffer, 2012; Saffer and Tobin, 2011). Modelling of fluid flow along splay faults in the wedge gives seepage rates of 0.08 cm yr^{-1} to 2.6 cm yr^{-1} for splay fault per-

meabilities of 10^{-16} to 10^{-12} m^2 (Lauer and Saffer, 2012). Slope sediment atop the upper plate wedge intensely reduces flow rates at the surface by distributing and slowing flow from localised splay faults at the top of the wedge (Lauer and Saffer, 2012). As much as $85 - 90\%$ of fluids expelled from subduction zones exit along localised zones of high permeability, with splay faults tapping the plate interface and expelling as much as 40% of total originating from incoming sediments (Lauer and Saffer, 2012; Saffer and Tobin, 2011).

The plate interface of a subduction zone is composed of multiple zones of anastomosing localised fault strands, commonly of high permeability parallel to fault orientation (Saffer, 2016). The shallow subduction plate interface (< 20 km depth) is commonly thought to form broad shear zones, 100 m to 1 km, wide containing several deforming strands 1-100 m thick (Rowe *et al.*, 2013). Active plate interface faults have been modelled to have an average permeability of 10^{-15} to 10^{-12} m^2 (Saffer, 2016). This probably represents a time-averaged value as transient pore fluid pressure and related permeability increases have become increasingly suspected as the cause of many fluid-associated characteristic signals observed in subduction zones (Saffer, 2016). Thorwart *et al.* (2014) performed analysis of seismic swarm migration along the Costa Rica plate interface and, assuming a transient fluid pressure increase allowed permeability-driven migration of fluid and associated seismicity, determined fault-parallel permeability values of 3.2×10^{-14} to 1.06×10^{-12} m^2 for the plate interface fault zone. Indeed, transient permeabilities are suggested to be between 10^{-13} and 10^{-11} m^2 due to increased pore fluid pressures reducing effective stress and driving rock fracturing during migration along the plate interface (Henry, 2000; Saffer, 2016). The sources of these fluids has been suggested to be from chemical alteration (e.g. smectite to illite) rather than sediment dewatering. Simple analysis of hydraulic communication of faults shows that a highly permeable fault (10^{-12} m^2) only drains adjacent sediments slightly faster than a similar, far less permeable (10^{-16} m^2) fault (Saffer, 2016). Fluids flowing along a décollement bounded by relatively consolidated sediments (i.e. at depths ≥ 5 km) are therefore likely to originate within sediments up to tens of metres from the fault zone (Saffer, 2016), probably dominantly from the footwall.

The lower plate composition of under-thrust sediments and variably-altered basalts varies in permeability, but are likely $\sim 10^{-16}$ m^2 (Saffer, 2016; Saffer and Tobin, 2011). The relative rates of fluid production and transport will control fluid pressure in under-thrust sequences, and the low permeability values estimated for these sequences increase the likelihood of fluid overpressures (Hüpers *et al.*, 2018; Skarbek and Saffer, 2009). Abundant hydrous phases are present in under-thrust sediment and altered oceanic crust and these have been modelled to generate fluid overpressure due to dehydration and compaction between 5 and 70 km of the Costa Rica trench (Kameda *et al.*, 2015). This is thought to enhance permeability and aid upward migration to the décollement, where permeability is higher (Saffer, 2016). Indeed, vein compositions around a paleo-décollement in the Mugi Mélange have been shown to be buffered by oceanic compositions (Yamaguchi *et al.*, 2012). This suggests fluid originating from under-thrust sediments and oceanic material beneath the plate interface can flow to the thrust at relatively high fluid pressures, forming veins.

1.5 Deformation and rheology of subduction shear zones

Slip rate in shear zones (V) is a function of the deforming width (H) and the strain rate ($\dot{\gamma}$) resulting from the dominant deformation mechanisms ($V = \dot{\gamma}H$). Shear zone width, and thus slip rate, is controlled by the mechanisms' resistance to deformation operating in its constituent rocks (Gardner *et al.*, 2017; Hull, 1988; Moore and Byrne, 1987). Though sliding on surfaces is frictional, deformation mechanisms in rocks are often described as viscous, ductile, or brittle, and there is some uncertainty regarding the definitions of these terms (Wang, 2021). Given the varied scales and temperatures of deformation structures and processes studied here, these terms are now defined for use in this thesis. Brittle deformation is use here to describe fracture and cataclasis, where the rock is deformed without significant intracrystalline or mass transfer processes. In contrast, ductile deformation is used to describe strain without significant brittle deformation at the scale of observation. This includes

deformation by mass transfer or intracrystalline mechanisms. As used in this thesis, the term viscous is used to describe irreversible deformation by grain-scale mechanisms at a rate which depends on the instantaneous applied stress. Mechanisms of viscous deformation are often thermally-controlled, and also include mass transfer and intracrystalline mechanisms. Later on, the term crystal-plastic is used. This broadly describes deformation by intracrystalline creep involving the migration of dislocations, specifically excluding mass transfer processes. An understanding of what mechanisms are operating, and what exerts control on them, is therefore of paramount importance when using this terminology.

1.5.1 Micro-scale deformation mechanisms

Pressure solution (or dissolution-precipitation creep) is a term used for stress-driven, fluid-assisted mass transfer, and represents the dominant ductile deformation mechanism in the upper crust (Durney, 1972; Gratier *et al.*, 2013; McClay, 1977; Rutter, 1983). On an idealised spherical grain, material on the side of the grain oriented perpendicular to the principal stress direction (σ_1) undergoes dissolution due to the increased normal stress present on that side of the grain and the dissolved mass is transferred to the sides of the grain oriented parallel to σ_1, where it may precipitate. Over long periods of time, commonly limited by the rate of mass transfer by diffusion along the grain boundary, the grain becomes elongated parallel to the minimum stress orientation (σ_3; Rutter, 1983). Pressure solution is severely limited by composition (the presence of clays dramatically increases pressure solution rates; Aharonov and Katsman, 2009), fracturing (which provides increased surface area and aids pressure solution; Gratier *et al.*, 1999), and healing (which limits the rate of precipitation; Yasuhara *et al.*, 2005). Pressure solution occurs at low temperature and pressure conditions, as evidenced by stylolites formed during the diagenesis of sedimentary rocks, and is therefore considered a likely mechanism by which shallow subduction interface shear zones may deform (Fagereng and Den Hartog, 2017).

Cataclasis describes grain fracturing, but is generally described alongside cataclastic flow which describes frictional sliding, and rotation of a mixed grain-size aggregate within a brittle fault zone (Passchier and Trouw, 2005). Cataclasis rep-

resents the initial stages of gouge formation within which cataclastic flow occurs (Paterson and Wong, 2005). Cataclasis and pressure solution often occur simultaneously in fault zones, leading to complex weakening and strengthening at shallow depths (Gratier *et al.*, 2013). For instance, pressure solution can act on the increased surface contact area of finer grains formed during fracturing and cataclastic flow, weakening the fault zone (Passchier and Trouw, 2005). Alternatively, pressure solution can increase the contact area of grains by dissolution at those contacts, strengthening the gouge in a fault zone (Gratier *et al.*, 2013). This could lead to migration of deformation elsewhere, or increased shear stresses required for deformation to continue within an existing shear zone. Cataclasis occurs at low pressure and forms fractures by microcrack formation and densification until a larger-scale crack forms along the microcrack-dense surface (Healy *et al.*, 2006; Reches and Lockner, 1994). Microcracks, and larger cracks, are generally planar but may curve if the stress field around the fracture tip interferes with that of another microcrack. Microfractures form by increases in stress at their nucleation sites, commonly due to increased differential stress in the bulk rock volume (i.e. pore pressure reduction in porous rocks; Healy *et al.*, 2006; Paterson and Wong, 2005). Individual offsets of microcracks are infinitesimal; material is commonly precipitated within microcracks, healing them and leaving only a trail of fluid inclusions as evidence of their existence. Cataclasis becomes a geologically significant deformation process when microcracks coalesce to form a fracture or fault surface and displacement across this surface is macroscopically-measurable. Once a fault with displacement has formed, cataclastic flow predominates within the localised shear zone as less work is required to deform the now pre-existing fault rather than form new fractures nearby (Reches and Lockner, 1994). Cataclastic flow can occur by any mode on a continuum between purely grain boundary sliding or purely grain fracturing, which is much slower.

Cataclastic aggregates often have fractal grain size distributions (Blenkinsop, 1991; Keulen *et al.*, 2007; Turcotte, 1992). Fractal grain size distributions in fault gouge can result from a variety of initial grain size distributions by fragmentation processes including shattering and crushing. Sammis *et al.* (1987) proposed a model of constrained comminution whereby finite simple shear strain is accommodated

along 'beams' of grains transferring stress throughout the gouge. Stresses within a beam parallel to the deforming volume margins reduce and stresses perpendicular to the deforming volume margins increase proportional to the constraining pressure, causing a pressure-dependence on gouge deformation. Grains comprising the beam are placed under uniaxial compression and will fail when the appropriate differential stress is reached. Grain failure accommodates shear strain and alters stress trajectories through the gouge. Similar processes have been described for 'force chains' comprising beams of clasts within a deforming subduction mélange in a shear zone (Beall *et al.*, 2019).

Veining is the process whereby fluids in a fault zone precipitate material within a fracture or crack. Veins can form within pre-existing voids in a rock by purely passive precipitation, but voids at depths are generally kept closed by the ambient stress field. In this case, for fluid to precipitate within the crack the crack must be opened by fluid pressure exceeding σ_3 (Bons *et al.*, 2012; Ramsay, 1980b; Secor, 1965). As this condition is achieved the crack will open parallel to σ_3 and solute in the fluid can precipitate within the crack. Material precipitates in a vein when its solution becomes supersaturated. The higher the degree of supersaturation, the higher the rate of precipitation will be (Fyfe *et al.*, 1978). Solute in the fluid is sourced from the dissolution of minerals by the fluid, dependent on their solubility at given conditions (e.g. Plummer and Busenberg, 1982; Rimstidt and Barnes, 1980). Rates of solution are generally low at low temperatures, meaning pressure solution is an important source of solute for precipitation in veins in the shallow crust (Rutter, 1983). Supersaturation can occur due to variations in temperature, pH or salinity, amongst other factors (Bons *et al.*, 2012). Fluid pressures in shear zones are often transient, leading to rapid variations in pressure (Saffer and Tobin, 2011; Sibson, 1994). Mineral solubilities increase with pressure (Fyfe *et al.*, 1978), so pressure drops associated with fluid escape can lead to rapid supersaturation and precipitation within veins. These veins are characterised by chaotic distributions of grains formed by supersaturation of mineralogies with contrasting solubility relationships (e.g. Meneghini and Moore, 2007). Analysis of vein opening directions can therefore lead to insights regarding the palaeo-orientation of σ_3 or shearing direction

across a vein (Bons *et al.*, 2012; Secor, 1965).

1.5.2 Shear zone rheology

A shear zone is here defined as a tabular volume accommodating high shear strain by localised slip, commonly upon multiple anastomosing strands (Ramsay, 1980a; Rowe *et al.*, 2013). Strain within shear zones varies locally between stronger fragments (commonly lenticular and termed phacoids) and weaker matrix material. The distribution of strain localisation and shear strain rate of the shear zone is dictated by the strength ratio of strong and weak material and the volume percent of weak matrix (Figure 1.5; Fagereng and Sibson, 2010). Shear zones containing relatively weak or very little matrix material will tend to deform by discontinuous deformation as interaction between phacoids will be constrained to stress bridges, causing localised peaks in shear strain rate. Shear zones with relatively strong or abundant matrix material will deform by continuous deformation whereby shear strain rate is near-homogeneously distributed across the shear zone due to the rare interaction of phacoids localising shear (Fagereng and Sibson, 2010). Interaction of phacoids can cause 'stress bridges' (sensu Webber *et al.*, 2018), areas of anomalously high stress dipping in the direction of slip transmitting strain between phacoids. In contrast, alignment of multiple matrix-rich pathways between phacoids causes localisation of strain onto surfaces throughout the pathways, transmitting little strain between phacoids (Webber *et al.*, 2018). The volume fraction of weak material is thought to have an effect on the seismic style of a shear zone by limiting (for high fractions) or not-limiting (for low fractions) the interaction of stronger material within the shear zone (Fagereng and Sibson, 2010).

Continuous-discontinuous shear zones contain intermediate volumes of matrix material and are characterised by continuous fabrics across their width, such as scaly clay foliations cut by discontinuous (i.e. localised) surfaces such as faults and fractures between phacoids (Fagereng and Sibson, 2010). In some mélanges the term 'block-in-matrix fabric' has been used to describe lenses of competent material between bands of foliated phyllosilicate-dominated matrix (Bettelli and Vannucchi, 2003; Remitti *et al.*, 2011; Vannucchi *et al.*, 2008, 2009). Shear strain

rates are dominantly higher in the matrix and lower in blocks of competent materials. Textures of weak and strong phases therefore reflect the relative proportions of strain each has accommodated. Strong phacoids within a weaker shear zone matrix may refract stress orientation and experience greater stress magnitudes than the surrounding material, resulting in distinct deformation structures (Fagereng, 2013).

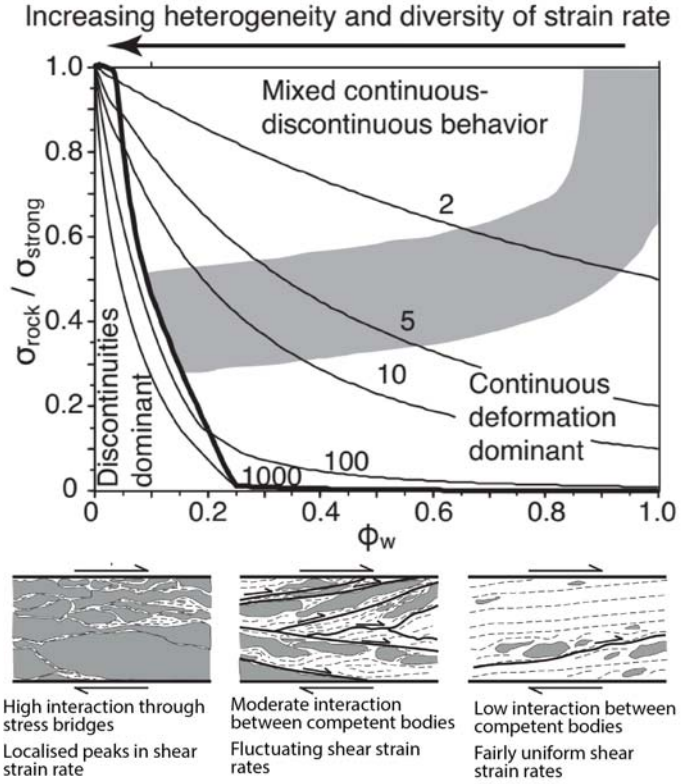

Figure 1.5: Graph and schematic figures showing the degree of deformation continuity in a two-phase aggregate due to relative strong/weak voume fraction (Φ_W) and normalised rock strength (σ). Region indicating deformation mode are discerened from the Chrystalls Beach Complex. Numbered contours illustrate the path of variable strength ratios. Illustrations and accompanying notes show the interaction of strong phacoids (grey) and weaker matrix (dashed white) and its effect on strain shear rate. From Fagereng and Sibson (2010).

Examples of discontinuous deformation fabrics include faults, fractures, and veins. Commonly observed within shear zones are both fault-fracture mesh and Riedel faulting schemes (Fagereng, 2011b; Kimura *et al.*, 2012; Sibson, 1996). A fault-fracture mesh describes interlinked shear and extensional surfaces which rep-

resent the brittle component of deformation within a shear zone. Faults commonly form marginal to competent phacoids, while extensional fractures form adjacent to and within competent phacoids (Fagereng, 2011b). Riedel shear schemes represent the systematic orientation of brittle faults at particular angles and shear senses relative to the bulk shear sense (Paterson and Wong, 2005). The development of Riedel shear surfaces is systematic; R surfaces develop at $+15°$ to the shear zone boundary, followed by R′ surfaces at $-105°$. Further deformation forms P, Y, and T surfaces at $-15°$, $0°$ (parallel), and $+45°$, respectively. It should be noted that these angles are not absolute and will vary depending upon the internal friction of the deforming material. Internal friction for many materials is most often $30°$, giving the orientations described above (Paterson and Wong, 2005). Continuous deformation fabrics may include S-C fabrics, dismembered bedding, and other cleavages continuous across the shear zone. These textures indicate a ductile mode of shear over a volume, analogous to homogeneous simple shear of the entire shear zone (Fagereng and Sibson, 2010).

1.6 Mechanisms of slow fault slip

Slow slip events (SSEs) are defined as periods of elevated slip rate 'at a rate intermediate between long-term tectonic plate motion and the slip velocity required to generate seismic waves' upon a region of the subduction interface (Saffer and Wallace, 2015). This thesis considers SSEs at shallow to intermediate depths, defined here to occur within or above the subduction thrust seismogenic zone. To understand the processes occurring during shallow SSEs, the principal controls on fault strength and slip on shallow (>20 km) areas of the subduction interface must be examined. Comparing spatial correlations between slow-slipping areas and conditions on the same subduction interface may allow more robust determination of the conditions controlling shallow SSEs.

The onset of slip in an SSE may be considered a pseudo-rupture as rupture propagation velocities are slow ($\sim$ 10 km/day) and stress drops are low ($<$ 1 MPa; Ando *et al.*, 2012). Initiation of slip on an area of the host fault is controlled by the shear

strength of the fault interface at the host region, itself controlled by the pore fluid pressure, friction coefficient and cohesive strength of fault materials, stiffness, and fault normal stress (Scholz, 1998). Within a subduction zone, parameters exerting a control on these factors (and thus interface shear strength) might be: temperature, frictional properties of the subduction interface, or fluid presence and generation within the subduction zone. In this section, the mechanisms by which these potentially important factors could affect shallow SSE occurrence are described.

1.6.1 Temperature

Advances in computer modelling have allowed the broad-scale estimation of subduction zone thermal regimes, but many relevant factors remain poorly constrained (Antriasian *et al.*, 2018; Harris *et al.*, 2013, 2017; Syracuse *et al.*, 2010). SSEs occur across a wide range of modelled temperatures due to the depth variation of shallow SSEs between individual subduction zones with distinct geothermal gradients (Table 1.1; Saffer and Wallace, 2015). Estimated temperatures at plate interface depths hosting slow slip vary between margins (Table 1.1). SSEs at Costa Rica and northern Japan seem to correlate with relatively low temperatures (∼12-60 °C and 65-110 °C, respectively), whereas the northern Hikurangi and Nankai subduction zones host SSEs to much greater depths and temperatures ($15 - 230$ °C; Antriasian *et al.*, 2018; Saffer and Wallace, 2015; Wallace, 2020a). Temperature estimates vary between subduction zones due to differences in convergence rate and geometry (Table 1.1). This wide variation in temperature suggests slow slip is largely temperature independent, especially if deep SSEs, which occur down-dip of the subduction thrust seismogenic zone at temperatures of 300-450 °C (Saffer and Wallace, 2015; Wallace *et al.*, 2009), are considered to be analogous and controlled by similar factors.

1.6.2 Subduction interface frictional and mechanical properties

Composition and fluid pressure remain relatively poorly constrained and variable factors with strong controls on deformation mechanisms in plate interface shear

Location	**Temperature range (°C)**	**Depth of SSEs (km)**	**Normalised pore pressure ratio**
Northern Hikurangi	85-230	∼3-16	$\sim 0.50 - 0.83$
Nankai	85-210	∼2-4	$\sim 0.54 - 0.77$
Northern Japan	65-110	∼7-11	∼0.91
Costa Rica	12-60	∼2-10	∼0.4-0.8

Table 1.1: Variation in properties of subduction zones hosting shallow SSEs. Data for Nankai, Costa Rica, and northern Japan from Saffer and Wallace (2015), data for the northern Hikurangi margin from Wallace (2020a) and Antriasian *et al.* (2018).

zones. The geological materials present on a subduction interface are derived from the materials entering the shear zone from the trench at the seaward extent of the subduction zone (Saffer and Wallace, 2015). These materials, along with the geometry of the subduction interface, control initial deformation mechanisms and mechanics, and therefore the resultant mechanical evolution of the plate interface shear zone (Fagereng and Sibson, 2010; Rowe *et al.*, 2013; Saffer and Marone, 2003; Scholz, 1998; Underwood, 2007).

Sediment composition on subduction margins is generally considered to be clay (smectite-illite) and quartz rich (Rowe *et al.*, 2013; Saffer and Wallace, 2015; Spinelli and Underwood, 2004), which, under the low normal stresses present in shallow areas of the subduction interface (Ellis *et al.*, 2015; Saffer and Wallace, 2015), have been shown to exhibit velocity-weakening behaviour (Saffer and Marone, 2003; Saito *et al.*, 2013). At low slip rates (< 1 μm s^{-1}) in moderate to low temperature conditions (< 250 °C), similar to those at the up-dip end of the seismogenic zone where shallow SSEs occur, values of $(a - b)$ in wet illite/quartz gouge may be low enough to allow slip nucleation followed by arrest prior to the development of dynamic rupture (Den Hartog *et al.*, 2014).

Lithologies involved in deformation at the plate interface have dominantly been thought to involve siliciclastic sediments (sand and mud) with a minor component of basalt (Fagereng, 2011b; Fisher and Byrne, 1987; Kimura and Mukai, 1991; Meneghini *et al.*, 2009; Remitti *et al.*, 2011; Rowe *et al.*, 2011; Ujiie, 2002; Vannucchi *et al.*,

2008). Recent work at various subduction zones and exhumed complexes has shown that lithological inputs can include significant volumes of carbonates and volcanics (Barnes *et al.*, 2020; Hüpers *et al.*, 2017; Plank and Manning, 2019; Spinelli and Underwood, 2004), and these can be deformed on the plate interface (Behr and Bürgmann, 2021; Meneghini and Moore, 2007; Tulley *et al.*, 2020). This shows there may be more lithological diversity at the plate interface than previously considered, even at shallow levels.

Although temperature may not offer a primary control on the occurrence of SSEs, temperature conditions on the interface may influence the mechanical properties of the interface material and influence possible modes of slip through the rate and state friction variable ($a - b$ in Equation 1.3). Stiffness (k) is proportional to the ratio of shear modulus to rupture nucleation patch size and would be reduced by large rupture nucleation patch sizes (Leeman *et al.*, 2016). When a larger area of fault nucleates rupture, the stiffness is lower than if a smaller area nucleated rupture. This might favour slow slip behaviour due to the large areas on the subduction interface involved in SSEs, though little is known about the rupture nucleation patch size of such events.

Globally, porosity in areas which produce SSEs and VLFEs spans a wide range of values (<2% to 30-40%). High values of porosity may translate to connected permeability throughout rock volumes which would allow the maintenance of fluid pressures. Elevated fluid pressures reduce effective stress, reducing the critical stiffness of the fault and possibly making the fault critically unstable and more susceptible to slow slip (Kodaira *et al.*, 2004). There are therefore several possible ways in which frictional behaviour could explain slow slip, but constraints on these are poor in natural settings.

1.6.3 Fluids

Fluids have been widely suggested as a mechanism for altering frictional properties and deformation mechanisms of materials within fault zones (Ellis *et al.*, 2015; Hickman *et al.*, 1995; Saffer and Wallace, 2015; Sibson, 2017; Wintsch *et al.*, 1995). Within subduction zones, fluid overpressure could reduce effective stress on the sub-

duction interface and actuate shallow slow slip under conditions otherwise favouring interseismic locking or stable creep (Bassett *et al.*, 2014; Ellis *et al.*, 2015; Husker *et al.*, 2018; Kodaira *et al.*, 2004). Evidence for high fluid pressures on plate boundary faults manifests as fabric-cutting veins in ancient accretionary terranes, and high fluid pressures in boreholes (Barnes *et al.*, 2010; Ellis *et al.*, 2015; Fisher and Byrne, 1987; Sibson, 2017). The extent of these overpressures on modern subduction interfaces, however, is poorly constrained both spatially and temporally. As well as using seismic and magnetotelluric methods to image subduction zones and infer the presence of fluids (e.g. Bell *et al.*, 2010; Eberhart-Phillips and Bannister, 2015; Heise *et al.*, 2017, 2012), an understanding of processes releasing and channelling fluids in subduction zones is required. The main processes thought to be operating within subducting materials to produce fluid are sediment compaction and mineral dehydration.

Compaction of sediment during subduction causes expulsion of water due to a bulk reduction in pore volume with increased pressure from overburden or tectonic stresses. The volume of water released is dependent on the consolidation state of the sediments, in turn related to their lithology and burial depth prior to subduction (Han *et al.*, 2017). Fluid release from porosity reduction has been modelled to produce large quantities of water in subduction zones, mostly within ∼40 km landward of the trench (Bekins and Dreiss, 1992; Ellis *et al.*, 2015; Saffer and Tobin, 2011). The released fluid is thought to migrate upwards towards the plate interface, where elevated permeability is likely to channel flow towards the thrust toe (Fig. 1.4; Ellis *et al.*, 2015).

The dehydration of minerals in subducted materials releases mineral-bound water during subduction due to rising temperatures (Ellis *et al.*, 2015; Peacock, 1996; Saffer and Tobin, 2011). Opal and smectite clay are common throughout sediment on the subducting slab (Spinelli and Underwood, 2004) and are considered to be the most likely to undergo dehydration reactions under the temperature and pressure ranges accompanying SSEs (Saffer and McKiernan, 2009; Saffer and Wallace, 2015); dehydration of opal and smectite occur at ∼60 °C and ∼80-150 °C, respectively (Saffer and McKiernan, 2009; Spinelli and Saffer, 2004).

Smectite group clays are abundant in the young oceanic sediments typically found on the subducting slab, making up ∼40 weight% of incoming sediment (Davy *et al.*, 2008; Ellis *et al.*, 2015; Spinelli and Underwood, 2004). Within their structure, smectite group clays can contain 40 vol% (or 20 weight%) water per m^3 of sediment (Saffer *et al.*, 2008; Spinelli and Underwood, 2004). Illite, in its purest form, contains no interlayer water within its crystal structure so the transformation from smectite to illite within the subduction zone volume is accompanied by the release of fresh water, possibly freshening water within the subduction zone (Saffer and McKiernan, 2009). The transformation from smectite to illite will also change the frictional properties of the material in the subduction zone and, if under-thrust, near the subduction interface (Saffer *et al.*, 2008). The smectite/illite transition may therefore provide a source of water released throughout shallow subduction, possibly producing volumes of water comparable to sediment compaction, though at depths near the up-dip limit of the seismogenic zone (Ellis *et al.*, 2015; Spinelli and Saffer, 2004). Water released by clay transformation may be important for cementation of lithologies nearer the trench by incorporation and transport of ions throughout the relatively high-permeability fault zone (Moore and Vrolijk, 1990). The transition to illite also appears to be associated with a mechanical strengthening due to the distinct frictional properties of smectite and illite (Morrow *et al.*, 1992).

The volumes of water liberated from mineral transformations at the subduction interface are dependent on the fraction of those minerals present within the subducting sediment. Despite pore volume hosting the dominant fraction of water in a sediment column, intracrystalline water in smectite and opal can represent >4 weight% water (Spinelli and Underwood, 2004). Clay transformational regions lie within the slow slipping zone of the northern Hikurangi margin and coincide with VLFE swarms on the Nankai margin, but dehydration maxima occur far downdip of SSE hypocentres on the northern Japan and Costa Rica subduction interfaces (Saffer and Wallace, 2015). As a thermally-activated process, mineral dehydration releases fluid over a large depth range, meaning the volume released is less than sediment dewatering at shallow depths (Ellis *et al.*, 2015; Spinelli and Saffer, 2004).

1.7 Main research questions

As the previous section has shown, deformation and rheology during creep and slow slip on the shallow subduction zone plate interface is controlled by many factors. The principal research topics that arise are the roles of lithological inputs, fluids, and plate interface geometry on shallow plate interface deformation. Research questions addressed in this thesis are framed around these topics and their relation to slow slip, and will be addressed using case studies of both an active and an exhumed subduction margin.

How do subduction zone input lithologies control deformation and resultant mechanical evolution?

Subduction zone input lithologies seaward of the northern Hikurangi margin are studied directly in Chapter 3 using samples and data from drilling. The role of input lithologies more broadly, as well as their role in controlling strain localisation, deformation, and mechanical evolution, is considered further using seismic, field, and modelling data throughout Chapters 4, 6, and 7.

Do elevated fluid pressures influence deformation at shallow (< 20 km) depth in subduction plate interface shear zones?

The influence of fluid pressure on deformation in a plate interface shear zone is most intensively studied in Chapter 6. This chapter presents field and microstructural data, as well as modelling informed by those data, from an exhumed subduction complex in Anglesey, UK. Fluid pressures are also considered at the northern Hikurangi margin in relation to deformation in input sediments and slip on the plate interface in Chapters 3 and 4.

How could subduction plate interface shear zone geometry influence deformation style?

Plate interface geometry is studied at varied scales throughout this thesis. Initially, input lithologies are used to estimate where grain-scale strain localisation will occur

at the northern Hikurangi margin thrust toe in Chapter 3. Receiver function analysis then considers the km-scale geometry of the same plate interface at 12-15 km depth in Chapter 4. To complement this analysis at a modern margin, the geometry of exhumed km to μm scale shear zones studied using field and microstructural analysis in an ancient subduction complex are presented in Chapters 6 and 7.

Which factors control shallow slow slip and how might they be better constrained?

Slow slip represents a dynamic process which is likely controlled by the interplay of several factors within a subduction plate interface shear zone, and is therefore relevant to all the research presented in this thesis. Specific mechanisms for slow slip are considered in Chapters 3, 4, and 6.

1.8 Chapter contributions

Chapters 1, 2, 5, 8, and 9 are all my work in introducing the thesis and its context, the study areas, and synthesising the data and interpretations from the original science chapters. The original science chapters are all outcomes of collaborative research, and author contributions are outlined below.

Chapter 3

The research presented in Chapter 3 uses a wide variety of data types obtained by a large collaborative team during IODP Expedition 375. The work forms the basis for a research article published in 2020 in the journal *Tectonics* titled "Mixed Brittle and Viscous Strain Localization in Pelagic Sediments Seaward of the Hikurangi Margin, New Zealand" (DOI: 10.1029/2019TC005965). The co-author contributions to the paper, and chapter, are as follows: Å. Fagereng participated in data collection during IODP Exp. 375, selected samples from the core, supervised the analysis and modelling, discussed the results and modelling, and provided input while writing the manuscript; F. Meneghini, J. K. Morgan, H. M. Savage, M. Wang, R. Bell, and M. J. Ikari all participated in data collection during IODP Exp. 375, reviewed

the manuscript and discussed the results and interpretations. The initial concept for the chapter was conceived by the shipboard party during IODP Exp. 375, but was adapted by myself to include modelling following microstructural analysis. Microstructural analysis, modelling, stylolite and fault counting, and writing of the chapter were carried out by myself.

Chapter 4

The receiver function analysis in Chapter 4 uses data from seismometers in the NZ3D temporary seismometer array, for which a field acquisition report has been published (Bell *et al.*, 2018). Seismometers in the NZ3D array were provided by SEIS-UK. Deployment and servicing of the seismometers was carried out by a large team led by R. Bell and including myself, Å. Fagereng, J. Morgan, M. Warner, L. McNeill, S. Henrys, K. Jacobs, B. Fry, J. Black, P. Upton, V. Lane, D. Daly, W. Stratford, S. Evans, T. Phillips, H. Lacey, M. Gray, S. Watkins, K. Chrapkiewicz, T. Kalinicheva, J. Hoadley, C. Woodsford, T. Merry, X. Wang, D. Stevens, D. Lindsay, L. Hughes, M. Kortink, P. Herath, J. Kearse, D. Orr, I. Hamling, R. Hart, E. Warren-Smith, and C. Van Houtte. Data Download and quality control at the end of the deployment was carried out by SEIS-UK and R. Bell. Initial implementation of receiver function deconvolution of the data was carried out by myself with the supervision of D. Thompson, and later analysis was supervised by I. Bastow. Å. Fagereng, I. Bastow, and R. Bell helped discuss results and interpretations, and Å. Fagereng and I. Bastow reviewed the chapter manuscript. The idea for the project was initially conceptualised by D. Thompson, Å. Fagereng and R. Bell, though noise analysis of data, selection of methods, adaptation and writing of code, interpretation, and writing of the chapter were carried out by myself.

Chapter 6

The geological map of Llanddwyn Island, Anglesey, UK, presented in Chapter 6 results from data collected by myself and N. Groome during field seasons throughout 2018 and 2019. N. Groome initially drafted the map, but later revisions were carried out together. N. Groome and D. Buchs helped discuss results and interpretations

presented in the chapter. Å. Fagereng supervised the data collection, discussed results and interpretations, and reviewed the chapter manuscript. The initial concept for the chapter was outlined by Å. Fagereng as part of the funding proposal for this project. Fieldwork, sampling, thin section selection and cutting, microstructural analysis, modelling, and writing of the chapter were all carried out myself.

Chapter 7

This chapter was conceptualised by myself from EBSD data collected on samples from the Gwna Complex. I carried out a review of ocean drilling cores, carried out microstructural analysis, interpretation, and writing of the chapter. Å. Fagereng discussed results and interpretations from microstructural analysis and reviewed the chapter manuscript.

Part I

The northern Hikurangi margin - a modern subduction margin

Chapter 2

The Hikurangi margin

The Hikurangi Margin, on the east coast of the North Island of New Zealand, is the result of the westward subduction of the Pacific Plate beneath the Australian plate at 40-50 mm yr^{-1} (Figure 2.1a-c; Wallace *et al.*, 2004). The subducting Pacific Plate comprises an 18-25 km thick Cretaceous-age buoyant oceanic plateau (the Hikurangi Plateau) (Davy *et al.*, 2008; Mortimer and Parkinson, 1996), which causes uplift and reduces the depth to the accretionary wedge and trench (Davy and Wood, 1994; Seebeck *et al.*, 2014), making geophysical observation of the margin more accessible than at other margins.

Shallow subduction of the buoyant Hikurangi Plateau may mean the Hikurangi margin plate interface has an anomalous character (Barnes *et al.*, 2020; Herath *et al.*, 2020), raising questions about its representativeness with regards to other subduction margins globally. Around the world, subduction margins have differing characteristics within a broadly similar structure (Syracuse *et al.*, 2010). Variations within this structure are present at most margins, but most host some similar observations which can be compared. Away from the Hikurangi margin, shallow slow slip events have been recognised at other margins (Saffer and Wallace, 2015), some of which have zones of high-amplitude reflections imaged in active seismic studies (Kimura *et al.*, 2009; Kodaira *et al.*, 2000; Nedimović *et al.*, 2003) similar to that imaged at the Hikurangi margin (Bell *et al.*, 2010). Whereas the particular condition of subducting an oceanic plateau may be anomalous, processes that the shallower plate interface allows us to interpret may be extended to other margins if carried

out with care.

The Pacific Plate is moving westward, towards an azimuth of 263°, at 45 mm yr^{-1} relative to the Australian Plate (Fig. 2.1b & c; Beavan *et al.*, 2002; Wallace *et al.*, 2004). Southward, this vector decreases in magnitude and rotates anticlockwise to become 42 mm yr^{-1}, oriented parallel to the margin at the south end of the North Island (Nicol *et al.*, 2007). This variation in velocity is associated with a clockwise rotation and consequent oblique convergence of the North Island fore arc relative to the Pacific Plate (Beavan *et al.*, 2002). Across the margin, slip appears to be partitioned between margin-parallel slip in NE-SW oriented axial ranges and margin-normal slip on the plate interface (Fig. 2.1d; Beanland and Haines, 1998; Wallace *et al.*, 2004). Interseismic coupling of the Hikurangi margin subduction interface varies in distribution along strike (Wallace *et al.*, 2004). Interseismic coupling of the subduction interface underlying the southern North Island range from 0.8-1.0 whereas north of Hawke's Bay values are much lower (0.1-0.2) (Wallace *et al.*, 2004, 2009). Low interseismic coupling values may reflect dominant aseismic creep on the subduction interface. Higher values of interseismic coupling suggest creep is much less dominant, and seismic slip accommodates a larger fraction of total slip on the plate interface (Wallace *et al.*, 2004, 2009).

Multiple slow slip events (SSEs) have been documented along the Hikurangi margin since the onset of data collection at continuous GPS stations in 2002 (Koulali *et al.*, 2017; Wallace, 2020a; Wallace and Beavan, 2006, 2010; Wallace *et al.*, 2012). SSEs on the northern Hikurangi margin occur at < 20 km depth, around a similar range of depths to other shallow SSEs globally (Saffer and Wallace, 2015), accommodate up to 250 mm of slip over several days or weeks, and recur every 2 to 5 years (Wallace, 2020a,b; Wallace and Beavan, 2010). In contrast, the subduction interface underlying the southern North Island produces SSEs of greater equivalent moment magnitude (>7.0), with durations of months, further down-dip at 25-70 km depth (Wallace and Beavan, 2006, 2010). SSEs in the north and south both occur immediately down-dip of interseismic coupling changes from high to low values (Wallace *et al.*, 2004). As well as slow slip, the northern part of the Hikurangi Margin is characterised by episodic seismicity of variable character, including large tsunami

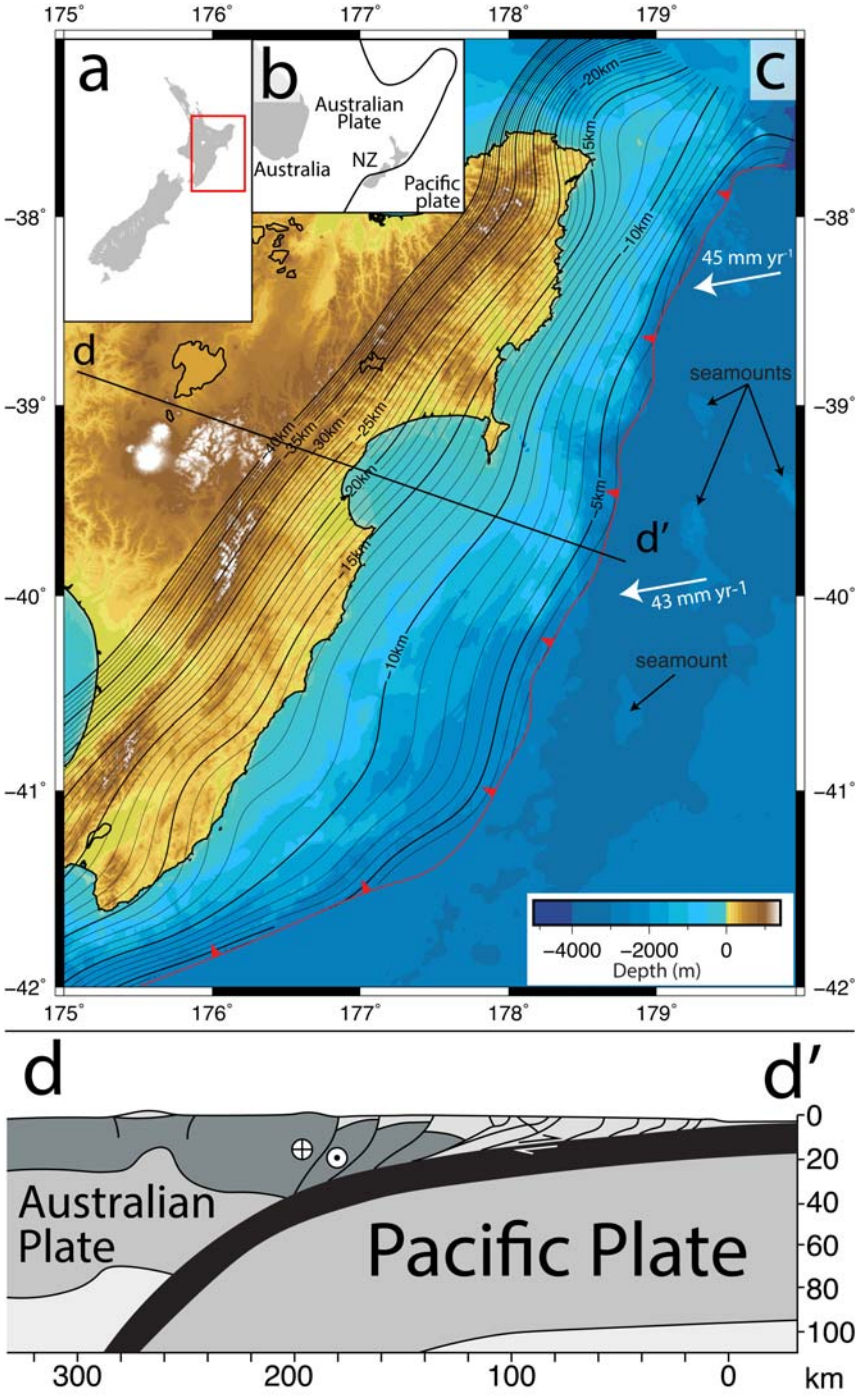

Figure 2.1: Map and interpretive section across the Hikurangi Margin. Panels show (a) map location relative to New Zealand, (b) broad tectonic setting of the Hikurangi-Kermadec-Tonga-Fiji arc adapted from Wallace *et al.* (2009), (c) coloured bathymetry and contoured plate interface depth from Williams *et al.* (2013) with convergence vectors from Beavan *et al.* (2002), (d) interpreted cross section, adapted from Wallace *et al.* (2009), with crustal thickness estimate from Davy *et al.* (2008). Location of (d) shown as NW-SE trending line in (a).

earthquakes ($\geq M_w7$, Clark *et al.*, 2019; Doser and Webb, 2003; Pouderoux *et al.*, 2014; Wallace *et al.*, 2014), microseismicity (Delahaye *et al.*, 2009), and tectonic tremor (Todd and Schwartz, 2016; Yabe *et al.*, 2014).

Seismicity at the northern Hikurangi margin is generally concentrated in the oceanic lower plate, though some tsunamigenic earthquakes have occurred on the plate interface there (Clark *et al.*, 2019; Shaddox and Schwartz, 2019; Todd *et al.*, 2018). The crustal volume hosting slow slip likely encompasses the plate interface and shallow tsunamigenic earthquake hypocentres, extending from near the trench to 15-20 km depth (Fig. 2.2a; Wallace, 2020b). Earthquakes in the southern Hikurangi margin are rare at shallow depths; at $>$ 20 km depth hypocentres are distributed throughout the lower plate, upper plate, and plate interface but are limited by varied terranes in the upper plate (Reyners, 1998). On the southern Hikurangi subduction interface, earthquakes delineate a seismogenic zone extending to $\sim$40 km depth (Reyners, 1998; Wallace *et al.*, 2009). Seismic transects have shown that sediment thickness on the incoming plate varies along strike, suggesting a link between sediment thickness and interseismic coupling (Wallace *et al.*, 2004). Sediment in the south is commonly $2-6$ km thick (Davy *et al.*, 2008; Ghisetti *et al.*, 2016), whereas sediment in the north is ≤ 1 km thick adjacent to seamounts $1-3$ km thick between them (Figs. 2.1c & 2.2; Barker *et al.*, 2009; Davy *et al.*, 2008). High amplitude reflections are present in both the incoming plate and down-dip of the slow slip-hosting volume in the northern part of the margin, suggesting incoming material may be under-thrust there(Fig. 2.2c; Bell *et al.*, 2010). The variable sediment cover, moderate convergence rate, rough incoming topography, and steep taper angle suggest the northern Hikurangi margin may be undergoing frontal erosion, and is consequently likely to under-thrust sediment rather than accrete it (Barker *et al.*, 2009; Fagereng, 2011c).

Shallow, well determined SSEs at the northern Hikurangi margin have become a key target for recent international drilling and seismic studies (e.g. Bell *et al.*, 2018; Wallace *et al.*, 2019). Data from both the NZ3D active seismic experiment and IODP Expedition 375 are used here. The Hikurangi Plateau has a rough surface topography; seamounts are exposed through thin ($\leq$ 1 km) sediment cover (Fig.

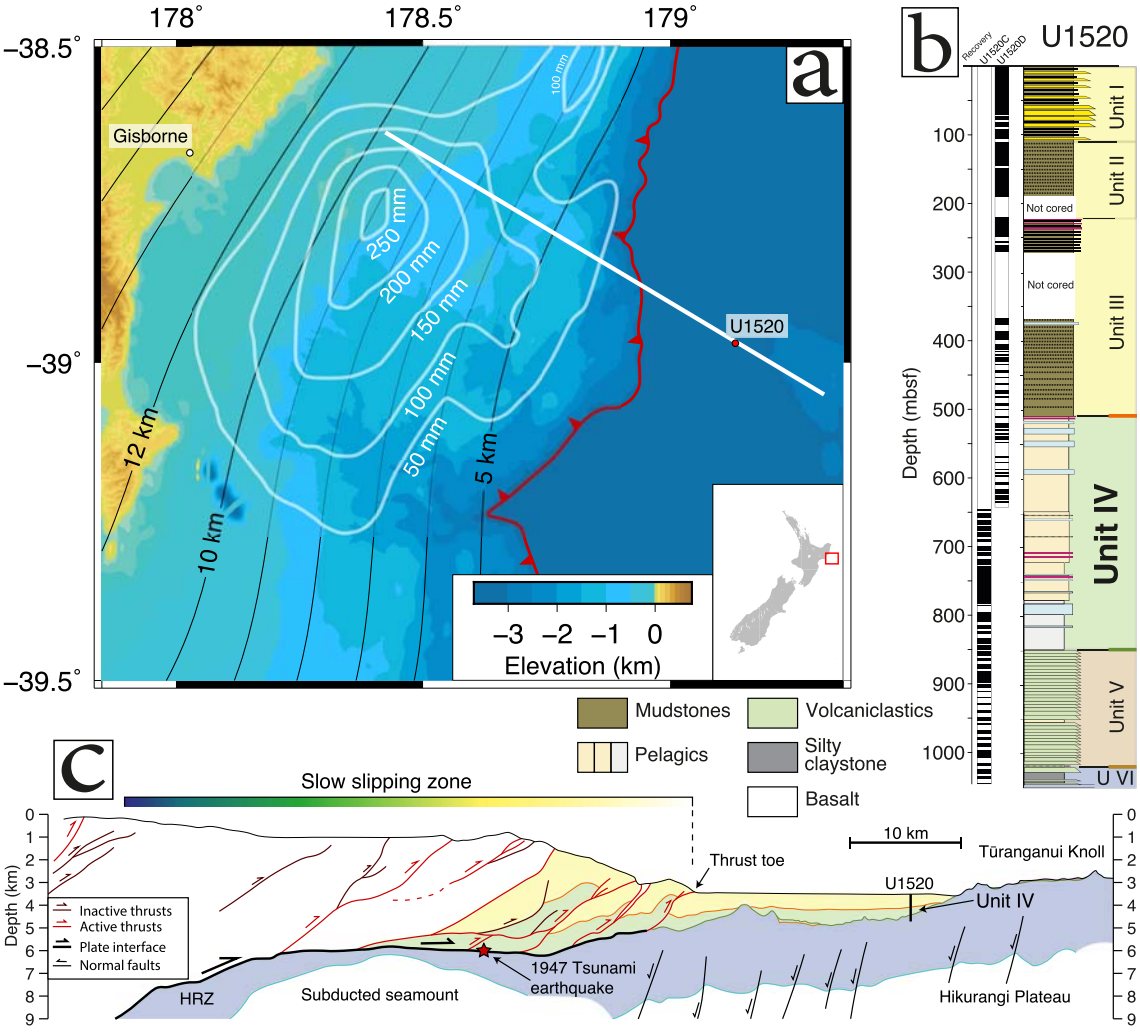

Figure 2.2: Hikurangi Margin map and section and stratigraphic logs from site U1520, cored during IODP Expedition 375. Map (a) shows contours of the plate interface depth (black) and slip during the October 2014 slow slip event (white) characterised by Wallace (2020b) east of North Island, New Zealand (inset map). The red point is IODP Expedition 375 drill site U1520, on the white line showing the 05CM-04 seismic section drawn below (c). The Hikurangi thrust toe is delineated in red. Lithostratigraphic log (b) shows core from site U1520. Colours of units (yellow, green, brown, and blue) and contacts between units (orange, green, and brown) are the same on section (c) below. Section (c) is redrawn from Barnes *et al.* (2020) and shows the relationship of the units cored at U1520 to the plate interface. Also shown are the décollement (thick black line), active faults (red lines), inactive faults (dark red lines), normal faults (thin black lines), base of volcanic basement (light blue line), approximate slow slipping zone, and the high-reflectivity zone (HRZ) as characterised by Bell *et al.* (2010).

2.2c). Seamounts are coated with an irregular cover of variably altered volcaniclastics with highly variable porosity (Fig. 2.2b & c; Barnes *et al.*, 2020). Volcaniclastic material is overlain by siliciclastic and calcareous-pelagic sediments which are thickest between seamounts (Fig. 2.2b & c; Barnes *et al.*, 2020). In this thesis I will explore the role of these input lithologies in plate interface deformation by studying structures in calcareous-pelagic sediments seaward of the trench (Chapter 3) and the structure at depth immediately down-dip of regular SSEs using receiver functions (Chapter 4).

Chapter 3

Brittle and viscous strain localisation and weakening in pelagic sediments seaward of the Hikurangi margin

3.1 Introduction

The mechanical behaviour of carbonate-rich sediments during subduction is not well understood, despite their recognition at several margins around the world (Moore and Mascle, 1990; Morris *et al.*, 2006; Wallace *et al.*, 2019). Rock deformation experiments have, however, shown that carbonates deform very differently to siliciclastic sand- and mudstones typically studied on subduction margins (Boulton *et al.*, 2019; Ikari *et al.*, 2013; Kurzawski *et al.*, 2018; Rabinowitz *et al.*, 2018). For pressure (P) and temperature (T) conditions at $<$ 15 km depth (T$<$ 200°C) in subduction margins, siliciclastic lithologies deform dominantly by cataclasis (combinations of fracture and frictional sliding) with slower pressure solution, whereas carbonates undergo more appreciable deformation by pressure solution and crystal-plastic deformation, possibly associated with seismic slip (Gratier *et al.*, 2013; Kennedy and White, 2001; Verberne *et al.*, 2013). The activity of pressure solution at low temper-

ature in carbonates could have significant implications for the rheological behaviour of subduction thrust interfaces that contain calcareous sediments.

Experimental deformation by pressure solution has been observed and modelled extensively (Macente *et al.*, 2018; Rutter, 1976, 1983; Zhang *et al.*, 2002, 2010), and stylolites resulting from localised pressure solution in natural settings are well characterised (Fletcher and Pollard, 1981; Laronne Ben-Itzhak *et al.*, 2014; Lind, 1993; Peacock and Azzam, 2006; Tondi *et al.*, 2006; Toussaint *et al.*, 2018; Viti *et al.*, 2014). Stylolites form by dissolution of material on discrete surfaces, or in thin tabular volumes, at elevated rates relative to the surrounding rock (Durney, 1972; Toussaint *et al.*, 2018). Therefore, stylolites are recognised by a higher content of relatively insoluble minerals, caused by passive concentration during intergranular pressure solution. Nomenclature for stylolites varies depending on their spatial extent and apparent strain. The term 'stylolites' is often used for laterally-extensive features associated with tectonic deformation of a cohesive rock mass; more localised diagenetic features in poorly-consolidated sediments are often called 'pressure solution features', 'solution seams', or 'dissolution features' (Buxton and Sibley, 1981; Safaricz and Davison, 2005; Toussaint *et al.*, 2018). In this work the term 'stylolites' is used for features formed by localised pressure solution, regardless of formation mechanism or spatial extent. Although the importance of pressure solution in the shallow deformation of carbonates is well documented (Baud *et al.*, 2016; Gratier *et al.*, 2013, 1999; Heald, 1955; Renard *et al.*, 2000; Tondi *et al.*, 2006), many of the controlling factors linking pressure solution to distribution, kinetics, and dynamics of stylolite formation remain unclear.

Several factors influence the rate of pressure solution, including clay content (Aharonov and Katsman, 2009; Hickman and Evans, 1995), grain surface area (Gratier *et al.*, 1999), mineral solubility (Rutter, 1976), grain contact area and microstructure (including variations due to porosity and grain boundary healing) (Croizé *et al.*, 2010; Ebner *et al.*, 2010; van den Ende *et al.*, 2019), fluid flow and composition (Lehner, 1995; Zhang and Spiers, 2005), and gradients in normal stress (Rutter, 1976). The constitutive equations for creep rate by pressure solution are distinct when rate-limited by either dissolution, diffusion, or precipitation, and each is

consequently described by a different model (Gratier *et al.*, 2013; Raj, 1982; Rutter, 1976). Pressure solution on stylolites at shallow depth represents viscous deformation in a depth range typically associated with brittle fracture and frictional sliding (< 15 km, McClay, 1976; Paterson and Wong, 2005). At constant environmental conditions, the rate of pressure solution is dominantly controlled by mineral solubility and grain size, facilitating greater ductility of the upper crust in lithologies containing more soluble minerals (Gratier *et al.*, 1999; Renard *et al.*, 2000). The brittle and viscous components of deformation in the upper crust therefore vary in relative intensity with lithology as well as depth and temperature. Where elevated rates of pressure solution form stylolites, changes in properties such as clay content and porosity affect localisation and frictional slip properties of faults (Baud *et al.*, 2016; Tondi *et al.*, 2006; Viti *et al.*, 2014; Watkinson and Geraghty Ward, 2006).

International Ocean Discovery Program (IODP) expeditions 372 and 375 drilled and sampled five sites on a transect across the Hikurangi Margin, New Zealand, between November 2017 and May 2018 (Wallace *et al.*, 2019). In this chapter calcareous-pelagic chalks and marls in the incoming sedimentary sequence, sampled at Site U5120, are studied. Fault and stylolite distribution are measured and microstructural observations are used to determine the extent and character of pre-subduction deformation before calculating uniaxial strain from pressure solution using chemical mass loss estimates and stylolite frequency. A possible relationship between $CaCO_3$ content and stylolite frequency could provide an insight into a key natural control on stylolite development.

The abundant data gathered during IODP Expedition 375 provide a unique opportunity to constrain the P-T-t history for the pelagic sequence at Site U1520, which I use to apply published models of intergranular pressure solution (Rutter, 1976, 1983). I then compare these results to those calculated from stylolite frequency and find agreement requires sustained high fluid pressures or larger length scales of material transport than the average grain size of lithologies hosting stylolites. Finally, I extend this model to the future subduction of the sediments and discuss the rheological impact of ongoing pressure solution and pre-subduction strain weakening on current subduction.

3.2 Methods

3.2.1 IODP drilling at Site U1520

This study uses samples and data collected during IODP Expedition 375 at Site U1520 (Chapter 2; Wallace *et al.*, 2019). Site U1520 is on the flank of the Tūranganui Knoll seamount and therefore represents a slightly condensed incoming sedimentary sequence (Fig. 2.2). Logging-while-drilling (LWD) data were collected at Site U1520 during Expedition 372 (Wallace *et al.*, 2019). The same site was subsequently cored and wireline logged during Expedition 375, from 0 to 642.3 m below sea floor (mbsf) in hole U1520D, and from 646.0 to 1054.1 mbsf in hole U1520C (Wallace *et al.*, 2019). Cores revealed a $\sim$ 1 km thick sequence of heterogeneous sediments including turbiditic silts and muds (Units I - III), pelagic muds and carbonates (Unit IV), and volcaniclastic conglomerates with minor mudstones (Units V and VI; Fig. 2.2b). In this work I am concerned with the pelagic carbonates and carbonaceous muds which comprise Unit IV. Unit IV was found at depths of 509.82 to 848.45 mbsf (Wallace *et al.*, 2019).

Site U1520 is approximately 20 km seaward of the toe of the Hikurangi megathrust (Fig. 2.2a). Assuming a convergence rate of $\sim$ 40 mm yr^{-1}, the sediments intersected at Site U1520 will reach the toe of the thrust in approximately 0.5 Myr. Comparing the depth of Unit IV at Site U1520 with interpretations of active seismic data along line 05CM-04 (Barker *et al.*, 2018), the shallower and deeper contacts likely correspond to the bases of seismic units 5 and 8 (Barnes *et al.*, 2020). These same horizons can be traced landward until truncated by the megathrust at depths of $\sim$ 4.5 and $\sim$ 5 km (Fig. 2.2c), where the mud and chalk-dominated rocks are inferred as a key protolith interval in which the plate interface will likely locate (Barnes *et al.*, 2020).

Measurements of many physical and chemical properties were collected by LWD and shipboard core-logging, details of which are described by Wallace *et al.* (2019). Here I use data concerning the density, temperature, age, porosity, mineralogy, and lithology of sediments in Unit IV of Site U1520.

Relative mineral abundance from X-ray diffraction (XRD) is normalised using

coulometric $CaCO_3$ content analysis (Wallace *et al.*, 2019). Relative abundances of minerals determined by XRD were calculated for a simplified suite of four mineral groups; calcite, quartz, feldspars, and clays. Clays are measured as a bulk single mineral, though dominant species present in Unit IV are smectite and illite (see XRD methods in Wallace *et al.*, 2019).

3.2.2 Conditions of pre-subduction compaction on stylolites

The physical properties of these sediments were logged by LWD during Expedition 372 and on extracted core during Expedition 375. From shipboard density measurements (i.e. moisture and density in Wallace *et al.*, 2019), in-situ effective vertical stress (σ_v^{eff}) was calculated as:

$$\sigma_v^{eff} = g \sum_{i=1}^{n} (\rho_{bi} - \rho_w) dz_i \tag{3.1}$$

where there are n intervals of bulk density measurement spacing dz with measured bulk density ρ_b. Gravitational acceleration (g) is equal to 9.81 ms^{-1} and average seawater density (ρ_w) is assumed to be 1024 kg m^{-3} (Nayar *et al.*, 2016). Typical values for $dz_{(i)}$ are $\sim$ 1 m, though this varies with gaps in coring and core recovery. Hydrostatic (and, for comparison, near-lithostatic) pore fluid pressure is assumed throughout the studied depths. The results of the hydrostatic pore fluid pressure calculation (Fig. 3.1a & b) show that effective stress in Unit IV increases approximately linearly from $\sim$ 4 MPa near the top (509.8 mbsf) to $\sim$ 8 MPa near the base of the unit (848.5 mbsf).

Following Wallace *et al.* (2019), five of the seven downhole temperature measurements (all of which were conducted in the shallowest 250 m of hole U1520D) form a linear trend corresponding to 38 °C km^{-1} (Fig. 3.1c). The other two values appear as outliers and are therefore ignored. Extrapolating a constant trend from these measurements to depths greater than the shallowest 250 mbsf, temperature increases from 19.4 °C at 509.8 mbsf to 32.2 °C at 848.5 mbsf (Fig. 3.1c). A detailed discussion of geothermal gradient in this type of sediment is beyond the scope of this thesis, so I focus on the conditions under which strain was likely accommodated

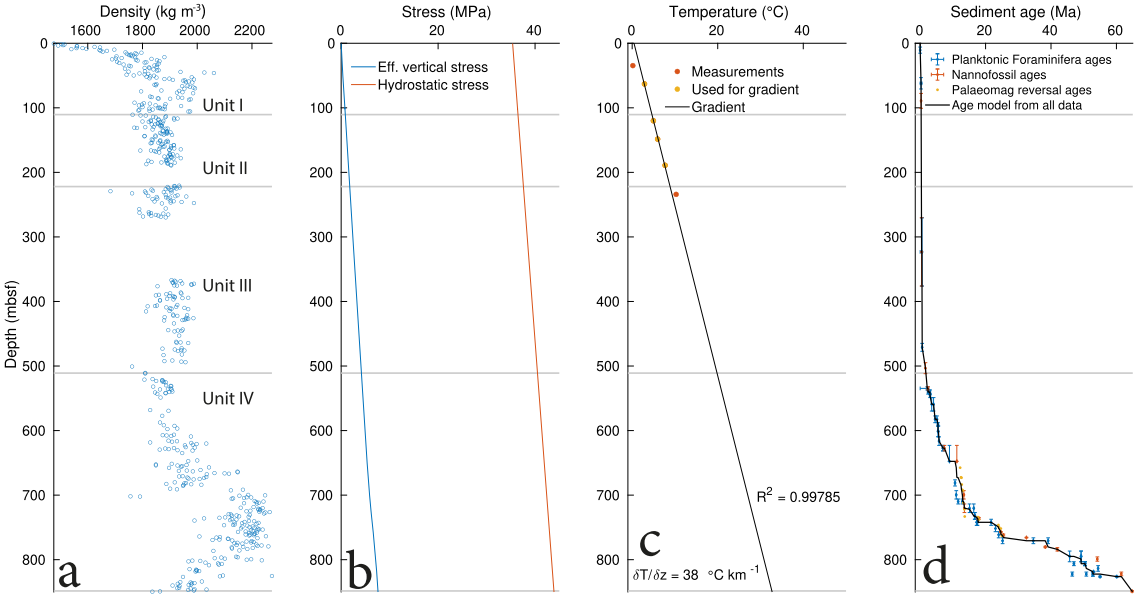

Figure 3.1: Physical conditions with depth in Site U1520 Units I-IV (contact depths shown as grey lines). Plots show density (a), effective vertical and hydrostatic stress (b), temperature (c), and age (d) measurements from shipboard analysis during IODP Exp. 375. Note that hydrostatic stress in (b) starts at $\sim$ 35 MPa, corresponding to the water depth of 3522.1 m.

in Unit IV. To constrain the depositional age of the sediments at Site U1520, I use an approximate age model based on nannofossil, planktonic foraminfera, and palaeomagnetic reversal ages (Fig. 3.1d, Wallace *et al.*, 2019).

3.2.3 Characterising stylolite and fault frequency and texture

To determine pre-subduction mechanisms of sediment deformation I counted faults and stylolites in core samples of lithostratigraphic Unit IV. Image scans of drill core (collected shipboard using the Section Half Imaging Logger, see core handling and analysis methods in Wallace *et al.*, 2019) were used to visually identify stylolites and faults (e.g. Fig. 3.2a). For the purposes of counting, stylolites were defined as typically dark, slightly wavy surfaces where material loss was apparent and concentration of insoluble materials was inferred. Faults were defined as closed or recrys-

tallised fractures with visible apparent offset. The use of these definitions aided in discounting fine clay-rich sedimentary layers and drilling damage from stylolite and fault populations. Horizons of increased deformation measured here coincide with those noted by shipboard structural geologists based on direct observation of the core (Wallace *et al.*, 2019). The depth where a fault or stylolite occurred within the core was recorded as the middle of an interval defined by the intersection between the planar structure and the two sides of the core liner. As noted by shipboard scientists measuring selected structures in 3D (Wallace *et al.*, 2019), most stylolites are approximately horizontal.

Six samples were collected from throughout the pelagic carbonate sequence (see repository files for data collected from all samples) and set in epoxy resin to avoid breakage during thin section preparation. By careful cutting and grinding using silicon carbide grit slurry and a Logitech PM5 polisher with 0.3 μm aluminium oxide, polished thin sections were made from samples cut either perpendicular to bedding, or parallel to lineation and perpendicular to fault surfaces. Polished thin sections were used to produce optical photomicrographs, backscatter electron images (BSE) and energy dispersive spectra (EDS). BSE and EDS data were captured using a Zeiss Sigma HD Field Emission Gun Analytical scanning electron microscope (SEM) at the School of Earth and Ocean Sciences in Cardiff University. BSE images were collected at 20 keV with an aperture of 120 μm and a working distance of 8.9 mm. I use the number of dark pixels per row of BSE image as a proxy for porosity as BSE returns no result when analysing a void. Following Verberne and Spiers (2017) and Heilbronner and Barrett (2014), images were cropped, rotated, histogram matched using the 'Match Color' function in Adobe Photoshop, and Gaussian filtered with a Gaussian width of 4 before the algorithm of Otsu (1979) was applied to determine a darkness threshold between 0 and 255 corresponding to porosity. Pixels values below this value (52 for sample 20R4W and 50 for sample 19R1W) were counted and their ratio to the total number of pixels per row was averaged over approximate areas to show a bulk porosity change. Where cracks were present, I cropped the averaging area; both cropped and uncropped averaging areas within the stylolite are shown in Fig. 3.3b. For EDS mapping of faults and stylolites, spot size was either 1.59, 2.49,

or 2.66 μm, accelerating voltage was 20 keV, dwell time was 100 μs, and aperture size was 120 μm. For determination of element concentrations from SEM EDS images, relative weight percentages were calculated in Oxford Instruments AZTEC software. The element concentrations calculated are relative within a single mapped area.

3.3 Description of stylolites and faults

Sediments within Unit IV are mostly dark green marl and light brown chalk with $>$ 40 wt% $CaCO_3$, with thin inter-bedded layers of dark brown calcareous mudstone with slightly lower carbonate content (Wallace *et al.*, 2019). Aside from the mudstone, these units are referred to as carbonates herein. Lithologies throughout Unit IV are variably lithified: marls are generally well lithified by recrystallised biocalcareous carbonate, calcareous mudstones are poorly lithified due to lower carbonate content, and chalks are well lithified and have high carbonate contents ($>$ 75 % $CaCO_3$; Wallace *et al.*, 2019).

Macroscopically, more well-developed stylolites appear as composite structures comprising discrete dark seams, frequently linked with more subtle seams within the adjacent few cm of core. Some stylolitic surfaces within Unit IV have relatively steep apparent dips ($>$ 45°), and host minor shear offset on undulating dark surfaces. These possibly represent poorly-developed early fault surfaces which have later undergone pressure solution or 'healing' (Fig. 3.2a). At the microscale, most seams are composed of several finer seams (Figs. 3.2b-c), with their most intense shared anastomosing branch representing the macroscopically-visible seam. Seams within these finer networks are relatively thin ($<$ 0.1 mm), undulating, and subparallel to bedding (Fig. 3.2b). Calcareous microfossils of uniform size are common throughout carbonaceous stylolite-bearing lithologies and are frequently dissolved on seams throughout Unit IV. Fossiliferous horizons coincide with thinner, less pervasive stylolites when compared to less fossiliferous, more clay rich horizons (Fig. 3.2c). Burrows have a randomised internal structure, within which discrete stylolitic horizons are not visible (Fig. 3.2c). In contrast, the margins of burrows are more concentrated in clay-rich material, and stylolites there are clearly visible and

well-developed.

SEM images of stylolites show dissolved edges of porosity-hosting microfossils and concentration of fine clays on stylolite seams (Figs. 3.2d & e). Microfossils up to 200 μm are the largest grains within the chalk and clearly show dissolution on thin ($<$ 20 μm wide) stylolite seams (Fig. 3.2d). The seams themselves concentrate along strings of adjacent fossils and host very fine clays ($<$ 5 μm), and have in places almost entirely dissolved fossils, resulting in collapse of their interior porosity (Fig. 3.2e). Remnant material within stylolite seams show a preferred subhorizontal orientation, in places mirrored in the matrix directly adjacent to the seam (Figs. 3.2d & e).

Element maps show a Ca-rich protolith matrix with stylolite seams relatively enriched in magnesium, silicon, iron, and aluminium (Fig. 3.2f & g). The bulk stylolite hosts increased silicon and magnesium while individual seams appear to dominantly concentrate iron (Fig. 3.2f & g). Individual seams are of variable thickness and anastomose throughout the width of the stylolite to form a weakly connected network with scattered parallel fractures (Fig. 3.2f & g). Fractures are open but host some aluminium, probably representing clays seen within seams in BSE images (Fig. 3.2d & e). Open fractures could be a result of sample preparation, where clay was removed by polishing, or core extension, where extension parallel to the core axis occurs when retrieving core from depth. Because I interpret them as formed either by sample preparation or drilling-induced damage, these open fractures are not included in any discussion or quantification of subseafloor deformation.

From BSE images and EDS maps it is qualitatively clear that stylolites have lower porosity than their surroundings (Fig. 3.2d-g); mean measured porosities adjacent to two stylolites are between 0.41 and 0.77 (Fig. 3.3). Shipboard porosity measurements, calculated using bulk density and MAD data from bulk intact samples, from within 1 m (19R1W) and 7 m (20R4W) depth of the samples shown in Fig. 3.3 were between 0.36 and 0.42, below the estimates from image analysis but within the wide spread of porosity data (0.25 to 0.5) within Unit IV (Fig. 3.1; Wallace *et al.*, 2019). Porosity measurements within well-developed stylolites are complicated by seam-parallel open fractures which host large areas of pore space (Fig. 3.3), and

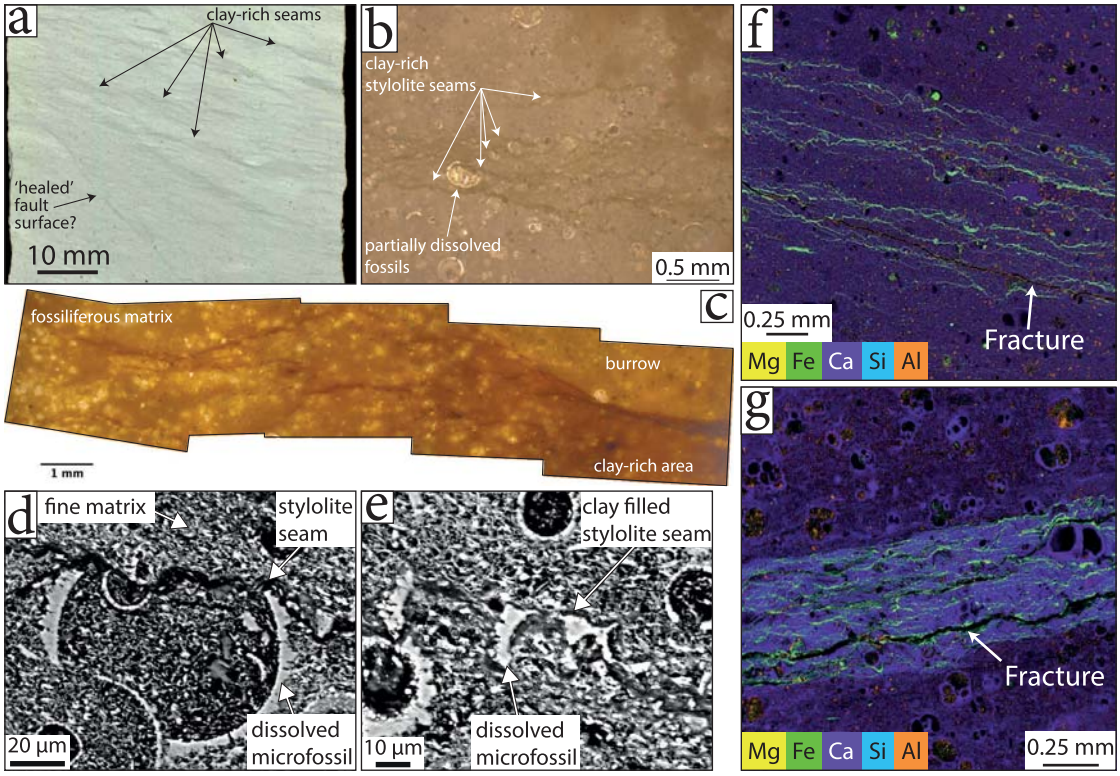

Figure 3.2: Texture of stylolites in Unit IV of the U1520 input sequence. Stylolites show (a) faint layering defined by darker layers, (b) variably-diffuse clay-rich layers at the micro-scale, (c) darker en-echelon seams anastomosing around burrows in clay-rich material and dying out in clay-poor, fossiliferous regions. SEM BSE images show (d) fossils dissolved on stylolite surfaces, (e) fine grained (< 10 μm) clay within a stylolite seam. SEM EDS maps show Ca depletion and Si, Mg, Al, and Fe enrichment within stylolite seams from (f & g). Colours in EDS maps are blended so lighter colours between stylolite seams represent the co-occurrence of several elements.

I therefore analyse well-developed stylolites both with and without open fractures. Mean porosities within stylolites vary from 0.08 to 0.26, corresponding to reductions of 0.35 to 0.42 compared to the surrounding sediments and ignoring fractures (Fig. 3.3). With further dissolution to develop a stylolite further, porosity loss is likely to increase (Toussaint *et al.*, 2018), suggesting 0.4 is a more appropriate figure for mean porosity loss in moderately well-developed stylolites. This porosity loss is a mean change over anastomosing seams and inter-seam areas of the bulk stylolite,

commonly hosting higher porosity ($0.4 - 0.8$) where undissolved shells are present and lower porosity (< 0.2) where clays are concentrated (Fig. 3.3). Because pore-space within intact shells becomes connected to other porosity as soon as shells break down either mechanically or by dissolution, I include this fossil-hosted porosity in the measurements.

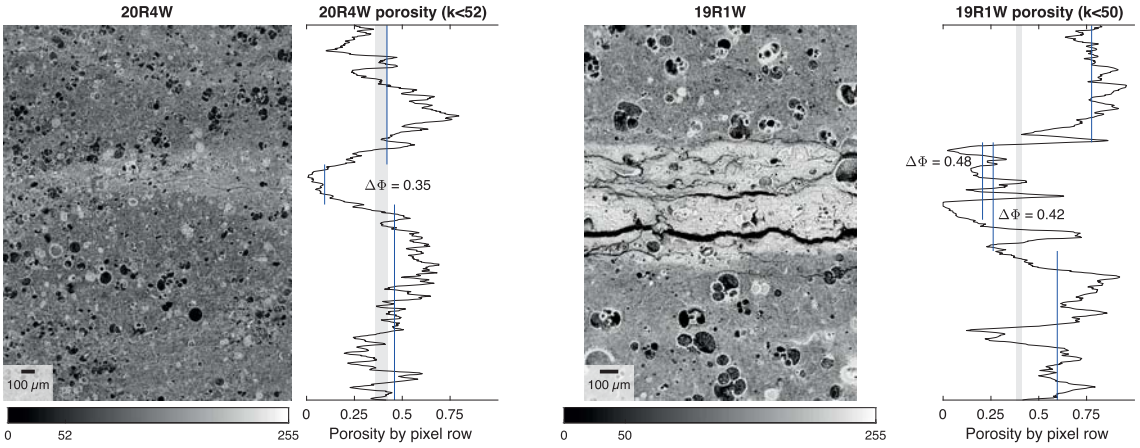

Figure 3.3: Porosity across variably-developed stylolites from SEM BSE images. Both the less well developed stylolite seam (left) and more well developed stylolite seam (right) show less darker shades and visibly lower porosity within the stylolite seam. SEM BSE images are rotated so the stylolite seam is parallel, and histogram normalised to distribute the image across the entire range of grey (0 is black, 255 is white), and the fraction of dark pixels (< 52 or < 50) per row is used as a porosity measurement.

Faults form localised slip surfaces within fracture zones up to 5 cm wide (Fig. 3.4a & b). Slip surfaces are sharp and smooth clay-coated surfaces (Fig. 3.4a), frequently with well defined straight striae showing slip direction. Due to their formation within a sedimentary stack under uniaxial vertical shortening, faults are assumed to be normal, confirmed by a normal sense of shear reported wherever shear sense was obtained from stepped, striated fault surfaces (Wallace *et al.*, 2019). Apparent displacements on faults range from a few millimetres to greater than the observed length of the fault ($\leq$12 cm, depending on apparent dip). Fault surfaces host little mineralisation (Fig. 3.4b & d), with striae likely forming by frictional wear. Fractures within the cm-scale damage zones around fault surfaces are mostly

a combination of extension and shear fractures and are mostly open, rarely 'healed' by veining (Fig. 3.4b-d). Clay-rich material is present as relatively thick ($\geq$ 3 mm) seams adjacent to some slip surfaces (Fig. 3.4a-d). In SEM BSE images, it is clear that thicker clay-rich seams adjacent to faults are connected to similar, thinner, seams which run along fractures adjacent to the fault surface (Fig. 3.4e). EDS maps show enrichment of magnesium, iron, silicon, and aluminium throughout the clay-rich network, including the material comprising the fault surface (Fig. 3.4f).

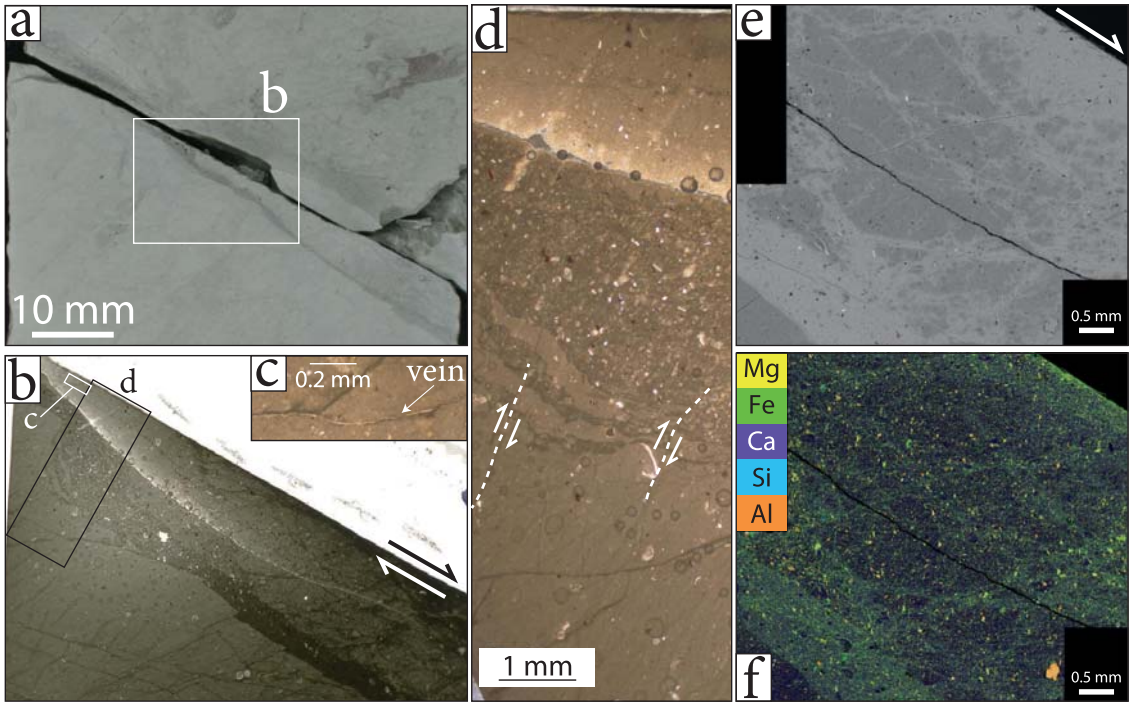

Figure 3.4: Texture of faults in Unit IV of the U1520 input sequence. Images show (a) localised sharp fault surface formed adjacent to clay-rich regions in fine-grained marl, (b) optical photomicrograph of the area shown in (a), (c) enlargement of rare veins in footwall of fault, area shown in (b), and (d) optical photomicrograph of footwall fracture hosting offset. SEM BSE image shows (e) common fractures with offset hosting brighter fine grained material and EDS map (f) details fine grained material around fractures comprised of dominantly aluminosilicate minerals (orange).

Faults and stylolites rarely occur on the same surface within Unit IV, except where early faults have been exploited by pressure solution (Fig. 3.2a). Where faults and stylolites occur within the same depth range, stylolites are typically intersected

and offset by faults. Some faults host clay-rich material immediately adjacent to their slip surface, possibly indicating the existence of stylolites prior to faulting. The existence of stylolites adjacent to fault slip surfaces is uncertain as faults obscure the stylolite texture. These possible stylolites have therefore been excluded from stylolite frequency counts.

3.4 Distribution of faults and stylolites in Unit IV

3.4.1 Downhole frequency of stylolites and faults

Following the evidence for pre-subduction deformation on faults and stylolites, I now quantify their frequency and distribution within core samples. To analyse the distribution of structures as a function of lithology, I use a simplified lithostratigraphic sequence, ignoring minor lithologic intervals (< 5 m thick) to get seven lithological units (Fig. 3.5). These thinner units are often local variations within the thicker surrounding units, and likely have minor a local effect on mechanics and fluid flow within the sediments, but add significant complexity to the interpretation.

Stylolites in Unit IV occur in distinct clusters within similar grain size sediments, increasing in intensity with depth. Clusters are more frequent and intense where $CaCO_3$ content is > 50 wt%, most notably in chalk near the deeper contact with the volcaniclastic conglomerate (Fig. 3.5). The deepest chalk unit sits between 797.99 and 848.45 mbsf, contains > 90 wt% $CaCO_3$, and hosts $\sim 75\%$ of stylolites in the section. Other significant peaks in stylolite frequency are in the two marl units (655.15 to 720.93 and 738.68 to 773.26 mbsf). Minor peaks in stylolite frequency occur throughout the deeper part of the sequence in the marl, chalk, and debris flow units (Fig. 3.5). Observations of stylolites are very rare in the dark-green calcareous mudstone and conspicuously absent in the brown mudstone unit, which contains less $CaCO_3$ (< 50 wt%). Similar to stylolites, faults are also clustered, but fault clusters are more distributed throughout the core than stylolite clusters.

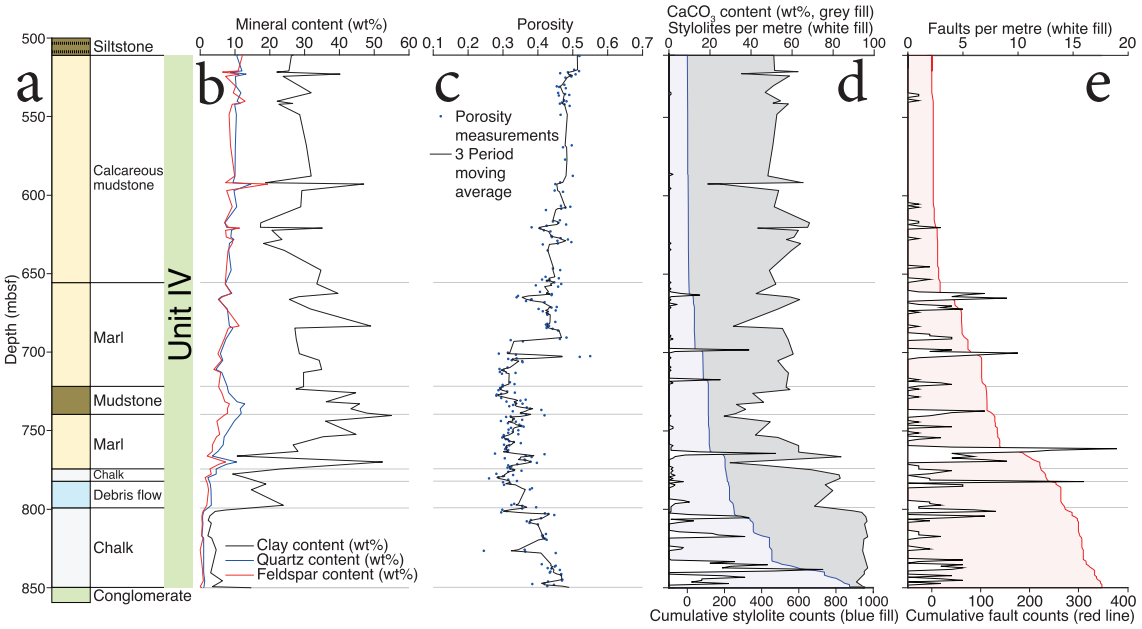

Figure 3.5: Summary of lithology, mineralogy, porosity, and stylolite and fault frequency throughout Unit IV. Plots show (a) simplified stratigraphy, (b) mineralogy, and (c) porosity from shipboard data (Wallace *et al.*, 2019). Depth-frequency plots of (d) stylolites and (e) faults (red) are from observations of core image scans. Both stylolite (d) and fault (e) plots show cumulative frequency (blue and red fill, respectively), frequency per metre (white fill). Calcium carbonate content is also shown on stylolite plot (grey filled line in d).

3.4.2 Clustering analysis of stylolites and faults

The coefficient of variation (C_v) is calculated as the ratio of the standard deviation of distances between features to the mean of distances between features (Gillespie *et al.*, 1999):

$$C_v = \frac{SD(s)}{\bar{s}} \tag{3.2}$$

where $SD(s)$ represents the standard deviation of the sample of distances between each fault or stylolite, and $\bar{s}$ represents the mean of the same sample distances. A C_v of 0 represents a periodic distribution, whereas a C_v of 1 represents a perfectly random distribution, and a C_v greater than one represents clustered features (Cox and Lewis, 1966). Coefficient of variation analysis has been carried out on one-

dimensional transects of discrete features to show the self-arrangement of stylolites (Railsback, 1998) and veins (Fagereng, 2011a; Gillespie *et al.*, 1999). Following the approach of Gillespie *et al.* (1999), I threshold the distances between features at incrementally larger values to discern over what length-scale clustering is apparent. To compare stylolite and fault distributions within each lithological unit, I present these data as C_v vs threshold thickness normalised to the thickness of the simplified lithological unit (Fig. 3.6).

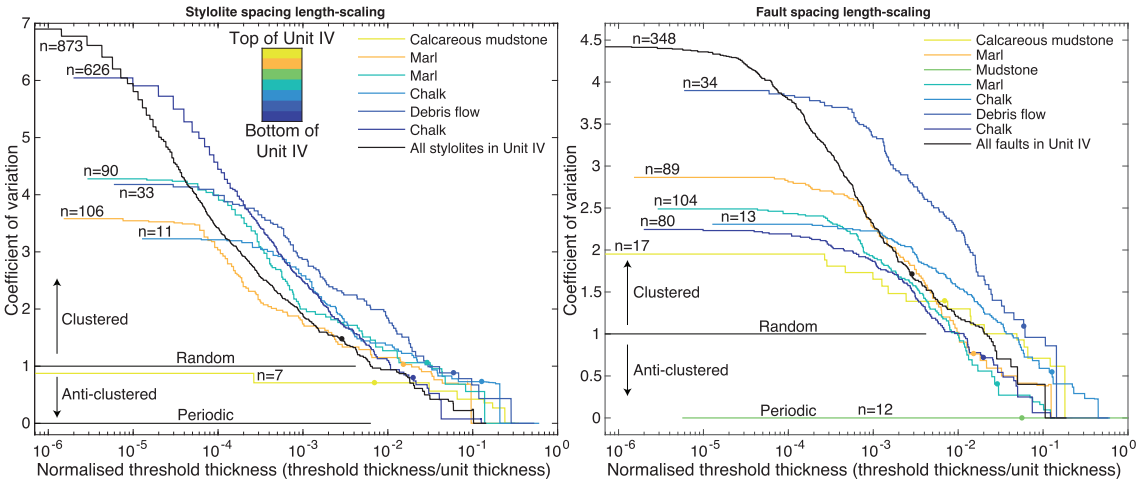

Figure 3.6: Normalised length-spacing coefficient of variation analysis for stylolites (left) and faults (right). Coefficient of variation was calculated using incrementally thresholded spacings, then normalised to lithology thickness.

Whole sample C_v values for faults are smaller than for stylolites throughout the studied threshold range, representing less intense clustering of faults than stylolites (Fig. 3.6). This is also reflected in the un-thresholded single value analysis ($C_v^{stylolite} = 6.993$, $C_v^{fault} = 4.426$). Stylolite spacing C_v-threshold scaling relationships appear to follow a power-law relationship within Unit IV (Fig. 3.6; cf. Gillespie et al. 1999). The degree of clustering of stylolites increases with smaller spacing in almost all lithologies; stylolites spaced > 1 m are randomly to periodically distributed in all lithologies (Fig. 3.6). The periodic nature of stylolites spaced at thresholds > 10 m probably reflects edge effects of the 350 metre section of core studied, limiting analysis over this scale. This is also shown by low C_v values in the

shallowest calcareous mudstone, where only seven stylolites are present over a short section of core, compared to the entirety of Unit IV, where 873 stylolites are present (Figs. 3.5 & 3.6). Stylolites are most clustered when spaced $<$ 1 cm apart in the deepest chalk unit. In all other considered lithologies, stylolites spaced 1 cm-1 m are similarly clustered regardless of lithology (Fig. 3.6).

Fault spacing C_v-threshold scaling relationships are more variable between lithologies than stylolites, though faults still cluster at spacings $<$ 1 m in randomly-distributed horizons throughout Unit IV (Figs. 3.5 & 3.6). Clustering within the marl, calcareous mudstone, and chalk lithologies is similar over all studied scales. Almost all faults spaced less than $\sim$ 1 m in these lithologies have $C_v > 1$, indicating clustering. When faults are $\sim$ 1 m apart, C_v is $\sim$ 1, indicating a random distribution (Fig. 3.6). Faults in the debris flow are consistently more clustered than in other lithologies, possibly related to debris flow deformation, maintaining a higher C_v throughout almost the entire threshold range. In stark contrast, the 12 faults within the mudstone are periodic throughout the studied threshold range (Fig. 3.6).

3.5 Strain within Unit IV

Strain within Unit IV of Site U1520 was accommodated by mixed brittle and viscous deformation in the form of faults and stylolites. At sites of stylolite and fault co-occurrence, stylolites are mostly cut by fault surfaces, suggesting faulting occurred either more recently or more rapidly than stylolite growth (i.e. if the fault and stylolite formed synchronously and fault slip rate was higher than strain rate on the stylolite). Faults and stylolites have therefore occurred over distinct time scales; stylolites appear to have accommodated strain more gradually through the history of the sediment while faulting occurred as a transient process, accommodating displacement rapidly before ceasing (Gratier *et al.*, 1999). Unit IV can be traced landward and downdip to the active plate interface (Fig. 2.2). With this in mind, I consider how vertical uniaxial strain from sedimentary load has been accommodated in Unit IV prior to subduction, and describe how clustered faults and stylolites affect the initial rheology of sediments which could be accommodating strain at the plate

interface.

3.5.1 Mass and volume loss within stylolites

Isocon plots use a known immobile species or, as in this case, an element present in a relatively insoluble mineral, to quantify mass changes between comparable analyses. Aluminium is present in clays and other relatively insoluble minerals (Aharonov and Katsman, 2009; Gratier *et al.*, 2015; Hickman and Evans, 1995), commonly visible around and within calcareous fossils in the nearby protolith (Fig. 3.2d-g). Original depositional clay content of the analysed areas within and without the stylolite are likely different as stylolites are more likely to form in areas of elevated clay concentration (Toussaint *et al.*, 2018). The self-organising nature of pressure solution, however, is likely to amplify these original differences as insoluble minerals are passively concentrated in zones of dissolution as more soluble carbonate is removed (Heald, 1955). I calculate bulk mass change by plotting the isocon through the plot origin and aluminium (Fig. 3.7, Grant, 1986), and note that this method will overestimate mass loss if the stylolite formed in an area of initial high clay content. Titanium is also commonly used in isocon analyses, but low concentrations in samples yield large errors and titanium was therefore not used here. From the bulk mass change, relative changes in calcium wt% are calculated (Fig. 3.7).

Despite minor plagioclase ($<$ 10 wt%) throughout Unit IV (Fig. 3.5), co-occurrence of elements typically found in plagioclase were not found in EDS maps, reiterating that calcite is the dominant calcium-hosting phase losing mass on stylolites in originally calcite-rich sediments. The loss of calcite is consistent with (1) dissolution of fossils (Fig. 3.2d-g), (2) clusters of stylolites forming peaks of increased frequency with high $CaCO_3$ content (Figs. 3.5 & 3.6), and (3) the relatively higher solubility of calcite, compared to silicates, under the studied conditions (Heald, 1955; Plummer and Busenberg, 1982), showing these data are consistent with mass loss by dissolution in calcareous rocks. The amount of CO_2 lost from calcite in the samples cannot be constrained. The bulk calcium mass change is therefore used to calculate volume change using calcite density and porosity.

Mass change in stylolite seams relative to the wall rock varies, but is generally dominated by loss of Ca and gain of Mg, Si, Al, Ti, K, and Fe (Fig. 3.7). Bulk mass change calculated within stylolite seams show loss of Ca-rich material, probably calcite, and concentration of aluminosilicates in highly-localised zones (Fig. 3.7). Relative total and calcium mass change estimates presented here are -11 to -45% and -3 to 49%, respectively (Fig. 3.7). Despite the possibility of overestimating mass loss due to initially higher concentrations of clay in stylolite-forming volumes, these mass losses are consistent with previous estimates of bulk mass change of -16

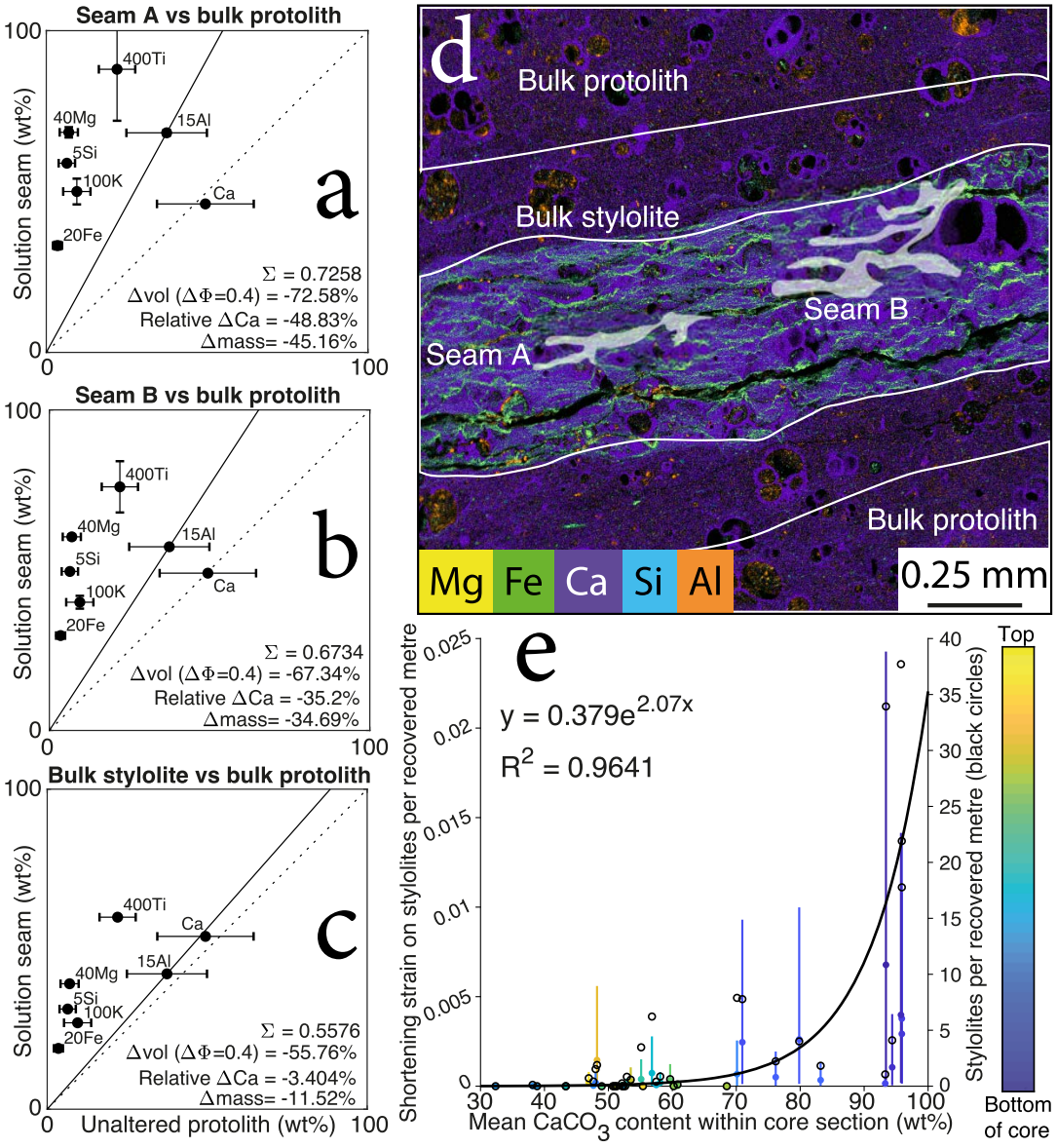

Figure 3.7: (Caption next page.)

Figure 3.7: (Previous page.) Analysis from SEM EDS to quantify mass loss and resultant shortening strain within stylolite seams. Isocon plots (a-c) show wt% calculated from bulk protolith and (a) Seam A, (b) Seam B, and (c) bulk stylolite, all areas outlined in (d). Numbers adjacent to elements are their multiplication factors. Dotted lines on isocon plots correspond to zero bulk mass change. Solid lines plotted through Al show actual bulk mass change, shown in percent in lower right of each plot. Horizontal error bars are one standard deviation of bulk protolith above and below stylolite, vertical error bars are 2σ from wt% analysis from EDS data. For details of mass change and strain calculations, see text. Plot (e) shows stylolite hosted strain per recovered metre and stylolite frequency per recovered metre vs average $CaCO_3$ content within each core section. $CaCO_3$ content is from coulometric analysis performed during IODP Expedition 375. Filled points and lines correspond to the left axis and are coloured according to depth downhole (see colorbar), coloured points are strains per recovered metre calculated assuming a strain on each stylolite seam of 0.7 (e.g. a & b), whereas coloured lines are strain ranges calculated assuming strains on stylolite seams from 0.1 to 0.9. Unfilled black circles are stylolite counts per recovered metre and correspond to the right axis. The exponential fit outline in part (e) corresponds to stylolite counts per recovered metre. As this chapter deals solely with shortening strains, they are presented as positive.

to -44% and $CaCO_3$ change of -15 to -45 % from early pressure solution in marl from Lacroix *et al.* (2015).

Relative elemental mass changes in stylolites are variable between individual seams, but the majority of strain derives from porosity loss within the seam due to closer grain packing and fine aluminosilicates filling in intergranular voids (Fig. 3.2). There is, again, the possibility that some of this calculated porosity change reflects initial spatial differences. The temporal volume change may therfore be overestimated if stylolites formed on clay-rich, low porosity horizons, or under-estimate it if stylolites reflect initial high-porosity horizons where local normal stresses were elevated. I assume a porosity change of -40 % based on porosity calculation from SEM BSE images (Fig. 3.3), producing volume losses of 56 % and 67 to 73 % for

bulk stylolites and individual seams, respectively (Fig. 3.7). The calculated bulk volume losses from dissolution are similar to those estimated from deformed shales in the Shimanto Belt in Japan (Kawabata *et al.*, 2007, 13 to 54 %,[]), stylolites in Cretaceous to Palaeocene chalks in the North Sea (34 to 58 %, Safaricz and Davison, 2005), pressure solution in a young marly thrust fault in the Spanish Pyrenees (14 to 44 %, Lacroix *et al.*, 2015), and stylolites in carbonates in the Permian Zechstein basin in Germany (25 to 39 %, Koehn *et al.*, 2016).

3.5.2 Strain in stylolites

I now convert volume loss to shortening strain per individual stylolite and scale up the observations, using stylolite distribution, to determine the vertical shortening throughout Unit IV. This is done assuming uniform strain on each stylolite and is therefore a function of stylolite frequency. As this chapter deals exclusively with shortening strain, longitudinal strain values are expressed as positive for decreases in length throughout the remainder of this work to more clearly express the degree of shortening. Observational and chemical analyses of stylolites indicate uniaxial, vertical shortening by pressure solution, but quantification of this strain is limited in scope to what is measurable within recovered core and by detailed study of selected, representative seams. All chemical volume loss is assumed to be parallel to vertical stress (σ_v), providing an upper limit on strain on each stylolite. I use an idealised stylolite, composed of seven 50 μm wide seams of shortening 0.7 (a simplified approximation of the stylolite in Fig. 3.7d), to calculate bulk uniaxial strain for recovered core within Unit IV. These data are presented with error bars illustrating a range in calculated strain for each individual stylolite seam from 0.1 to 0.9 (Fig. 3.7e). Bulk strain was calculated as change in length per recovered core length for each core section from holes U1520C & D using the equation:

$$\varepsilon_{recovered} = 1 - \left(L_{recovered} / L_o \right), \tag{3.3}$$

where

$$L_o = (L_{recovered} - L_{styl}) + \left(\frac{L_{styl}}{1 - \varepsilon_{styl}} \right) \tag{3.4}$$

and $\varepsilon_{recovered}$ is the shortening strain in recovered core, $L_{recovered}$ is length of recovered core, L_o is the undeformed thickness of recovered core, L_{styl} is the thickness of stylolites within recovered core, calculated using the aforementioned idealised stylolite and the frequency of stylolites observed within recovered core, and ε_{styl} is the shortening strain on an individual stylolite (0.7 from isocon plots and porosity loss; Fig. 3.7a & b). Where core sections spanned the contact between two lithostratigraphic units, the percentage recovery was assumed to be the same either side of the boundary. The resultant shortening for each core section is plotted per recovered metre of core against average $CaCO_3$ content for the core section in Fig. 3.7e. Also plotted is stylolite number per recovered metre within each core section, which shows an approximately exponential increase in strain as $CaCO_3$ contents increase above 70 %. Increased stylolite-hosted strain with increasing $CaCO_3$ content is also particularly clear in the deeper sections of the core (Fig. 3.7).

3.6 Controls on fault and stylolite distribution

Both faults and stylolites cluster when spaced $<$ 1 m apart (Fig. 3.6), meaning they are more likely to form near an existing feature than elsewhere (Gillespie *et al.*, 1999). Clustering of features therefore suggests either: (1) feature formation changes conditions to make further nearby feature formation more likely, or (2) conditions in areas hosting many clustered features must be preferential for their formation. While some factors controlling the distribution of faults and stylolites are shared (differential stress, fluid pressure, etc), the distinct nature of faulting and pressure solution (i.e. physical vs physiochemical) means that many of the factors controlling fault and stylolite distributions are distinct. Faults likely span several small scale lithological boundaries with far greater lengths than stylolites, and may have initiated in different lithologies before propagating through the core. I therefore refrain from suggesting any bulk controls on faulting based upon observations from drill core and focus on stylolites and stylolite-fault interaction.

3.6.1 Controls on stylolite formation

Because numerous factors influence stylolite formation (Toussaint *et al.*, 2018, e.g.), despite the large range of properties measured by IODP Expeditions 372 and 375 (Wallace *et al.*, 2019), a peak in stylolite frequency does not always coincide with a measured change in core properties. I therefore do not attempt to fully characterise all factors which could influence stylolite formation, but rather suggest some indicative variations which correlate with stylolite frequency.

Mineralogical control on dissolution

At a macroscopic scale, stylolites in Unit IV form anastomosing networks with low amplitude, long wavelength roughness (Fig. 3.2a). This is probably due to the lack of distinct mineralogical heterogeneities in a sediment dominated by carbonate and clay (Ebner *et al.*, 2010; Railsback, 1993). Sediments in Unit IV rarely host more than 20% quartz and feldspar and there are no discernible peaks in stylolite frequency correlating solely with an increase in quartz, feldspar, or clay content (Fig. 3.5). In contrast, stylolite frequency within clusters shows a correlation with $CaCO_3$ content throughout Unit IV (Figs. 3.5 & 3.7e). This is logical as calcite, which the $CaCO_3$ probably represents, is more soluble than the other minerals present in Unit IV at the in situ P-T conditions (Heald, 1955; Plummer and Busenberg, 1982) and appears to be the main dissolved material (Fig. 3.2d & e). Having said this, stylolites are not ubiquitous throughout all high $CaCO_3$ content lithologies, suggesting high $CaCO_3$ content influences the intensity of dissolution rather than the location of stylolite formation. This $CaCO_3$ content control on dissolution magnitude likely exists between a lower bound where its presence allows dissolution and an upper bound where there is not enough phyllosilicates to form a stylolitic residue and localise pressure solution (*cf.* Zubtsov *et al.*, 2004). This is reinforced by the total absence of observed stylolites in the mudstone, where $CaCO_3$ content is very low, the upper bound, as observed after dissolution is likely < 95 wt% based upon observations of abundant stylolites within the $CaCO_3$-dominated chalk at the base of Unit IV.

The relationship of stylolites and lithology

Stylolites are most common in the deepest chalk unit, ~ 650 out of 873 total stylolites occur there, and as $CaCO_3$ content is high throughout the chalks, this stylolite clustering requires an additional factor to explain heterogeneous stylolite development in space. On a sub-mm scale, stylolites dissolve relatively large (< 200 μm) fossils throughout the sediments on discrete localised seams (Figs. 3.2d & e). Fine clay leftover from dissolution is preserved within some stylolites as fine, elongate, grains with seam-parallel long axes (Fig. 3.2e). Dissolution of a grain would continue until the grain contact area becomes so large that stress on that contact is below a critical value that is needed for pressure solution to operate, and grain boundary healing occurs (Rutter, 1983; van den Ende *et al.*, 2019). Over the stress history of the sediments, grain contact surfaces probably dip below this critical value when the grain is elongated parallel to the seam, developing a shape-preferred orientation (Fig. 3.2d & e). Such a shape-preferred orientation adjacent to stylolites has also been reported by many previous workers (Durney, 1972; Ebner *et al.*, 2010; Toussaint *et al.*, 2018). This interaction could explain the undulating nature of stylolites around and between fossils as they follow the path of maximum positive normal stress perturbation relative to the background (Fig. 3.2d & e). Coupled with the accelerating effect of clay-rich and mineralogically-diverse lithologies on dissolution (Aharonov and Katsman, 2009; Hickman and Evans, 1995), a clay-rich horizon with fossils interacting to concentrate stress would produce more rapid development of stylolites than a lithology without either clay or fossils. Indeed, Railsback (1993) shows that abundant contrast of clasts with a clay-rich matrix would host greater dissolution than either more abundant clasts or a more clay-poor matrix.

In contrast to fossiliferous lithologies, burrow margins within bioturbated lithologies host more well-developed stylolites and are more enriched in insoluble clay than both the internal volume of the burrow and the surrounding material (Fig. 3.2c). This enrichment suggests that where an initial concentration of clays or other insoluble material exists, dissolution is more localised and forms zones of well-developed stylolites, in agreement with observations from experimentally-deformed diatomite and gypsum-illite composite by Gratier *et al.* (2015) and modelling by Aharonov

and Katsman (2009) and Hickman and Evans (1995). Bioturbated and fossiliferous lithologies therefore have contrasting effects on stylolite development; bioturbated lithologies concentrate fewer, more intense, stylolites locally on burrow margins while fossiliferous lithologies host many, less intense, more spaced stylolites.

Porosity around stylolites

Porosity is lower in stylolites than in the immediately adjacent material (Fig. 3.3), suggesting porosity loss on the order of 0.4 by material dissolution causing closer grain packing (Macente *et al.*, 2018; Pluymakers and Spiers, 2015). Larger porosity losses in more porous sediments (19R1W in Fig. 3.3) show stylolites develop better in finer grained, higher porosity sediments. Similar to previous workers, zones of slightly increased porosity are apparent immediately adjacent to stylolites (Fig. 3.3, Heap *et al.*, 2018). This is consistent with smaller grain contact areas supporting higher stresses, therefore localising dissolution. Microfossils in stylolites are partially dissolved, showing porosity reduction where stylolites developed within sediments hosting fossil-bound void space (Figs. 3.2 & 3.3). Absence of overgrowths adjacent to stylolites indicates that calcite did not precipitate immediately adjacent to the natural stylolites studied here, suggesting either precipitation rates were prohibitively low (i.e. precipitation-limited pressure solution), or there was limited solute available for precipitation. Diffusion-limited and precipitation-limited pressure solution have been reported at low temperature ($< 150°C$) for uniaxial compression of calcite at low (<0.04) and moderate strains (>0.04), respectively (Zhang *et al.*, 2010). Although not well constrained, higher stylolite-marginal porosity may promote through-flow of fluids, allowing faster solute transport away from sites of dissolution and effectively limiting precipitation immediately adjacent to stylolites. Through-flow of fluids would likely freshen pore water at depth by lateral flow. This is not reflected in downhole chlorinity data at the specific depths where stylolite clusters were observed, but pore water sampling was too sparse to identify localised flow around individual stylolite clusters (Wallace *et al.*, 2019). In concert with reduced grain size and slight shape-preferred orientation bordering stylolites (Fig. 3.2), dissolution may also have occurred within a volume surrounding the stylolite,

as previously suggested by Ebner *et al.* (2010). The outward propagation of the dissolution front from a clay-rich seam coincident with porosity reduction within stylolites has also been recognised by Macente *et al.* (2018) in experiments on a halite-biotite composite. This may explain how more well-developed stylolites grow to encompass several seams of phyllosilicates (Fig. 3.2).

Temporal and spatial variations in a stylolite population

Given the lithological, physical, and chemical controls on the self-organising process of stylolite formation, the final distribution in Unit IV reflects spatial changes in carbonate and clay content, porosity and sedimentary structure, and grain-scale stress concentration and relative solubility (Fig. 3.5), in decreasing order of importance. It seems the stylolite population within Unit IV is controlled dominantly by protolith properties rather than by stylolite formation altering initial conditions. The reasons for this are that stylolite seams (1) individually appear to have very localised regions of influence, only altering grain shape within tens of micrometres (Fig. 3.2d & e), (2) form very closely without directly interacting, as would be expected if exerting a strong control on stylolite formation (Fig. 3.2b & c), (3) correlate in frequency with peaks in bulk properties such as $CaCO_3$ content (Fig. 3.5), and (4) occur in frequency peaks which are randomly distributed over the length of Unit IV when spaced > 1 m apart (Fig. 3.6). It has been postulated that the concentration of clays during stylolite formation accelerates and localised further dissolution, meaning stylolite formation may cause further stylolite formation there (i.e. strain localisation) (Aharonov and Katsman, 2009; Gratier *et al.*, 2015; Hickman and Evans, 1995; Macente *et al.*, 2018). This self-organisation means that minor initial perturbations in the conditions outlined earlier are amplified once dissolution on stylolites begins. The subsequent temporal evolution of a stylolite is therefore conditional upon every previous feedback of evolving conditions with dissolution on that stylolite. It is entirely possible that when stylolites occur within tens of micrometres of one another they are also influenced by changes in conditions resulting from adjacent stylolites, attested to by increasing clustering of closely-spaced stylolites (Fig. 3.6), but this is not a control on the macro-scale distribution of stylolites.

Comparing stylolite frequency from 509 to 848 mbsf at Site U1520 to that from 790 to 1350 mbsf on the Ontong Java Plateau to the north (Lind, 1993), it is clear a far higher frequency of less well developed stylolites is present at shallower depths at Site U1520. Lind (1993) describes an erratic, highly localised, stylolite frequency, overall increasing in abundance with depth. Stylolites are said to be irregular in size and localise along burrows and clasts of contrasting mineralogy. This description is similar to what is seen at Site U1520, where randomly-distributed peaks in stylolite frequency increase in intensity with depth (Fig. 3.5), burrows localise intense stylolite-rich regions along their margins (Fig. 3.2c), and more fossiliferous regions host more spaced, less well developed stylolites (Fig. 3.2c). Carbonate content in the Ontong Java Plateau sediments is $> 90\%$, similar to the chalk at the base of Unit IV (Wallace *et al.*, 2019). The difference in frequency is probably a result of a contrast in the intensity of stylolite development at each site; the limited depth range of Unit IV (509 to 848 mbsf) means stylolites at Site U1520 are less well developed than they would be at the depths studied by Lind (1993). Counting is therefore more likely to be sensitive to less well developed stylolites, leading to a higher frequency. Regardless, controls on stylolite formation appear to be similar at both sites, suggesting observations of calcareous-pelagic sequences are valid beyond the Hikurangi sedimentary input sequence.

Various stylolite populations from onshore carbonate terranes have been described so as to characterise controls on their formation and development (Andrews and Railsback, 1997; Laronne Ben-Itzhak *et al.*, 2014; Railsback, 1993; Toussaint *et al.*, 2018). Field studies of stylolites have shown they can extend hundreds of metres parallel to bedding surfaces with either constant spacing, or as part of anastomosing networks (Laronne Ben-Itzhak *et al.*, 2014). The nature of this study precludes the comparison of lateral continuity of the stylolites described here, but local comparisons of the spacing and interconnectivity can be made. Published studies of stylolites focus almost exclusively on chalks and marbles, so only stylolites from the chalks within Unit IV are compared. Spacings between stylolites within clusters in the chalks of Unit IV are generally < 20 cm, but with much larger spacing between randomly-distributed clusters (Fig. 3.5d). Similar spacings between indi-

vidual stylolites have been observed in field-studies over 10's m perpendicular to bedding (Laronne Ben-Itzhak *et al.*, 2014; Toussaint *et al.*, 2018), but few studies have observations over 100's m such as those presented here. Stylolites have often been described as being evenly spaced (Merino *et al.*, 1983; Simpson, 2009), as odds with observations presented here. This difference may a result of more complete lithification of limestones studied in the field, or merely more time for the stylolite population to develop, as characteristic factors associated with stylolites can change through time (Peacock and Azzam, 2006). Field-based stylolite studies have found a clear association of stylolites and fractures (Laronne Ben-Itzhak *et al.*, 2014; Peacock and Sanderson, 1995), likely due to the concentration of stress at stylolite tips and surfaces (Zhou and Aydin, 2012). The lateral tips of stylolites were not observed in this study due to the narrow sampling width of the drill core used, but the co-occurrence of fault and stylolite clusters suggests an association of stylolites and faults (discussed in more detail in Section 3.6.2).

At the grain scale the stylolites observed here are much lower amplitude, and therefore likely lower strain (Heald, 1955) than those often presented in field studies (Laronne Ben-Itzhak *et al.*, 2012). The width of insoluble residue within stylolites observed here varies but is generally < 1 mm in core image scans and < 250 μm in individual seams (Fig. 3.2). In more well-developed stylolites observed elsewhere the thickness of insoluble material has been recorded as up to 2 mm in individual seams and 1 cm for the stylolite as a whole (Peacock and Azzam, 2006; Railsback, 1993). Stylolites observed in the field also appear to show more variety in their amplitude and grain-related morphology (Toussaint *et al.*, 2018) than the anastomosing seams observed in oceanic carbonate sediments (Fig. 3.2; Lind, 1993). The greater variety of rock types, longer development time, and greater overburden associated with stylolites observed within calcareous lithologies in the field likely led to higher amplitude, more complex stylolites with more varied morphologies.

3.6.2 Interactions between stylolites and faults

Micro-scale observations of faulting within Unit IV were limited, but faults appear to coincide with clay-rich weak layers prior to later alteration of their damage zone

(Fig. 3.4). Thick ($\leq$ 3 mm) clay-rich seams, concentrated by pressure solution, are present either side of normal faults. These seams likely formed prior to fault formation, based on good preservation of the fault surface and the low strain rates at which pressure solution occurs relative to brittle fault formation by fracturing (Fig. 3.4, Gratier *et al.*, 2013; Paterson and Wong, 2005). The brittle faulting therefore probably localised within pre-existing clay-rich seams, exploiting thin zones of relative weakness from previous viscous deformation (Viti *et al.*, 2014). Both fault textural and distribution data, therefore, suggest stylolites are at least partially responsible for fault localisation in Unit IV.

Where brittle fault surfaces are localised on strain-weakened low-angle surfaces, slip would result in cm-scale damage zones comprising both tensile and shear fractures adjacent to the slip surfaces (Fig. 3.4). These fractures represent new fluid pathways, rapidly increasing the surface area (*sensu.* Gratier *et al.*, 1999) on which pressure solution can occur.

3.7 Modelling uniaxial strain accommodation by pressure solution

The age, depth, and chemical constraints on the stylolite population described in this study provide an opportunity to compare strain accommodation from published constitutive models of pressure solution (Rutter, 1976; Spiers *et al.*, 2004, 1990; Zhang *et al.*, 2010) to strains calculated from direct observations of core from Site U1520 (Section 3.5.2). Strain rates on individual stylolite seams studied here (of strain 0.7; Fig. 3.7a & b) range from 3.7×10^{-16} to 2.2×10^{-14} s^{-1} for ages of 60 Ma and 1 Ma (Fig. 3.1d), respectively. Although these are at the slow end of typical average geological strain rates in deforming zones (Fagereng and Biggs, 2019; Pfiffner and Ramsay, 1982). Calculations of strain from stylolite frequency likely underestimates strain as they do not account for dissolution outside stylolite seams. The population of stylolites described here has been well characterised under well-defined P-T conditions, providing a directly comparable natural analogue for the pressure solution described in the aforementioned models. I therefore use data from

Site U1520 to construct a history of physical conditions and strain from intergranular pressure solution for the $\sim$ 60 Myr history of Unit IV.

As pressure solution is rate-limited by the slowest of the serial processes of dissolution, diffusion, or precipitation, it is important to select the most appropriate model. The presence of partially-dissolved fossils suggests dissolution is not the rate-limiting factor for pressure solution on stylolites (Fig. 3.2), but as transitional diffusion or precipitation-limited behaviour has been reported for calcite under conditions analogous to those studied here (Zhang *et al.*, 2010), discerning the dominant rate-limiting factor from diffusion and precipitation is less clear. Based upon the observed lack of overgrowths adjacent to stylolites, I earlier inferred fluid flow and solute removal away from sites of dissolution in a system that is at least partially open (Section 3.6.1), limiting local re-precipitation. If solute was rapidly removed from sites of dissolution, geochemical gradients would have been high at sites of dissolution and diffusion-limited pressure solution would have been faster than modelled in a closed system. I therefore use equations for diffusion-limited pressure solution as a lower bound on strain rate. As the number of assumptions within the modelling is large, I limit discussion of absolute strain magnitudes, instead focusing on the location of pressure solution localisation onto stylolites and which factors within the modelling could be better constrained.

I use the age model described earlier and reported in Wallace *et al.* (2019) to calculate past sediment depth at each depth and time step before calculating temperature and vertical stress using density data and a modern geotherm derived from measurements collected at the site (Fig. 3.1). I calculate stress conditions for pore fluid factors of 0.4 and 0.95 for comparison of the effect of elevated pore fluid factor. Solubility (Plummer and Busenberg, 1982) and diffusivity (Nakashima, 1995) are calculated from estimated temperatures (20-33 °C, Fig. 3.2.2) and are used with a relatively thin grain boundary fluid film thickness of 1×10^{-9} m (Renard *et al.*, 1997) and an equation accounting for measured porosity at each depth (Pluymakers and Spiers, 2015) to calculate strain rate using published equations for diffusion-limited pressure solution (Rutter, 1976; Spiers *et al.*, 2004, 1990; Zhang *et al.*, 2010). I scale this modelled strain rate by the calcite content at that depth, both linearly and fol-

lowing the scaling relation of (Zubtsov *et al.*, 2004) (see Section 3.7.2). Full details of the modelling methodology are available in the supplementary information (Text S1 to S2).

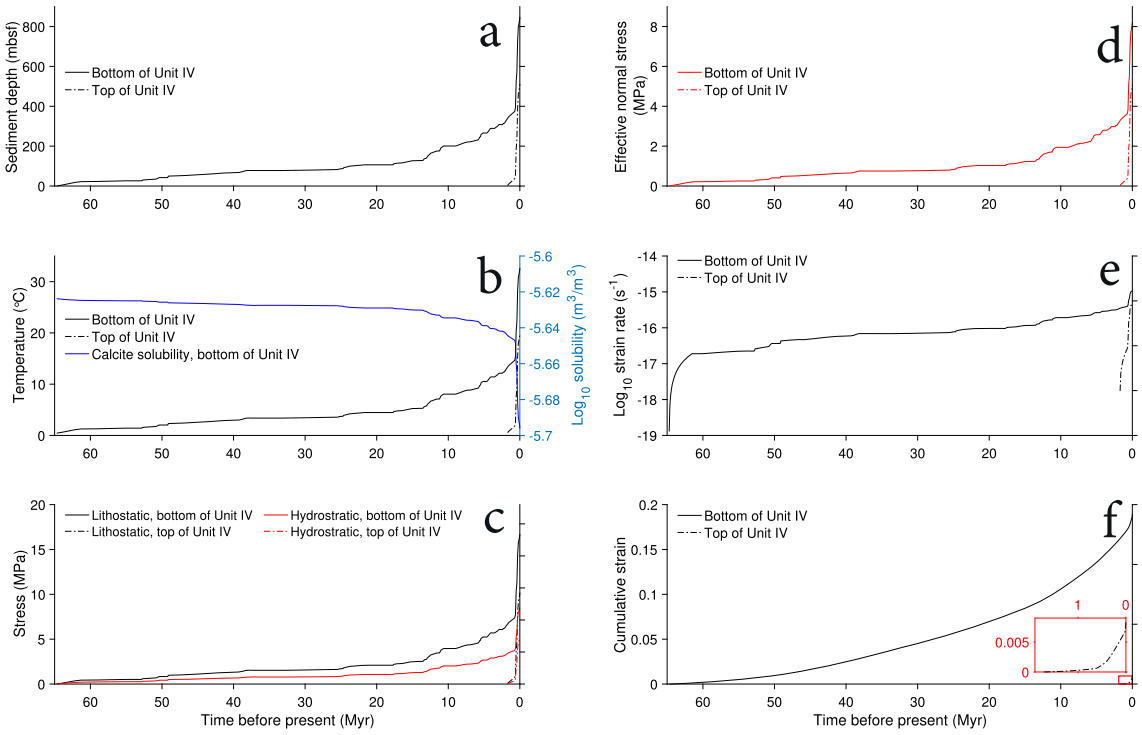

Figure 3.8: Pressure solution model inputs and outputs with time. Plots show (a) sediment depth, (b) temperature and solubility calculated from Plummer and Busenberg (1982), (c) lithostatic and hydrostatic stress, (d) effective normal stress, (e) strain rate from diffusion controlled dissolution of calcite according to published models for pressure solution (Rutter, 1976, 1983), and (f) cumulative strain from diffusion controlled dissolution of calcite at the top and bottom of Unit IV with time. Inset in (f) is zoomed area showing cumulative strain at top of Unit IV. Most plots show results for the bottom (848.45 mbsf) and top (510.96 mbsf) of Unit IV. Plots of are for a grain size of 100 μm. As this chapter deals solely with shortening strains, they are presented as positive.

Several assumptions are made within the history of physical conditions. Not least that data collected at a point during IODP Exp. 375 are representative for density, composition, porosity, and temperature gradient in the incoming sequence. I extrapolate these values back in time using an age model based upon macrofossils,

microfossils, and palaeomagnetic reversal ages, all of which have varying degrees of dating error (Fig. 3.1d). The only assumed constant condition throughout the history of the sediment is the modern temperature gradient from the seafloor downward, applied at each time step during the history of deposition. The main consequence of the temperature gradient is variability in the solubility of calcite, which is inversely correlated with temperature (Plummer and Busenberg, 1982). A higher temperature gradient, possibly due to higher heat flow from younger underlying oceanic crust (Villinger *et al.*, 2002), would therefore reduce calcite solubility early in the sediment history. The model therefore probably overestimate calcite solubility in the early history of the sediment. Further to this, no attempt is made to quantify calcite solubility with increasing stress due to the lack of empirical published data.

Following constituitive equations for diffusion-limited pressure solution, grain scale diffusivity effects within the model are captured within the diffusion coefficient and mass transfer width terms (Rutter, 1976, 1983). A simple Arrhenius temperature dependency (Nakashima, 1995) is unlikely to capture the complexity of electrochemical and grain boundary effects on the diffusion coefficient (D), while a single value for the mass transfer path width (S) ignores the complexity of sub-grainsize fluid pathways throughout grain boundaries between like and unlike minerals (Renard *et al.*, 1997; Zubtsov *et al.*, 2004). Furthermore, these values are likely to evolve with time and strain as well as the physical background conditions modelled here, possibly explaining the difference between modelled and observed strains (Fig. 3.10). I note that I have used a low-end value for the grain boundary fluid film thickness, and current rather than initial porosities - these assumptions will tend to underestimate strain rates. Porosity within the sediments is present within and without spherical fossils (Fig. 3.3), meaning porosity estimates from the core are likely greater than what is realistically available for precipitation of solute, if such precipitation does not occur within shells. The intra-fossil porosity is not accounted for in the model, and the resulting strains are therefore likely to be overestimated. I consider this to be of relatively minor importance given the number of assumptions in the modelling, and choose to focus discussion on the distribution, rather than magnitude, of strain from pressure solution.

3.7.1 Modelling results and pressure solution controls

Modelled strain rates and cumulative strains are shown for the top and bottom of Unit IV in Figs. 3.8e & f, and for the whole of Unit IV in Figs. 3.9c & d. Throughout the history since sediment deposition the dominant control on the modelled strain rate is the sediment depth (Fig. 3.9a), controlled by the age model for the site (Fig. 3.1d) and expressed by effective normal stress (Figs. 3.8d & 3.9a) and temperature (Fig. 3.8b). After initial deposition, slow accumulation of sediment caused strain rate to increase gradually in the deepest 125 m of Unit IV during the first 50 Myr of the modelled history (from $> 10^{-16.5}$ to $\sim 10^{-16}$ s^{-1}; Figs. 3.1e, 3.8e, & 3.9c). These strain rates are relatively slow by geological standards (Fagereng and Biggs, 2019; Pfiffner and Ramsay, 1982), but were sustained long enough (until 15 Myr ago) to accommodate strains of up to ∼0.08 before the upper ∼ 215 m of Unit IV were deposited (Figs. 3.8a, 3.8f, & 3.9e). Around 15 Myr ago, the age model dictates continuous sedimentation rate increases up to the present (Fig. 3.8a). This manifests as fluctuating, relatively rapid increases in modelled strain rate (up to $\sim 10^{-15.5}$ s^{-1}) over ∼ 14 Myr, until rapid loading of turbidites in Units I-III in the last ∼ 1 Myr increases strain rates further (up to $\sim 10^{-15}$ s^{-1}; Figs. 3.8e & f, & 3.9c & d). This strain rate increase has the most marked effect in the deepest 100 m of Unit IV, where sediments are over 25 Myr old (Figs. 3.8f & 3.9d).

At a given time-step modelled strain rates generally increase with depth, fluctuating locally because of local variations in porosity and calcite content (Fig. 3.9d). Strain rates are highest between 825 and 850 mbsf, where calcite content is high, with local maxima coinciding with large fluctuations in measured porosity (e.g. ∼ 830 and ∼ 840 mbsf in Fig. 3.9c). Unsurprisingly, this depth range of higher modelled strain rates, and the local maxima within it, have the highest modelled strain within Unit IV (Fig. 3.9d). Final strains at the local maxima are up to 0.05 above the background within this depth range, even when the lower strain sediments are > 10 Myr older (∼ 840 mbsf vs ∼ 845 mbsf in Fig. 3.9d).

The constant geothermal gradient applied during the modelling means temperature-dependent factors effectively become depth-dependent, and the variation of solubility and diffusivity with temperature can be discussed alongside that of depth-dependent

factors such as effective normal stress. During the first 50 Myr of the model, the deepest calcareous sediments (> 700 mbsf) maintain low effective normal stresses (< 2 MPa) and temperatures (< 10°C), corresponding to high solubilities (> $10^{-5.6}$ m^3/m^3; Figs. 3.8b-d & 3.9a & b). The strain accumulated over this period (up to 0.08) is not negligible compared to final totals in the model (up to 0.15), but rapid loading in the more recent history of the model increases strain rates from $\sim 10^{-16}$ s^{-1} to around 10^{-15} s^{-1}, adding an extra strain of 0.07 over the final 15 Myr of Unit IV at average strain rates of approximately $10^{-15.6}$ s^{-1}. This is similar to the accumulated strain over the previous $\sim$ 50 Myr and, while not surprising, illustrates how a non-linear history of sedimentation or stress loading may affect rates of pressure solution during the history of deformation. Changes in effective normal stress, reflected in the modelled strain rate (Fig. 3.9c), are even more apparent when pore fluid pressure is increased to near-lithostatic levels, reducing the stress driving dissolution and the modelled strain rate, and limiting the resultant strain (Fig. S1).

3.7.2 Comparing modelled and calculated strains from pressure solution in Unit IV

Calculation of stylolite-hosted strain within Unit IV is based on stylolite frequency and strain on each individual stylolite seam (Fig. 3.7), meaning total calculated strain reflects stylolite frequency in core image logs (Figs. 3.5 & 3.9). This stylolite-hosted strain is likely a minimum value for strain within the whole of Unit IV, as pressure solution is likely to act upon much of the depositional layering as a diagenetic process (Gratier *et al.*, 2015) and I have not quantified strains caused by granular flow or faulting. Modelled strains, however, are calculated using equations derived from experiments of distributed dissolution and bulk shortening rather than that localised on stylolites (Rutter, 1976, 1983; Zhang *et al.*, 2002, 2010). Strains are therefore comparable within the depth range of stylolite clusters or over length scales encompassing several clusters (> 1 m). Modelled strain from pressure solution at hydrostatic fluid pressure is almost always higher than observed strain, each

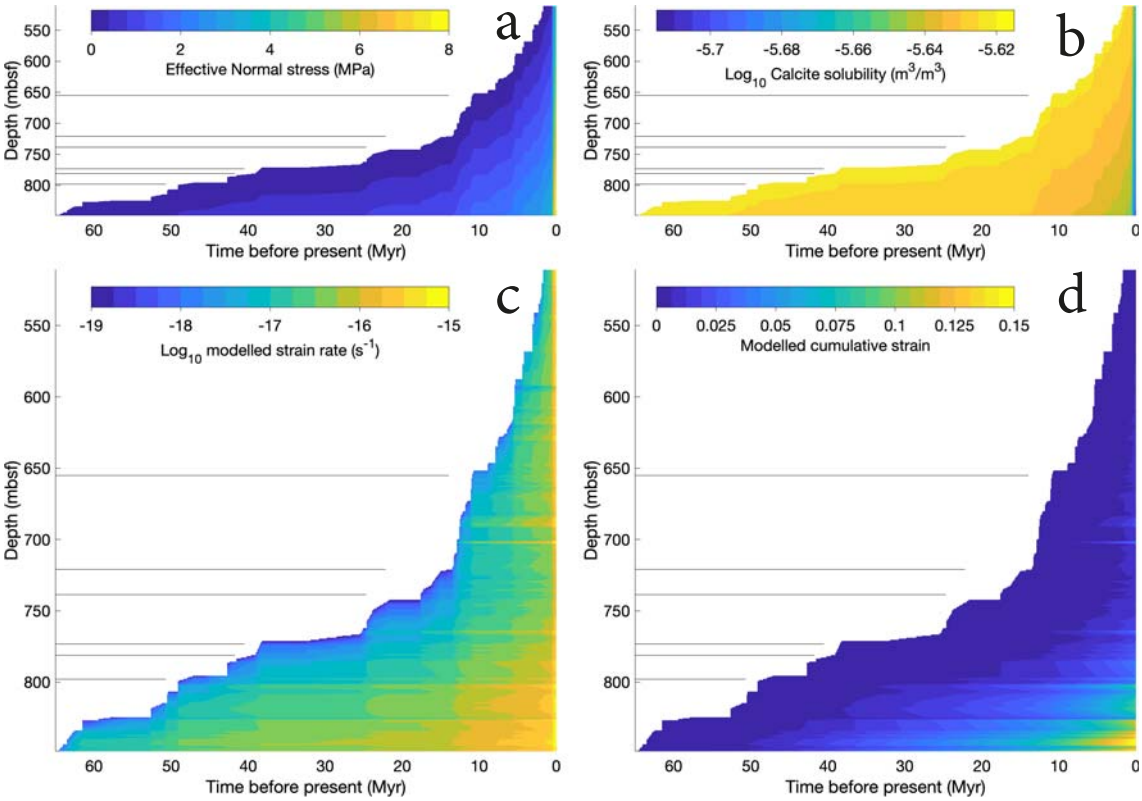

Figure 3.9: Calculated conditions for the full depth of Site U1520 with time. Coloured plots show (a) effective normal stress, (b) calcite solubility, (c) strain rate, and (d) cumulative strain with depth and time. Grey lines on colour plots show contacts between simplified lithological units within Unit IV, model results are for a grain size of 100 μm. As this chapter deals solely with shortening strains, they are presented as positive.

with peaks which rarely coincide (Fig. 3.10a). When studied at the length-scales of lithological units (10s to 100s m) or core sections ($\sim$ 10 m), calculated and modelled strains rarely agree, with modelled strains almost always exceeding the measured magnitude of strain (Figs. 3.10b & c). At near-lithostatic pore fluid pressures, the model reproduces the average strain magnitude when compared over larger length scales (Figs. 3.10e & f), but does not reproduce observed stylolite clustering, giving lower than measured strain within stylolite clusters and higher than measured strain between clusters (Fig. 3.10d). As modelled strain uses bulk properties throughout the core and stylolites host highly localised dissolution, it seems that stylolite formation is controlled by local perturbations not accounted for in the models. This is

not surprising as I cannot model unknown initial heterogeneities in the sediment column, and the models are therefore averages over multiple clusters. Despite attempts to integrate the evolution of some of the parameters controlling stylolite evolution, the use of the constitutive equations of pressure solution (Gratier *et al.*, 2013; Rutter, 1976, 1983; Spiers *et al.*, 2004, 1990) conceived and calibrated with constant or controlled parameter values do not accurately predict the location or magnitude of cumulative strain of intensive dissolution on stylolites. Beside the possible uncertainty on the values of the various parameters of the equations, the evolution of the parameter values with stylolite evolution is not yet enough constrained within the model, particularly the effects of self-organized processes.

Porosity is variable both within Unit IV and locally around stylolites (Section 3.6.1 & Fig. 3.3). The coincidence of observed stylolite clusters and localised porosity peaks (e.g. at $\sim$ 760 and $\sim$ 805 mbsf) is consistent with observations of greater volume loss and increased resultant shortening strain in higher-porosity zones (19R1W in Fig. 3.3). Modelled strains have local high-frequency variations with depth due to variable porosity and calcite content measured throughout Unit IV (Figs. 3.5c & d). With depth, some peaks in cumulative modelled strain coincide with peaks in stylolite-hosted strain (Figs. 3.10a & d). Previous studies that show strain increases with increased contact stress over reduced grain contact area (Niemeijer *et al.*, 2002; Pluymakers and Spiers, 2015; vanădenăEnde *et al.*, 2018; Zhang *et al.*, 2010), suggesting that applied variations in strain rate with porosity may be, at least partially, representative of variations in pressure solution within natural basins containing calcareous sediment.

Composition is another important difference between the sediments studied here and the materials used to study the dissolution of pure calcite (Rutter, 1976, 1983; Zhang *et al.*, 2002, 2010). My attempt to account for the heterogeneous mineralogy of Unit IV by limiting strain from dissolution to soluble grains does not account for: (1) the accelerating effects of electrochemical potential on pressure solution across mineralogically-heterogeneous grain boundaries; or (2) stylolite localisation associated with increased clay fraction at particular horizons (Aharonov and Katsman, 2009; Greene *et al.*, 2009; Hickman and Evans, 1995). Furthermore, stylolites are

typical of pressure solution in dominantly-calcareous sediments whereas pressure solution within more clay-rich sediments would likely occur on depositional layering, accommodating vertical shortening without forming stylolites (Gratier *et al.*, 2015). Evidence for this pressure solution in more clay-rich lithologies would be difficult to observe and has not been counted here as a straining feature, meaning measurements of stylolite-hosted strain are likely a minimum value for the whole of Unit IV. Previous experiments on pressure-solution in two-phase mixtures found a linear scaling relationship exists between strain rate and soluble species content up to 50%, where it plateaus until 70% soluble species, before decreasing linearly at soluble species contents of 70-100% (Zubtsov *et al.*, 2004). This was thought to be because diffusion in a fluid phase trapped along grain contacts between different minerals is faster than along grain contacts between the same mineral. The mineral assemblage varies significantly throughout Unit IV (Fig. 3.5), and variations in grain-scale factors such as these could account for variations in observed strain that have not been recreated in the model. I apply the scaling relation of Zubtsov *et al.* (2004) but find it does not better recreate calculated stylolite-hosted strain distribution or magnitude (Fig. S2). Better quantitative constraints to measure and model the effect of grain-scale processes on macroscopic strain, by both distributed and localised pressure solution, would aid the ability of models to recreate observed trends in strain.

Cumulative strains modelled over the history of Unit IV vary significantly in magnitude from those estimated from stylolite mass loss and frequency. Model results for grain sizes of 10 and 100 μm vary over three to four orders of magnitude, and agreement of calculated and modelled strains is only achieved at hydrostatic fluid pressures when the modelled grain size is ≥ 100 μm (Figs. 3.10b & c) and at near-lithostatic fluid pressures when the modelled grain size is ≥ 50 μm (Figs. 3.10e & f). The mean grain size measured in the chalks in Unit IV is < 40 μm, with larger microfossils ≤ 200 μm (Fig. 3.2), suggesting either (1) the model overestimates strain rate from grain dissolution, (2) near-lithostatic pore fluid pressures have been sustained for long periods of the sediment history, (3) not all pressure solution forms stylolites, or (4) strain within Unit IV is controlled by the dissolution of

grains larger than those comprising the matrix (Figs. 3.9 & 3.10). The dissolution of microfossils seen in microstructural observations suggests the latter may be the case, though matrix grains also appear to be dissolved, showing a shape-preferred orientation adjacent to stylolites (Fig. 3.2). Alternatively, the fine-grained nature of the sediment, and possible fluid compartmentalisation by overlying low permeability mudstones (Fig. 2.2b), may locally lead to greater than hydrostatic pore fluid pressures during the history of the sediment, reducing effective vertical stress and subsequent dissolution. However, there is no other evidence, such as fractures, veins, or fluid escape structures, indicative of sustained near-lithostatic fluid overpressures at Site U1520 (Wallace *et al.*, 2019). A further point for consideration is the diffusive distance (d) is assumed to be equal to the grain size in the model. It may be that in systems where lateral long-range solute transport may be operating (e.g. in an open system with advective transport of calcite) diffusive distance can be larger than grain size (Dewers and Ortoleva, 1990; Gundersen *et al.*, 2002; Lehner, 1995).

3.7.3 Forward modelling pressure solution to the plate interface

Having modelled pressure solution in Unit IV through the last $\sim$ 60 Myr to the present day, I also extend the dissolution model to show the final effect of pressure solution when the sediments reach the toe of the Hikurangi plate interface. I use the thickness of sediment overlying Unit IV from Site U1520 to the toe of the thrust on seismic line 05CM-04 to calculate vertical stress into the future (Fig. 2.2; Barnes *et al.*, 2020). Strain rate from pressure solution is calculated as previously.

The thickness of sediment added is less than 500 m at the toe (Fig. 2.2), reflected by a change in normal stress of $\sim$ 4 MPa (Fig.S3). Similarly, a minor change in calcite solubility results from higher temperature with increased depth. The distance between Site U1520 and the toe of the megathrust is relatively short ($\sim$ 20 km), occurring rapidly compared to the previous model and hosting shortening strain increases of less than 0.025 throughout Unit IV (Fig. S3). The small difference in strains indicates the majority of pre-subduction dissolution-hosted strain has already

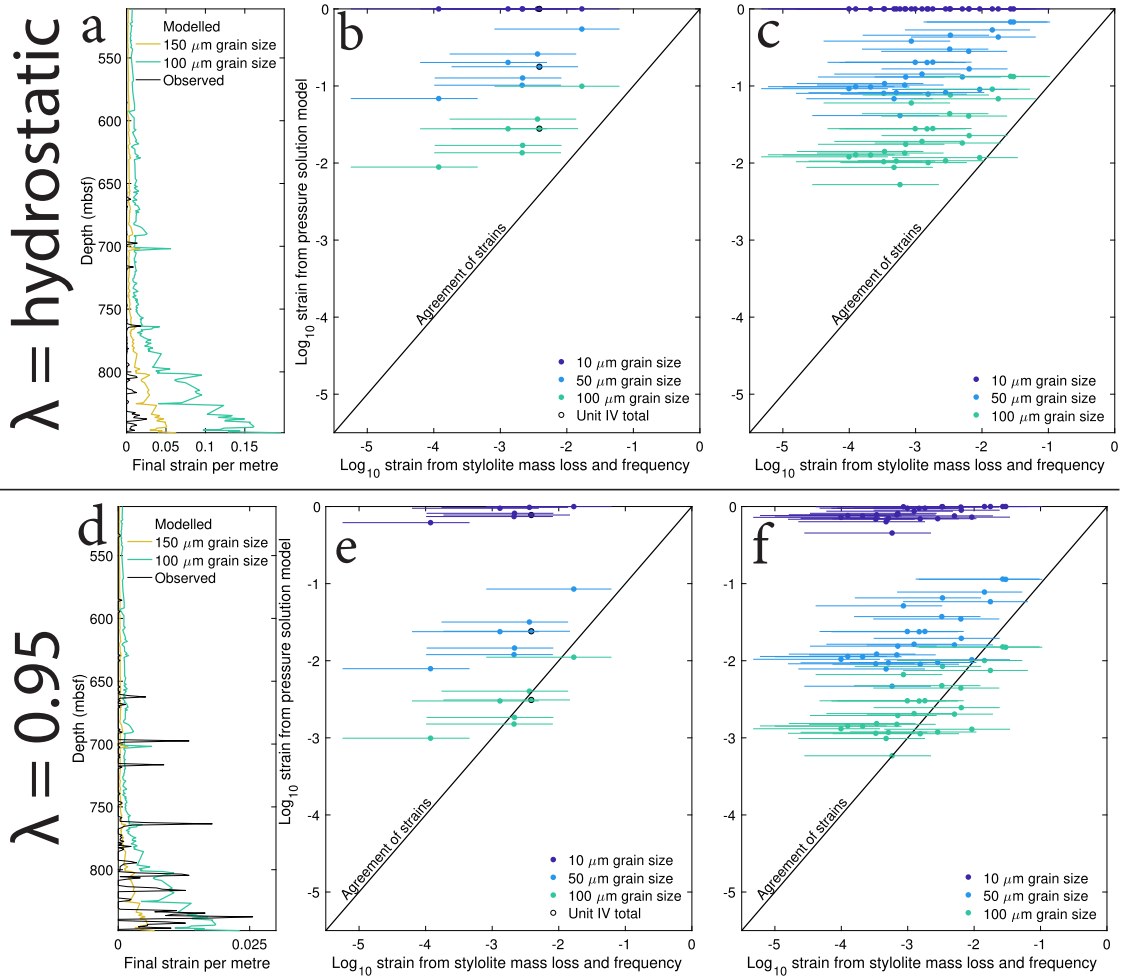

Figure 3.10: Comparison of modelled and calculated strains for compaction by stylolites at hydrostatic or near lithostatic fluid pressures within Unit IV. Plots show (a & d) final strain with depth per metre, (b & e) strain within each lithology and all of Unit IV (outlined in black), and strain within each core section (c & f) for hydrostatic (a-c) and near-lithostatic (d-f) pore fluid pressures. Error bars show strain ranges for individual stylolite seams of strain 0.1 to 0.9 used in calculation of bulk strain. As this chapter deals solely with shortening strains, they are presented as positive.

been accommodated within Unit IV over the last ($\sim$ 60 Myr), so that stylolites observed at Site U1520 are likely very similar to those existing within Unit IV at the toe of the megathrust.

3.8 Future subduction of Unit IV and rheology of the current plate interface

Modelled and observed strains from pressure solution in Unit IV at site U1520 are comparable when averaged over tens of metres and using a diffusion length scale comparable to the coarsest sediment fraction. Forward modelling to the toe of the megathrust shows only a slight change in strain, suggesting the majority of pre-subduction compaction had already been accommodated by the time the sediment reached Site U1520 (Fig. S3). Depth-converted seismic profiles indicate the lower part of Unit IV is likely the protolith for the localised plate interface, where it is likely to accommodate shear strain during subduction (Barnes *et al.*, 2020).

3.8.1 Rheological variation throughout Unit IV

Unit IV is highly variable with regards to mineralogy, porosity, and lithological texture (Fig. 3.5). These factors, along with partial lithification and abundant pore water, are likely to influence slip and deformation style and contribute to a heterogeneous plate interface (Barnes *et al.*, 2020; Delle Piane *et al.*, 2017; Mittempergher *et al.*, 2018; Sample, 1990; Skarbek and Rempel, 2017; Wallace *et al.*, 2019). Compounding this, the calcareous-pelagics in Unit IV overlie a sequence of volcanic conglomerates, completely rheologically distinct and even more locally variable (Barnes *et al.*, 2020; Wallace *et al.*, 2019). The rheology of intact lithologies comprising Unit IV at the plate interface would therefore already be locally variable, but pre-subduction strain on faults and stylolites will cause local changes in rheology from those predicted for the intact sediments of Unit IV.

Strains calculated from stylolites within Unit IV are not large. Uniaxial shortening strain for the entirety of Unit IV is $\sim$0.004, but represent local accumulation of insoluble clays within each discrete $<$ 1 mm-thick stylolite (Fig. 3.2). Each stylolite does not host enough insoluble clay to significantly alter the rheology of the bulk rock, but where stylolites cluster the accumulation of clays within stylolites may become locally-significant (Fig. 3.5). Stylolites cluster when less than 1 m apart (Fig. 3.6), with clusters hosting up to 80 stylolites per metre (Fig. 3.5). Clay

concentrated on stylolites in these clusters represents strain-weakened horizons from early viscous deformation due to the weakness of clay relative to the encompassing carbonate (Boulton *et al.*, 2019; Rabinowitz *et al.*, 2018), possibly significant enough to locally alter bulk deformation style. Indeed, some faults in Unit IV are localised along clay-rich seams of similar thickness to those within stylolites (Figs. 3.2 & 3.4). Clusters of stylolites increase in intensity with depth, increasingly altering lithological texture and resultant deformation style on increasingly interconnected anastomosing stylolite seams (Figs. 3.2, 3.5, & 3.11).

Faults within Unit IV are rheologically variable, with weak surfaces between two moderately weak zones of damaged material (Figs. 3.4 & 3.11). Individual fault and fracture zones are more commonly considered than stylolites as zones of strain-weakening, likely to host later deformation (Ferraro *et al.*, 2018; Leah *et al.*, 2018; Mitchell and Faulkner, 2009), but clustering of faults in Unit IV makes contemporaneous reactivation of several faults within a centimetre to metre-thick volume likely at the plate interface (Figs. 3.5, 3.6 & 3.11). In addition, pressure solution has concentrated phyllosilicates on fractures in damage zones, concentrating clays and further weakening areas hosting fault clusters (Figs. 3.4 & 3.11).

3.8.2 Future décollement location and deformation localisation

Within Unit IV, clusters of clay-rich stylolite seams or fracture-bound faults represent these low volume-fraction phases with lower shear strengths than the host rock, likely to localise deformation at the plate interface. Rheological heterogeneity is another key factor in deformation localisation during reactivation of pre-existing weaknesses (Imber *et al.*, 2008; Leah *et al.*, 2018; Lyakhovsky *et al.*, 1997; Willemse *et al.*, 1997) and stylolite and fault clusters represent heterogeneous intervals throughout Unit IV. One particular interval, near the base of Unit IV (835 to 845 mbsf; Fig. 3.5), hosts nearly 400 stylolites in two large clusters, increasing the volume fraction of clay present by localised pressure solution (Fig. 3.5). This increased clay fraction creates a shear strength contrast within the sediments, making strain more likely to

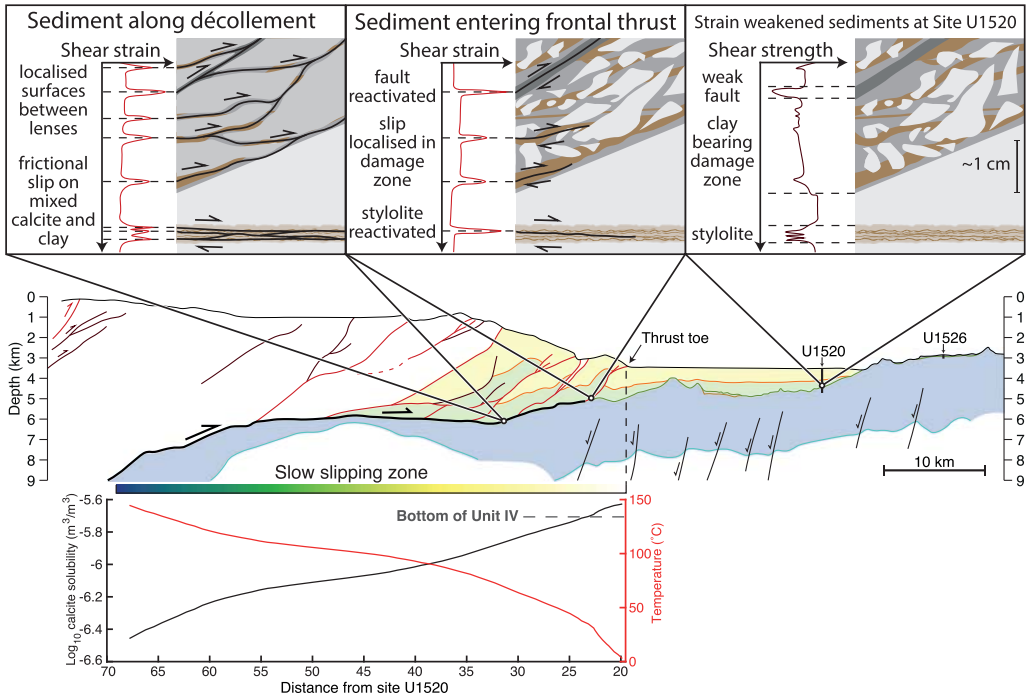

Figure 3.11: Schematic overview of strain localisation and weakening in Unit IV at Site U1520 and its possible future rheological behaviour during subduction. Sketches with notes (above) show locally important textures and rheological notes from Unit IV at various stages during subduction (middle). Thermal gradient (below) is from Antriasian *et al.* (2018), resultant calcite solubility is calculated using the method of Plummer and Busenberg (1982).

localise there when subject to shear stress. Shallower in the sediment stack, mudstones within Unit IV (e.g. $\sim$ 720 to 740 mbsf) may also be significantly weaker layers likely to localise shear strain. The localisation of deformation likely to occur upon reaching the plate interface would manifest as incrementally greater shear strain is accommodated in the weaker horizons rather than in the stronger intervals, creating a thin cumulative volume hosting high shear strain, including a likely horizon near the base of Unit IV (Fig. 3.11). This localisation of strain in the sediments adjacent to the volcanic basement could be complicated by basement topography, which has been shown to be highly variable at the Hikurangi margin (Barnes *et al.*, 2020).

3.8.3 Deformation mechanisms at the plate interface, implications for slow slip

Slip on faults and fractures within their damage zones will be frictional, with properties controlled by that of the material on the fault. Where faults have localised upon pre-existing stylolites, therefore, slip character is likely to be controlled by phyllosilicates localised in the stylolite seam (Fig. 3.4). Where faults have formed away from stylolites, frictional slip is likely to reflect the bulk protolith, dominantly calcite (Fig. 3.5). Calcite and clays are likely to mix during slip, possibly by weak phase smearing (Rutter *et al.*, 2013). Friction on these surfaces would likely be dominated by phyllosilicate-hosted slip with a lesser component of calcite. This would lead to a mixture of velocity strengthening and weakening conditions over varying conditions and could provide appropriate conditions for unstable slow slip on the plate interface (Boulton *et al.*, 2019; Rabinowitz *et al.*, 2018; Tesei *et al.*, 2014).

Localised slip surfaces are also likely to form on weak, clay-rich stylolites, where they could accommodate shear strain by a combined frictional-viscous flow mechanism (Bos, 2002; Gratier *et al.*, 2013; Willemse *et al.*, 1997). This entails frictional slip on an anastomosing phyllosilicate foliation with removal of material from grains within the foliation by pressure solution, similar to deformation modelled for quartz-bearing gouge by Den Hartog and Spiers (2014) or less phyllosilicate-rich halite or quartz-bearing gouge by Bos (2002). As calcite solubility is high at low temperatures (Plummer and Busenberg, 1982), abundant calcite within these deforming zones will likely deform by pressure solution at the shallow plate interface. Intensive pressure solution would cause volume loss from the volume accommodating shear between clasts, possibly increasing relative clay volume fraction within the sliding portion of the plate interface shear zone and altering the shape of clasts (Gratier *et al.*, 2015), thereby causing strain weakening. Alongside this, carbonates experience significantly more variable deformation at relatively low temperatures than their siliciclastic counterparts, including recrystallisation (Kennedy and White, 2001), crystal plasticity (Verberne *et al.*, 2013), and variable frictional properties (Verberne *et al.*, 2014).

Within a plate interface shear zone hosting grain size reduction of heterogeneous materials over varying depths, pore fluid pressures, and temperatures (Barnes *et al.*, 2020), it is likely pressure solution will be locally variable on the sub-mm scale, removing and re-depositing material locally around grains or clasts. At shallow depths, the temperature gradient of the northern Hikurangi Margin is thought to be relatively high (Antriasian *et al.*, 2018), corresponding to a rapid reduction in calcite solubility as materials are buried (Fig. 3.11). The ability of pressure solution to cause removal of calcite, therefore, is greatly reduced outside regions of low temperature, likely corresponding to less than $\sim$ 150 °C or 10 to 15 km depth (Fig. 3.11; Antriasian *et al.*, 2018). This is a similar depth to the deeper end of the slow-slipping zone, possibly indicating that pressure solution of calcite may decrease in relative importance as a mechanism accommodating deformation at the plate interface outside the area recognised to host slow slip.

3.9 Conclusions

- Unit IV at Site U1520 hosts clustered faults and stylolites within muddy pelagic carbonates with variable composition. The frequency of stylolites increases with depth, whereas faults are more common within several shallower horizons.

- Stylolite frequency increases approximately exponentially with $CaCO_3$ content. Stylolites comprise anastomosing individual seams, each hosting mass losses of 11 to 45% within a horizon of lower porosity compared to the host rock. Uniaxial shortening, accounting for porosity change, is high on individual stylolite seams ($\sim$ 0.5) but small over greater distances because localised horizons host dissolution. Stylolites concentrate clays by dissolution, forming localised clay-rich surfaces within a mostly intact host rock.

- Stylolite distribution reflects an interplay of grain-scale physical and larger scale compositional factors, forming most commonly where calcite content is high, clay is present to accelerate dissolution, or high initial porosities localise

dissolution.

- Faults in Unit IV are present in more lithified units, locally exploiting pre-existing stylolites. Slip surfaces host adjacent cm-scale damage zones which have themselves undergone pressure solution, showing that mixed brittle and viscous deformation occurs at very shallow depths in calcareous sediments.

- I model pressure solution using published models for intergranular pressure solution of carbonates over the depositional history of Unit IV. To do this I determine an absolute P-T-t history using porosity, density, age, and temperature constraints from IODP Exp. 375.

- Despite incorporating modern day composition and the temporal evolution of stress and temperature into the pressure solution model, the locations and magnitudes of strain within stylolite clusters observed within Unit IV are not well reproduced at hydrostatic or near-lithostatic fluid pressures. At hydrostatic fluid pressures I find agreement at grain sizes corresponding to coarse fossils within the sediment, possibly consistent with porosity loss inferred from stylolite microstructure. At near-lithostatic fluid pressure, observed and modelled strains agree at more common grain sizes in the sample, though this requires sustained periods of high pore fluid during the $\sim$ 60 Myr history of Unit IV.

- Strain from localised dissolution on stylolites is likely overestimated using a bulk pressure solution model due to the complexity and evolution of sub-grain scale fluid pathways and diffusivities not fully captured within the applied model. I show that a linear scaling of calcite volume percent and strain rate is overly simplistic, and that the relationship of grain-scale effects within pressure solution models must be better constrained with composition, time, and strain.

- I extend the model to the toe of the megathrust and show that dissolution causes negligible change in strain between present day and initial subduction of the sediment column at Site U1520.

- Shear within the carbonaceous Unit IV at the plate interface is likely to localise in weak horizontal horizons including clay-rich stylolite clusters at the bottom of Unit IV, slipping by frictional-viscous mechanisms with variable frictional stability due to composition heterogeneity within stylolite clusters.

- Pressure solution of calcite is likely an important viscous mechanism acting on the grain scale throughout the slow-slipping zone and at shallow depths on the plate interface. Indeed, the down-dip end of slow slip events ($15 - 20$ km) roughly correlates with where carbonate solubility becomes negligible. Throughout the slow-slipping zone and the shallow plate interface, other deformation mechanisms in the chalks and clay-rich muds are likely highly variable.

- The role of carbonate in accommodating shear at the Hikurangi Margin is emphasised, as this dramatically alters slip characteristics and deformation style compared to siliciclastic sediment.

Chapter 4

3D Imaging of the northern Hikurangi margin using high-resolution receiver functions

Whereas drilling provides very good near-surface data and active seismic surveys provide high-resolution data within ∼10 km of the surface (e.g. Barnes *et al.*, 2010; Bell *et al.*, 2010), deeper parts of subduction zones are more difficult to study. At depths where wide-angle controlled-source reflected seismic waves are too weak to coherently image (> 10 km depth), converted seismic waves from distant global earthquakes can be imaged with the use of teleseismic receiver functions (e.g. Langston, 1979). This chapter is concerned with imaging actively-deforming volumes of the northern Hikurangi margin and tracking input sediments down-dip (Chapter 3) using the receiver function method applied to teleseismic data recorded by the NZ3D array. The receiver function method is usually applied to image deeper horizons, such as the Moho at ≥ 25 km depth, due to its frequency content of ≤ 1 Hz (Langston, 1979). In this chapter I use a new method to deconvolve receiver functions with a frequency content up to 4 Hz, allowing imaging of shallower horizons than has previously been possible in a subduction zone setting.

4.1 The receiver function method

Consider a P wave arriving at a seismometer from a large magnitude (M6+) earthquake 30-90° epicentral distance away. The arrival time series recorded at the station can be considered the result of a convolution of (1) the pure incident wave, (2) seismic noise, (3) the response of the instrument, and (4) the Earth structure through which the wave has travelled. As the wave travels through the Earth, and encounters velocity discontinuities (e.g. the Moho), P wave energy is converted into an S wave that radiates from the discontinuity (Fig. 4.1). The direct P wave comprises motion parallel to its path and is therefore dominant on the vertical component of a 3-component seismometer. P-to-S converted phases are recorded best on radial component seismograms, but further analysis is required to isolate the arrivals within the P-wave coda. To achieve this, teleseismic receiver functions are calculated by deconvolving the vertical from radial component seismograms (e.g. Langston, 1979).

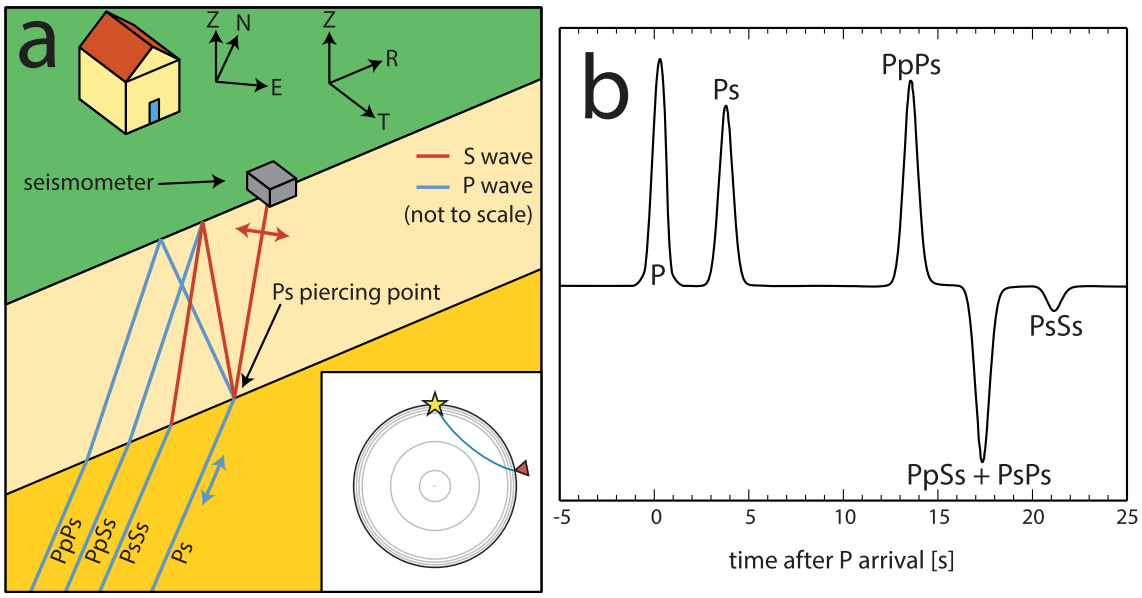

Figure 4.1: Schematic summary of earthquake arrival at a seismometer showing (a) the approximate geometry of various converted and reflected phases and the ZNE (vertical, north, east) and ZRT (vertical, radial, transverse) coordinate systems and (b) the resultant radial receiver function. Part (b) redrawn after Ammon *et al.* (1990).

A radial P-to-S receiver function begins at the P wave arrival time ($t = 0$) and

comprises a series of peaks and troughs representing arrivals and multiples from conversion horizons in the subsurface (Fig. 4.1b). Conversions are strongest at horizons of high velocity contrast; smooth velocity depth profiles with no strong contrasts will produce receiver functions with no clearly-defined peaks (e.g. Ogden *et al.*, 2019). Where crustal structure is relatively simple, the direct Ps conversion and several multiples (PpPs, PsPs, and PpSs) can be observed (Fig. 4.1). These multiples arrive at different times, controlled by the velocity structure through which they have passed.

Rays arrive at the station sub-vertically, at an angle between the arrival and Earth's surface (θ) controlled by the velocity (v) structure. These parameters are used to define the horizontal slowness ($p = sin(\theta)/v$) which can be used to calculate the theoretical arrival time of a P to S conversion using

$$t_{Ps} = z * \left[\sqrt{\frac{1}{V_s^2} - p^2} - \sqrt{\frac{1}{V_p^2} - p^2} \right], \tag{4.1}$$

where z is the thickness of the layer, V_s is the S wave velocity of the layer, p is the slowness of the ray, and V_p is the P wave velocity of the layer. The points where each conversion occurs are known as piercing points (Fig. 4.1a). Additional complexity is included when imaging anisotropic or dipping layers. Subduction zones host dipping shear zones and folded lithologies, meaning they have much inherent heterogeneity and imaging them with receiver functions is therefore non-trivial (e.g. Abers *et al.*, 2009).

4.2 The NZ3D seismic array

The NZ3D seismic experiment is a large project to elucidate slow slip observed at the northern Hikurangi margin (see Chapter 2) using land-based and ocean-bottom seismometer (OBS) arrays and offshore 3D active seismic surveys to collect wide angle refraction and reflection data with broad ray coverage (Bell *et al.*, 2018). The land-based NZ3D array was situated so that wide-angle ray paths from the NZ3D-FWI offshore seismic survey would image a patch of repeated slow slip (Fig.

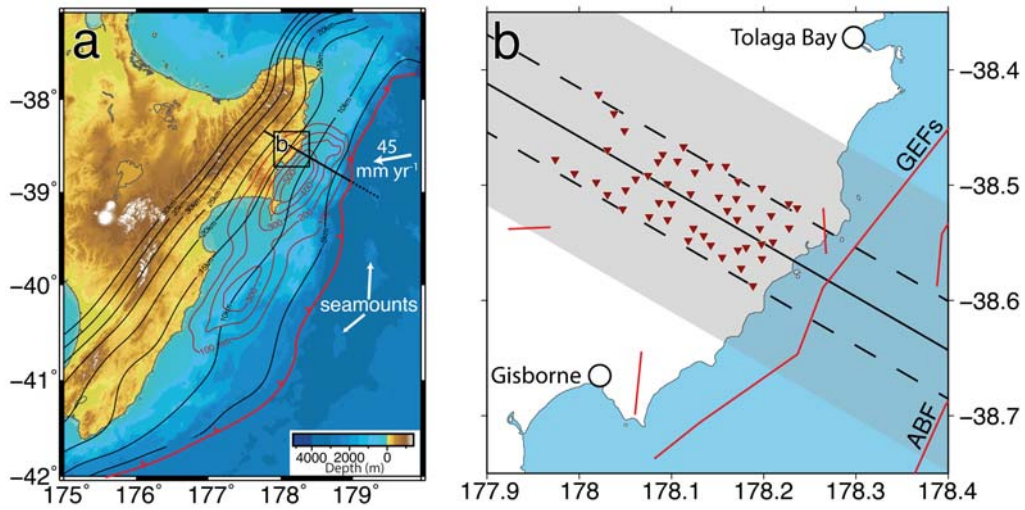

Figure 4.2: Map of the NZ3D array and section locations. Panel (a) shows elevation across the Hikurangi margin with the trench (red flagged line), plate interface depth (black labelled contours), cumulative slow slip (dark red labelled contours), section line for later figures (thick black line), and approximate 05CM-04 transect location (dotted black line). Plate interface depth is from Williams *et al.* (2013), cumulative slow slip is from Wallace (2020a), labelled white arrow shows Pacific/Australia relative plate motion from Beavan *et al.* (2002). Rectangle shows location of panel (b). Map in (b) shows 6TD seismometer locations (inverted dark red triangles), active faults (red lines; Litchfield *et al.*, 2014), section line used in CCP figures (solid black line), section lines used in Fig. 4.14 (black dashed lines), and CCP volume area (transparent grey fill). GEFs is the Gable End Fault south, ABF is the Ariel Bank Fault (Litchfield *et al.*, 2014; Mountjoy and Barnes, 2011).

4.2). The array was deployed in December 2017 and included a dense array ($\sim$ 2 km spacing) of 50 broadband Güralp 6TD seismometers in shallow sand-filled holes within fenced enclosures (Figs. 4.2b & 4.3; Bell *et al.*, 2018).

4.3 Instrument noise

Most of the 50 6TD stations record relatively high seismic noise (Fig. 4.4; Peterson, 1993), median amplitudes for most stations are very close to the Peterson High Noise

Figure 4.3: A field photo showing an example of 6TD station deployment. Seismometers were deployed underneath a tarpaulin, with batteries and cables in the adjacent box. Solar panels provided power and a raised position for the GPS unit.

Model at frequencies above 0.9 Hz, and are sometimes above it at frequencies above 20 Hz (Fig. 4.4). Below 0.9 Hz, median amplitudes at all stations are between the high and low noise model curves, but are generally closer to the high noise model (Fig. 4.4). Bearing this in mind, signal to noise ratios of earthquake arrivals are expected to be low.

4.4 Applying the receiver function method

Receiver functions are calculated from the seismograms of earthquakes in the teleseismic distance range 30-90° (Fig. 4.5). On initial inspection some arrivals showed clear P wave onsets with minimal pre-arrival noise, but others showed significant noise with minimal evidence for any clear arrival. The signal to noise ratio (SNR) was calculated using frequency-amplitude curves generated using a Fourier transform on 30 second time windows before (noise) and after the P wave arrival (signal)

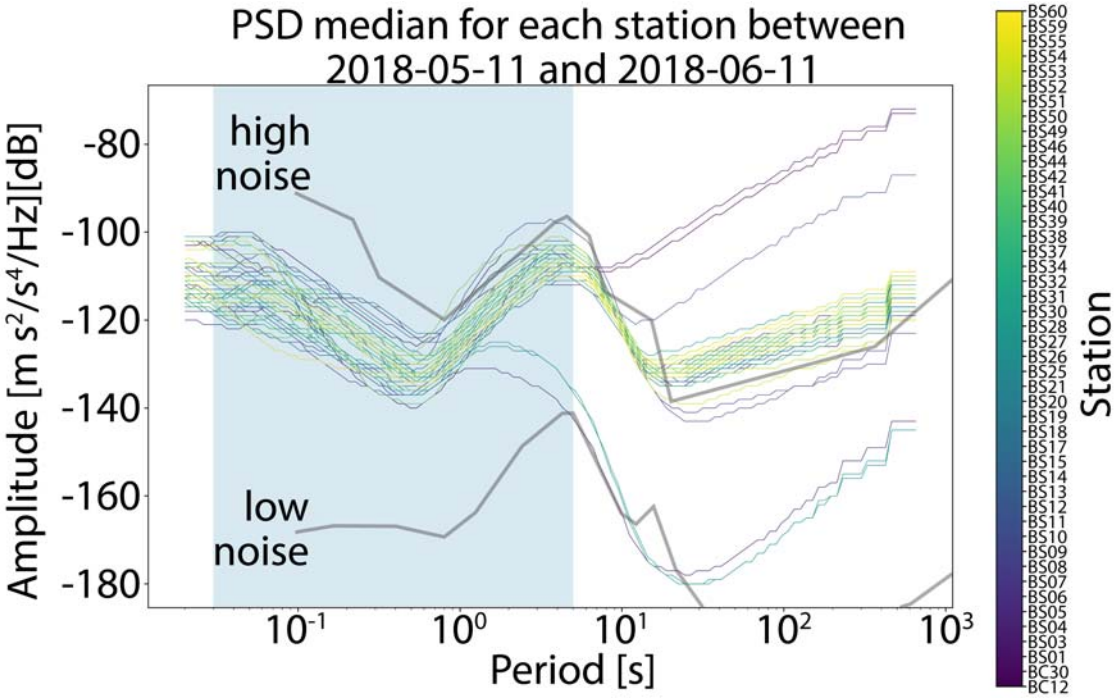

Figure 4.4: Frequency-amplitude curves of station noise during May 2018. Typical high and low noise curves are based on Peterson (1993). Light blue area is frequencies of concern to receiver functions.

on the Z component. Signal and noise frequency-amplitude curves are similar across much of the frequency range except between 0.03 and 4-5 Hz where the mean signal amplitude is greater than the mean noise amplitude (Fig. 4.6). This suggests, despite major overlap in the signal and noise amplitude ranges, that the arriving P waves generated usable signal in the 0.03 to 4-5 Hz frequency range. SNR was calculated by dividing signal amplitudes by noise amplitudes at each frequency. The mean SNR between 0.03 and 5 Hz was used as the SNR for each arrival (Fig. 4.6). Following SNR analysis the three component station streams were rotated to the ZRT coordinate system (Fig. 4.1a), demeaned, detrended, bandpass filtered between 0.03 Hz and 5 Hz, and downsampled from an original 100 Hz or 200 Hz recording frequency to 20 Hz. To reduce computation time, traces were trimmed to 3 seconds before and 60 seconds after the P wave arrival.

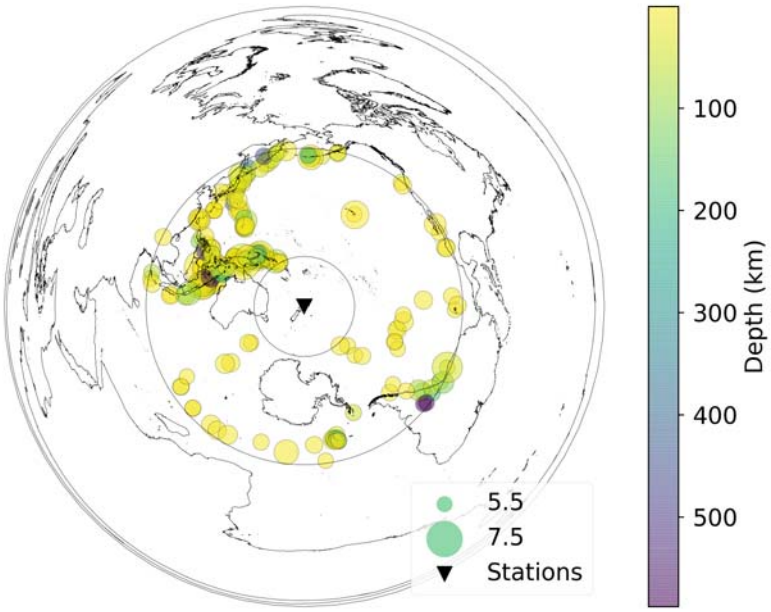

Figure 4.5: Map of all earthquakes used for deconvolution of receiver functions in the study. Grey circles are 30 and 90° epicentral distance.

4.5 Comparison of deconvolution methods

Two methods which are thought to provide stable receiver functions from noisy traces are iterative time-domain deconvolution (Ligorría and Ammon, 1999) and a recently reported trans-dimensional Bayesian Green's function estimation method which uses a reversible-jump Markov Chain Monte Carlo (RJMCMC) algorithm (github.com/akuhara/MC3deconv; Akuhara *et al.*, 2019). Both methods insert pulses in the resulting receiver function to reduce misfit between a function applied to radial and vertical seismograms, but the RJMCMC method can remove or move pulses after insertion to explore the most probably noise level and fit using Bayesian statistics. Despite some minor over-fitting to noise (Fig. B.3), the receiver functions obtained from the RJMCMC inversion appear consistent at each station, have less apparent noise, and more consistent peaks than corresponding receiver functions obtained by the iterative time-domain method (Fig. 4.7). Given

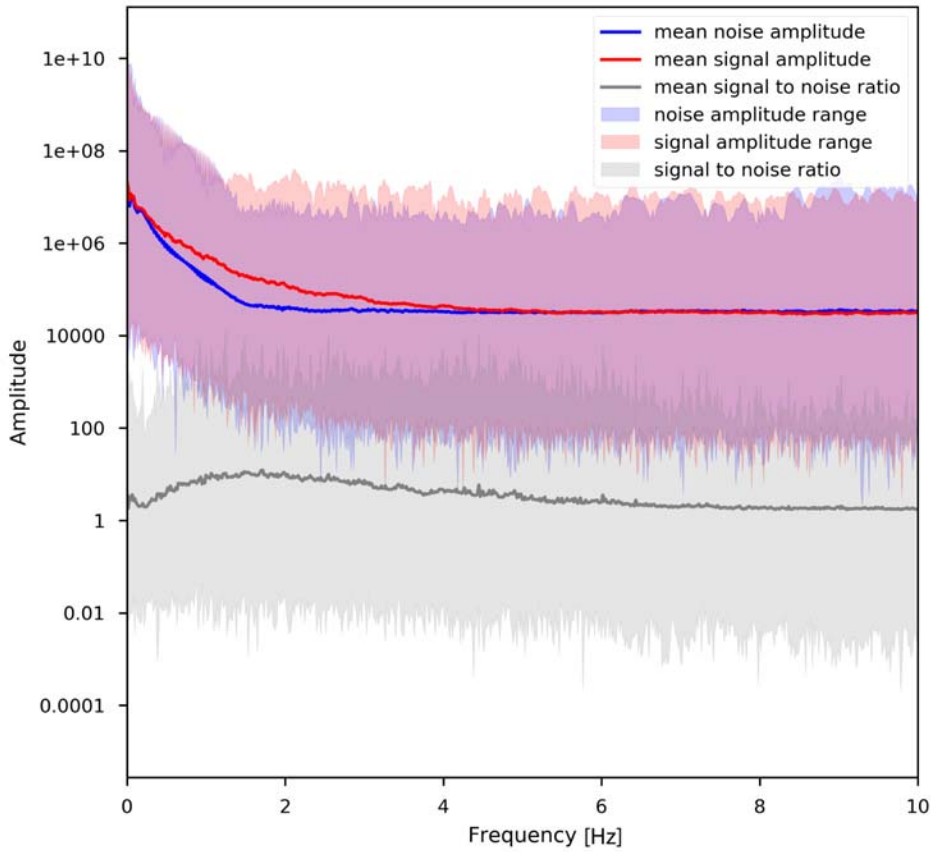

Figure 4.6: Signal and noise frequency-amplitude ranges and mean curves and signal-to-noise ratios range and curve calculated from 30 second windows before and after P wave arrival.

the greater reliability and lower error (Akuhara *et al.*, 2019), the RJMCMC receiver functions are used for the remaining analysis. For a detailed description of these methods and their application see Appendix B.1.

4.6 Major P-to-S conversion times

Receiver functions at each station show coherent arrivals at many time intervals throughout the first 30 s after the P wave arrival (Fig. 4.8). Many of these are likely multiples of shallow conversions at depths of < 40 km; between 5 and 7 peaks

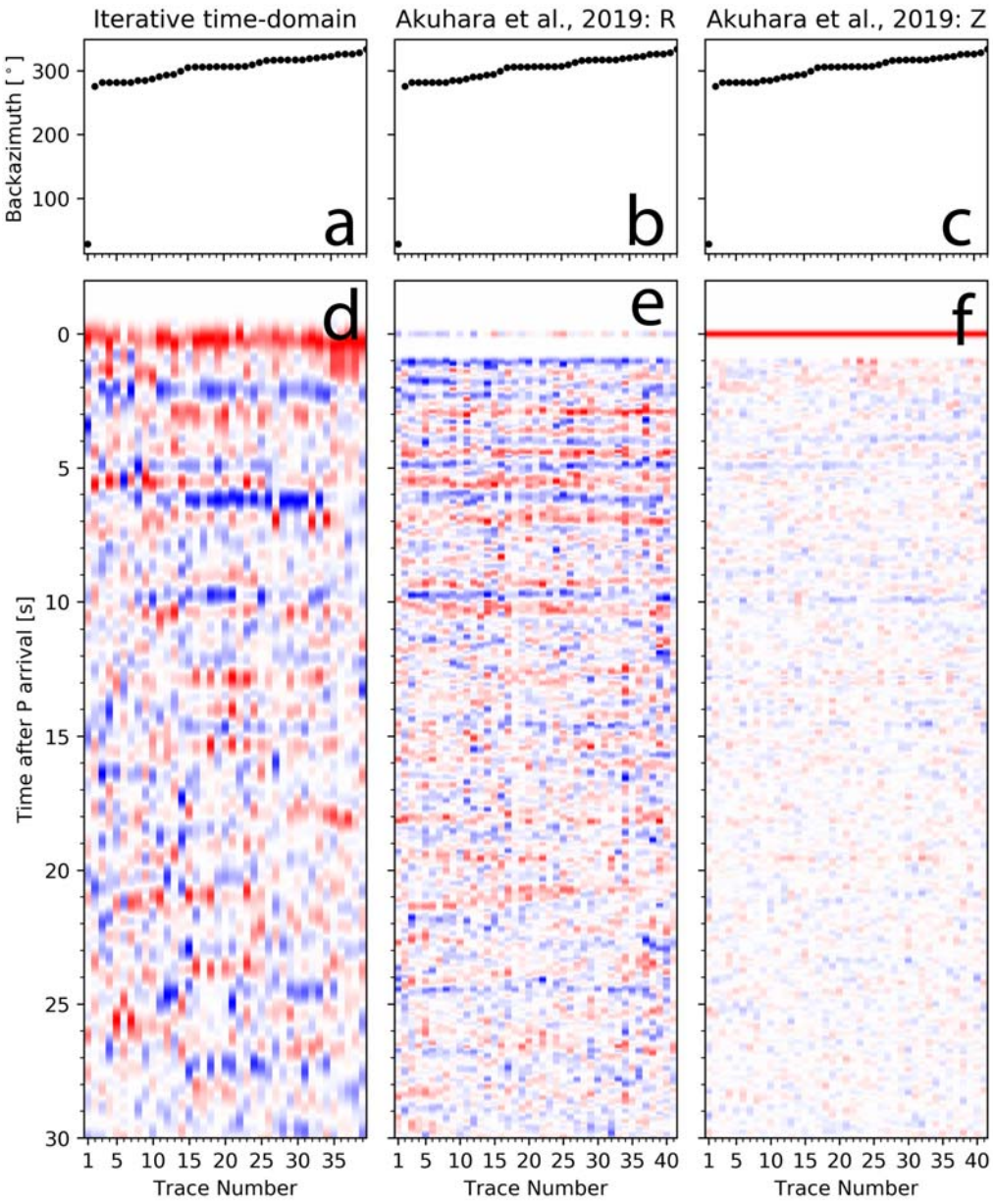

Figure 4.7: A comparison between the same high quality (SNR> 3) arrivals at station BS05 deconvolved to receiver functions using the iterative time-domain method and a Gaussian width of 4 (parts a & d; Ligorría and Ammon, 1999) and inverted as receiver functions using the RJMCMC method (parts b,c,e & f; Akuhara *et al.*, 2019). Upper plots (a-c) show the backazimuth of each trace, lower plots (d-f) show normalised trace amplitudes with time for each trace. Positive amplitudes are coloured red and negative amplitudes are coloured blue. The higher frequency content of the RFs inverted using the RJMCMC method of Akuhara *et al.* (2019) is visible as thinner blue and red horizons, representing the shorter wavelengths of each peak.

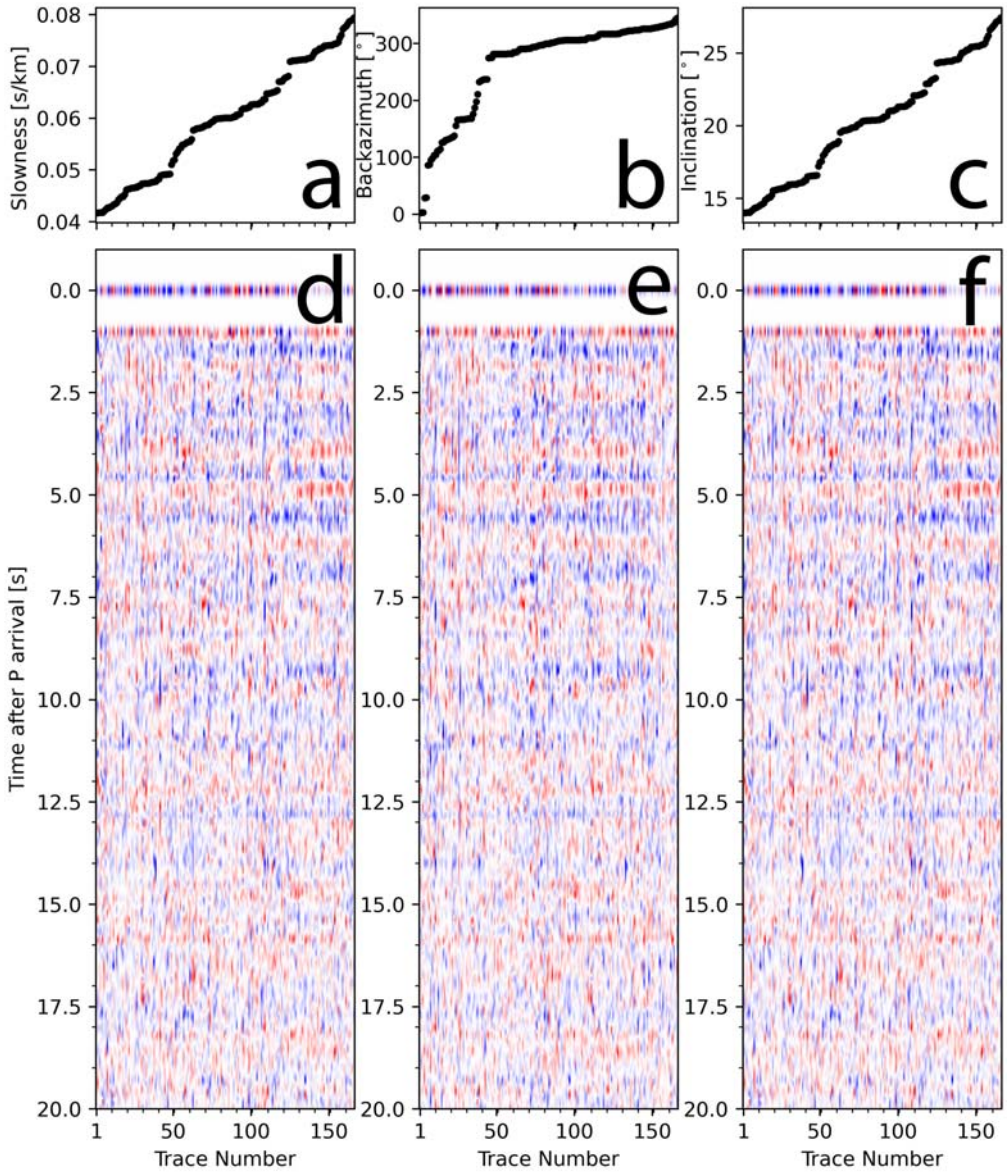

Figure 4.8: Dense ray stacks sorted by slowness (a & d), back azimuth (b & e), and inclination (c & f) for all arrivals at station BS05. Each trace is normalised to its maxima, positive amplitudes are shown as red and negative amplitudes are shown as blue.

occur in all receiver functions in the first 5-10 s (Fig. 4.8), these are likely direct Ps arrivals due to their early arrival time (Fig. 4.1). The relatively high number of likely Ps conversions in the first 10 s indicates a complex crustal structure with several major velocity contrasts in the top $\sim$ 100 km.

4.7 Volume and depth migration

Further analysis and modelling requires a velocity profile with depth; there are several global 1D velocity profiles, derived from long-term seismological datasets and often employed in the study of receiver functions, such as iasp91 (Kennett, 1991) or ak135 (Kennett *et al.*, 1995). Subduction zones can exhibit local variation in the shallow part of their velocity profiles, which significantly differs from velocities in generic earth models for the crust such as iasp91 (Eberhart-Phillips and Bannister, 2015; Eberhart-Phillips *et al.*, 2017, 2010). A three-dimensional velocity model of New Zealand was established by Eberhart-Phillips *et al.* (2010), and has since been updated to include more recent studies (Eberhart-Phillips and Bannister, 2015; Eberhart-Phillips *et al.*, 2017). The velocity model covering the study area was produced by fitting frequency-amplitude velocity spectra from high quality events across the margin (Eberhart-Phillips *et al.*, 2017). The method allows for inversion of V_p, V_s, and seismic attenuation coefficients (Q_p and Q_s), but is sensitive to raypath density and is relatively low resolution compared to this study (the model is evaluated on a $dx = 5$ km, $dy = 5$ km, $dz = 9$ km grid).

Vertical depth-velocity profiles interpolated below the NZ3D stations show significant variation in V_p and V_s in the upper 50 km (Fig. 4.9). Velocities to 10 km depth are higher nearer the trench, and between 10 and 50 km depth velocities are higher further from the trench (Bannister *et al.*, 2007; Barker *et al.*, 2009; Eberhart-Phillips *et al.*, 2017). To the east, a minor velocity decrease with depth around 50 km depth underlies a low V_s depth interval between 40 and 15 km depth, leading to high V_p/V_s ratios over this depth range. The velocity decrease with depth at 50 km depth is more pronounced beneath stations in the west, where V_s is higher throughout the upper 50 km, leading to lower V_p/V_s ratios throughout that depth range (Fig. 4.9).

To capture the local V_p and V_s variation, ray paths and their corresponding velocity profiles were interpolated from the regional three-dimensional model (Eberhart-Phillips *et al.*, 2010). The iasp91 model (Kennett, 1991) was used for an initial estimate for the depth of each time sample and the piercing point at that

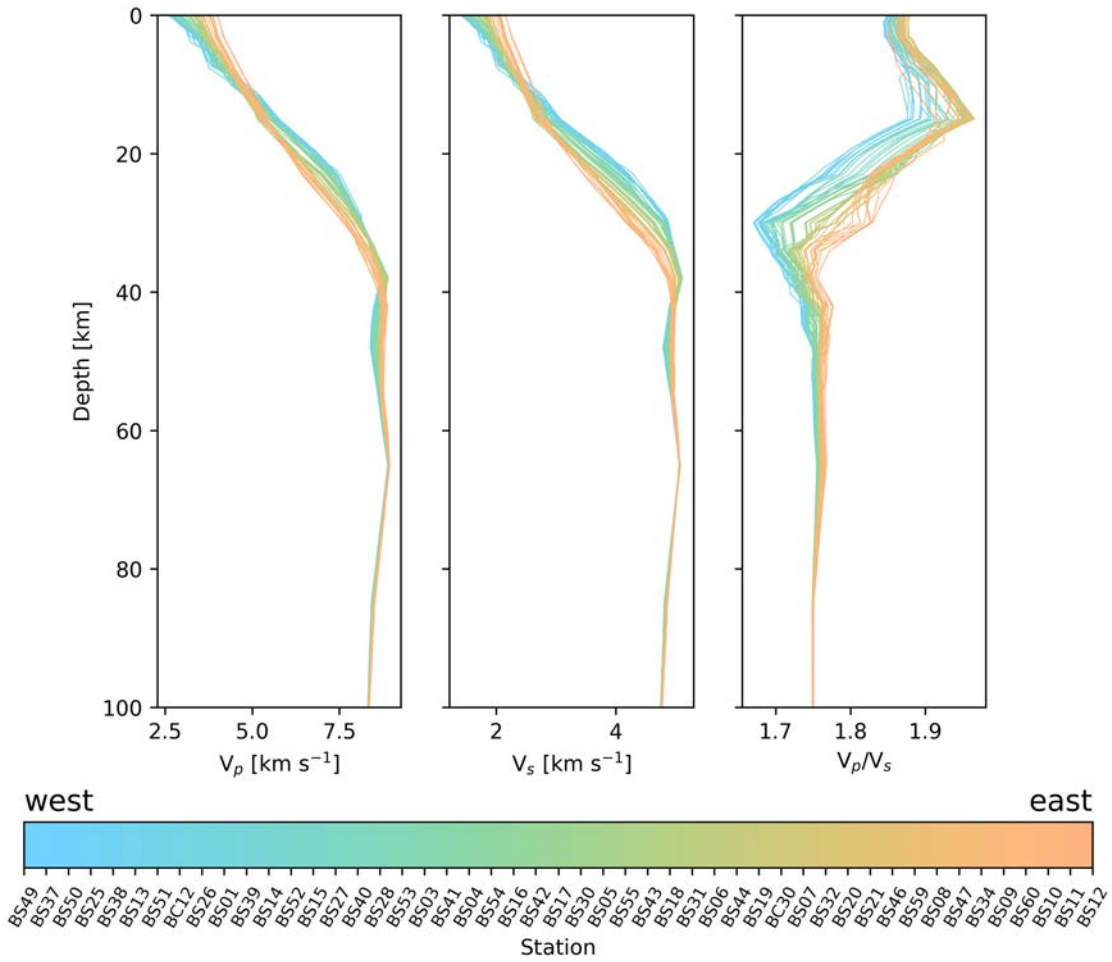

Figure 4.9: Velocities interpolated from the regional velocity model of Eberhart-Phillips *et al.* (2010) for 100 km depth below each station in the NZ3D array. Note the very low values for V_s near the surface, possibly due to allochthonous sediments overlying the Whakoua Fault (Mazengarb and Speden, 2000).

depth. The velocity-depth profile was then linearly interpolated at depths of < 100 km along that depth-piercing point ray path from the three-dimensional velocity model of Eberhart-Phillips *et al.* (2010). Repeated piercing point calculation and depth-velocity interpolation was then carried out until the change in the velocity profile at each depth was < 0.01 km s^{-1}. This was repeated for each ray using the piercing points along the theoretical ray path of a Ps conversion for later imaging.

4.8 3D CCP imaging

Common conversion point (CCP) stacking (e.g. Dueker and Sheehan, 1997) images conversion amplitudes in a spatial format, and is therefore a good way of exploring receiver function energy in space. The method involves correcting receiver functions for move out, back-projecting each receiver function to latitude, longitude, and depth along its P wave ray path at each time sample (see Section 4.7), and stacking the average amplitudes which occur within gridded bins. These amplitudes are assumed to sample the same volume of the subsurface and averaging them suppresses noise in the final model. CCP stacking can be used to construct a volume of average Ps and multiple amplitudes, but doesn't differentiate between the two. It allows the visual tracing of conversion horizons (which reflect structural discontinuities) laterally beneath the array (Frassetto *et al.*, 2011; Gilbert, 2004; Gilbert *et al.*, 2003). Though pioneered as a method to map the Moho beneath continental crust, receiver function CCP imaging has been successfully applied to depths $>$ 30 km at several subduction zones (Abers *et al.*, 2009; Audet and Kim, 2016; Audet and Schaeffer, 2018; Bannister *et al.*, 2007; Kim *et al.*, 2012; Phillips and Clayton, 2014; Shi *et al.*, 2015). Imaging dipping or anisotropic structures, or linearly stacking direct and multiple phases within a CCP can lead to incoherent patterns in the stacked amplitudes. A commonly applied correction uses a Hilbert transform to reduce spurious noise and suppress apparent arrivals from multiples, producing a phase-weighted stack (Frassetto *et al.*, 2010). The code to achieve CCP stacking was adapted from the *rfpy* toolbox (Audet, 2020). For a detailed description of CCP stacking methods see Appendix B.1.

To assess the effect of volume counts per CCP cell, a single two-dimensional CCP section was constructed with a 250 m CCP cell width and height. This is a smaller CCP cell dimension than that used in the 3D CCP volume and was selected to determine the maximum resolution when using many counts per CCP volume cell. This section encompasses the entire volume of arrivals projected onto a single section plane. This section shows smooth, laterally continuous horizons throughout the study area (Fig. 4.10). Counts throughout much of the section are in excess of

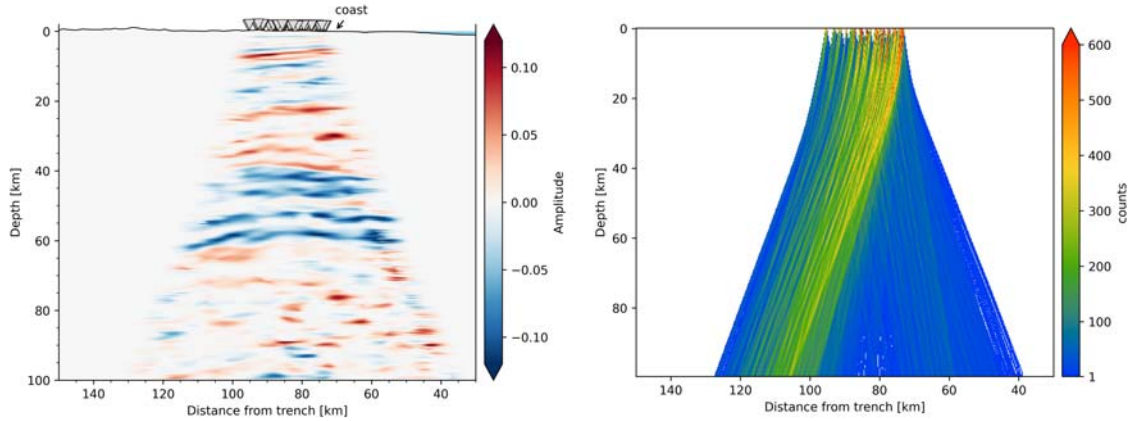

Figure 4.10: Two-dimensional CCP cross-section showing the phase-weighted stack of amplitudes (left) and the counts per bin (right). Cross-section is constructed of 0.25 × 0.25 km cells on a bearing of 121° and plotted against distance from the trench at 38.884°S/178.942°E, section line shown in Fig. 4.2b.

100 amplitudes per bin, suggesting the structure observed in Fig. 4.10 is reliable and similar amplitudes in the 3D CCP volume represent the same conversions in the subsurface.

4.9 Forward modelling of conversion horizons

Positive-amplitude conversion horizons imaged in the CCP volume result from stacked peaks in the first 30 seconds of the receiver functions (Fig. 4.1). Direct Ps conversion peak times, and their corresponding piercing points, can be used to create depth maps of specific horizons, but care must be taken to avoid interpreting multiples from shallower conversions. Simple forward modelling of conversion horizons in the upper 50 km of the subsurface can test which peaks are likely direct conversions (rather than multiples).

Each arrival's particular parameters (e.g. slowness and back azimuth) were used to forward model conversions using a simplified velocity model which averaged velocities between specified conversion depths (Eberhart-Phillips *et al.*, 2010). The simplified velocity model was then used with the forward modelling method of Frederiksen and Bostock (2000) to produce synthetic seismograms from which receiver

functions were subsequently calculated. Conversion depths were adjusted to visually match peaks for direct conversions and multiples in the observed receiver functions. A detailed description of how the modelling methodology was implemented is set out in Appendix B.3. Forward modelled horizons beneath Station BS05 at 6.25, 9.5, 13.5, 15.5, 33, and 44 km depth all result in peaks which show good agreement with peaks observed in receiver functions at the station (A-F in Fig 4.11). Scatter in peaks from direct and multiple conversions is also similar between real and synthetic receiver functions (Fig. 4.11).

Forward modelled direct arrivals (red triangles alongside y axes in Fig. 4.11) are around 1.5, 2.25, 2.9, 3.5, 5.5, and 7 seconds, suggesting peaks at similar times in the real receiver functions result from P-to-S wave conversions at approximately similar depths to those modelled (A-F in Fig 4.11). Forward modelled multiples of direct arrivals (light red triangles for PpPs and blue triangles for PsPs and PpSs alongside y axes in Fig. 4.11) also correspond well to peaks in the real receiver functions. A clear positive peak in the real receiver functions around 4.5 s could be interpreted as a direct conversion but modelling shows this approximately corresponds to a PpPs multiple of the Ps arrival at $\sim$ 1.5 s (Fig. 4.11). Reverberation amplitudes (PpPs, PpSs, & PsPs) are lower than amplitudes at the corresponding direct conversion (Ps) arrival times as energy is lost each time the ray is reflected (Langston, 1979). This is shown in the forward modelling by horizon E, which produces the highest-amplitude PpPs arrival as the velocity contrast at that horizon is the greatest (Fig. 4.11). Times of multiple arrivals are more sensitive to velocities in the input model, the forward modelled arrival around 4.5 s is slightly later than that observed in the real receiver functions, suggesting the average P velocity in the input model may be slightly lower than reality.

4.10 Mapping conversion horizons using arrival peak times

Having explored which arrivals in the data are most likely to result from direct conversions, conversion times from the likely Ps arrival peaks can be used to map

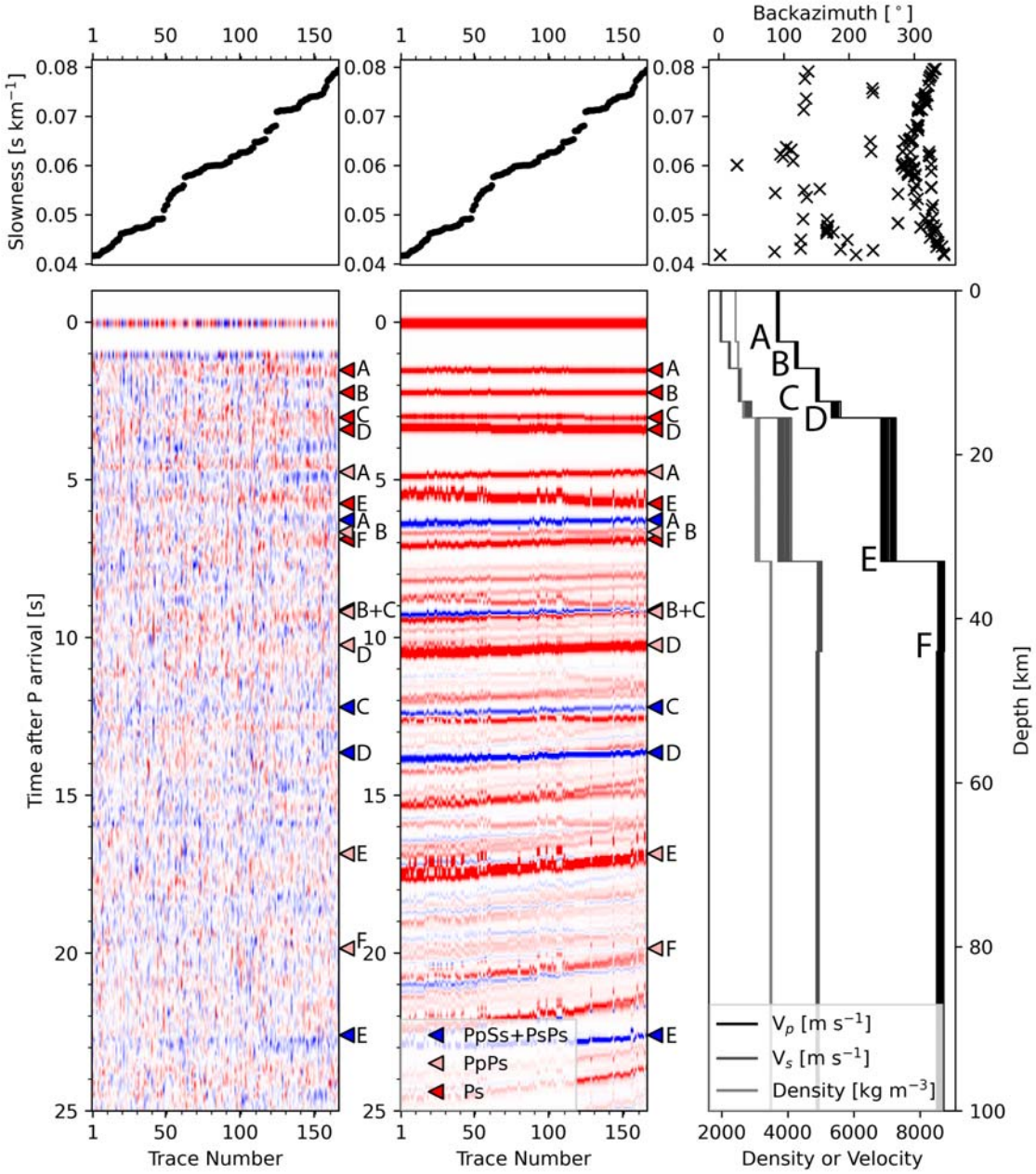

Figure 4.11: Example of forward modelling several conversion horizons for every arrival at a station. Receiver function amplitudes at each time are plotted (real on the left, synthetic in the middle) using red for positive peaks and blue for negative peaks. The slowness of each trace is plotted above. The velocities and densities (lower right) are modelled with the back azimuth and slowness (upper right) of each trace. Average velocities for each layer are the same over their depth range (< 100 km depth) as interpolated along the ray path from the 3D regional velocity model of Eberhart-Phillips *et al.* (2010).

conversion horizons at depth. These horizons may correspond to structural discontinuities in the subsurface. Mapping the surfaces involves: (1) peak time picking, (2) back-projection of picked peak times to latitude, longitude, and depth, and (3) surface fitting to the resulting scattered points. Manual peak picking was not used given the large number of receiver functions (around 7000). Instead, automatic peak picking was carried out. To filter out minor peaks, positive and negative peaks were picked in order of descending amplitude if their amplitude was greater than 0.05 (assumed to correspond to noise) and they were more than 0.5 s apart in the same arrival. Peaks were picked in the first 7.5 s after P wave arrival for each trace to capture all the horizons forward modelled earlier (Section 4.9). An example of the results of this procedure is shown for some arrivals at station BS05 in Fig. B.9. When considering all time picks it appears the peaks identified from forward modelling (Fig. 4.11) are representative of those across the entire NZ3D array (Fig. 4.12). Time pick piercing points were fitted with a surface using Gaussian process regression (*sensu.* Rasmussen and Williams, 2006) which assumes noise follows a Gaussian distribution with zero mean about the surface and a variance of σ^2, where σ is the standard deviation of the sample. Confidence limits (95%) presented here are 2 standard deviations calculated using the dip, undulation, and noise kernels specified in the fitting procedure (see Appendix B.1 for more detail). Forward modelling (Fig 4.11) suggests the peak at around 4.5 s likely corresponds to a PpPs multiple of the earlier PS arrival peak around 1.5 s, this peak was therefore not used to map a new velocity discontinuity. Nine time ranges were used to define velocity discontinuities, these will be referred to as horizons A through to I for the remainder of this section (Fig. 4.12).

Inspection of the estimated horizons reveals a series of north-west dipping surfaces with local undulations varying in wavelength from about 10 km in shallower surfaces to $>$ 40 km (Fig. 4.13). Time ranges used for mapping of each horizon are consistent across all stations (Figs. 4.8 & 4.12) so most of the surface dip and broad undulations in horizons F-I are the result of interpolation through the regional velocity model (Section 4.7). Error associated with the surfaces scales with the depth of the surface (Fig. 4.13); horizons A-F have 95% confidence limits of $\sim$2 km either

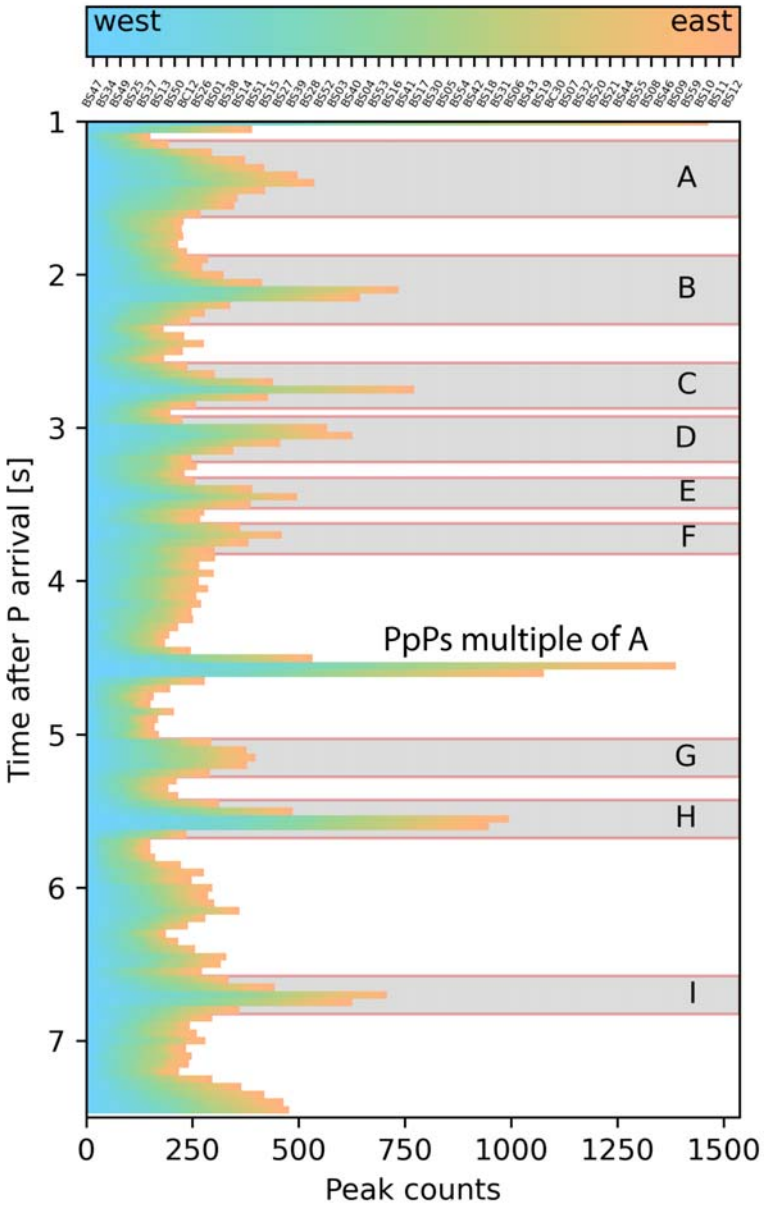

Figure 4.12: Picked positive-amplitude peak distribution in the first 7.5 seconds of each arrival at all stations. Bars show number of peaks per station and are stacked at each time sample. Bars are coloured blue to orange from west to east. Forward modelling suggests that eight major peaks likely correspond to major horizons in the subsurface. Note that the peak at 4.5 seconds was not used due to it likely corresponds to a multiple of peak A (Section 4.11).

side of the surface throughout the mapped area, increasing to ~ 3 km for horizons G-I. There is minor overlap in the 95% confidence limits of horizons C-D and E-F (Fig. 4.13), suggesting conversion coordinates used to map these surfaces overlap. Horizons G and H show substantial overlap in their error bars on their north-western extents but are separate in the SE (Fig. 4.13).

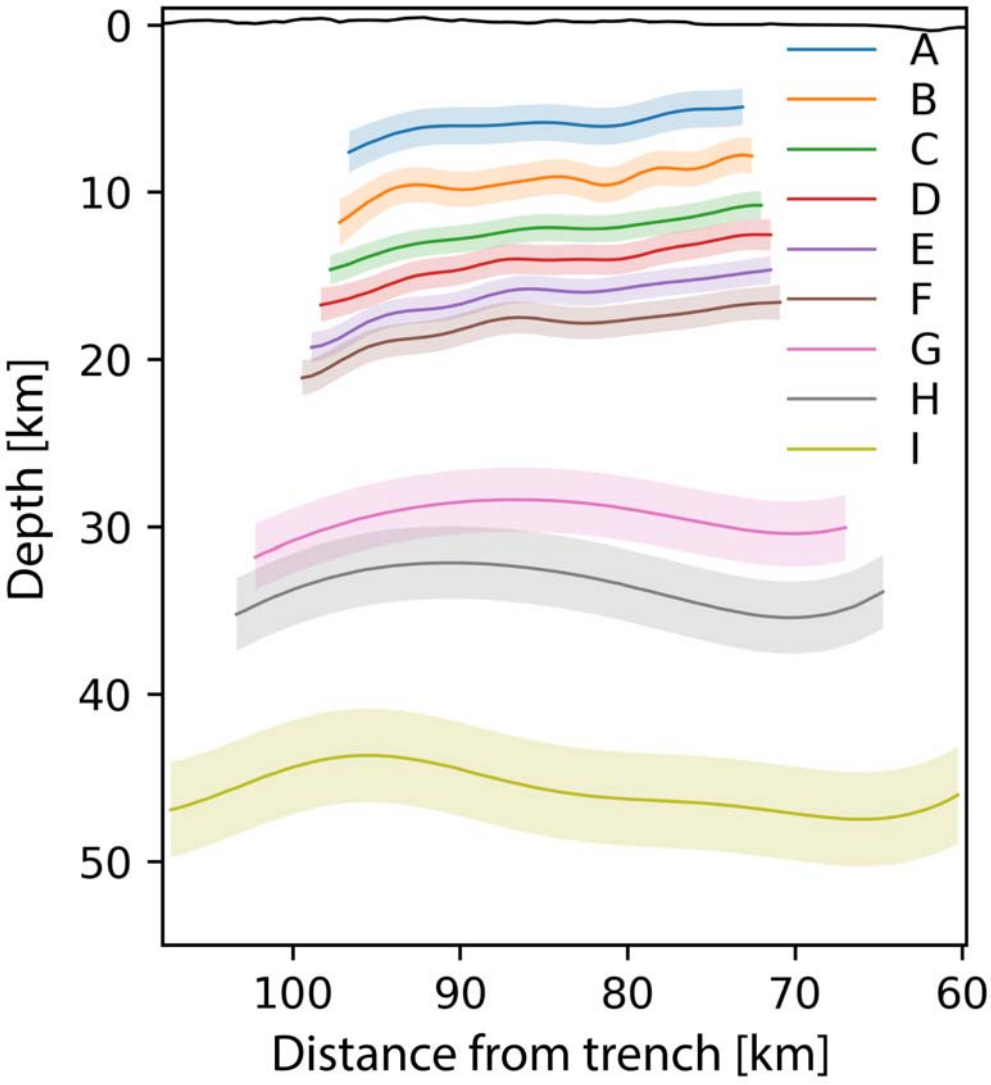

Figure 4.13: Cross-section through surfaces and errors estimated with Gaussian process regression. Cross-section is constructed on a bearing of 121° and plotted against distance from the trench at 38.884°S/178.942°E measured along line, section line shown in Fig. 4.2b. Each surface shows a distinct geometry about a generally north-west dipping trend.

4.11 Discussion

4.11.1 Comparing surfaces from pick mapping and CCP stacking

Both mapping of depth-converted Ps arrivals and CCP stacking show several velocity discontinuities occurring at depths of < 50 km below the NZ3D array (Figs. 4.10-4.13). Most of the surfaces mapped from Ps picks do not agree with amplitudes at those depths resulting from CCP stacking (Fig. 4.14). This is likely because the surface fitting was carried out solely on positive-amplitude picks from time series and did not take multiples into account. This could be attempted again using negative-amplitude peaks and incorporating multiples. Surfaces delineated by the CCP stacking are regarded as more reliable here as they are defined by several coherent arrivals in the receiver functions. The coherence of these arrivals is, however, a result of the velocity model used (Section 4.7). There was not sufficient time during this project to test the effect of varying the velocity model, but this could be a useful way of validating velocities beneath the array.

4.11.2 Signal and noise levels, and the limitations of the data

Despite clear later arrivals from the Moho PpSs+PsPs peak (blue peak labelled E in Fig. 4.11), peaks from intra-crustal arrivals in the first 10 s are only slightly pronounced relative to the background noise amplitudes between peaks (Figs. 4.8 & 4.11). This is consistent with low SNRs due to high noise at the NZ3D sites (Sections 4.3 & 4.4), and suggests the data are too noisy to glean velocity information that departs significantly from existing regional starting models. Interpretations of the data are therefore limited to clear results offered by the CCP imaging and local seismicity.

4.11.3 Geometry and seismic properties of major conversion horizons

Amplitudes in the CCP volume and local earthquake hypocentres delineate several clear volumes to $\sim$ 100 km depth (Fig. 4.15a). Local seismicity presented alongside the CCP imaging is either from Yarce *et al.* (2019) or the GeoNet catalogue (https://www.geonet.org.nz/). Earthquake hypocentres from GeoNet occurred since 1950 and had local magnitudes > 2. Hypocentres with default depths of 5 or 12 km were assumed inaccurate and excluded. Hypocentres plotted on sections occurred within 10 km of the section line. A simple seismic stratigraphy describing these volumes is now presented, and summarised in Table 4.2.

The shallowest unit (Unit I) shows patchy, variable amplitudes to $\sim$12 km depth (Fig. 4.15a). The upper 4 km show little information, as expected from < 4 Hz receiver functions. A high-amplitude positive conversion volume between 4 and 8 km depth within the upper plate dips to the NW in un-smoothed data (Fig. B.14). The dip and location of this conversion volume approximately align with the down-dip extension of the Gable End Fault south (GEFs). Between 8 and 12 km, patchy negative-amplitude conversions are common, suggesting velocity reductions immediately above Unit II. Seismicity is lacking in this layer, only a few earthquake hypocentres are present at 7-12 km depth.

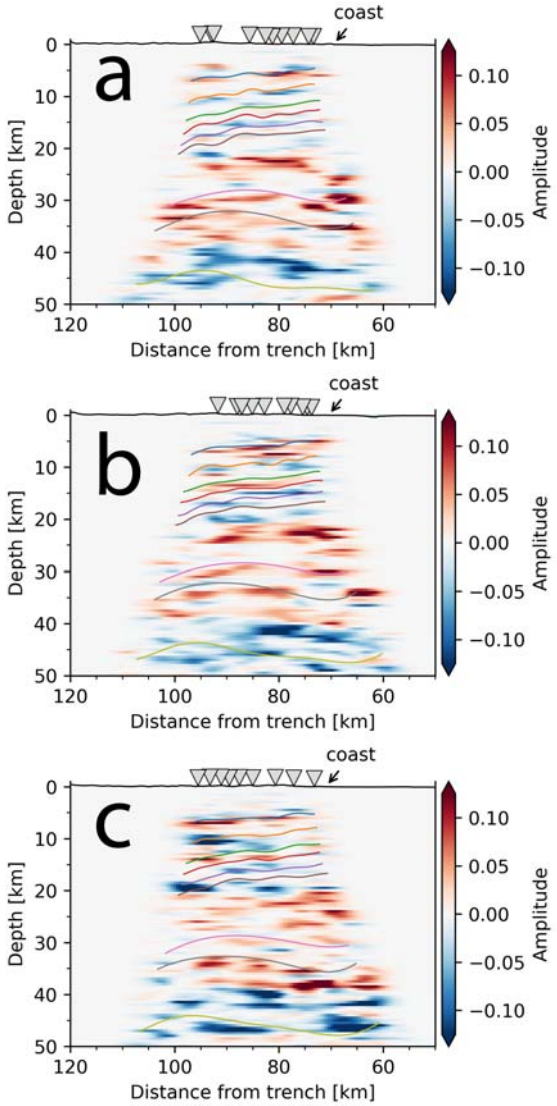

Figure 4.14: Cross-sections through the north (a), centre (b), and south (c) of the CCP volume and NZ3D array. Sections show phase-weighted stack amplitudes and surface depths determined using Gaussian regression (Section 4.10). Cross-section (b) is constructed of 0.5 × 2 × 0.5 km cells on a bearing of 121° and plotted against distance from the trench at 38.884°S/178.942°E, section line shown in Fig. 4.2b. a) and (c) are 4 km to the NE and SW of (b), respectively.

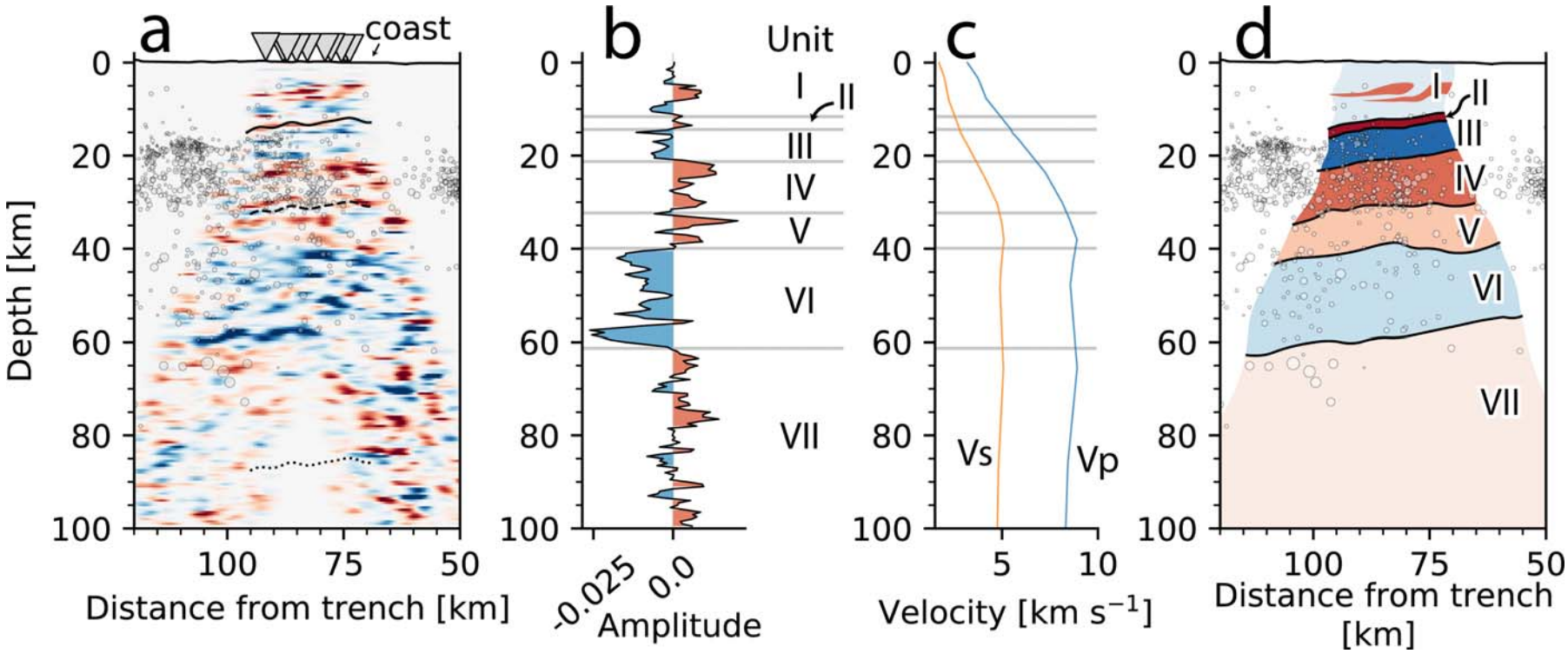

Figure 4.15: Seismic structure based on the CCP volume and earthquake distribution. The CCP volume (a) shows several volumes with distinctly positive or negative amplitudes. This is verified in (b), the average horizontal amplitude with depth and associated seismic unit. The velocity model of Eberhart-Phillips *et al.* (2017) below station BS05 (c) shows that velocities increase with depth over depth ranges where positive amplitudes occur and velocities mostly decrease with depth over depth ranges where negative amplitudes occur. Amplitudes and earthquake hypocentre depth have been used to delineate 7 volumes (d) which represent a structure below the NZ3D array. Earthquake hypocentres are from Geonet (see Section 4.11.3 for details). Dashed black line in (a) indicates a crustal thickness of 18 km, as suggested by Davy *et al.* (2008) for this part of the Hikurangi Plateau. Black dotted line in (a) indicates a total oceanic lithospheric thickness of 73 km, as suggested by Stern *et al.* (2015). Section line shown in Fig. 4.2b.

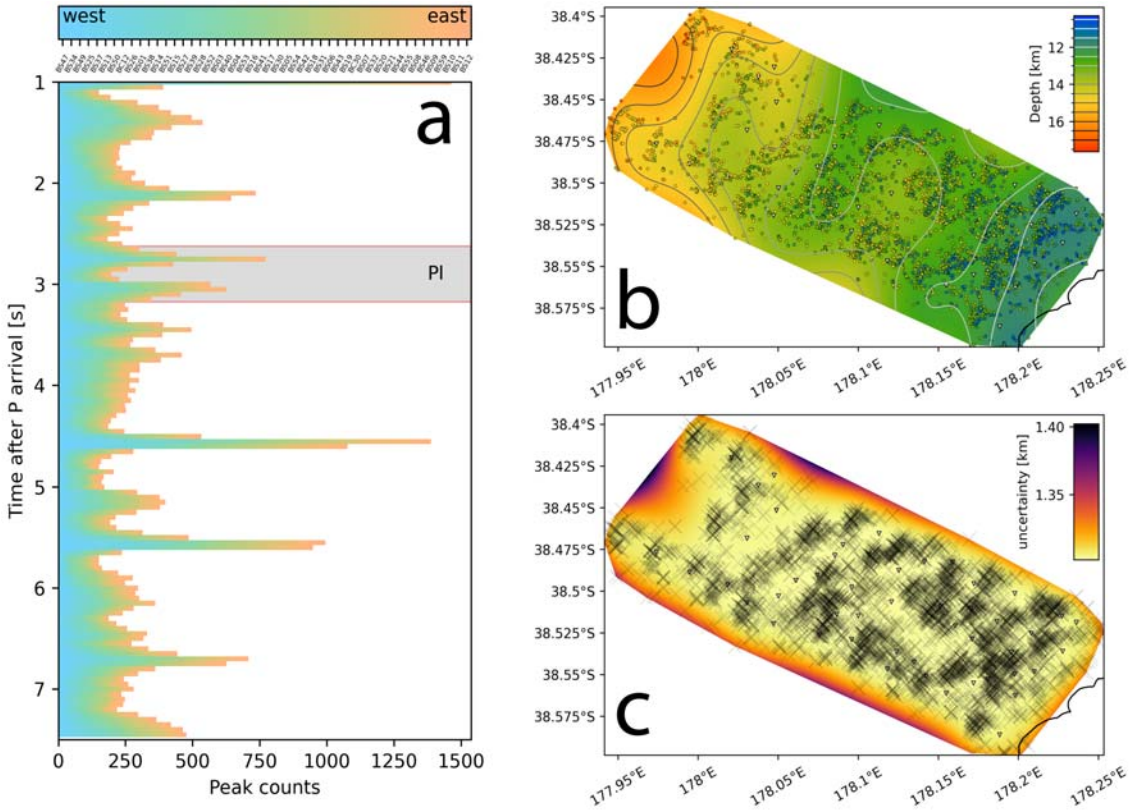

Figure 4.16: Time picks (a) used to map the depth (b) and error (c) of the geometry of Unit II. Assuming Unit II represents the plate interface, (a) shows selected time range used for plate interface mapping in grey fill labelled PI. From fitted depth-converted time picks, (b) shows stations (inverted grey-filled triangles), coastline (black line in the SE), individual time picks coloured by depth, surface depth from Gaussian regression on plotted time picks as colour, and contours every 0.5 km (see colourbar). Also from the mapping, (c) shows error of the surface and piercing points of time picks used to fit the surface (black crosses). Note that error rapidly increases away from piercing points, surfaces have been truncated at bounding polygon of points because of this.

Unit II is a single consistent positive-amplitude conversion at ∼12 km depth bounded by patchy negative-amplitudes (Fig. 4.15a). The conversion is also bounded on its upper and lower sides by mapped surfaces C and D, which are 1-2.5 km apart, but if both time windows are taken together and fitted, the resulting surface shows a good fit to the positive amplitude horizon (Figs. 4.15-4.17). The fitted surface

shows local depth variations about a general NW-dipping trend (Fig. 4.17). Though the depth progressively changes from 11 km in the SE to 16 km in the NW, both CCP images and the mapped surface show local horizontal areas, NNE-SSW oriented ridges, and a general increase in dip and roughness towards the NW (Figs. 4.10-4.17). Much of the interface topography is within error estimated during the Gaussian regression ($2\sigma \simeq 1.3$ km, Fig. 4.16) so the finer-scale (< 5 km wavelength) features imaged may be artefacts. Nevertheless, the agreement of broad features (> 5 km wavelength) between the CCP volume and the fitted surface suggests they are likely reliable. Though there is a general NW-dipping trend, large areas of the mapped surface show a generally westward dip (Fig. 4.17). Westward-dipping areas generally form more steeply-dipping parts of the surface (Fig. 4.17). This gives the surface a locally-stepped geometry, though this variation is within error for the regression (Fig. 4.17). Longer wavelength depth variations are also present in the fitted surface; the surface shows a broad bulge ∼90 km from the trench in the NW of the area (Figs. 4.16 & 4.17). The bulge appears to approximately bound a cluster of local earthquake hypocentres (Fig. 4.15). In the NW, Unit II dips more steeply on the down-dip side of the bulge (Fig. 4.17).

Unit III comprises a 5-7 km thick volume between ∼15 and ∼21 km depth showing discontinuous negative-amplitude conversions and a scattering of earthquake hypocentres in the north-west (Fig. 4.15a & b). The top of Unit III is defined by a continuous negative-amplitude conversion but the base is less clearly defined. Unit IV is ∼10 km thick, comprising a volume of high amplitude positive conversions in laterally-continuous horizons between 21 and 31 km depth (Fig. 4.15a). The volume hosts nearly all of the local earthquake hypocentres and, though positive amplitude conversions extend to greater depths, a clear lower bound on seismicity within Unit IV is defined as its base (Fig. 4.15a). This lower bound sits approximately 18 km beneath Unit II. Unit V also has continuous positive-amplitude conversions but earthquake hypocentres are sparse throughout its depth range of 31-40 km (Fig. 4.15a & b). Unit VI extends for 20 km between 40 and 60 km depth and comprises patchy negative-amplitude conversions (Fig. 4.15a & b). Earthquake hypocentres are moderately common in this volume, more so than in the overlying Unit V, and

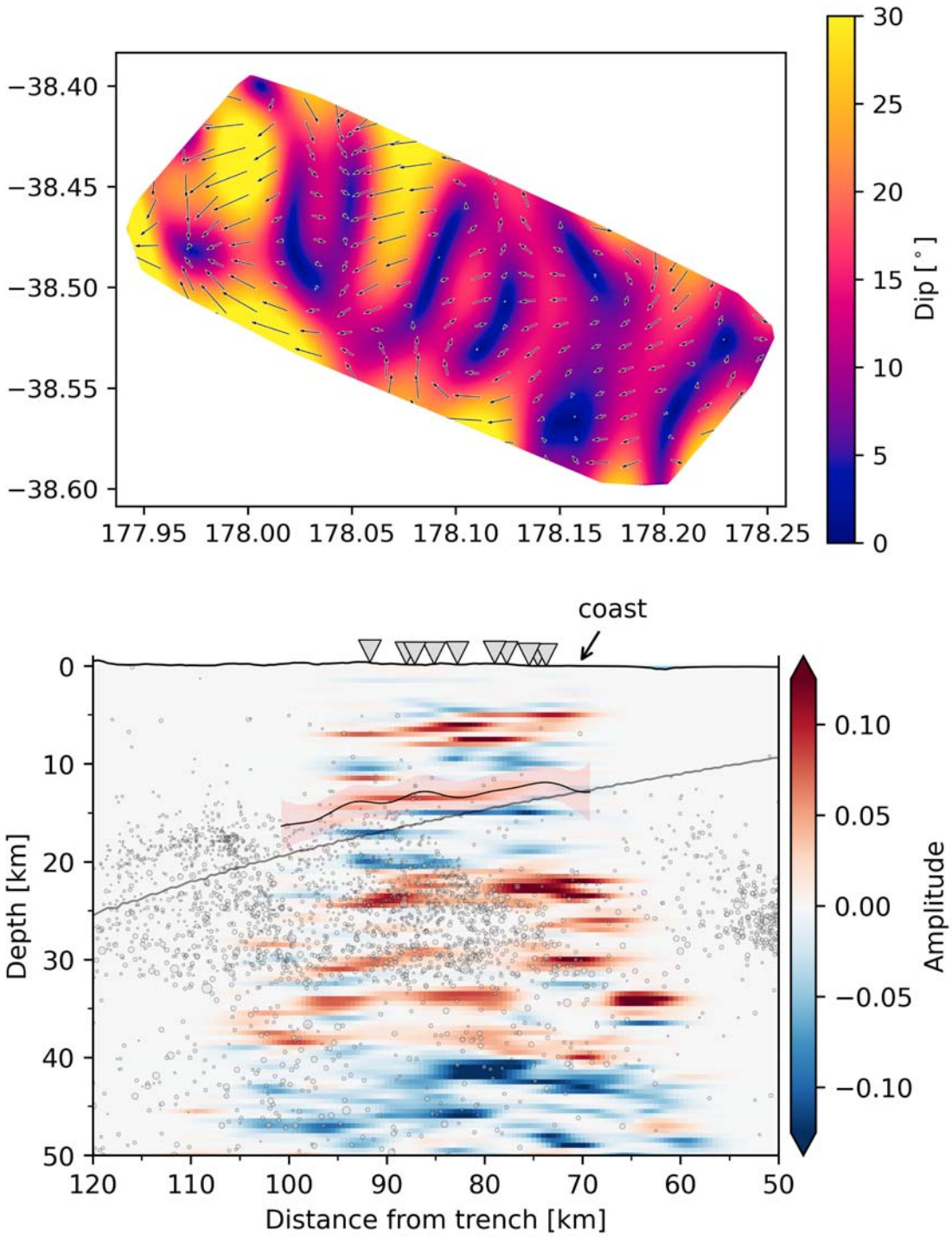

Figure 4.17: Dip and dip direction (top) of the mapped Unit II, which shows a good agreement with the phase-weighted stack through the centre of the 0.5 by 2 by 0.5 km CCP volume (bottom). Arrows on top plot show dip direction. On the lower panel, the black line shows mapped plate interface, the red transparent fill shows the error associated with the regression, and the grey line is the plate interface of Williams *et al.* (2013). Section line shown in Fig. 4.2b.

increase in density towards the NW. Unit VII covers depths > 60 km and comprises patchy and low amplitude positive and negative amplitudes; there are few earthquakes below the top 10 km of this interval (Fig. 4.15a & b).

4.11.4 Geological interpretation of the upper plate

CCP imaging of Unit I highlights two NW-dipping positive-amplitude volumes with a low-amplitude volume between them (Fig. 4.15). The low-amplitude volume bounds the lower side of a volume of moderately low resistivity (7-15 Ω m) from the magnetotelluric (MT) inversion of Heise *et al.* (2017). The moderately low-resistivity volume extends to the surface from the low-amplitude volume at > 5 km depth (Fig. 4.18). Away from the low-amplitude volume, resistivity values in the area are lower, suggesting shallow fluid-saturated sediments dominate the shallow upper plate (Heise *et al.*, 2017, 2012). Several workers have postulated low-velocity sediments overlie the plate interface at the northern Hikurangi margin (Mazengarb and Speden, 2000; Wallace *et al.*, 2017). Poorly-consolidated, fluid-saturated sediments would be both low velocity and low resistivity, consistent with MT and seismic data (Eberhart-Phillips and Bannister, 2015; Eberhart-Phillips *et al.*, 2010; Heise *et al.*, 2017). High V_p/V_s ratios in the upper plate have recently been imaged by Yarce (2020), also suggesting fluids are present in the shallow sediments. MT data show these sediments may extend to ∼10 km depth, where positive-amplitude conversions in the CCP volume may show their lower bound (Fig. 4.18). At 8-12 km depth, patchy negative-amplitude conversions suggest velocity reductions at the base of Unit I (Fig 4.15a).

Unit	Depth Range [km]	Amplitude characteristics	Earthquake distribution	hypocentre	Interpretation
I	0-12 km	Mostly negative with a positive horizon, patchy	Uncommon		Upper plate sediments
II	12-15 km	Continuous positive amplitudes	Rare within unit, which bounds common seismicity in Unit III		Plate interface
III	15-21 km	Discontinuous negative amplitudes	Moderately common throughout, more common towards the NW		Volcaniclastics ± basalts
IV	21-31 km	Continuous positive amplitudes	Common throughout the unit		High-velocity oceanic crust (Hochmuth *et al.*, 2019)
V	31-40 km	Continuous positive amplitudes	Rare and distributed earthquakes		Upper (Locally-serpentinised?) olivine aggregate (Stern *et al.*, 2020)
VI	40-60 km	Patchy negative amplitudes	Moderately common distributed earthquakes		Dehydrating locally-serpentinised olivine aggregate (Herath *et al.*, 2020)
VII	> 60 km	Patchy negative and positive amplitudes	Rare earthquakes in upper 10 km		Lower oceanic lithopshere

Table 4.2: Seismic layer characteristics from CCP imaging and seismicity distribution and interpretation.

The low-amplitude and moderately low resistivity volume align well with the surface trace of the southern Gable End Fault (GEFs; Heise *et al.*, 2017; Mountjoy and Barnes, 2011). The GEFs is estimated to dip 30-40°, the volume highlighted in MT data likely corresponds to the hanging wall of the thrust fault (Fig. 4.18; Litchfield *et al.*, 2014). The reverse sense of shear on the thrust fault exhumes more consolidated material from depth, and this material is likely to be lower resistivity due to lower porosity and resultant saturation (Heise *et al.*, 2017). The low-amplitude volume shows the GEFs may extend from > 10 km depth to the surface (Fig. 4.18). Further offshore, MT data are bounded on their SE side by a surface that dips at a similar angle to that estimated for the Ariel Bank Fault (ABF), though there are no receiver function data to corroborate this (Fig. 4.18; Heise *et al.*, 2017; Mountjoy and Barnes, 2011).

4.11.5 Geological interpretation of the plate interface

Unit II likely represents the plate interface of the northern Hikurangi margin. The conversion is 2-3 km shallower than the interface of Williams *et al.* (2013) and is bounded on its top and base by patchy negative amplitude conversions. The interface of Williams *et al.* (2013) is outside error for the regressed plate interface in the NW side of the study area (Fig. 4.17), no error was given in the previous study. At 12 km depth this unit coincides with the plate interface estimated by Bell *et al.* (2010), but differs significantly from the estimate of ∼18 km just offshore by Barker *et al.* (2009). Depth estimates, both here and in the studies of Barker *et al.* (2009) and Bell *et al.* (2010), are dependent on the velocity model. The agreement of the interface of Bell *et al.* (2010) with the interpretation shown here suggests the regional velocity-model of Eberhart-Phillips *et al.* (2010) captures velocities sufficiently to image this depth range. The plate interface estimated by Barker *et al.* (2009) dips steeply (> 12°) within the negative-amplitude zone beneath this interface and does not correspond to any clear conversion horizon in the CCP volume (Fig. 4.17). The plate interface estimated by Williams *et al.* (2013) has a roughly uniform dip over 10s of km, but the interface imaged here shows significant local variation about its general dip. The locally-stepped geometry described here bears similarity to that described by

Henrys *et al.* (2006) further south, where it was attributed to reactivation of normal faults in the lower plate. Steps imaged here trend NNE-SSW, but no orientation constraints on normal faults in the lower plate are available for this part of the margin for comparison. The source of the roughness is therefore unclear. It may be that the geometric roughness is caused by topography on the down-going Hikurangi Plateau, which is comprised of common seamounts topped with variable thicknesses of sediment (Barnes *et al.*, 2020; Davy *et al.*, 2008). Up-dip, the plate interface has been correlated to the top of a volcaniclastic unit using seismic and offshore drilling data from IODP Expedition 375 (Fig. 4.19; Barnes *et al.*, 2020; Wallace *et al.*, 2019), supporting this interpretation.

The margins of the plate interface, bounded by horizons C and D (Section 4.10), are 1-2.5 km apart (Figs. 4.15 & 4.19). Studies of exhumed subduction-related faults suggest it is unlikely the actively deforming plate interface is $\sim$ 2 km thick at depths of 12-15 km, though this may represent a volume containing several more localised deforming zones or lenses of material imbricated during deformation (Fagereng, 2011b; Kimura *et al.*, 2012; McKay *et al.*, 2021; Rowe *et al.*, 2013; Wakabayashi and Rowe, 2015). The plate interface in other receiver function studies has been imaged as a negative-amplitude horizon as velocities decrease into either a plate interface shear zone or a low-velocity layer beneath over-consolidated material in the upper plate (Audet and Kim, 2016; Bannister *et al.*, 2007; Kato *et al.*, 2010). Given the interpreted location of the plate interface atop the volcaniclastics in the incoming sequence (Fig. 4.19), the positive amplitude of the plate interface volume in this study could result from Ps conversions at the boundary between the plate interface and the underlying volcaniclastic unit. The volcaniclastics have highly variable P and S wave velocities (Barnes *et al.*, 2020; Wallace *et al.*, 2019), but they are likely higher velocity, on average, than a deformed zone hosting multiple fault strands and elevated fluid pressure (Barker *et al.*, 2018; Plaza-Faverola *et al.*, 2016). The resolution of the CCP volume is 0.5 km^3 and the wavelength of a 4 Hz wavelength at 5 km s^{-1} is 1.25 km. This means a $<$ 1 km thick plate interface, typical for plate boundary faults (McKay *et al.*, 2021), is below what is resolvable using these receiver functions. The volume highlighted as the plate interface is therefore a range

based on the distribution of positive amplitude conversions and the upper surface bounding earthquakes in the negative amplitude volume beneath (Fig. 4.15d).

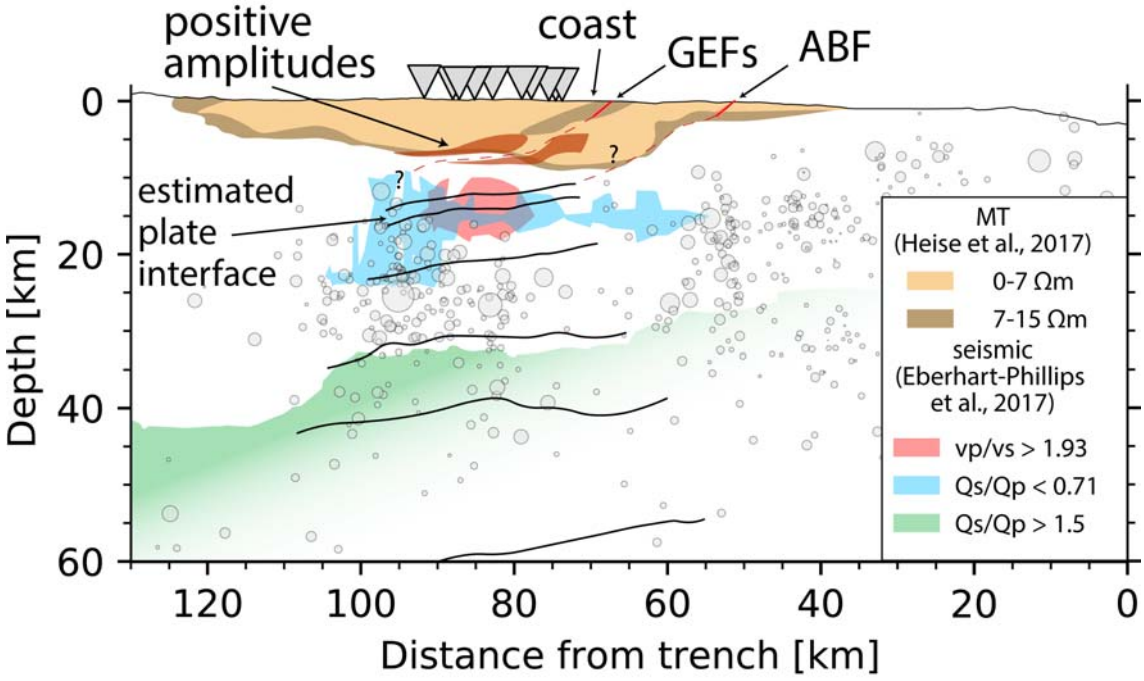

Figure 4.18: Comparing interpretation to MT and seismic velocity and attenuation data. Horizons beneath the NZ3D array stations (inverted grey triangles) are those shown in Fig 4.15. Low resistivity volumes from Heise *et al.* (2017) near the surface are interpreted be bounded and cut by splay faults. GEFs and ABF are the Gable End Fault south and the Ariel Bank Fault, respectively. These locations were intersected from the active fault database of Litchfield *et al.* (2014). Plotted seismicity is from the dataset of Yarce *et al.* (2019) and occurred within 20 km of the section line. Green Q_s/Q_p volume is faded where resolution is poor as the spread function is > 4, see Eberhart-Phillips *et al.* (2017) for details. Section line shown in Fig. 4.2a.

4.11.6 Geological interpretation of the lower plate

Based on patchy negative-amplitude conversions and the correlation of active seismic data up-dip with materials drilled seaward of the trench, Unit III likely corresponds to a volume of volcaniclastics and variably-altered basalts at the top of the Hiku-

rangi Plateau, directly beneath the plate interface (Unit II; Figs. 4.15 & 4.19). Negative-amplitude conversions indicate a velocity reduction with depth, but their patchy distribution suggests laterally-discontinuous conversion horizons. The regional model of Eberhart-Phillips *et al.* (2017) shows elevated V_p/V_s and low S/P wave attenuation ratios beneath the plate interface, which were interpreted as a fluid-rich, ponded sediment pile. The northern Hikurangi margin does not appear to have ∼7 km of continuous sediments anywhere on the incoming plate (Davy *et al.*, 2008; Wallace *et al.*, 2009), but recent correlation of boreholes drilled during IODP expedition 375 with active seismic transect 05CM-04 has shown 3-4 km thick units of volcaniclastic and volcanic basement material beneath < 1 km of sediments seaward of the trench (Fig. 4.19; Barnes *et al.*, 2020; Wallace *et al.*, 2019). These volcaniclastics are locally variable in texture, have highly variable porosities ($20 - 60$ %), and are interbedded with thin clay beds (Barnes *et al.*, 2020; Wallace *et al.*, 2019). Throughout the thickness of the volcaniclastics they exhibit high amplitude reflections in active seismic surveys and logging-while-drilling data show common velocity inversions with depth (Barnes *et al.*, 2020; Wallace *et al.*, 2019). Full waveform inversion of the 05CM-04 active seismic transect offshore also shows common velocity inversions occur with depth throughout the offshore volcanic units away from Site U1520, though it is possible these are an artefact of the inversion (Gray *et al.*, 2019). If subducted, a thick unit of heterogeneous volcaniclastics could host voluminous pore fluids and local seismic velocity inversions. Compression of the unit during subduction could produce elevated V_p/V_s ratios, low P/S wave attenuation ratios (Eberhart-Phillips *et al.*, 2017), and the patchy negative amplitude CCP amplitudes observed here. The thickness of this unit is greater than that observed offshore on the 05CM-04 transect (5-7 km vs 3-4 km), though this estimated thickness of the volcaniclastics and variably-altered basalts is approximate and highly dependent on velocity (Barnes *et al.*, 2020). The 7 km thick sequence may represent either a very thick volcanic sequence, including lava flows or other material below the volcaniclastics and variably-altered basalts, or several km of sediments atop a few km of volcaniclastics and variably-altered basalts (Figs. 4.15 & 4.19).

A high-amplitude reflectivity zone (HRZ) imaged up-dip in active seismic data

(Bell *et al.*, 2010) correlates well with Unit III (Fig. 4.19). High-amplitude reflections are consistent with fluid-rich material; the HRZ was initially interpreted to represent fluid-rich sediments under-thrust below the plate interface by Bell *et al.* (2010). Recently, it has been correlated with volcaniclastics and variably-altered basalts cored seaward of the trench at Site U1520 (Barnes *et al.*, 2020). The HRZ lies immediately down-dip of a subducting seamount, imaged weakly in active seismic data but coincident with a positive magnetic anomaly (Bell *et al.*, 2010). Recent estimates of P wave velocities from ocean-bottom seismometers suggest either the seamount is further down-dip than previously thought or is it highly fractured (Arai *et al.*, 2020). P-wave velocities from the regional model in the upper part of Unit III (5.5-7 km s^{-1}, Fig. 4.15c) are slightly above those estimated for the volcaniclastics and variably-altered basalts at the toe of the thrust (4-5.5 km s^{-1}, Arai *et al.*, 2020). Velocities in Unit III are more consistent with either the Hikurangi Plateau basement or volcaniclastics and variably-altered basalts down-dip of the seamount where strong compaction has been hypothesised in the HRZ (Arai *et al.*, 2020; Bell *et al.*, 2010).

Continuous positive amplitudes within Unit IV could correspond to the top of the basaltic oceanic crust, distinguished from the underlying mantle comprising Unit V by dense earthquakes throughout its 21-31 km depth range (Fig. 4.15a & d). Conversions at the top of Unit IV are distributed over 4 km depth range (Fig. 4.15a), consistent with a gradual change from altered basaltic material and lava flows in Unit III to more coherent basaltic sequence. Positive amplitude conversions within Unit IV may mark the top of gabbroic or doleritic volumes of the oceanic crust (Fig. 4.15a). The oceanic crust hosts consistently-increasing velocities, whereas velocities in Unit V, possibly the underlying mantle, are consistently high for both P and S waves (Fig. 4.15c; Eberhart-Phillips *et al.*, 2017). Average V_p and V_s values in the inferred crust and mantle are $V_p \simeq 7.4$ and $V_s \simeq 4.1$, and $V_p \simeq 8.5$ and $V_s \simeq 4.9$, respectively (Fig. 4.9). Crustal velocities are high compared to normal values and may represent a high-velocity zone normally found near the base of oceanic plateaus (Herath *et al.*, 2020; Hochmuth *et al.*, 2019). The boundary between units IV and V can therefore be considered the subducted oceanic Moho.

This subducted Moho corresponds well with a crustal thickness of 18 km estimated by Davy *et al.* (Fig. 4.15a; 2008). There is little direct evidence that the interpreted depth range of the basaltic crust between 21 and 31 km depth is correct except seismicity concentrated within its thickness (Fig. 4.18 Yarce *et al.*, 2019). Seismicity becomes more common away from the trench, where a low Q_s/Q_p volume was imaged by Eberhart-Phillips *et al.* (2017). The increased prevalence of seismicity is similar to that within the seamount up-dip (Fig. 4.19), suggesting the low Q_s/Q_p volume may represent intense fracturing as the seamount is subducted (Wang and Bilek, 2014).

Continuous positive-amplitude conversions between 31 and 40 km depth and a lack of earthquake hypocentres throughout Unit V coincide with high seismic velocities (Fig. 4.15), suggesting it may be the oceanic mantle immediately beneath the subducted Moho. The upper mantle corresponds well to a high Q_s/Q_p volume (Fig. 4.18; Eberhart-Phillips *et al.*, 2017). Q_s/Q_p ratios in this volume are > 1.5, consistent with relatively dry, dense material. Further south on the Hikurangi margin, similar V_p and vertically-slow S wave anisotropy were documented by Stern *et al.* (2020). V_p and V_p/V_s ratios both here and further south are consistent with these velocities representing a mantle layer comprising an olivine aggregate with a horizontally-isotropic, vertically-slow, AG fabric (Christensen, 1966; Kobussen *et al.*, 2006; Michibayashi *et al.*, 2016). A horizontally-isotropic AG fabric is consistent with forsterite-rich olivine subject to vertical uniaxial compression, interpreted by Stern *et al.* (2020) to suggest the fabric records the collapse of a spreading superplume responsible for the formation of the Ontong-Java-Manihiki-Hikurangi Plateau. These high-velocity layers have been recorded beneath large areas of the Hikurangi Plateau but appear to vary dramatically in thickness and depth (Herath *et al.*, 2020), making their origins unclear.

Between 40 and 60 km depth, patchy negative amplitude conversions in Unit VI indicate local reductions in velocity with depth, consistent with the velocity model of Eberhart-Phillips *et al.* (2010, & Fig. 4.15c). The volume shows several continuous horizons but velocities from the regional model are high throughout ($V_p \simeq 8.4$ km s^{-1} and $V_s \simeq 4.75$ km s^{-1}; Fig. 4.15c), suggesting the magnitude of the velocity

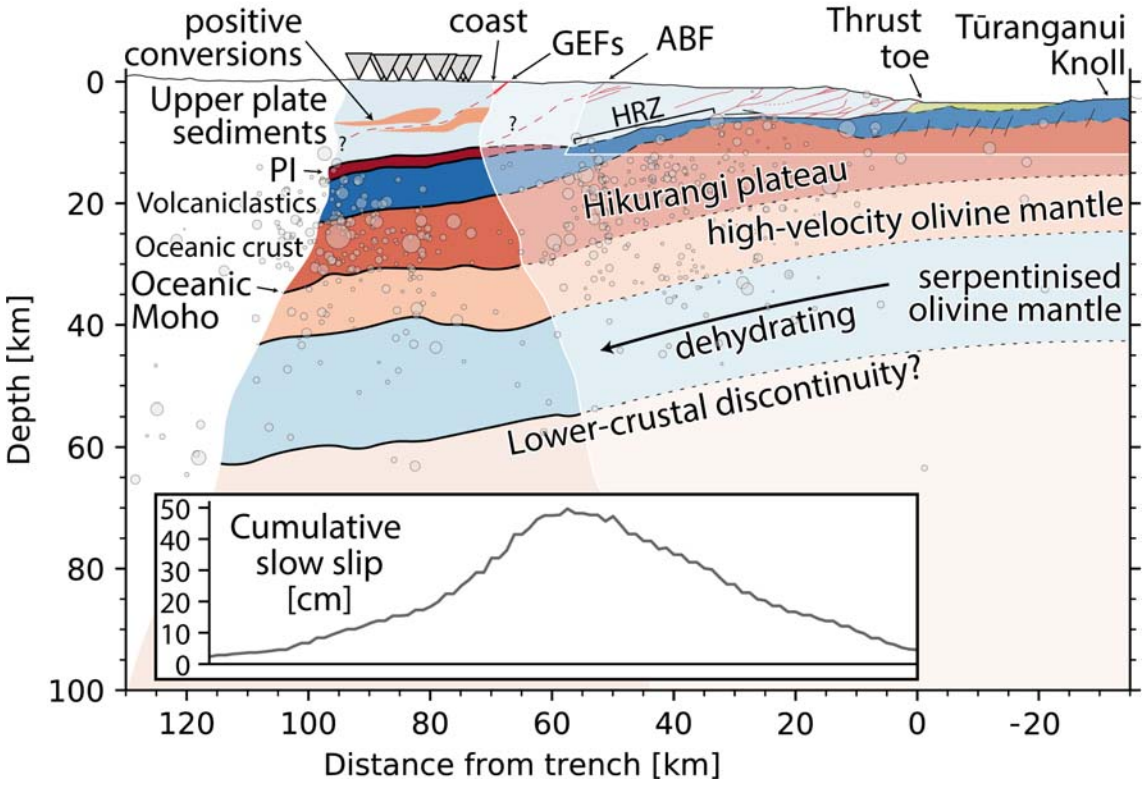

Figure 4.19: A to-scale section through the fore-arc of the Hikurangi margin. Volumes beneath the NZ3D array stations (inverted grey triangles) are those shown in Fig 4.15. Seismic section crossing trench is redrawn from Barnes *et al.* (2020) and horizons projected between the two based on earthquake hypocentres from Yarce *et al.* (2019). Seamount drawn beneath the wedge corresponds to the low velocity seamount described by Arai *et al.* (2020). GEFs is the Gable End Fault south, intersected from the active fault database of Litchfield *et al.* (2014). HRZ indicates the area of high-amplitude reflectivity described by Bell *et al.* (2010). Volumes are projected between sections with ray coverage (outlined in white). Section line shown in Fig. 4.2a.

inversions are likely relatively small or the low-velocity volumes are very localised. The high velocities throughout Unit VI indicates it is likely composed of an olivine aggregate similar to that in the upper mantle (Unit V) above (Fig. 4.15c). The discontinuous negative amplitudes from receiver functions within this layer could result from V_s reductions associated with localised patches of fluid from serpentine dehydration on deep-reaching outer-rise faults (Fig. 4.15a; Herath *et al.*, 2020).

Indeed, temperatures between 40 and 60 km depth are thought to be 450-650 °C (Antriasian *et al.*, 2018), consistent with antigorite dehydration as the lower plate is subducted (Fagereng and Ellis, 2009). The antigorite-bearing zones would be localised around through-going faults, so the background velocity may still be high due to the presence of an olivine aggregate (Stern *et al.*, 2020), in agreement with velocities from Eberhart-Phillips *et al.* (2017).

Below 60 km depth, velocities in Unit VII from the regional velocity model are high (Fig. 4.15c) though this is outside the area of good ray coverage (Eberhart-Phillips *et al.*, 2017). High velocities are consistent with olivine aggregates inferred in the overlying layers (Stern *et al.*, 2020; Tonegawa *et al.*, 2019). In contrast to Unit VI, this aggregate would be un-hydrated as serpentine is unstable at temperatures $>$ 600 °C modelled at these depths (Antriasian *et al.*, 2018; Fagereng and Ellis, 2009). The oceanic lithosphere on the southern Hikurangi margin is thought to be around 73 km thick (Stern *et al.*, 2015), this would occur close to 90 km depth in the study area due to the subduction of the oceanic plateau (Fig. 4.15a). Several discontinuous positive and negative amplitude conversions are visible around 90 km depth, but it is unclear if any of these represent a transition to the mantle or a lithosphere-asthenosphere boundary (Fig. 4.15a).

4.11.7 Insights into deformation mechanics

The CCP amplitude characteristics and earthquake hypocentre distribution throughout the forearc indicate varied mechanics are active throughout the depth range imaged below the NZ3D array. Marine terraces near the NZ3D array show several slip events on the GEFs have caused uplift in the last 1800 years (Litchfield *et al.*, 2016), though no earthquake hypocentres have been observed near the estimated fault surface (Figs. 4.18). Further offshore, the ABF is actively accommodating compression and is deforming at vertical slip rates of 3-5 mm yr^{-1} (Mountjoy and Barnes, 2011). The presence of large active splay faults branching off the plate interface has been associated with regions of high intraplate shear stress, inter-seismic coupling (Mountjoy and Barnes, 2011), and complex plate interface geometry (Plaza-Faverola *et al.*, 2016). The splay fault geometries estimated here would intersect the plate interface

down-dip of most slow slip recorded in the study area (Fig. 4.19), suggesting there may be a link between splay fault occurrence and plate coupling (Mountjoy and Barnes, 2011). Better constraints on splay fault geometries near the plate interface would clarify their role here.

Earthquakes in the northern Hikurangi margin are more common in the basaltic lower plate (Wallace *et al.*, 2009; Yarce *et al.*, 2019) and a bulge in the inferred plate interface bounds the upper side of a cluster below the NZ3D array (Fig. 4.15d). To the NW of the bulge the plate interface becomes rougher and dips more steeply, at a similar angle to that of Williams *et al.* (2013). Around 15 km depth, there is a cluster of small earthquakes around the plate interface, possibly due to its increased roughness causing stress build up and seismic slip as surface asperities move past one another (Fig. 4.17; Wang and Bilek, 2014). The times of events in this cluster do not show a simple spatial progression, suggesting the pattern of seismicity associated with deforming asperities is complex.

Within low-magnitude earthquake clusters related to seamount fracturing and deformation (Wang and Bilek, 2014; Yarce *et al.*, 2019), bursts of earthquakes have been associated with fluid migration from below the plate interface during slow slip events (Shaddox and Schwartz, 2019). Though previously regarded as sediments (Bell *et al.*, 2010; Shaddox and Schwartz, 2019), data presented here and compared to IODP drill core and regional seismic reflection studies (Barnes *et al.*, 2020), indicate a thick unit of volcaniclastics underlie the plate interface. The extent to which the volcaniclastics and variably-altered basalts cored at Site U1520 would be dewatered by higher pressures during subduction is unclear; volcaniclastic units seaward of the margin are clay-rich and irregularly interbedded with low-permeability clay units and these may channelise fluids during dewatering (Barnes *et al.*, 2020). The plate interface overlying these volcaniclastics is likely to limit vertical flow and channelise fluids up-dip (Ellis *et al.*, 2015), meaning a large quantity of fluid is likely to be migrating seaward within Unit III. Though some fluid may be lost through upper plate faulting, the majority is likely to be concentrated immediately down-dip of the subducting seamount (Fig. 4.19). This fluid in this volume (HRZ-2 in Bell *et al.*, 2010) may be at pressures greater than hydrostatic beneath the plate interface,

escaping by fracturing during slow slip events and causing seismicity in the upper plate (Shaddox and Schwartz, 2019).

The down-dip end of maximum cumulative slow slip coincides with a seismicity gap described by Yarce *et al.* (2019). There is no clear change in geometry or amplitude of the receiver functions in the seismicity gap (Fig. 4.15a), suggesting a localised or mechanistic rather than compositional reason for its prevalence. Yarce *et al.* (2019) suggest inter-seismic locking between plates, which is high at the location of the gap (Dimitrova *et al.*, 2016; Wallace *et al.*, 2009), could cause a plate-wide gap in seismicity. The interpreted intersection of the ABF with the plate interface is around the location of the seismicity gap (Fig. 4.19). This suggests the higher locking in this area may manifest as low-rate aseismic slip on the ABF rather than seismic slip, supporting the hypothesis of Mountjoy and Barnes (2011) that plate interface properties may influence the distribution of compressional structures in the upper plate. Slow slip on the shallow interface immediately seaward of the ABF branch may result from a stress build up in the locked patch down-dip, propagating up the plate interface and slipping there between the fluid-rich volcaniclastics with variably-altered basalts and the overlying plate sediments (Fig. 4.19). Seismicity in the upper plate coincident with slow slip events, interpreted to result from fluid migration, shows the plate interface deforms and opens up pathways during the event to release fluids from the under-thrust volcaniclastics and variably-altered basalts (Shaddox and Schwartz, 2019). The correlation of units with similar seismic properties, interpreted to be volcaniclastics (Plaza-Faverola *et al.*, 2016), and slow slip further south on the margin also suggests the heterogeneous composition and fluid content of volcaniclastics and variably-altered basalts may be a dominant control on shallow slow slip at the Hikurangi margin.

In the Pacific Plate, pressures at 40-60 km depth are likely very high (> 1 GPa), meaning that earthquakes observed within Unit VI would require fluids to cause dehydration-embrittlement or dehydration driven stress transfer (Ferrand *et al.*, 2017). The dehydration reaction responsible for the earthquakes is unclear, but it has been suggested further south on the Hikurangi margin that outer-rise faults may provide fluid pathways to depths of 25-30 km below the upper side of the crust

into the upper mantle and the seismicity may result from dehydration of the serpentinised mantle there (Herath *et al.*, 2020). This could account for the double Wadati-Benioff zone associated with the subducting slab further south in the Hikurangi and at other margins (Audet and Kim, 2016; Bannister *et al.*, 2007; McCrory *et al.*, 2012).

4.12 Conclusions

- The northern Hikurangi margin hosts complex slip patterns and heterogeneous lithologies and was investigated using receiver functions from stations in the NZ3D array.

- A three-dimensional CCP volume shows a continuous positive conversion horizon between 12 and 15 km depth, interpreted to be the plate interface. The plate interface has much local variation about a dip towards the NW. The average estimated dip of the plate interface is lower than previous estimates within the study area.

- The plate interface is interpreted to bound the upper surface of a unit of heterogeneous volcaniclastic material drilled seaward of the trench during IODP Exp. 375 at Site U1520. This unit is imaged to be $\sim$ 7 km thick and interpreted to be variably altered and cemented, becoming less altered towards a gradual lower contact with more coherent basalt. Up-dip, fluids in these volcaniclastics may represent high-amplitude reflectivity zones described in previous studies (Bell *et al.*, 2010), possibly being released during slow slip events up-dip of the study area (Shaddox and Schwartz, 2019).

- In the upper plate, un-smoothed data highlighted a moderately-dipping horizon which aligns well with the offshore trace of the Gable End Fault. This is corroborated by a dipping volume in magnetotelluric data from a previous study, which highlights the hanging wall of the fault. Tracing the fault through the volume shows it extends to at least 8 km depth and may sole onto the plate interface.

- Below the volcaniclastics, positive conversions mark the top of a high velocity basaltic crust which overlies extremely high velocities in the mantle (> 8.5 km s^{-1}). The high velocity mantle hosts patchy negative-amplitude conversions, which could indicate locally-serpentinised volumes where outer-rise faulting has allowed ingress of water. As it subducts, depths corresponding to temperatures of 500-600 °C show negative amplitudes and increased earthquake density consistent with dehydration of the serpentine causing embrittlement and seismic slip.

Part II

The Gwna Complex - an ancient subduction system

Chapter 5

The Gwna Complex

The Gwna Complex (commonly referred to as the Gwna Mélange or Gwna Group) is an Ediacaran to Cambrian-age collection of mixed-grade metasediments and meta-igneous lithologies found throughout much of Anglesey (Fig. 5.1; Greenly, 1919). The Gwna Complex comprises the stratigraphically-highest Group of three within the Monian Supergroup, the others being the New Harbour (intermediate) and South Stack (lowest) Groups (Gibbons and Ball, 1991). Of the three Groups, the Gwna is the most widespread across Anglesey and comprises several chaotic assemblages of heterogeneous lithologies; the term 'mélange', French for mixture, was coined to describe this Group (Greenly, 1919). The lithologies are commonly deformed and imbricated (Chapter 6 & Maruyama *et al.*, 2010) with no clear preserved stratigraphy. Units comprising the Gwna are therefore referred to as the Gwna Complex for the remainder of this thesis. Since its initial description by Greenly (1919), the Gwna Complex has been reinterpreted as the product of ancient subduction (Kawai *et al.*, 2007; Maruyama *et al.*, 2010; Schofield *et al.*, 2021). This section outlines the geological history and tectonic setting of the Gwna Complex and reviews previous work on the origin and deformation of rocks exposed at Llanddwyn Island, in the SW of Anglesey, where Chapters 6 and 7 are focused (Fig. 5.1).

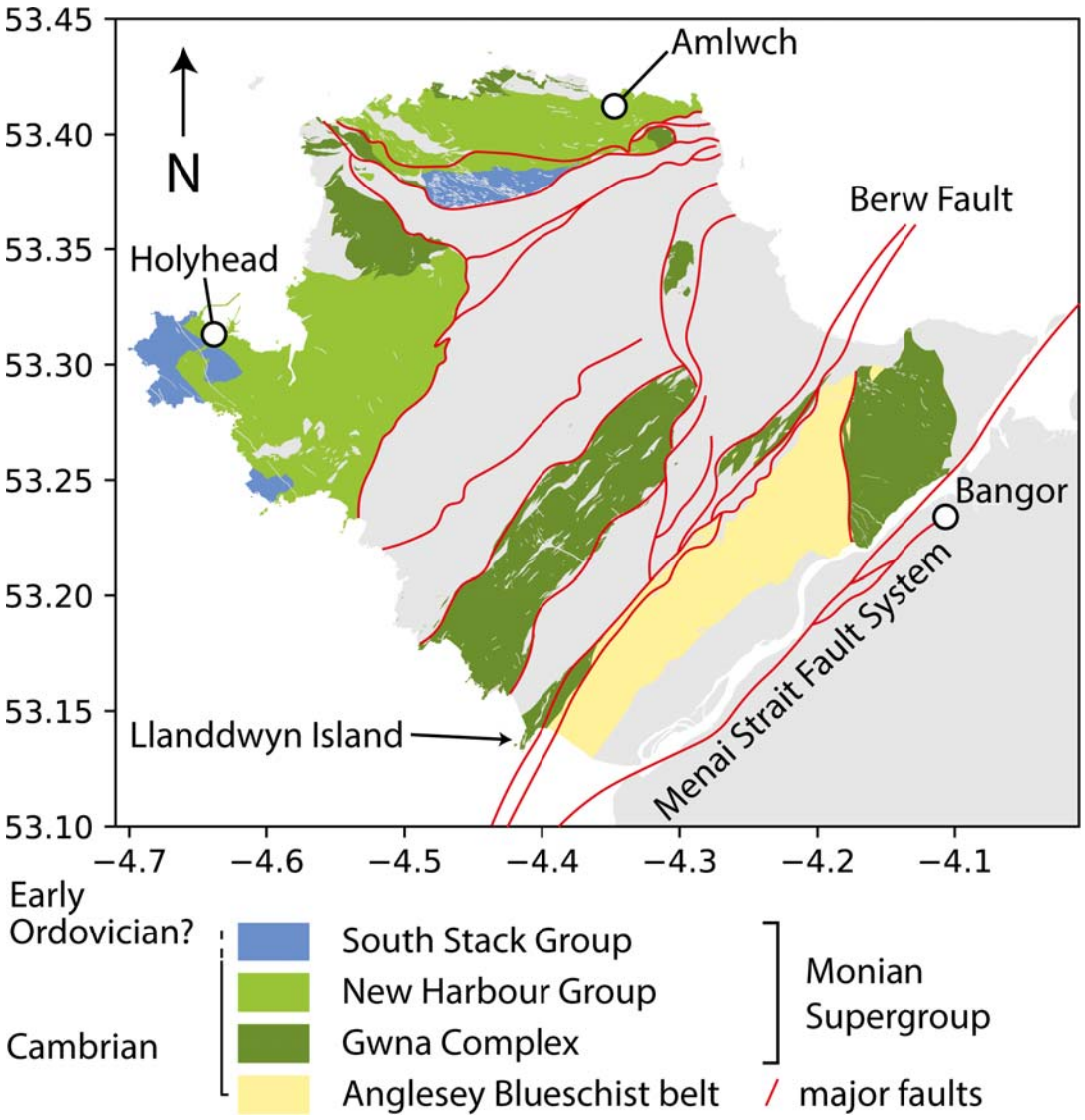

Figure 5.1: Simplified geological map of Anglesey, adapted from Maruyama *et al.* (2010), Schofield *et al.* (2021), Wood (2012), and Greenly (1919). Note that many units and faults have been omitted for simplicity.

5.1 Geological history and tectonic setting

The Gwna Complex is thought to represent the earliest preserved material accreted to the upper plate during south-eastward subduction beneath Avalonia between 488 and 448 Ma (Figure 5.2; Kawai *et al.*, 2007). Sediment in the Monian Supergroup was deposited between ∼500 and 475 Ma (Collins and Buchan, 2004). The preserved sequence is overall downward-younging, inferred to be caused by teconic underplating (Kawai *et al.*, 2007). Rocks on Anglesey accreted after the Monian

Supergroup are (in order of decreasing age) the New Harbour Group and South Stack Group, whereas olistostrome-type units are present on the Llŷn Peninsula to the SW (Kawai *et al.*, 2007). All of these units were subject to low-grade (zeolite or prehnite-pumpellyite facies) metamorphic conditions except a blueschist unit in the central southern part of Anglesey (Figure 5.1; Kawai *et al.*, 2007). The blueschist unit represents exhumed high-pressure metamorphic rocks derived from MORB-chemistry pillow lavas (Thorpe, 1972). These distinct units are thought to have been emplaced along NE-SW trending strike-slip faults (Fig. 5.1) with sinistral senses of shear (Gibbons and Horák, 1990), possibly consistent with significant lateral translation during subduction (Schofield *et al.*, 2021).

Recently, a reinterpretation of lithologies across Anglesey has resulted in the Gwna Complex at Llanddwyn Island being reclassified as the Llanddwyn Island Volcanic Member, part of a mega-conglomerate called the Bodorgan Formation (Schofield *et al.*, 2021). The Bodorgan Formation is thought to record NW-vergent folding and thrusting associated with Early Devonian subduction; the Llanddwyn Island Volcanic Member is said to lie in strands of the strike-slip Berw Fault Zone which extends across Anglesey (Fig. 5.1 Schofield *et al.*, 2021). The Gwna Complex comprises a varied sequence of rocks resulting from a complicated deformation sequence with many events, and Anglesey as a whole is even more complex (Asanuma *et al.*, 2017; Maruyama *et al.*, 2010; Saito *et al.*, 2014). This thesis focuses on processes of subduction deformation so the research presented in Chapters 6 and 7 is based on work conducted on Llanddwyn Island (Fig. 5.1), where subduction-related structures are clearly preserved (Kawai *et al.*, 2008; Maruyama *et al.*, 2010). On Llanddwyn Island, I have avoided outcrops where later strike-slip faulting has clearly overprinted the earlier, subduction-related structures with thrust-sense kinematics. Parts of the geological history of Anglesey not related to subduction or structures observed at Llanddwyn Island are therefore not discussed in detail here.

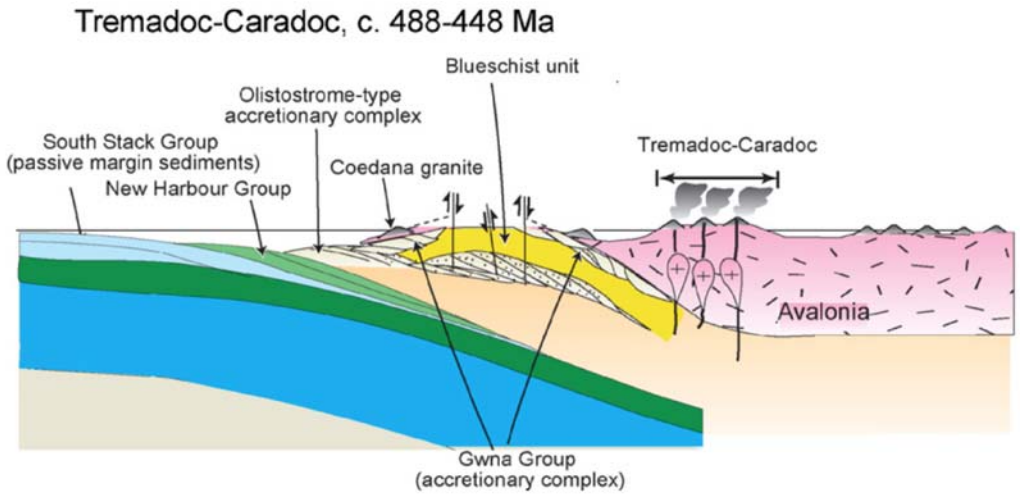

Figure 5.2: Schematic cross section of the tectonic environment of the Monian Supergroup, with progressively younger units occurring stratigraphically lower due to accretion after under-thrusting. From Kawai *et al.* (2007).

5.2 Origins and deformation of the Gwna Complex at Llanddwyn Island

The Gwna Group at Llanddwyn Island is lithologically consistent with ocean plate stratigraphy (OPS), including lavas and volcaniclastics, jaspers, limestones, mudstones, and more coarse foliated siliciclastic sedimentary rocks (Greenly, 1919; Maruyama *et al.*, 2010). Pillow lavas at Llanddwyn Island have both MORB and OIB chemistries (Saito *et al.*, 2014; Thorpe, 1993) and are thought to be the basal unit of repeated OPS imbricated in a duplex configuration between floor and roof thrusts (Maruyama *et al.*, 2010). Pillow-tops are convex to the SE, consistent with SE-ward subduction and accretion beneath a wedge in that direction. Cherts on Llanddwyn Island are folded and faulted parallel to, and locally across, bedding, with shear senses consistent with SE-ward subduction (Maruyama *et al.*, 2010). Massive carbonates are found throughout the island, commonly associated with altered basalts (Maruyama *et al.*, 2010). Constraints on the depositional and deformational ages of these lithologies are poor; Neoproterozoic carbonates from the north of Anglesey likely formed 880-750 Ma (Horák and Evans, 2011) and Cambrian siliciclastic sediments on Llanddwyn Island were deposited after 550 ± 24 Ma (Asanuma *et al.*, 2017). Subduction

of the Gwna Group likely began before 600 Ma, accreting the Gwna Complex at Llanddwyn Island after the deposition of the coarsest siliciclastic lithologies around 550 Ma (Asanuma *et al.*, 2017) and continuing until the Ordovician (448 – 488 Ma; Kawai *et al.*, 2007).

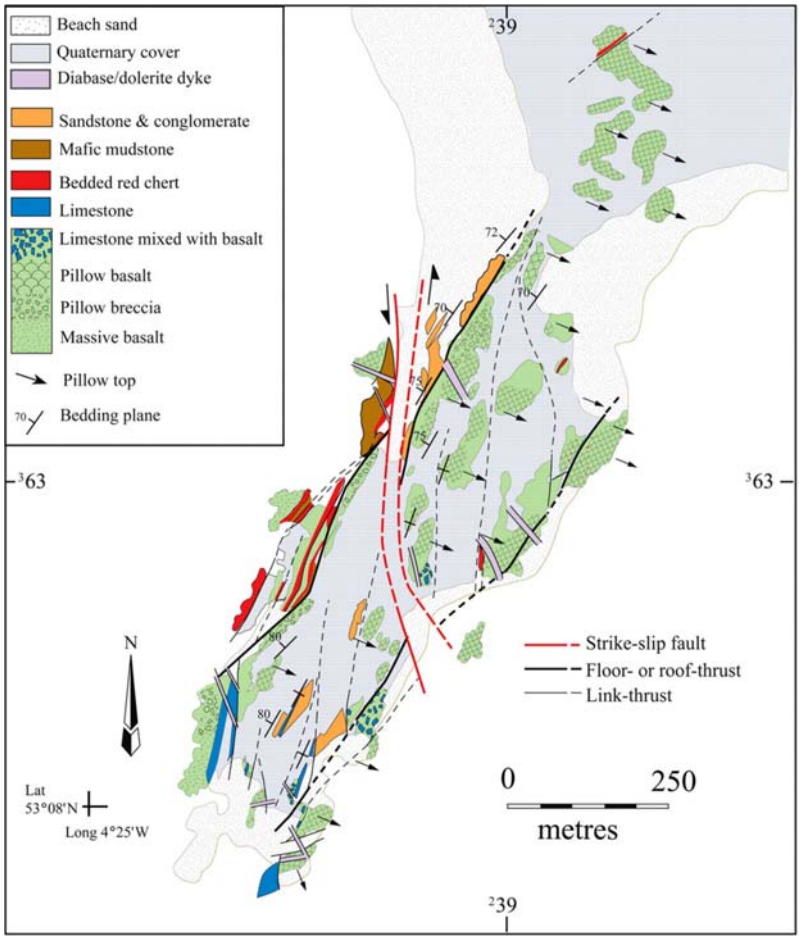

Figure 5.3: Map of structures and lithologies in the Gwna Mélange on Llanddwyn Island, Anglesey. From Maruyama *et al.* (2010).

Exhumation of the Gwna Group is associated with an antiformal stack of variable-grade up to blueschist facies (Kawai *et al.*, 2007; Schofield *et al.*, 2021). Though difficult to discern due to several later high-angle strike-slip faults, the Gwna Complex at Llanddwyn Island has been interpreted to sit structurally above this blueschist unit (Kawai *et al.*, 2007). High angle normal faults found throughout Anglesey are thought to have accommodated much of the exhumation-related deformation throughout the Gwna Complex, but generally cross-cut the Precambrian to Ordovician sequence and juxtapose subunits of the Monian Supergroup on a much larger

scale than is considered in Chapters 6 or 7. Finally, north-south trending dolerite dykes found throughout Anglesey are associated with the opening of the Atlantic Ocean and intruded around 55 ± 1.7 Ma (Allott and Lomax, 1988; Hailwood *et al.*, 1992; Kirton and Donato, 1985). Similar to strike-slip structures on the island these later dykes were avoided in the field, where possible. The next two chapters provide more details of subduction-related structures on Llanddwyn Island, but do not discuss any earlier or later structures on Anglesey described in this chapter.

Chapter 6

Heterogeneous subgreenschist deformation in an exhumed sediment-poor mélange

6.1 Introduction

Many descriptions of subduction complexes (or mélanges) exhumed from seismogenic depths describe thick, turbidite-dominated sequences with deforming zones containing clasts of more competent boudinaged sandstone or basalt (e.g. the Crystalls Beach, Kodiak, Sestola-Vidiciatico, and Shimanto complexes; Fagereng, 2011b; Fisher and Byrne, 1987; Kimura and Mukai, 1991; Meneghini *et al.*, 2009; Remitti *et al.*, 2011; Rowe *et al.*, 2011; Ujiie, 2002; Vannucchi *et al.*, 2008). In contrast, many active subduction zones have a relatively small thickness of sedimentary inputs (< 2 km; Heuret *et al.*, 2012), and the degree to which pelagic sediments and basalt are incorporated into the deforming zone near the plate interface is poorly understood. Input sequences containing volcaniclastic and calcareous sediments have been sampled by drilling and characterised seaward of the Costa Rica and Hikurangi subduction zones (Harris *et al.*, 2013; McKiernan and Saffer, 2006; Wallace *et al.*, 2019), where it has been suggested they may become entrained within the décollement (Chapter 4 & Barnes *et al.*, 2020) and deform in distinct lithologically-controlled styles at depth (Ikari *et al.*, 2013). Heterogeneity within the incoming sequence

and the plate interface is also thought to contribute to complex slip behaviours, such as slow slip and tremor, often in concert with high pore fluid pressures (Agard *et al.*, 2018; Barnes *et al.*, 2020; Beall *et al.*, 2019; Boulton *et al.*, 2019; Fagereng, 2011b; French and Condit, 2019). A further contributor to this heterogeneity may be seamounts (and other geometrical irregularities), which are present seaward of many subduction zones and have also been associated with complex slip styles (Bell *et al.*, 2010; Bonnet *et al.*, 2019; Shaddox and Schwartz, 2019; Sun *et al.*, 2020; Todd *et al.*, 2018; Wang and Bilek, 2011).

Seamounts are exposed at margins with less siliciclastic turbidites in thinner incoming sediment sequences, where deformation of more heterogeneous basalts and pelagic sediments is relatively more important. Insights on how these more heterogeneous rocks influence deformation style and slip partitioning on the plate interface of modern subduction zone seismogenic zones may be gleaned from characterising the texture, heterogeneity, and geometry of ancient plate interface shear zones from the rock record. Here I present data from the Gwna Complex at Llanddwyn Island, Anglesey (see Chapter 5), a subgreenschist subduction complex containing narrow imbricated deforming zones with < 100 m thick sedimentary rock packages. I characterise the role of heterogeneous volcanic and dominantly pelagic sedimentary material in plate interface deformation and show that altered volcaniclastic materials can be of similar strength to under-thrust siliciclastic sediments when subject to plate interface deformation and veining at temperatures $< 300°$C.

6.2 Methods

Lithological mapping, sampling, and orientation data collection was carried out across Llanddwyn Island and the adjacent Newborough Forest. Orientation data dominantly comprise bedding within lenticular slices and foliation measurements within thin (< 20 m) zones of more intense macroscopically-ductile deformation as few to no discrete slip surfaces were recognised. Pillow basalt way-up indicators were also measured, along with the length and orientation of the longest axes of a subset of pillows. Samples were cut perpendicular to foliation or bedding to produce polished

thin sections, most often on a subvertical plane oriented NW-SE encompassing the long axes of basalt pillows measured in the study area. Optical microscopy of thin sections was used to identify sample texture and areas for further study.

Thin sections were coated with 5-8 nm of carbon to prevent charging before backscatter electron (BSE) imaging and energy dispersive spectroscopy (EDS) mapping were carried out at the School of Earth and Ocean Sciences in Cardiff University with a Zeiss Sigma HD Field Emission Gun Analytical scanning electron microscope (SEM) fitted with two Oxford Instruments 150 mm^2 energy dispersive X-ray spectrometers and a Nordlys EBSD system with Oxford Instruments Aztec software. EDS mapping was carried out at 15 or 20 keV accelerating voltage, a beam current of 4.3nA, an aperture of 120 μm, a working distance of 8.9 mm, and stepsizes of 1.2 or 5 μm. Recrystallised calcite veins were mapped with electron backscatter diffraction (EBSD) on thin sections polished with colloidal silica and tilted at 70° to the electron beam at a stepsize of 2 μm, a working distance of 13 μm, an accelerating voltage of 20 keV, a beam current of 8.5 nA, and a 120 μm aperture. Raw EBSD backscatter patterns were processes using Oxford Instruments Aztec software with a gain of 5 and 2x2 binning. EBSD data were then processed using the MTEX toolbox for Matlab (Bachmann *et al.*, 2010) and the grain orientation spread thresholding method of Cross *et al.* (2017) to determine recrystallised grain size.

Hybrid shear failure criteria were calculated following Cox (2011) and Sibson (1998) using typical cohesion values of 10 or 20 MPa for accretionary prism-forming mudstones (Schumann *et al.*, 2014). The cohesion of mudstones in accretionary prisms varies up to $\sim$ 30 MPa with depth (Schumann *et al.*, 2014), so these values are taken as representative estimates. Chlorite geothermometry used SEM EDS map data from 214 analyses of chlorite-dominated areas quantified using Oxford Instruments Aztec Software. The chlorite geothermometers of Cathelineau and Nieva (1985) and Zang and Fyfe (1995) were used as they were calibrated over the same Fe/Mg ratios as those found within the analysed chlorite.

6.3 Structu e of the Gwna Complex at Llanddwyn Island

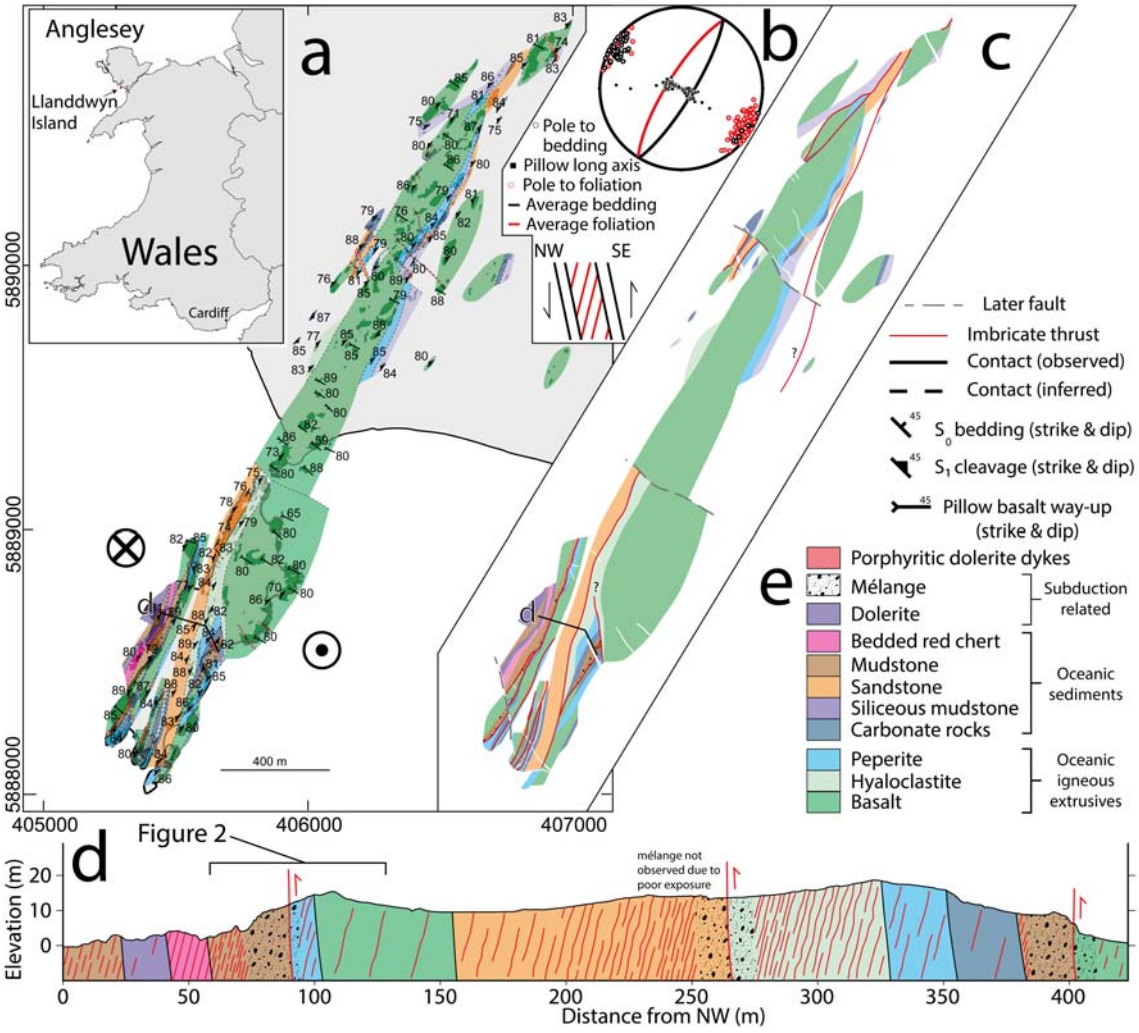

Figure 6.1: Map and section of Gwna Complex lithologies and structure at Llanddwyn Island, Anglesey, Wales, UK. Parts show (a) lithology distribution throughout the complex, inset shows location of Llanddwyn Island in north Wales, (b) bedding and foliation measurements from throughout the area covered in (a), (c) stratigraphic units and locations of imbricate thrusts, (d) cross-section across Llanddwyn island showing thrust positions and large-scale lithological texture (highlighted area shows position of Fig. 6.2), (e) approximate ocean plate stratigraphy reconstructed from the area, variably-sampled in lenses between imbricate thrusts.

Exposures across Llanddwyn Island are dominantly coastal, with irregular 5 to 200 m thick lenticular slices of dismembered ocean plate stratigraphy (OPS) cropping out parallel to the NE-SW trend of the island (Fig. 6.1a). Bedding, foliation, and mélange units dominantly strike NE-SW and dip sub-vertically, consistent with a dip-slip shear sense (Fig. 6.1b). Pillow basalts throughout the island have subvertical layering and pillows convex toward the SE, suggesting younging in this direction consistent with previous work (Maruyama *et al.*, 2010). Deformation is localised on $<$ 20 m thick imbricated mélange-bearing thrusts, which anastomose throughout the study area at the margins of lenticular slices of OPS (Fig. 6.1). Pillow basalts adjacent to mélange-bearing thrusts are commonly deformed, appearing elongated with a subvertical long axis subparallel to bedding and foliation, corroborating a dip-slip shear sense (Fig. 6.1b).

6.3.1 Ocean plate stratigraphy within lenses

Lenticular slices of OPS record a variably-sampled upward succession from pillow basalts, hyaloclastites, and peperites to dismembered layers of carbonate, chert, mudstone, and fine-grained sandstone (Fig. 6.1). Where outcrop of mélange units between lenticular slices is limited, they have been traced along-strike between adjacent lithologies in the neighbouring lenticular slices (Fig. 6.1c). The origin, history, and emplacement of this OPS is discussed in more detail by Maruyama *et al.* (2010) and in Chapter 5, whereas this chapter focuses on the composition, properties, and rheology of the deformed zones between lenticular slices of relatively intact OPS.

6.3.2 Lithologies forming imbricated mélange shear zones

Within the Gwna Complex at Llanddwyn Island, mélange shear zones occur as non-planar tabular zones of locally-variable thickness (5-20 m) and increased apparent shear strain. Throughout the study area, mélange shear zones form an anastomosing array of imbricated deformed zones that strike approximately NE-SW and separate internally-coherent, lenticular slices of OPS. The composition of each mélange shear zone is variable, but most commonly comprises mud- or sandstone in the footwall,

and altered basaltic material (hyaloclastite or peperite) in the hanging wall (Fig. 6.2). This repetition of OPS astride subparallel mélange shear zones of consistent shear sense defines an irregular imbricated structure (Fig. 6.1d), similar to what has been observed in other subduction-related mélanges (Fisher and Byrne, 1992; Kimura *et al.*, 2012; Onishi *et al.*, 2001; Regalla *et al.*, 2018; Shibata *et al.*, 2008; Wakabayashi, 2015).

Imbricated mélange shear zones most commonly occur on the contact between foliated illite-rich sediments in the footwall and foliated and fractured chloritic volcanics in the hanging wall, incorporating material from both lithologies to form fault zones up to 10 m wide with block-in-matrix textures (Fig. 6.2). Boudinaged elongate blocks within the matrix are generally massive and derived from more phyllosilicate-poor areas of the adjacent lithologies (e.g. sandstone clasts from the footwall and basaltic clasts from the hanging wall; Figs. 6.2b-d & 6.3). Mixing of the two mélanges, evidenced by the presence of basalt clasts in the illitic mélange, is limited to a thin volume ($<$ 50 cm wide) encompassing the contact between the two units (Fig. 6.3a). Similar limited mixing has recently been recognised in the core of the Highland Boundary fault (McKay *et al.*, 2020), another ancient plate boundary fault with juxtaposed discrete fault core units. Matrix material in the mélange units forms a foliation wrapping around boudinaged blocks and is dominated by phyllosilicates; namely illite and chlorite, derived from the footwall sediments or hanging wall volcanics, respectively. Adjacent to mélange units, the thickness (including the damage zone) of footwall sediments ($10 - 100$ m) is commonly greater than that of hanging wall volcanics ($<$ 50 m; Fig. 6.1a,c & d); the change from block-in-matrix texture to sedimentary sequence is also more gradational ($2 - 10$ m) than that to relatively undeformed volcanics ($<$ 5 m; Fig. 6.2).

Figure 6.2: Field-scale relation of mélange units to imbricated stratigraphy. Panels show (a) panorama of imbricate thrust exposure between two lenses of intact stratigraphy, (b) close-up of illitic mélange containing clasts of carbonate and basalt, (c) schematic sketch with indicative textures across lithologies found in (a), and (d) field photo of chloritic melange containing clasts of basalt. Approximate location of (a) shown in Fig. 6.1d.

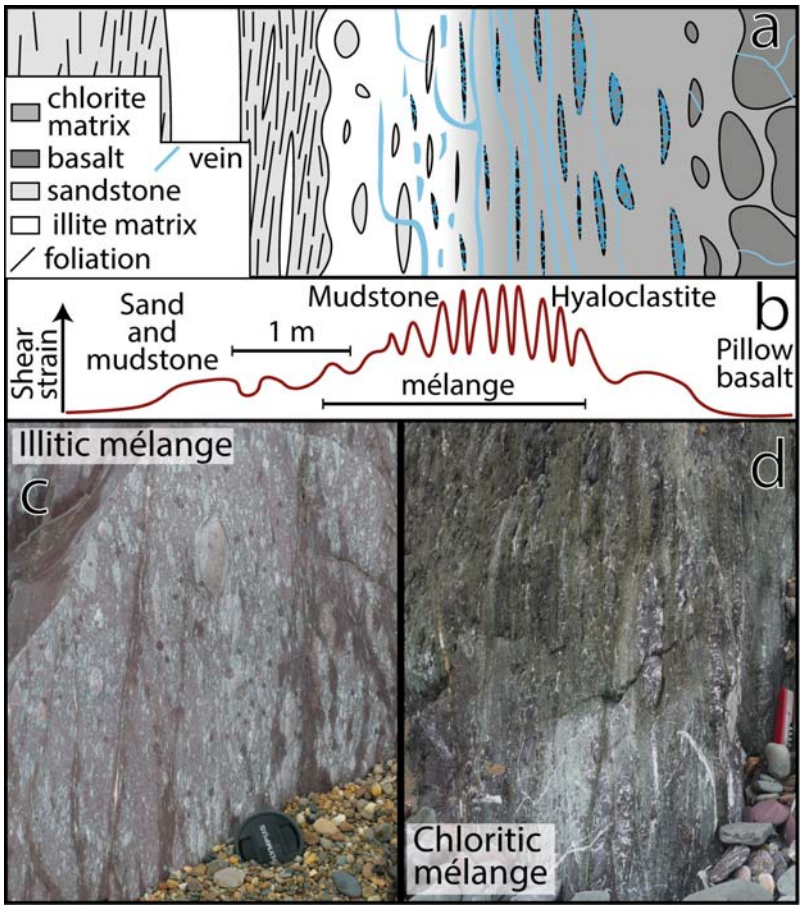

Figure 6.3: Schematic sketch of an idealised imbricated mélange shear zone. Across the shear zone, parts show (a) schematic sketch of lithology and texture, (b) approximate interpreted shear strain distribution (*sensu.* Fagereng and Sibson, 2010), (c) field photo of illitic mélange texture (lens cap is approx. 6 cm across), (d) field photo of chloritic mélange texture (penknife is approx (9 cm long).

6.3.3 Post-subduction deformation

The most recent deformation of the Gwna Complex at Llanddwyn Island (see Chapter 5) is apparent from N-S trending high-angle strike-slip faults and dolerite dykes found throughout the study area (Fig. 6.1a & c). Strike-slip faults are poorly exposed but where visible host little distributed deformation, tending to be localised to < 20 cm thick fault zones. Both strike-slip faults and dolerite dykes are associated with braided, coarse-grained quartz veins that trend N-S, cross-cutting mélange

shear zones and bedding throughout the island. Dolerite dykes in Anglesey have been dated to 55 ± 1.7 Ma and been associated with the opening of the Atlantic ocean (Allott and Lomax, 1988; Hailwood *et al.*, 1992; Kirton and Donato, 1985). Because early, mélange-forming deformation is characterised by a distinct structural style of distributed dip-slip deformation on a NE-SW trending foliation, it is readily separated from highly localised N-S trending faulting, dyking, and veining across the aforementioned foliation characterising later brittle features. The later brittle deformation is therefore not considered any further here, instead the focus remains on the distributed deformation which bounds repeating OPS, consistent with subduction zone deformation.

6.4 Deformation texture and composition of imbricated mélange shear zones

To simplify descriptions and interpretation, the two volumetrically-dominant matrix types within mélange-bearing shear zones are referred to as chloritic mélange and illitic mélange for the remainder of this chapter (Fig. 6.3), after their major phyllosilicate components (chlorite as the pale green mineral in Fig. 6.4 and illite as the K-rich species in Fig. 6.5). Within mélange shear zones, microstructures are dominated by clast-in-matrix textures with variable clast content and composition (Figs. 6.3-6.5). Phyllosilicates (either chlorite or illite) between clasts are fine-grained (< 20 μm), forming a sub-planar foliation that wraps around less deformed clasts (Figs. 6.4 & 6.5).

Chloritic mélange typically comprises variably-altered sigmoidal basalt clasts within a strongly foliated chlorite matrix (Fig. 6.4a-c). Approaching the contact between chloritic and illitic mélange within a mélange shear zone, continuous calcite veins up to 1.5 mm wide are oriented $\sim 15°$ from the bulk subvertical foliation, in places bisecting basalt clasts (Fig. 6.4a-c). Calcite veins contain minor quartz and are nearly completely recrystallised to 10-15 μm where they form continuous through-going volumes (Fig. 6.4d-f). Calcite away from these veins is coarse-grained, with visible curved twins and subgrains of similar size to adjacent recrystallised

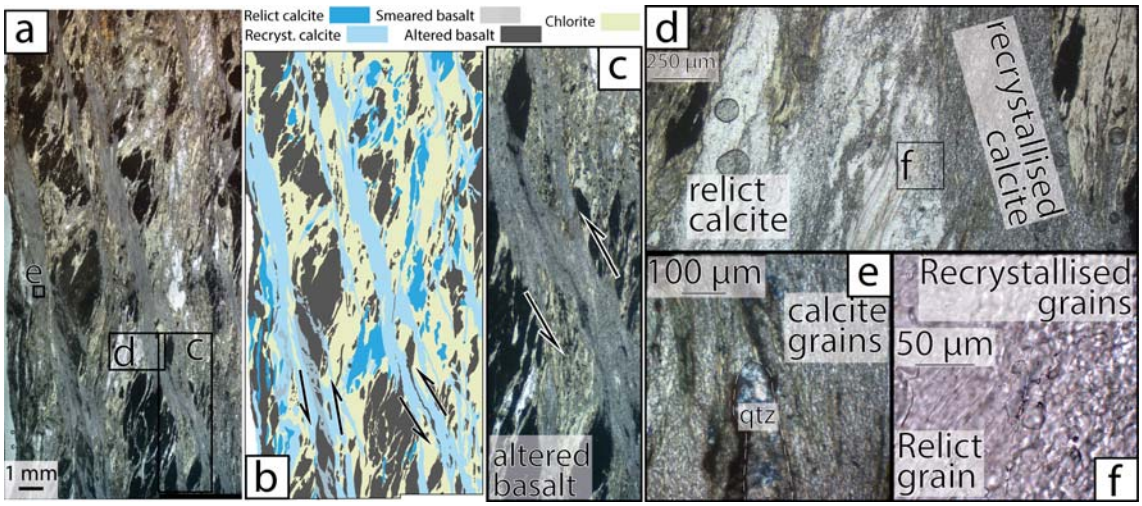

Figure 6.4: Deformation microstructures of chloritic mélange. Thin section photo mosaic (a) and associated sketch (b) show through-going calcite veins cross-cutting the dominantly foliated chlorite matrix which encompasses clasts of altered basalt. Recrystallised calcite veins have smeared out altered basalt during deformation to shear strains of ~ 4.5 in part (c). Away from through-going veins, calcite is not as fully recrystallised (d) as minor quartz-bearing veins (e) but contains subgrains of similar size to adjacent recrystallised grains (f).

grains (Fig. 6.4a, b, d & f).

Illitic mélange contains clasts of massive carbonate, variably-altered basalt, and fine-grained sandstone containing quartz, chlorite and albite, within a foliated illite-rich matrix (Fig. 6.5). The illite matrix contains very fine-grained hematite, giving illitic mélange a distinctive red appearance and making the matrix opaque in transmitted light (Fig. 6.5a & g). Clasts within illitic mélange typically form phacoids, commonly strung out into elongate, sub-rounded boudins along a horizon within the phyllosilicate foliation (Fig. 6.5a, d, e & f). Throughout the matrix of illitic mélange, multiple generations of variably folded, boudinaged, and fractured chlorite-quartz-calcite veins are present at varying angles to foliation (Fig. 6.5a-g). Opening vectors of veins generally plunge NW, 20-30° from bulk foliation orientation. This means foliation-parallel veins have a hybrid extensional-shear opening sense, consistent with the bulk SE-upward shear sense, and veins at higher angles to foliation have a more extensional opening sense in places bifurcating from foliation-parallel

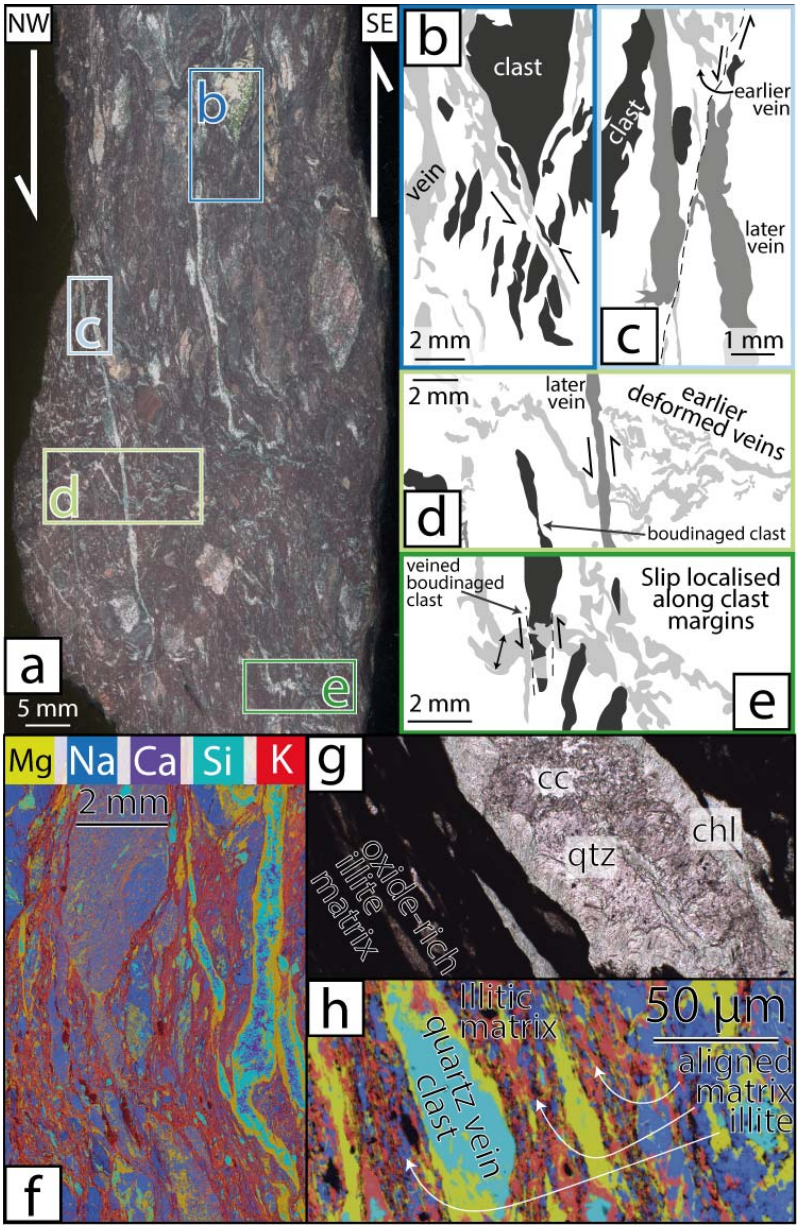

Figure 6.5: Deformation microstructures of illitic mélange. Hand specimen cut face (a) and associated sketches show (b) hybrid shear vein localisation adjacent to clasts, (c) foliation-parallel veins cut by localised shear bands, (d) foliation-parallel veins cutting deformed foliation-oblique veins adjacent to boudinaged clasts, (e) shear band localisation adjacent to a boudinaged clast infilled with vein material. SEM-EDS maps and photomicrographs show (f) hybrid shear quartz-calcite-chlorite veins cross-cutting an illitic matrix, (g) hybrid shear veins bordered by greenish chlorite adjacent to the matrix, (h) clasts within the matrix derived from fragmented quartz-calcite-chlorite veins.

veins (Fig. 6.5a & e). Multiple generations of veins are present, with dismembered foliation-oblique veins cross-cut by more continuous foliation-parallel veins of similar composition (Fig. 6.5a, d, & e). More continuous veins are irregularly cut by localised slip surfaces, particularly adjacent to phacoids in the matrix, which localise slip at their margins on 'Y' shear surfaces oriented parallel to the margins of the mélange-bearing shear zone (Fig. 6.5a, c, & e; Logan *et al.*, 1992). Where some clasts have been boudinaged, veins fill in voids between boudin segments (Fig. 6.5e), and are locally cut by localised slip surfaces at the margin of the clast. Veins contain mixed calcite and quartz with Mg-rich chlorite along their contact with wall rock (Fig. 6.5f-h).

6.5 Deformation sequence and kinematics (formation of the imbricated plate interface)

Throughout Llanddwyn Island, repeated lenticular slices of OPS containing SE-younging pillow basalts are bounded by mélange shear zones with a SE-upward shear sense, both consistent with SE-directed subduction (Figs. 6.1-6.5). To imbricate multiple slices, OPS must therefore have been repeatedly delaminated and accreted during subduction by thrusting hyaloclastite and pillow basalt (from the lower part of the OPS) over siliciclastic sediments (from the upper part of the OPS) on each mélange shear zone (Figs. 6.1 & 6.6). Mudstone and hyaloclastite are therefore interpreted to be the protoliths to illitic and chloritic mélange, respectively. Imbricated lenticular slices of variably-sampled OPS at Llanddwyn Island are therefore interpreted to have been delaminated and accreted from the lower plate by sequential downstepping of the plate interface during subduction-related deformation (Fig. 6.6c & d). Mélange bearing shear zones between lenticular slices are therefore interpreted to represent the plate interface during that episode of downstepping.

Within each shear zone chloritic mélange typically comprises the shear zone boundary on the up-thrown side, bounding the structurally-lower NW side of each lens (Figs. 6.1 & 6.2), and its protolith hyaloclastite is therefore interpreted to be

the lithology along which slices of OPS were delaminated from the lower plate during subduction. As pillow basalts are sampled within OPS slices at Llanddwyn Island (Fig. 6.1), hyaloclastite must have underlain or intermingled with pillow basalts on the incoming plate prior to subduction. The foliated chlorite matrix within chloritic mélange is likely the reason for its ease of deformation relative to the basalt, though not insignificant shear strains are visible on some through-going calcite veins within the chloritic mélange (Fig. 6.4a-c). The origin of the matrix chlorite is unclear, though its foliated texture suggests it formed either before or during deformation of the mélange shear zone (Fig. 6.4a, c, & d). If not primary, the chlorite likely formed by interaction of basaltic glass with fluids, either on the sea floor or near the plate interface (Humphris and Thompson, 1978; Kameda *et al.*, 2017; Seyfried and Mottl, 1982).

The presence of basalt clasts within the illitic mélange and the absence of sandstone clasts within the chloritic mélange (Fig. 6.5 & 6.4) suggests a preferential mixing effect occurred within the illitic mélange during deformation. The relative timing of deformation on thrusts in the Gwna Complex is unclear so the temporal evolution of mixing is unknown. Mixing of exotic blocks (i.e. basalt in the illitic mélange) has been associated with large shear strains during shear of mélanges (Festa *et al.*, 2012). The presence of basalt in the illitic mélange but not sandstone in the chloritic mélange therefore suggests higher shear strains were achieved in the illitic mélange, possibly due to strain localisation during deformation. Localisation of shear during deformation is a response to the rheology of the deforming material, possibly indicating that the illitic mélange deformed at higher strain rates during deformation than the chloritic mélange.

Most previously-studied tectonic mélanges associated with subduction are volumetrically dominated by siliciclastic sequences (Fagereng, 2011b; Fisher and Byrne, 1987; Kimura and Mukai, 1991; Meneghini *et al.*, 2009; Remitti *et al.*, 2011; Rowe *et al.*, 2011; Ujiie, 2002; Vannucchi *et al.*, 2008), suggesting increased sediment thickness aids in accretion and eventual exhumation. The smaller volumetric component of siliciclastic sediments at Llanddwyn Island shows less sediment was incorporated into the mélange during accretion, either due to lower sedimentary input thickness

or preferential incorporation of less siliciclastic material at the plate interface. Repeated delamination of OPS slices along hyaloclastite horizons suggests the structure of the incoming oceanic volcanic sequence may play a role in dictating the geometry of the plate interface (Fig. 6.1 & 6.6).

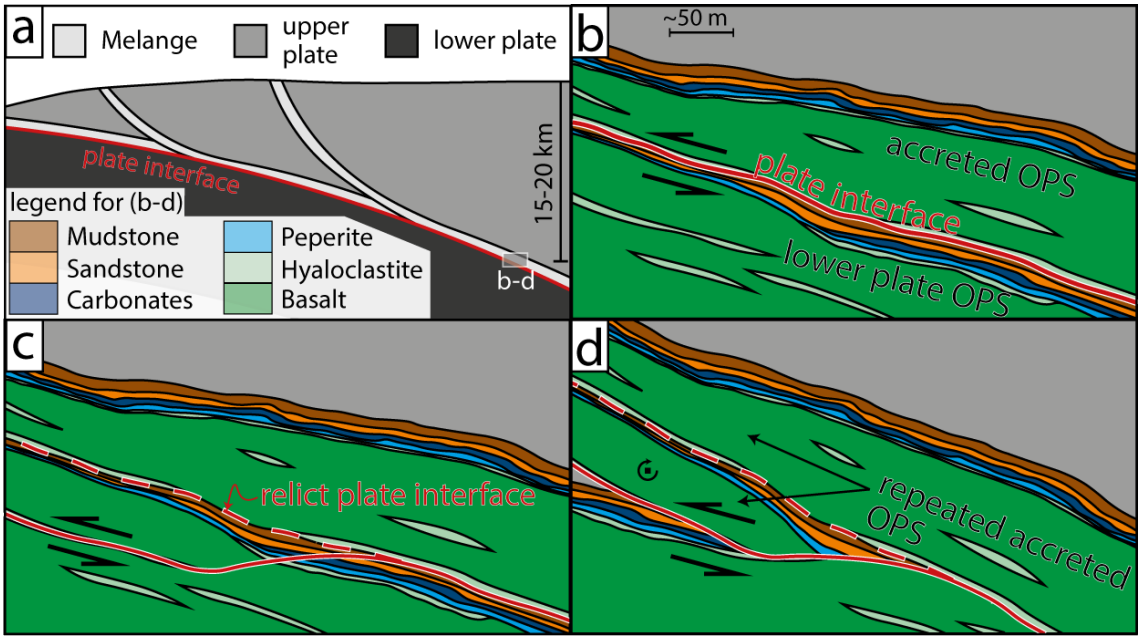

Figure 6.6: Schematic sketch of the suggested mode of exhumation and rotation of the tectonic mélange from the plate interface to the outcrop observed at Llanddwyn Island.

6.6 Heterogeneous deformation within imbricated plate interface shear zones

Deformation of mélange shear zones across Llanddwyn Island is heterogeneous due to the variable rheology, composition, thickness (i.e. strain rate) and physical properties (including fluid content and pressure) of each part of the deforming volume. The bulk rheology of mélange shear zones, likely sources of heterogeneity from mélange texture, and effects of local heterogeneity on deformation of the plate interface are now characterised.

6.6.1 Qualitative bulk rheology from grain-scale observations

Temporarily disregarding veins, the phyllosilicate matrix of both chloritic and illitic mélanges host the most visible deformation around and between less deformed clasts of more rigid lithologies (e.g. basalt, sandstone, carbonate; Figs. 6.4 & 6.5). Phyllosilicates within mélange units are fine-grained (≤ 20 μm) and dominantly foliated, commonly forming interconnected anastomosing networks capable of hosting simple shear deformation by basal or frictional sliding (*sensu* Kronenberg *et al.*, 1990; Okamoto *et al.*, 2019). Clasts within the illitic mélange are commonly sub-rounded, asymmetrical, and elongate parallel to foliation (Fig. 6.5), consistent with material removal by pressure solution during simple shear (Bos and Spiers, 2001). As material is moved from high to low stress sites along clasts and they elongate parallel to foliation orientation, phyllosilicate foliations become less curved and translation of clasts relative to one another requires lower shear stresses. Mélange shear zones therefore weaken with increased strain by pressure solution (Bos and Spiers, 2001). The incorporation of new material into the shear zone (e.g. at the intersection of anastomosing shear zones within the plate interface), would likely alter grain-scale stress distribution and allow the influx of fluids with different chemistry, possibly leading to accelerated dissolution or precipitation in the short term (Yasuhara, 2003).

The highly locally variable clast proportion within both illitic and chloritic mélange likely controls the bulk rheology of mélange shear zones to a first order by inhibiting sliding on the matrix where clasts become 'locked up' (Beall *et al.*, 2019). Where stress is below that required for brittle shear failure of the clast-forming material, frictional-viscous mechanisms combining pressure solution of clasts and frictional or basal slip on phyllosilicates likely dominate the rheology (Bos, 2002; Niemeijer and Spiers, 2005). In contrast, it is likely that the rheology of clast-poor areas more resembles that of basal sliding on the matrix-forming phyllosilicate (Kronenberg *et al.*, 1990), especially where through-going shears are present without interrupting clasts (Handy, 1990).

6.6.2 The role of veins: strain hardening, and variable P_f

Veins up to several mm across are common within both illitic and chloritic mélange (Figs. 6.4 & 6.5). Chlorite-quartz-calcite veins within the illitic mélange are commonly boudinaged, cut, or otherwise sheared, forming clasts of vein-derived quartz and calcite within the illitic matrix. Formation of these veins likely occurred during foliation-parallel extension during deformation (Schmalholz and Maeder, 2012), with mineral precipitation cementing fractures as the vein formed. The role of these veins, therefore, was to strain-harden a through-going horizon before gradually weakening as the vein was disaggregated. The bulk strength of the vein-hosting mélange after veining must have been higher than before, even after disaggregation, as veining of dominantly quartz and calcite increased the volume percent of material stronger than the matrix-forming illite.

The foliation-parallel veins found throughout mélange shear zones accommodated opening and shear (Figs. 6.4a & 6.5a), requiring supra-lithostatic pore fluid pressures at the instant of formation (Fig. 6.7c & e; Cox, 2011). The source of the solute is not clear, but local pressure solution occurring on clasts or longer-range fluid flow within the mélange are both reasonable candidates. Several generations of variably-deformed veins are present within illitic mélange, suggesting pore fluid pressures were cyclically elevated to supra-lithostatic levels during deformation (Fig. 6.5a & d). An alternative model invokes the mechanical creation of space during a slip event driving an influx of fluid into a fracture (e.g. Gülyüz *et al.*, 2018). This model would produce a similar texture in the resulting vein but lacks a clear mechanism for weakening of the host rock to form a fracture and create the void volume, especially through pre-existing veins of cohesive quartz and calcite.

Regardless of the degree of involvement of fluids in fracture formation, the illitic mélange therefore episodically strengthened with each pore fluid pressure cycle as vein material precipitated, exploiting and hardening deforming horizons with the lowest cohesion and tensional strength (Fig. 6.7e). Previous work in granitic rocks has suggested the the evolution of a fault may be related to the hydrological properties of the fault, where more permeable faults develop weak cores and less permeable faults remain stronger (Lawther *et al.*, 2016). While the permeability structure of

a subduction-related mélange shear zone is very different to that of a granitic shear zone, the strength of the shear zones studied here is clearly linked to the hydrological structure and fluid chemistry at the instant of vein formation. Quartz and calcite have opposite solubility relationships with temperature (Plummer and Busenberg, 1982; Rimstidt and Barnes, 1980), meaning veins formed by pressure drops rather than precipitation with cooling (*sensu.* Meneghini and Moore, 2007). Mineral precipitation due to pressure drop is consistent with short-lived fluid pressure pulses forming veins by hydrofractures that rapidly fill with quartz and calcite as pore fluid pressure reverts toward hydrostatic. Whether veins partially or totally fill during each hydrofracture event is unclear, but the lack of crack-seal textures suggests veins were not systematically re-fractured and filled further. Magnesium-rich marginal chlorite within the veins could have formed by either precipitation or reaction with the mélange matrix (Fig. 6.5f-h), though the lack of magnesium-rich species within the matrix suggests the former.

Chloritic mélange also hosts quartz-calcite veins, though calcite volumetrically dominates these (Figs. 6.4 & 6.7a). Unlike veins in the illitic mélange, veins in the chloritic mélange are not boudinaged or disaggregated, suggesting they deformed at similar strain rates to the mélange matrix (Fig. 6.4a). Basalt clasts are bisected by, and smeared along, foliation-parallel calcite veins (Figs. 6.4a & c). It is unclear if these veins have an extensional or shear opening sense but basalt clasts are smeared along the calcite veins with offsets consistent with strains ≤ 4.5 (maximum ~ 4.5 mm offset across a 1 mm vein; Figs. 6.4a & c). Calcite within the veins is almost completely recrystallised to ~ 12 μm (Figs. 6.4d-f & 6.7a & b), recrystallisation to fine grain sizes may have facilitated deformation by a combination of grain-size sensitive (*sensu* Herwegh *et al.*, 2003) and dislocation creep (Renner *et al.*, 2002). Creep of calcite in these veins would have been inhibited (i.e. required greater stresses to achieve the same strain) by greater amounts of quartz pinning calcite grains, such as within veins throughout illitic mélange. Composition of the vein filling, resulting from fluid chemistry at the instant of fracture formation, therefore exhibits a demonstrable effect on the bulk strength of the mélange where veining is common. This is exemplified by the deformation of calcite-rich veins in the chloritic

mélange to high strains and the dismemberment of less deformed quartz-rich veins in the illitic mélange (Figs. 6.4 & 6.5).

6.7 Quantifying rheology from observations

Observations of chloritic and illitic mélange units show that both experienced distinct modes of shear deformation within localised shear zones. Both calcite veins and the chlorite matrix have been deformed to moderate-high shear strains within the chloritic mélange. Shear deformation in the illitic mélange appears to have dominantly occurred by slip on illite in the matrix, aided by foliation-normal pressure solution of clasts, and was cyclically punctuated by transient hybrid extensional-shear veining. Several methods are now used to calculate the differential stress and temperature during deformation, which are then used to model the relative contributions of matrix and clast deformation within each mélange unit to the overall strain rate and velocity of the shear zone.

6.7.1 Differential stress and temperature estimates on Gwna Complex Deformation

Different methods were used to estimate differential stresses (σ_d) and temperature (T) for illitic and chloritic mélanges. Calcite veins throughout the chloritic mélange were analysed with EBSD and recrystallised grains were segregated from relict grains based upon the spread of orientations within a grain around a threshold value of 1.88° (Cross *et al.*, 2017). The mean size of recrystallised calcite grains from the nominally monomineralic veins was then used to determine the differential stress during steady state vein deformation using the paleopiezometer of Platt and De Bresser (2017). Recrystallised grains had a mean grain size of 11.4 μm, corresponding to a differential stress of 88 MPa. Ranges in exponent values in the method of Platt and De Bresser (2017) cause broad 95% confidence limits, between 30 and 255 MPa (Fig. 6.7a & b). Assuming these veins recrystallised before or during deformation, this measurement reflects the background differential stress during recrystallisation of calcite, and from optical microscopy the grain size appears consistent between veins within the

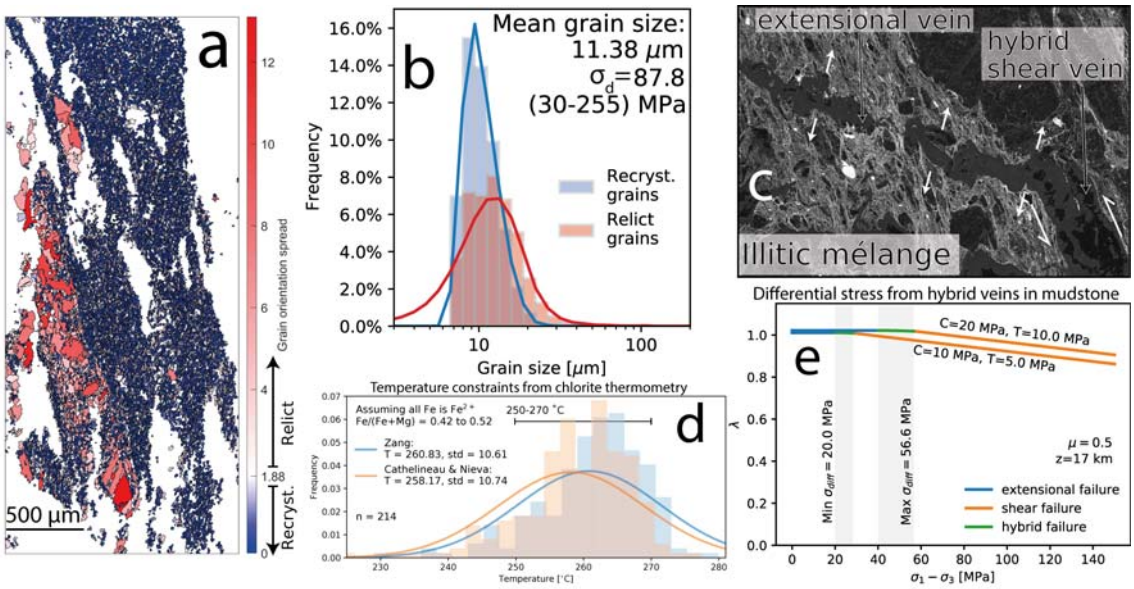

Figure 6.7: Differential stress-T constraints from both mélanges from analysis of hybrid extensional vein failure under estimated conditions, recrystallised calcite piezometry from Platt and De Bresser (2017), and chlorite geothermometry.

mélange.

Foliation-parallel calcite-quartz-chlorite veins within illitic mélange have opened oblique to foliation, hosting both extensional and shear offset (Figs. 6.5d & e). Foliation-oblique veins locally merge with those oriented parallel to foliation with the same opening sense, suggesting local variations in cohesion and tensional strength affected vein style (Fig. 6.7c). Assuming typical values for cohesion (C) and tensional strength (T) from accretionary complex sediments ($C = 10 - 20$ MPa, $T = 5 - 10$ MPa; Schumann *et al.*, 2014), a pore fluid factor-differential stress (λ vs. $\sigma_1 - \sigma_3$) plot is constructed (*sensu.* Cox, 2011) to assess the differential stress range over which these hybrid extensional shear veins might have occurred (Fig. 6.7e). Hybrid extensional-shear veins should occur at supra-lithostatic pore fluid pressures and differential stresses in the range between $4T$ and $5.66T$ (Secor, 1965), the assumed cohesion and tensional strength values therefore constrain the differential stress range at the instant of hybrid vein formation to between 20 and 57 MPa (Fig. 6.7e). As we do not know the actual values for C or T, we take this range (38 ± 18 MPa) as the estimated differential stress at the instant of hybrid fracture formation.

Chlorite is also present in many variably-deformed veins within the illitic mélange, allowing us to use geothermometry to discern syn-kinematic temperatures of chlorite crystallisation. In this case chlorite crystallisation is likely coincident with vein formation due to chlorite almost exclusively lining the margins of almost all veins within the illitic mélange (Fig. 6.5f-h). Analyses used here are quantified from SEM-EDS maps and have Fe/Mg ratios of 0.42 to 0.52 (Fig. 6.7d). The chlorite geothermometers of Cathelineau and Nieva (1985) and Zang and Fyfe (1995) are used as they were calibrated over similar Fe/Mg ratios. Analysis of 214 vein-hosted chlorite areas ($50 - 100$ μm^2) yields two distributions with means of 261 and 258 °C for the geothermometers of Zang and Fyfe (1995) and Cathelineau and Nieva (1985), respectively, and standard deviations of 11 °C for both (Fig. 6.7d). These temperatures are consistent with both (1) the preservation of original lithological texture visible across the island and (2) the onset of recrystallisation and crystal-plastic deformation of calcite (Fig. 6.4). We therefore take $\sim 260 \pm 10$°C as the approximate temperature of deformation.

Differential stress estimates from recrystallised calcite grain size and the hybrid failure criterion yield very different values ($\sim$ 88 and 38 MPa, respectively; Fig 6.8). Errors for the two values (30-255 and 10-57 MPa, respectively) overlap between 30 and 57 MPa due to poorly constrained exponents in the recrystallised calcite piezometer of Platt and De Bresser (2017). Differing stress estimates may be expected as recrystallised calcite grain size is used to estimate a steady state differential stress during recrystallisation and the hybrid failure criterion estimates differential stress at the instant of failure. Previously, variable differential stress estimates within a shear zone have been interpreted to represent the stress within that phase (Stenvall *et al.*, 2019). Similarly, it may be that differential stress in a through-going calcite vein that is deforming slowly and providing a barrier to more rapid deformation of the surrounding matrix records a higher stress than failure within the more rapidly-deforming matrix (Beall *et al.*, 2019). The differential stress estimate from recrystallised calcite grain size with the piezometer of Platt and De Bresser (2017) is therefore used to interpolate velocities in the following modelling. To account for the large uncertainty of the differential stress estimate,

models are shown with variable stress and strain rate or velocity.

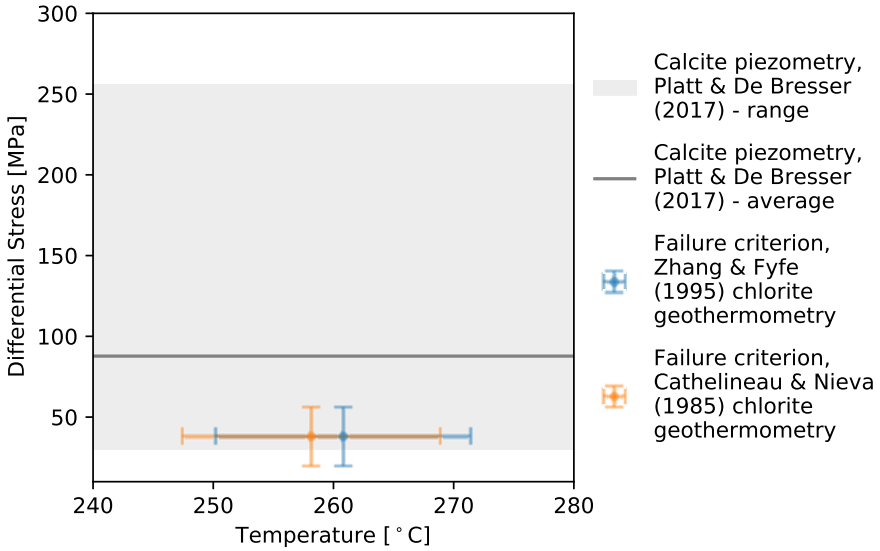

Figure 6.8: Differential stress (σ_d)-T constraints from analysis of hybrid extensional vein failure under estimated conditions, recrystallised calcite piezometry from Platt and De Bresser (2017), and chlorite geothermometry plotted together.

6.7.2 Modelling stress and strain rate in chloritic and illitic mélange

Given the evidence for various deformation mechanisms operating in each mélange unit under variable fluid pressure (sections 6.4 & 6.6.2), I now attempt to quantify a bulk shear stress (τ)/strain rate($\dot{\gamma}$) or velocity (V)/pore fluid pressure (P_f)-dependent rheology using the field-scale outcrop and mineralogy of each mélange unit and following the approach outlined by French and Condit (2019). This model assumes an idealised plate interface shear zone (Fig. 6.3a) dipping at 10° (δ) and deforming at a temperature (T) of 260°C (based on chlorite geothermometry; Figs. 6.7d & 6.8). I assume an interface depth of 17 km, consistent with the estimate of T from chlorite geothermometry on a ∼15 °C km^{-1} geotherm, and a density of the upper crust of 2750 kg m^{-3} to calculate a vertical stress (σ_v) of ∼ 458 MPa. The maximum differential stress (σ_1) was assumed to have negligible impact on the

vertical stress and plunge 35° antithetic to the plate interface (ψ), the minimum differential stress (σ_3) plunges 90° from this, synthetic to the plate interface (See French and Condit, 2019, Figure 2 for summary).

I followed both Bletery *et al.* (2017) and French and Condit (2019) in modelling the layer-parallel τ required for frictional slip at a given V as

$$\tau = \frac{\mu(T,V)(\sigma_v - P_f)sin(2\delta + 2\psi)}{sin(2\delta + 2\psi) + \mu(T,V)(cos(2\delta + 2\psi) - cos(2\psi))} \tag{6.1}$$

where $\mu(T,V)$ is the frictional coefficient of the material at temperature T and velocity V. This was calculated using

$$\mu(T,V) = \mu_0 + (d\mu_{ss}/dlnV)_T ln\frac{V}{V0} \tag{6.2}$$

where μ_0 is the friction coefficient at temperature T and pre-step slip velocity V_0. The rate-and-state parameter ($(d\mu_{ss}/dlnV)_T$) determines the response of $\mu(T,V)$ with a change from V_0 to V (Chester, 1994); if $(d\mu_{ss}/dlnV)_T$ is less than 0 then $\mu(T,V)$ reduces with increased velocity and the material velocity-weakens, if $(d\mu_{ss}/dlnV)_T$ is greater than 0 then $\mu(T,V)$ increases with increased velocity and the material velocity-strengthens. This velocity-dependent behaviour has been considered by many to be a measure of the propensity for seismic slip in a material, as velocity-weakening materials will further weaken with increased velocity and therefore host "runaway", or seismic, slip. Friction was modelled at constant T and variable V, meaning values for $\mu(T,V)$ were controlled by initial inputs of V_0, μ_0, and $(d\mu_{ss}/dlnV)_T$. To retain comparability from experimental data, values for μ_0 and $(d\mu_{ss}/dlnV)_T$ were selected if they were measured at velocity steps originating with a V_0 of 1 μm s^{-1}. Values of μ_0 and $(d\mu_{ss}/dlnV)_T$ for calcite and chlorite were not measured at the modelling T so, following den Hartog *et al.* (2012), values were linearly interpolated between data measured at temperatures above and below 260 °C.

For the chloritic mélange (Fig. 6.9a), τ-$\dot{\gamma}$ curves were modelled for pressure solution (Bos, 2002), diffusion creep (Herwegh *et al.*, 2003), dislocation creep (Renner *et al.*, 2002; Rutter, 1974), grain size insensitive cross slip (De Bresser, 2002), and

friction of calcite for veins (Verberne *et al.*, 2015) and friction for chlorite in the matrix (Okamoto *et al.*, 2019). Following French and Condit (2019), dislocation creep of calcite was modelled using the flow law of Renner *et al.* (2002) at lower values of τ and the flow law of Rutter (1974) at higher values of τ, this transition occurs at $\sim$ 35 MPa at 260 °C. Verberne *et al.* (2015) measured calcite friction values at velocity steps of 1-3 μm s^{-1}, temperatures of 20 to 600 °C, and effective normal stresses (σ^n_{eff}) of 30, 50, 80, and 100 MPa. At $\lambda = 0.8$, σ^n_{eff} on the modelled plate interface were $\sim$97 MPa, making a σ^n_{eff} value of 100 MPa the most appropriate here. Values of μ_0 and $(d\mu_{ss}/dlnV)_T$ are 0.52 and -0.003 at 199 °C and 0.43 and -0.014 at 398 °C, respectively. Both of these values were linearly interpolated at 260 °C to yield values of 0.49 for μ_0 and -0.00637 for $(d\mu_{ss}/dlnV)_T$. This suggests calcite at this temperature would be relatively strongly velocity weakening but have a relatively high initial strength. For chlorite, Okamoto *et al.* (2019) measured friction values at velocity steps of 1-3 μm s^{-1}. Values at $\lambda = 0.4$ were interpolated between measurements of $\mu_0 = 0.258$ and $(d\mu_{ss}/dlnV)_T = 0.00193$ of at 200 °C and $\mu_0 = 0.299$ and $(d\mu_{ss}/dlnV)_T = 0.00081$ at 300 °C. This yielded a μ_0 of 0.28 and a $(d\mu_{ss}/dlnV)_T$ of 0.001258 at 260 °C. This suggests chlorite at this temperature would be velocity strengthening, but have a lower initial strength than calcite.

Though the illitic mélange has clasts of varied composition including basalt, carbonate, and foliated sandstone containing quartz, albite, and chlorite (Fig. 6.5f & h), I assumed a quartz-dominated sandstone clast lithology due to the limited availability of data for albite solubility and its low temperature deformation mechanisms. Under the interpreted conditions albite would be expected to be stronger than quartz and calcite (Borg and Heard, 1970; Lu and Jiang, 2019; Renner *et al.*, 2002), so the assumption of a quartz aggregate increases the amount of deformation modelled to occur in the clasts. In the resulting model most of the deformation occurs in the albite-free matrix so the impact of this assumption appears minimal given the number of others. Quartz deformation was modelled using pressure solution creep (Rutter, 1976) and dislocation creep (Lu and Jiang, 2019), combined with a flow law for the frictional-viscous flow of a quartz-phyllosilicate aggregate (Bos, 2002; Niemeijer and Spiers, 2005) to represent sandstone within the clasts and

Mélange unit	Component & mineral(s)	Deformation mechanism	Parameters	Reference
Illitic	Clasts - quartz	Dislocation creep	As reported	(Lu and Jiang, 2019)
		Pressure solution	As reported	(Rutter, 1976)
	Clasts - Quartz & illite	Frictional-viscous flow	As reported	(Bos, 2002; Niemeijer and Spiers, 2005)
	Matrix - illite	Frictional sliding	$\mu_0 = 0.52$, $(d\mu_{ss}/dlnV)_T = 0.00484$	(den Hartog *et al.*, 2012)
Chloritic	Veins - calcite	Dislocation creep	As reported	(Renner *et al.*, 2002)
		Dislocation creep	As reported	(Rutter, 1974)
		Cross slip	As reported	(De Bresser, 2002; Verberne *et al.*, 2015)
		Diffusion creep	As reported	(Herwegh *et al.*, 2003)
		Pressure solution	As reported	(Bos, 2002)
		Frictional sliding	$\mu_0 = 0.49$*, $(d\mu_{ss}/dlnV)_T = -0.00637$*	(Verberne *et al.*, 2015)
	Matrix - chlorite	Frictional sliding	$\mu_0 = 0.28$*, $(d\mu_{ss}/dlnV)_T = 0.001258$*	(Okamoto *et al.*, 2019)

Table 6.2: Summary of materials and mechanisms used in modelling shear stress-strain rate curves. Parameters marked with * were linearly interpolated at 260 °C from values at higher and lower temperatures.

encompass the transition between viscous and frictional behaviour at low and high $\dot{\gamma}$ or V. The frictional behaviour of illite was modelled using experimental data from den Hartog *et al.* (2012) measured at a velocity step of 1-10 μm s^{-1} and a T of 250 °C. Values of μ_0 were not fully modelled for these data, but are instead pre-velocity step measurements of μ_{start}, corrected for background slip-hardening trends. In lieu of fully modelled data, this value of $\mu_{start} = 0.52$ was treated as μ_0 along with the associated value of $(d\mu_{ss}/dlnV)_T$ of 0.00484. These values were used without any interpolation as they were measured at 250 °C, within error of the estimates of T from chlorite geothermometry. This suggests illite at this temperature would be both velocity strengthening and relatively strong for a phyllosilicate.

Curves for τ-$\dot{\gamma}$ from different mechanisms were combined by assuming additive shear strain rate deformation at a given shear stress (Fig. 6.9). For a summary of all deformation mechanism modelled for each mélange, see Table 6.2. I have, throughout, assumed that deformation occurs by the mechanism requiring the smallest τ. Where appropriate, V was converted to $\dot{\gamma}$ by dividing by the unit thickness and converting $\dot{\gamma}$ to V was achieved by performing the inverse. Thicknesses used in the modelling are based on an idealised mélange shear zone (Fig. 6.3a) and are: calcite veins= 1 mm, chlorite matrix= 2 m, illite matrix= 1.2 m, quartz clasts= 1 m.

6.7.3 Shear stress, strain rate, and velocity of modelled chloritic and illitic mélange

Shear stress-shear strain rate (τ-$\dot{\gamma}$) curves for sandstone clasts and calcite veins follow similar trajectories of increasing τ from low to high $\dot{\gamma}$ (Fig. 6.9a-b). In all curves the low τ, low $\dot{\gamma}$ region is dominated by pressure solution of calcite or quartz, becoming frictional-viscous (*sensu* Bos, 2002) in sandstone with increasing τ and $\dot{\gamma}$ (Fig. 6.9b). At $\dot{\gamma} \geq 1 \times 10^{-5}$ s^{-1}, the strength of sandstone becomes dominated by phyllosilicate friction. Within the low $\dot{\gamma}$ regime, calcite deforms by rate-strengthening pressure solution (Bos, 2002) until $\dot{\gamma} \geq 1 \times 10^{-13}$ s^{-1} and $\tau \geq 20$ MPa where diffusion creep accommodates deformation at higher $\dot{\gamma}$ (Fig. 6.9b). Dislocation creep (*sensu* Rutter, 1974) becomes less $\dot{\gamma}$-strengthening with increased τ until grain size-

insensitive cross-slip (*sensu.* De Bresser, 2002) becomes dominant at $\tau \approx 90$ MPa. Cross-slip dominates at high stresses, and is modelled to control deformation at $\dot{\gamma} \geq 1 \times 10^{-10}$ s^{-1} by allowing deformation at lower stresses than velocity-weakening calcite friction at hydrostatic pore-fluid factors (Fig. 6.4). Calcite friction becomes dominant at very high strain rates ($\dot{\gamma} \geq 1 \times 10^{-1}$ s^{-1}), suggesting it would control seismic slip.

Frictional sliding on chlorite and illite foliations in represented by τ-$\dot{\gamma}$ curves just below and above 100 MPa, respectively (Fig. 6.9c-d). Chlorite is only marginally velocity strengthening, meaning little change in τ with increased V. Chlorite frictional sliding requires lower shear stresses than viscous deformation of calcite at $V = 1 \times 10^{-14}$ m s^{-1} and $\tau \approx 80$ MPa (before cross-slip becomes rate-controlling), where it dominates at increased velocities well into seismic slip rates of 1 m s^{-1}. At aseismic creep velocities consistent with plate convergence (10-100 mm yr^{-1}) and geodetically-modelled slow slip events (300-1500 mm yr^{-1}; Bürgmann, 2018), chloritic mélange deforms dominantly by frictional sliding on chlorite at shear stresses of 83 and 85 MPa, respectively (blue and red shaded areas on Fig. 6.9c), with very little contribution from viscous or frictional deformation of calcite. Illite is more velocity strengthening than chlorite and its τ therefore doubles with increasing V between 1×10^{-18} and 1 m s^{-1}. Illitic frictional sliding requires lower shear stresses than frictional-viscous deformation of sandstone clasts at $V = 5 \times 10^{-6}$ m s^{-1} and $\tau \approx 180$ MPa and continues to be dominant at greater V. Unlike chloritic mélange, illitic mélange deforms by mixed frictional-viscous deformation at both plate convergence and slow slip velocities (Fig. 6.9d). Plate convergence-rate slip requires shear stresses of 44-50 MPa and slow slip velocities require higher shear stresses of 53-58 MPa due to the relatively greater contribution of friction required at higher velocities.

6.7.4 Modelled effects of pore fluid pressure

Cross-cutting and deformed hybrid extensional-shear veins indicate that elevated pore fluid pressures (P_f) were cyclically reached during shear deformation within the illitic mélange (Figs. 6.5 & 6.7). Based on this evidence of variable P_f within

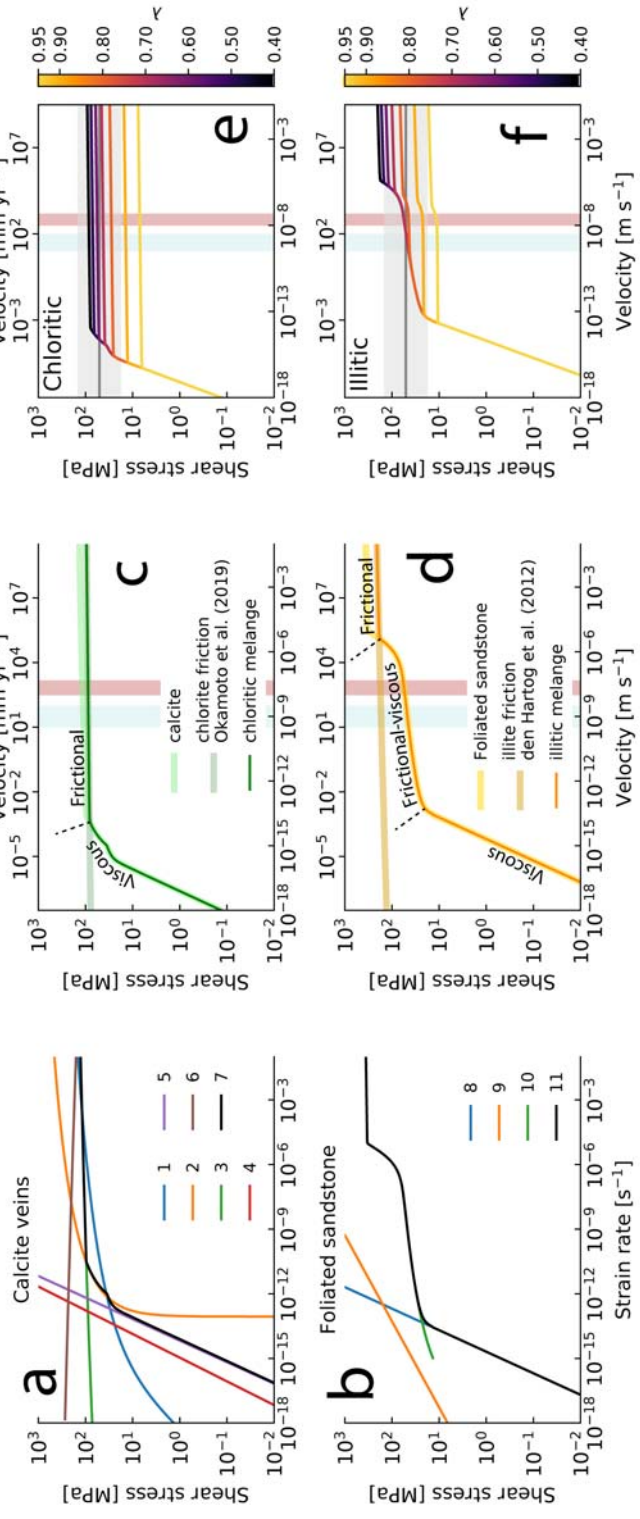

Figure 6.9: Modelled shear stress-shear strain rate (or velocity) curves for chloritic and illitic mélange. Modelled curves for (a) calcite are 1-dislocation creep (Renner *et al.*, 2002), 2-dislocation creep (Rutter, 1974), 3-grain size-insensitive cross slip (De Bresser, 2002) in the exponential form (Verberne *et al.*, 2015), 4-diffusion creep (Herwegh *et al.*, 2003), 5-pressure solution (Bos, 2002), 6-frictional slip (Verberne *et al.*, 2015), 7-combined τ-$\dot{\gamma}$ curve for calcite; (b) quartz are 8-pressure solution (Rutter, 1976), 9-dislocation creep (Lu and Jiang, 2019), 10-frictional-viscous flow of a quartz-phyllosilicate aggregate (Bos, 2002; Niemeijer and Spiers, 2005), 11-combined τ-$\dot{\gamma}$ curve for quartz. Parts c and d show curves for combined calcite with chlorite and combined quartz with illite, respectively. Chlorite and illite strengths were modelled using frictional parameters from Okamoto *et al.* (2019) and den Hartog *et al.* (2012). Curves for parts c and d follow the mechanism of minimum shear stress at hydrostatic pore fluid factor (λ) for chloritic and illitic mélange, respectively. Plots e and f show these overall curves for each melange at variable λ. Red and blue shaded areas correspond to velocity ranges for plate convergence (10-100 mm yr^{-1}) and slow slip (300-1500 mm yr^{-1}), respectively. Modelling follows the methodology of French and Condit (2019) on an interface dipping 10° at 260 °C and 17 km depth.

mélange shear zones at Llanddwyn, the effect of variable P_f on the strength, velocity, and mechanisms of modelled deformation within the mélange units is now investigated. Pore fluid factor (λ) is calculated as the ratio of P_f to σ_v ($\lambda = \frac{P_f}{\sigma_v}$), meaning at hydrostatic P_f, $\lambda = 0.4$ and at lithostatic P_f, $\lambda = 1$. Increases in P_f, therefore reduce the shear stress required to activate deformation mechanisms sensitive to effective normal stress (σ^n_{eff}). Viscous mechanisms, which according to modelled deformation occur at low strain rates and velocities, are not sensitive to σ^n_{eff}, meaning the τ-$\dot{\gamma}$ curve for each mélange unit is unaffected at low strain rates by increases in P_f (Fig. 6.9e-f). Frictional sliding, as outlined in Equation 6.1, is sensitive to both σ_v and interface dip (δ). In the models frictional sliding requires lower τ to activate with increasing λ, requiring lower shear stresses to deform than viscous or frictional-viscous mechanisms at incrementally lower values of τ. Within the chloritic mélange, chlorite weakens with increased λ to truncate the deformation of calcite and become the dominant mechanism at almost all modelled velocities (Fig. 6.9e). Plate rate and slow slip velocities require reduced shear stresses to occur within the chlorite matrix, down to a minimum of 5 and 9 MPa, respectively, at $\lambda = 0.95$. Within the illitic mélange both frictional-viscous and frictional deformation weaken with increasing λ; plate rate convergence velocities require shear stresses of 10-11 MPa and slow slip velocities require shear stresses of 11-12 MPa at $\lambda = 0.95$.

An example of how variable composition within heterogeneous deforming zones may control slip is well illustrated by the model results; the weakening effect of higher P_f on frictional sliding is greater in chloritic mélange than in illitic mélange (Fig. 6.9e-f). Shear stresses required for chloritic mélange shearing at plate convergence rates reduce from 83 MPa at (hydrostatic) $\lambda = 0.4$ to 5 MPa at (near-lithostatic) $\lambda = 0.95$. Shear stresses for illitic mélange shearing at plate convergence rates reduce from 44-50 MPa at (hydrostatic) $\lambda = 0.4$ to 10-11 MPa at (near-lithostatic) $\lambda = 0.95$. The same is true for slow slip velocities (Fig. 6.9e-f). The rheology of the imbricated mélange shear zones observed on Llanddwyn island, therefore, is highly dependent on both the composition of the material and the P_f it is deforming at.

When considering the entire deforming zone (Fig. 6.10), the τ-$\dot{\gamma}$ curve is con-

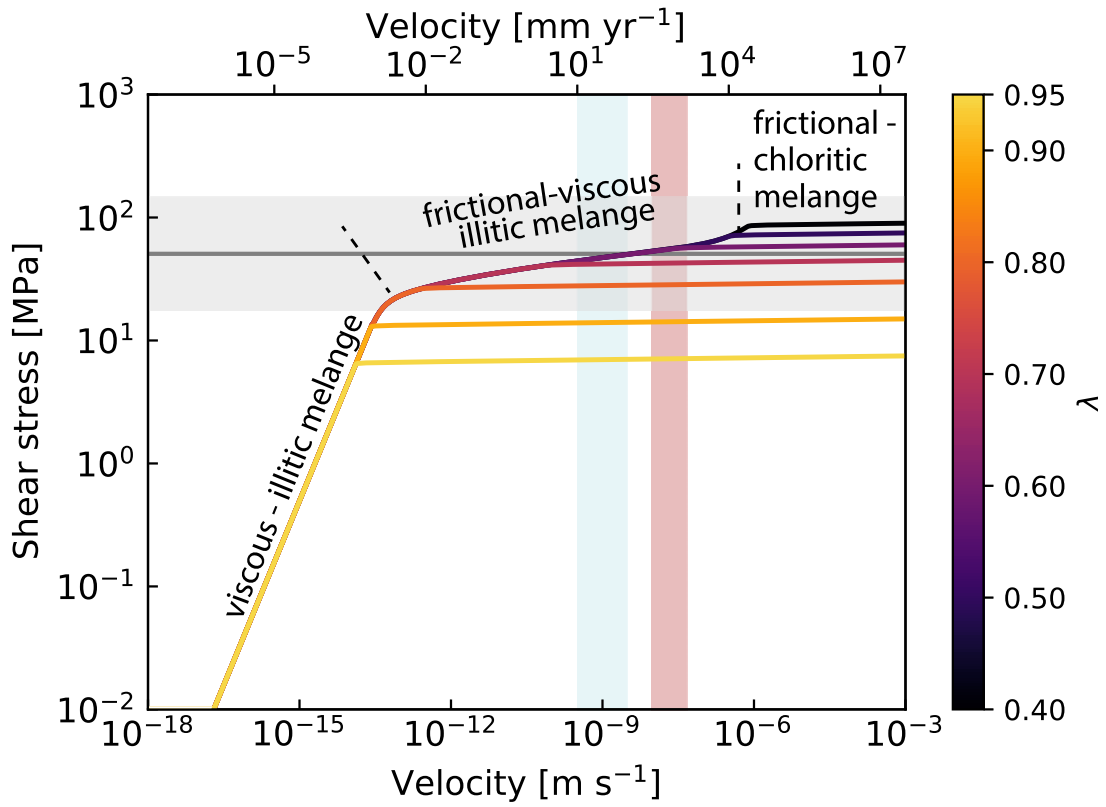

Figure 6.10: Shear stress-shear velocity curves for combined chloritic and illitic mélange under variable pore fluid factor (λ). Modelling follows the methodology of French and Condit (2019) on an interface dipping 10° at 260 °C and 17 km depth.

trolled by various mechanisms throughout all lithologies at a range of λ. The lowest velocities and shear stresses can be achieved by viscous deformation of clasts within the illitic mélange by pressure solution. With increased velocity and shear stress frictional sliding begins to also occur, leading to frictional-viscous slip at rates encompassing the plate convergence and slow slip velocity range at hydrostatic P_f (Fig. 6.10). At $V > 1 \times 10^{-6}$ m s^{-1} and hydrostatic P_f, frictional sliding of chlorite becomes dominant at shear stresses$\sim$ 100 MPa. With increased λ, it is the frictional sliding of chlorite that weakens the most, becoming the dominant mechanism at incrementally lower shear stresses (Fig. 6.10). Slip partitioning (i.e. the distribution of slip between units) within mélange shear zones is dependent on λ (Fig. 6.11), with chloritic mélange accommodating increasing proportions of the total slip budget at

greater pore fluid pressures (Fig. 6.11). At plate-rate and slow slip velocities, slip occurs in both mélanges at $0.6 < \lambda < 0.7$ (Fig. 6.11).

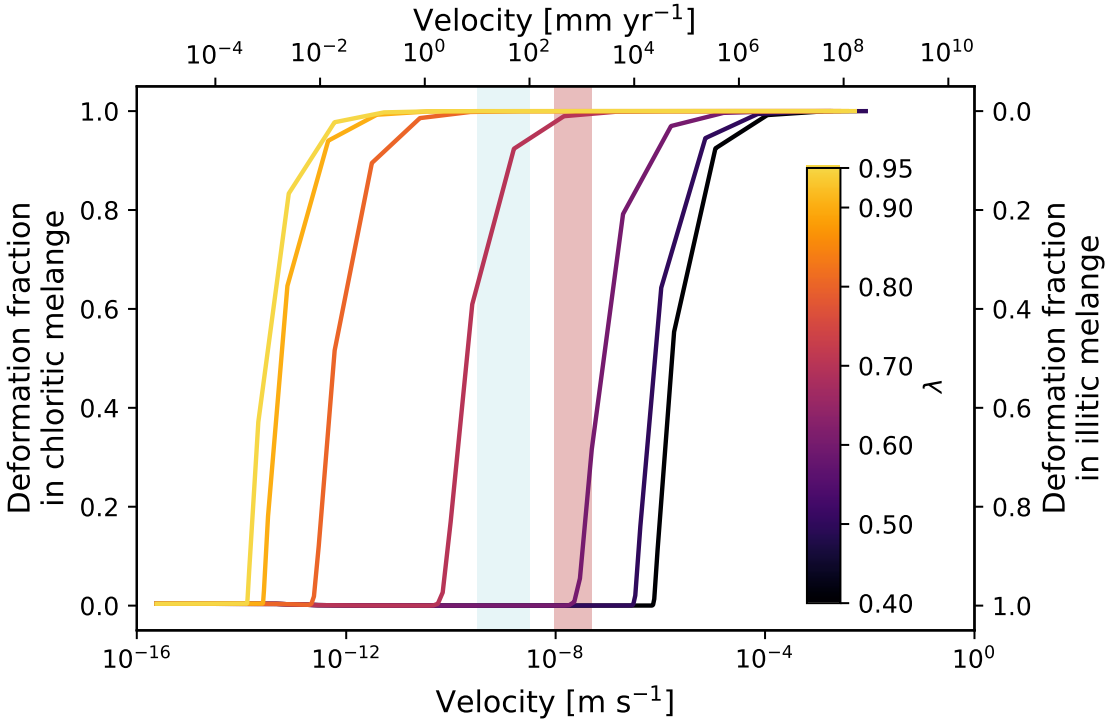

Figure 6.11: Modelled slip partitioning between illitic and chloritc mélanges within the idealised shear zone.

6.7.5 Comparing differential stress and pore fluid factor estimates with modelled velocities

Constraints from hybrid extensional-shear veins and recrystallised calcite within mélange shear zones on Llanddywn Island yielded differential stresses of 88 MPa with an uncertainty range of 30-255 MPa. Using $\tau = \sigma/\sqrt{3}$ (Nye, 1953), this corresponds to a shear stress of 51 MPa with an uncertainty range of 17-147 MPa. This shear stress is used to estimate shear strain rates and velocities under stress constraints from shear zones on Llanddywn Island. At hydrostatic pore fluid pressures ($\lambda = 0.4$), frictional-viscous slip in foliated sandstone clasts within the illitic mélange occurs at velocities consistent with plate boundary deformation ($V < 1 \times 10^{-9}$ mm yr^{-1}; Fig. 6.12). Calcite in the chloritic mélange deforms by dislocation creep at very

low slip rates ($\dot{\gamma} \approx 1 \times 10^{-15}$ s^{-1}; Fig. 6.12) under similar conditions, and shear stresses are not high enough to cause frictional slip in the chlorite matrix. At shear stresses estimated from the hybrid failure criterion in the illite matrix ($\sim$ 24 MPa) the illitic mélange deforms by pressure solution at rates below plate-rate (Fig. 6.9f), highlighting the stress sensitivity of deformation within shear zones of varied composition. At near-lithostatic pore fluid pressures ($\lambda = 0.9$), frictional slip at shear stresses of 51 MPa in chlorite and calcite causes modelled slip rates to exceed 1 m s^{-1} in the chloritic mélange (Fig. 6.9e-f). No clear evidence of seismic slip is present within the subduction complex, suggesting this is unrealistic. Slip in the illitic mélange under the same conditions occurs by frictional sliding at rates between those consistent with slow slip and seismic slip (Fig. 6.12).

For stress constraints from the subduction complex and velocity constraints from modern margins to agree, sub-lithostatic pore fluid factors (between 0.7 and 0.8; Fig. 6.12) or strain-rate dependent deforming thicknesses are required. Elevated pore fluid factors are evidenced at Llanddwyn by abundant veining throughout deforming zones (Figs. 6.3-6.5), and this does not rule out localised rapid slip at elevated P_f, as abundant localised slip surfaces adjacent to clasts are present throughout the illitic mélange (Fig. 6.5). Nevertheless, differential weakening at pore fluid factors between hydrostatic and lithostatic suggests slip on the plate interface will variably partition with increased P_f and frictional or compositional heterogeneity.

The dependence of rheology on a block in matrix structure, apparent from modelling a shear zone from Llanddwyn Island and from other modelling studies (Beall *et al.*, 2019; Fagereng and Beall, 2021), suggests that other, larger scale structures, may also impact rheology. In subduction zones one major structure which controls deformation on the plate interface is the geometry of lithologies over 10's to 100's of km (Heuret *et al.*, 2012). Similar to the block in matrix textures modelled here, where the distribution materials coming in to the plate interface is complex, plate interface deformation is likely to reflect that with highly non-linear rheology.

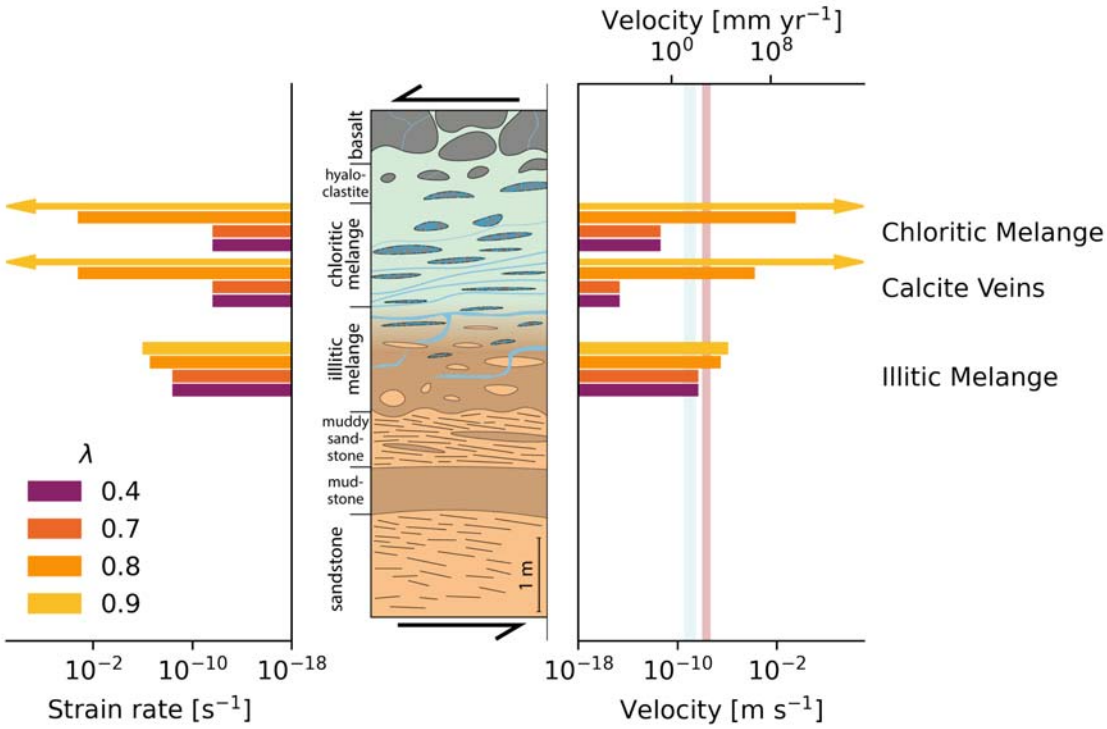

Figure 6.12: Shear strain rates (left) and velocities (right) for different lithologies at variable pore fluid factors (λ). Modelling follows the methodology of French and Condit (2019) on an interface dipping 10° at 260 °C and 17 km depth. Yellow arrows for the chloritic mélange and calcite veins at $\lambda = 0.9$ represent rapid slip rates > 1 m s^{-1}.

6.7.6 Slip instabilities during frictional sliding at elevated P_f

For slip to transiently accelerate from plate-rate to slow slip velocities, it has been widely suggested that instabilities during slip must alter the rheology of the plate interface (Bürgmann, 2018). These instabilities are as yet poorly understood, but are likely dominantly controlled by the deforming geometry and composition within the plate interface shear zone leading to conditionally-dependent values of the rate-and-state parameter ($(d\mu_{ss}/dlnV)_T$; Eq. 6.2). One such example of a conditionally-sensitive instability is P_f-dependent variability in the critical nucleation length recorded at depths near the up-dip limit of the seismogenic zone by Phillips *et al.* (2020). This variability would mean that as P_f increases, the propensity for chlorite

bordering basalt clasts to produce unstable seismic slip is replaced by an increased propensity for slow slip. This increased propensity for slow slip requires mixing of velocity strengthening illite and velocity weakening altered basalt at the appropriate conditions (Phillips *et al.*, 2020). At the estimated temperature of 260 ± 10 °C both chlorite and illite are velocity strengthening (Den Hartog and Spiers, 2014; Okamoto *et al.*, 2019). Some chlorite-bearing gouges have been determined as velocity weakening at $T > 200$ °C (Boulton *et al.*, 2014), but these gouges had major components of quartz and feldspars, and no through-going discrete slip surfaces are recognised within the chloritic mélange described here. At a larger scale, the adjacent shearing of chloritic and illitic mélange along shear zones at the base of delaminated oceanic crust may allow for mixing of velocity-strengthening and velocity-weakening materials. This suggests greater involvement of altered oceanic material in plate interface deformation could increase the propensity for slow slip, though this is dependent on the degree of mixing. Limited mixing was observed in mélange-bearing shear zones at Llanddwyn Island (Fig. 6.2a), meaning this effect would be confined to the narrow mixed volume near the middle of each shear zone.

A more mechanistic approach based on the recent modelling work of van den Ende *et al.* (2020) may yield insights into how unstable slip may nucleate in the clast-bearing illitic mélange (Fig. 6.5a). Modelling suggests that at estimated differential stresses of ~ 88 MPa and $P_f < 0.8$ the illitic mélange should be creeping by frictional-viscous pressure solution-mediated creep (Fig. 6.9f). Slow creep of phyllosilicates between clasts would reduce pore volume there, locally increasing P_f (Ikari *et al.*, 2009; van den Ende *et al.*, 2020). Locally increased P_f would reduce frictional resistance, increasing the likelihood of granular flow of clasts within the illitic mélange (Bos *et al.*, 2000). Then, following van den Ende *et al.* (2020), shear stresses would increase until they approach the onset of granular flow. Granular flow increases the porosity between clasts, rapidly reducing shear strength and weakening the mélange. If the melange has a sufficiently low stiffness a frictional instability would be generated and fault slip would accelerate, transiently increasing porosity along the sliding surface (van den Ende *et al.*, 2020). Observations of foliation-parallel veins consistent with cyclical formation at transiently elevated P_f

within the illitic mélange (Figs 6.5-6.7) suggest that this porosity increase would be associated with fluid propagation along the slip surface, and the resultant pressure drop would lead to precipitation of quartz-calcite-chlorite veins (e.g. Fig. 6.5f-h). Precipitation of the vein along the slip surface would harden it and reduce porosity, arresting slip. This could be repeated numerous times with slow creep deforming veins between slip events to produce the variably-deformed veins throughout the mélange (Fig. 6.5f-h). Hybrid extensional-shear veins observed within the mélange are consistent with this hypothesis, suggesting instabilities within the illitic mélange could be generated by deformation of a block-in-matrix texture rather than by frictional processes. As shown by the combined field and modelling approach taken here, the generation of instabilities within a heterogeneous creeping shear zone could occur by various material and texture-dependent mechanisms, and discerning how these processes operate within natural shear zones to generate slip transients is an exciting new challenge.

6.8 Conclusions

- The plate interface represented at Llanddwyn Island is locally-variable and heterogeneous, forming < 15 m wide shear zones imbricated of over tens to hundreds of metres. Imbricated shear zones host tectonic mélange units derived from the deformation of both silicalastic sediments and altered volcaniclastics.

- Illitic mélange, likely derived from siliciclastic material, has a block-in-matrix texture with albite, quartz, and calcite clasts within an illite matrix, all cut by variably-deformed cross-cutting quartz-chlorite-calcite veins. Transient supralithostatic pore fluid factors must have occurred cyclically during deformation to form multiple generations of variably-boudinaged veins, strain hardening the illitic mélange.

- Chloritic mélange, likely derived from altered volcanic material, has a chlorite matrix and altered basalt clasts, with recrystallised through-going calcite veins

deforming to strains of 4-5.

- Both mélange units have deformed by slip on phyllosilicates in the matrix, but the rheology of each have been altered by syn-kinematic veining of different compositions.

- A hybrid extensional-shear failure criterion suggests the differential stress at the instant of failure for the illitic mélange was 20-57 MPa, and recrystallised calcite grains within calcite veins viscous creep occurred at differential stresses of $\sim$ 88 MPa in the chloritic mélange. Geothermometry on synkinematic chlorite within veins in the illitic mélange yields a temperature of 260 ± 10 °C, meaning deformation occurred under subgreenschist conditions.

- To model shear stress-strain rate/velocity curves for each component of the illitic and chloritic mélanges, published flow laws were used for viscous mechanisms and parameters measured under in-situ conditions were used for rate-and-state friction.

- At hydrostatic pore fluid pressures ($\lambda = 0.4$), viscous deformation mechanisms (crystal plasticity, pressure solution) dominate and modelled slip rates only agree with those required for plate boundary deformation in metre-thick siliciclastic quartz under the highest stress estimate from the shear zone. Slip rates in mm-thick calcite-dominated domains are below those required for plate boundary-rate slip.

- At near-lithostatic pore fluid pressures ($\lambda = 0.95$), frictional slip distributed throughout matrix-forming chlorite and vein-bound calcite causes modelled slip rates to exceed 1 m s^{-1}.

- For stress constraints from the subduction complex and velocity constraints from modern margins to agree, sub-lithostatic pore fluid pressures or strain-rate dependent deforming thicknesses are required. Modelling of variable deformation mechanisms at depth shows heterogeneous material within a plate interface shear zone likely undergo differential weakening at elevated P_f, suggesting variable slip partitioning with the presence of fluids.

- Slip transients such as slow slip events require instabilities to develop during slow velocity creep. Compositional or textural constraints observed within shear zones on Llanddwyn Island indicate these instabilities may develop by local P_f variations induced by pore compaction during creep. Foliation-parallel quartz-calcite-chlorite veins cross-cutting similar but earlier deformed veins within the illitic mélange are consistent with pressure drops caused by repeated instability-driven slip transients at elevated P_f.

Chapter 7

Subduction zone deformation of carbonates at seismogenic depths

Aseismic slip in subduction zones is common at temperatures < 350 °C (Bürgmann, 2018; Wallace, 2020a), even though this is colder than both the frictional-viscous transition in calcite and the base of the subduction thrust seismogenic zone in many conceptual models (Hyndman and Wang, 1993; Scholz, 1998; Sibson, 1986). The role of silicates has frequently been considered in relation to frictional-viscous and intracrystalline creep on the subduction thrust (Fagereng and Den Hartog, 2017; French and Condit, 2019), but carbonates are also an important component of lithological inputs at many subduction zones (Plank and Manning, 2019). Carbonate deformation defines a different rheology to silicates with a frictional-viscous transition occurring at a different, poorly defined, temperature (100-300°C Bauer *et al.*, 2018; Chen *et al.*, 2020; Fredrich *et al.*, 1989; Kim *et al.*, 2018). To determine how aseismic deformation of carbonates could occur at strain rates relevant to actively-deforming zones ($> 10^{-14}$ s^{-1} Fagereng and Biggs, 2019) around the frictional-viscous transition, I investigated microstructures in carbonates deformed during ancient subduction at temperatures of 260±10 °C from the Gwna Complex (Chapter 6). This chapter is primarily concerned with linking microscale textures and interpreted slip mechanisms to the evolution of volumes viscously deforming at or near the plate interface during subduction.

7.1 Carbonates in subduction zones

Carbonates are subducted at all margins, although the mass of carbonate in the down-going plates varies greatly (Plank and Manning, 2019). The majority of carbonate enters subduction zones as sediments, though these have the greatest thicknesses at low latitudes and are commonly irregularly distributed along single margins (Fig. 7.1a). Carbonates present within veins throughout volcanic basement are a volumetrically less important, but more spatially uniform, source of carbonates to subduction zones (Plank and Manning, 2019). Though other carbonate minerals with distinct rheologies do occur in the inputs to subduction zones, calcite volumetrically dominates (Plank and Manning, 2019; Underwood, 2007). To investigate calcite rheology spanning the frictional-viscous transition, I consider calcite deformation up to temperatures equivalent to those found at the mantle wedge corner ($\approx$ 500 °C). Calcite deformation at temperatures above this occurs at relatively high strain rates ($> 1 \times 10^{-10}$ s^{-1}) by dislocation and diffusion creep (Fig 7.1d; Herwegh *et al.*, 2003; Renner *et al.*, 2002), and can therefore be considered purely viscous. At micrometre to millimetre grain sizes and long-term geological strain rates (10^{-14}-10^{-10} s^{-1}; Fagereng and Biggs, 2019) calcite typically deforms viscously at both low (<150 °C) and high (>350 °C) temperatures, by fluid-assisted dissolution-precipitation creep (pressure solution) and solid-state diffusion (Coble and/or Nebarro-Herring) or dislocation creep, respectively (Herwegh *et al.*, 2003; Renner *et al.*, 2002; Rutter, 1976). Between these temperatures some combination of frictional deformation and the aforementioned viscous deformation mechanisms likely occurs, but is not well understood. Classically, the seismogenic portion of a subduction zone also lies between these temperatures (Oleskevich *et al.*, 1999). To understand deformation of carbonates in the seismogenic zone it is important to understand their path from their origin as sediments or veins to their possible arrangements within the plate interface shear zone. I briefly review carbonate deformation at temperatures from the seafloor to the mantle wedge corner, and use samples from the Gwna Complex subduction mélange (Anglesey, Wales, UK, Chapter 6) to analyse calcite microstructures resulting from deformation to shear strains $\sim$ 5

by dislocation and grain size-sensitive creep at $\sim$ 260 °C. These examples of creep-dominated microstructures are significantly affected by grain-scale heterogeneities such as local chemical variations or secondary phase composition and distribution. Two small scale shear zones are described in detail, both are localised within calcite veins formed during earlier brittle deformation.

7.2 Laboratory constraints on carbonate deformation

7.2.1 Diffusion/pressure solution

Calcareous sediments deform by pressure solution and cataclasis under uniaxial compaction prior to, and during, subduction (Chapter 3) and during shear on the plate interface (Fagereng and Den Hartog, 2017; Kawabata *et al.*, 2007; Rowe *et al.*, 2011; Schwarz and Stöckhert, 1996). Bos *et al.* (2000) showed that pressure solution during constant volume shear deformation of gouge primarily accommodates compaction to allow grain boundary sliding (GBS, *sensu.* Paterson, 1995). In pure calcite aggregates with negligible porosity (such as those expected within carbonate veins, Fig. 7.1b), equations for pure pressure solution creep closely resemble those for solid state grain boundary diffusion (i.e. Coble) creep (Bos *et al.*, 2000; Poirier, 1985; Raj, 1982). This creep requires shear stresses far beyond the frictional strength of calcite at low temperatures ($<$ 150°C), so simple shear deformation of calcite at shallow depths occurs by some locally-variable combination of frictional sliding and pressure solution (Bos *et al.*, 2000; Bos and Spiers, 2001). Pressure solution is limited by either: (1) the rate of dissolution at the source, (2) the rate of solute diffusion between source and sink, or (3) the rate of precipitation at the sink (Rutter, 1976). In the case of calcite, pressure solution has been shown to be diffusion-limited at low strains, becoming precipitation-limited at high strains as precipitation is slowed by increased pore fluid impurity content (Zhang *et al.*, 2010). In the case of diffusion-limited pressure solution with no fluid advection, strain rate is controlled by (1) diffusion pathway width, (2) diffusivity, (3) solubility, and (4)

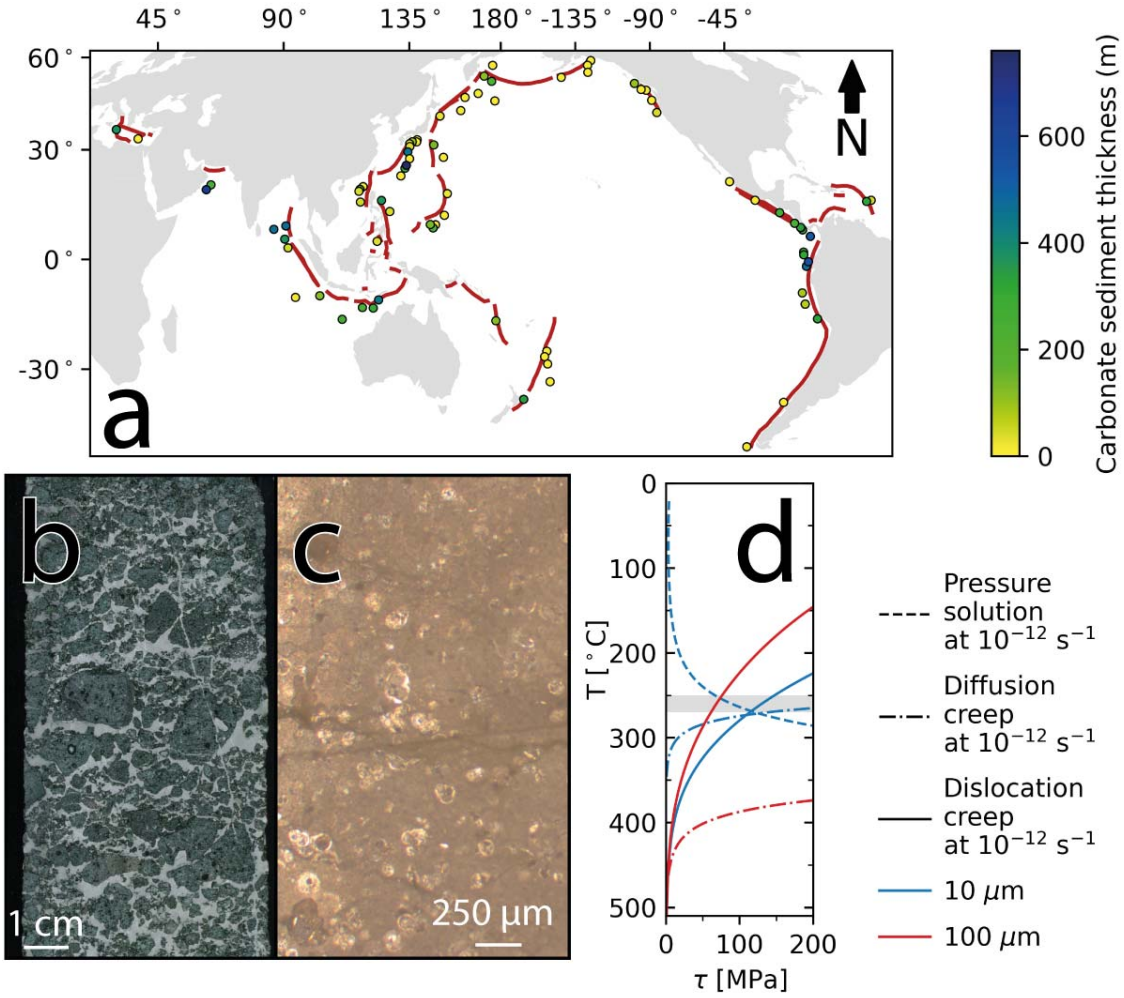

Figure 7.1: Summary of carbonates in subduction zones. Map (a) shows carbonate sediment thicknesses sampled by DSDP, ODP, or IODP expeditions seaward of subduction zone trenches (dark red). Images show the nature of calcite in volcanics (white veins in b) and calcareous sediments (throughout c) from IODP Expedition 375 Site U1520. Plot (d) shows shear stress (τ) at which pressure solution (Bos, 2002), diffusion creep (Herwegh *et al.*, 2003), and dislocation creep (Renner *et al.*, 2002) deform aggregates of 10 and 200 μm size grains of calcite at 10^{-12} s^{-1}. Note that shear stresses for pressure solution of 100 μm size grains are $>$ 200 MPa, so are not plotted here.

diffusive distance (Zhang *et al.*, 2010). Diffusive pathway width is not thought to change with increased temperature, though evolves with strain (van den Ende *et al.*, 2019), and increases by an order of magnitude when calcite grains are adjacent to

phyllosilicate grains (Aharonov and Katsman, 2009; Gratier *et al.*, 2015; Macente *et al.*, 2018). Whereas diffusivity increases with increasing temperature (Nakashima, 1995), calcite solubility decreases by larger magnitudes over the temperature intervals considered here (0-350 °C Plummer and Busenberg, 1982). Reducing solubility means pressure solution (at constant diffusive distance and stress) becomes less efficient with increased temperature until dissolution and strain rates are below those relevant to deforming zones at 200-300°C ($< 1 \times 10^{-16}$ s^{-1}; Fig 7.1d). Pressure solution is highly sensitive to the diffusive distance (usually assumed to be on the order of grain size; Gratier *et al.*, 2013); diffusion-limited strain rates are inversely proportional to grain size to the power of 3 (Fig. 7.1d; Bos, 2002; Zhang *et al.*, 2010).

Similar to pressure solution, solid state diffusion creep is also highly sensitive to grain size. Herwegh *et al.* (2003) performed triaxial creep tests on synthetic marbles with varying amounts of dissolved magnesium at 700-850 °C and determined a grain size exponent of 3.26 in the resulting fitted flow law, consistent with Coble creep (Coble, 1963). Similar creep tests on pure calcite aggregates at 400-700 °C by Walker *et al.* (1990) showed that grain size sensitive deformation occurred by two distinct stress-related regimes; intracrystalline plasticity was thought to operate at high stresses, but deformation at low stresses ($\sigma < 25$ MPa) occurred by GBS accommodated by dislocation activity and intragranular solid-state volume diffusion. The low-stress flow law of Walker *et al.* (1990) is similar to that determined for calcite superplasticity by Schmid *et al.* (1977), though neither Coble nor Nebarro-Herring creep could be ascribed to deformation there. Superplastic behaviour (i.e. deformation to large strain without localisation or fracture, Ashby and Verrall, 1973; Karato, 2008) has been reported for GBS in limestones during both steady creep (Casey *et al.*, 1998; Kushnir *et al.*, 2015; Rutter *et al.*, 1994; Schmid *et al.*, 1977) and seismogenic slip in nanometric grains (De Paola *et al.*, 2015; Verberne *et al.*, 2014). The exact mechanism of grain size sensitive slip by solid-state diffusion therefore remains elusive, but grain boundary diffusion has lower activation energies than volume diffusion at crustal temperature ranges (Herwegh *et al.*, 2003; Schmid *et al.*, 1977) so is considered more probable here.

7.2.2 Frictional-viscous flow and microphysical models

Experiments on granular gouge at various conditions and slip velocities over the last $\sim$ 20 years have lead to development of the Chen-Niemeijer-Spiers (CNS) microphysical model (Chen and Niemeijer, 2017; Chen *et al.*, 2017, 2021; Chen and Spiers, 2016; Den Hartog and Spiers, 2014; Niemeijer and Spiers, 2007; van den Ende *et al.*, 2018). The CNS model is based on the interplay between rate-insensitive frictional GBS and rate-sensitive pressure solution, and incorporates comminution to reduce grain sizes and shear heating to thermally activate plastic grain-scale deformation mechanisms at elevated slip velocities (Chen *et al.*, 2021). The model is appropriate for the frictional behaviour of spherically-grained calcite gouge at temperatures below the onset of significant crystal plasticity and under nominally dry conditions (Chen *et al.*, 2021). Several regimes are outlined by the model at various velocities; low velocity solution-dominated viscous creep, higher-velocity dilatant granular flow and, finally, dynamically-weak plastic flow at seismic slip rates enabled by frictional heating (Chen *et al.*, 2021). Modelled frictional behaviours are consistent with experimental tests on carbonate gouge and those described by rate-and-state friction (Chen and Niemeijer, 2017; Chen *et al.*, 2017; Chen and Spiers, 2016).

When applied to shallow carbonate-bearing faults (such as those in the Apennines, Italy) the model predicts marked transient velocity-strengthening immediately prior to dynamic weakening and resultant seismic slip, likely to delay or inhibit that dynamic weakening (Chen *et al.*, 2021). The predicted transient strengthening becomes less effective at higher normal stresses (i.e. greater depths; Chen *et al.*, 2021), suggesting dynamic rupture propagation would be more likely. Transient strengthening at low sliding velocities is predicted to be very effective, requiring very large displacements at elevated slip rate to activate dynamic weakening and resultant seismic clip (Chen *et al.*, 2021). This prediction suggests carbonate aggregates sliding at low velocities are unlikely to suddenly dynamically weaken and host seismic slip, and larger afterslip displacements may be observed instead. This may be analogous to velocity-dependent rate-and-state friction parameters ($a - b$ and D_c) hypothesised to cause slow slip events by reducing peak slip velocities (Im *et al.*, 2020). The idealised granular calcite gouge assumed in the CNS model is likely similar

to nearly-pure chalks found seaward of several subduction zones (see Table C.1). The model may therefore be of use to understand deformation within geometrically-constrained units at temperatures < 150 °C, but as it describes deformation under dry conditions its applicability to fluid-saturated subduction interface shear zones is limited.

7.2.3 Dislocation creep

Natural intracrystalline deformation of calcite by dislocation creep has been reported at temperatures below 150 °C (Bauer *et al.*, 2018), but is more common at temperatures > 300 °C (Bestmann and Prior, 2003; Ratschbacher *et al.*, 1991; Schmid *et al.*, 1981). Single crystal deformation in calcite is recognised to occur by several slip systems. Expressed as $\{plane\} < direction >$, the most important slip systems in increasing order of temperature are e^+ $\{\bar{1}018\} < 40\bar{4}1 >$, $r^\pm$ $\{10\bar{1}4\} < \bar{2}021 >$, f^- $\{\bar{1}012\} < 2\bar{2}01 >$, $f^\pm$ $\{\bar{1}012\} < 10\bar{1}1 >$, and basal $c < a >$ (De Bresser and Spiers, 1997; Griggs *et al.*, 1960; Pieri *et al.*, 2001; Turner *et al.*, 1954; Weiss and Turner, 2013). These slip systems can be subdivided into those active at lower temperatures (the e^+, $r^\pm$, and f^- systems) and those thought to be more important at higher temperatures (c and $f^\pm$; De Bresser and Spiers, 1997; Pieri *et al.*, 2001; Turner *et al.*, 1954). For laboratory strain rates on the order of 10^{-5} s^{-1} this transition is around 400 °C, but how well this extrapolates to natural conditions has been the subject of debate (De Bresser *et al.*, 2002; Renner and Evans, 2002).

The strength of calcite undergoing dislocation creep has been well characterised at a range of stresses and temperatures, and is inversely related to grain size (Renner *et al.*, 2002). This phenomenon is commonly recognised in deformed metals as the Hall-Petch relationship (Hall, 1951), and is thought to be due to dislocation pile-up at grain boundaries due to recovery rates too low to relieve internal stresses (Li and Chou, 1970). Because of this, there is no truly grain size-insensitive viscous creep mechanism of calcite and classic power-law equations are not appropriate to fit experimental data (Renner and Evans, 2002). Renner *et al.* (2002) accounted for this using a grain size-dependent Pierls stress term, resulting in a similar flow law to that derived by De Bresser (2002) for pressure-sensitive cross-slip controlled

by dislocation dissociation. Both models accurately predict calcite experimental strain rates at high temperature and coarse grain sizes. Their application to natural deformation of calcite in subduction zones will be explored in Section 7.3.3.

7.2.4 Cataclasis

Initiating frictional sliding in carbonates requires high stresses or pore fluid pressures due to its relatively high coefficient of friction (Verberne *et al.*, 2015), whereas viscous creep occurs at variable rates over a greater range of stresses. At temperatures > 75 °C this frictional slip is velocity weakening in carbonates (Verberne *et al.*, 2015) and may reach fast slip rates. High slip rates in discrete slip zones are often associated with localised grain size reduction by cataclasis (Sammis *et al.*, 1987). Grain size reduction by comminution is thought to be slip rate-dependent, with finer grains forming at higher slip rates (Sammis and Ben-Zion, 2008). When the resulting grains are very fine ($\ll 1$ μm), shear heating can activate grain-size sensitive slip at rates approaching seismic (~ 1 m s^{-1}; De Paola *et al.*, 2015; Demurtas *et al.*, 2019; Smith *et al.*, 2015), though this can lead to rapid grain growth and fault 'healing' during post-seismic slip (Pozzi *et al.*, 2018). At temperatures > 600 °C, calcite decomposition can result in the formation of nanometric calcia (CaO) grains (Singh *et al.*, 2002). Han *et al.* (2010) showed that seismic slip rates in dry calcite marble resulted in localised flash heating within the slip zone to temperatures 600-830 °C, forming a decomposition layer of high-porosity nanometric CaO grains and releasing CO2 during slip. Nanoparticles can lubricate fault slip surfaces and maintain very low frictional coefficients (≥ 0.1) at seismic slip rates (Han *et al.*, 2011), suggesting shear heating during seismic slip may provide a strong weakening mechanism. $MgCO_3$ has an even lower dissociation temperature (~ 200 °C lower; L'Vov, 2002), meaning coseismic decomposition from shear heating may be more effective in dolomites. During decomposition, fluids in the slip zone are likely to undergo rapid changes in chemistry which could cause mineral precipitation or enhanced dissolution and grain rounding (Rowe *et al.*, 2012). At lower slip rates comminution can still reduce grain sizes towards a lower 'grinding limit', below which grains will tend to deform plastically (~ 1 μm, Sammis and Ben-Zion, 2008). Cataclasis can there-

fore reduce grain sizes dramatically where frictional sliding within discrete volumes occurs, strongly affecting the strength of faults and the resulting microstructure.

7.2.5 Depth/temperature dependence of governing mechanisms

Similar to other minerals, experimental calcite deformation has shown that, although several mechanisms may be operating simultaneously, the dominant creep form varies with stress, grain size, and temperature. At low temperatures ($<$ 150 °C), high stresses lead to cataclasis and frictional sliding, whereas at low stresses pressure solution in calcite dominates (Rutter, 1976; Zhang *et al.*, 2010). Frictional sliding can result in cataclasis and reduced grain size, decreasing the diffusive distance and increasing the efficiency of pressure solution (see Chapter 3).

With increasing temperature, calcite deforms by viscous mechanisms at decreasing stresses until, at temperatures $>$ 350 °C, both grain size sensitive and intracrystalline creep occur at strain rates of 10^{-12} s^{-1} under a few $\sim$ 10 MPa differential stress (Fig. 7.1d; Herwegh *et al.*, 2003; Renner *et al.*, 2002; Rutter, 1974; Schmid *et al.*, 1987; Walker *et al.*, 1990). Experiments have show a progressive increase in the strain rates of calcite deformed at constant experimental temperatures with increasing differential stress (Renner and Evans, 2002). This was defined into three regimes by Schmid *et al.* (1977): (1) a high stress regime where stress-strain rate relations follow an exponential law, also thought to dominate experiments performed at $<$ 400 °C (Rutter, 1974), (2) an intermediate stress regime where a high stress exponent (4-5) power law describes stress-strain rate relations, sometimes altered to account for Hall-Petch behaviour (Renner *et al.*, 2002), (3) a low stress regime where stress-strain rate relations can be fit by a power law with a much lower stress exponent consistent with grain size-sensitive creep (1-2, Herwegh *et al.*, 2003; Walker *et al.*, 1990) and superplastic flow has been reported (Schmid *et al.*, 1977). Regimes 1-3 are therefore also controlled by grain size. Calcite deforming at $T >$ 350 °C is dominated by dislocation creep at high stresses and large grain sizes (Renner *et al.*, 2002), giving way to grain-size sensitive creep at lower stresses and smaller

grain sizes (Herwegh *et al.*, 2003; Walker *et al.*, 1990). The interaction between these mechanisms is complex and influenced by local variations in the deforming aggregate.

Deformation between the low temperature pressure-solution and high temperature intracrystalline deformation regimes ($150 < T < 350$ °C) is commonly attributed to an interplay of mechanisms. Dislocation creep has been observed to have occurred due to stress concentrations at the boundaries of pinched microlithons deformed at temperatures below 150 °C, leading to the expectation that low temperature crystal plasticity may occur only locally (Bauer *et al.*, 2018). A more commonly-described process is recrystallisation resulting in grain-size reduction and rheological weakening (Bestmann and Prior, 2003; De Bresser *et al.*, 2001). This weakening is thought to compete against grain growth by dislocation creep to cause grain size and strain rate to converge around the boundary between dislocation and diffusion creep, an idea called the field boundary hypothesis (De Bresser *et al.*, 2001; Etheridge and Wilkie, 1979). This hypothesis requires both dislocation and diffusion creep to be active. Temperatures high enough to activate dislocation and diffusion creep ($\sim$ 200 °C, Fig 7.1a) are likely at $\geq$ 15 km depth along subduction plate boundary interfaces (Syracuse *et al.*, 2010). Time-averaged normal stresses in shear zones at these depths are likely too high for frictional shear deformation of carbonates to continuously occur. Episodic elevated fluid pressure pulses may cause brief but repeated episodes of brittle failure and cataclasis, reducing grain size (Sammis and Ben-Zion, 2008) and activating grain size-sensitive mechanisms during rapid slip (De Paola *et al.*, 2015; Demurtas *et al.*, 2019). Long-term calcite rheology within this transitional temperature range is likely a combination of these rapid slip episodes during slower creep mechanisms by one or more mechanisms.

7.3 Examples of carbonate deformation in the frictional-viscous transition temperature range

As described in Chapter 6, imbricated shear zones with mélange textures make up much of Llanddwyn Island (Fig. 5.3). Carbonate-rich block-in-matrix textures

are relatively rare on Llanddwyn Island when compared to the volume of massive carbonates. Carbonate deformation is also relevant to volcaniclastic rocks, where calcite veins are deformed to high shear strains. To discuss the deformation of calcite within the frictional-viscous transition, two examples of localised shear deformation from contrasting lithologies will now be considered. The selected samples were chosen to be representative of processes observed in carbonates within the shear zone, though natural variability is clearly expected in deforming volumes with complex compositions and geometries. The focus in this work is on the general application of processes interpreted from each sample, rather than the specific sample itself. Both examples were deformed at temperatures of 260±10 °C (Fig. 6.7), below those traditionally considered relevant for geological deformation by viscous mechanisms at strain rates relevant to shear zones (10^{-14}-10^{-10} s^{-1} Fagereng and Biggs, 2019). The first example is a shear zone in a clast; this clast is a carbonate block in a phyllosilicate matrix, representative of calcareous sediments likely to be subducted at many margins (Fig. 7.1a & c). The second is a shear zone localised in a calcite vein within volcaniclastic hyaloclastites, representative of carbonate veins in subducting volcanics (Fig. 7.1a & b). For simplicity these two example will be referred to as the clast shear zone and volcaniclastic shear zone, respectively.

Both samples were investigated using optical microscopy, secondary electron (SE), backscattered electron (BSE), energy dispersive spectroscopy (EDS), and electron backscatter diffraction (EBSD). SE, BSE, EDS, and EBSD mapping was carried out at the School of Earth and Environmental Sciences at Cardiff University with a Zeiss Sigma HD Field Emission Gun Analytical scanning electron microscope (SEM) fitted with two Oxford Instruments 150 mm^2 energy dispersive X-ray spectrometers and a Nordlys EBSD system with Oxford Instruments Aztec software. EDS mapping was carried out at 15 or 20 keV accelerating voltage, a beam current of 4.3 nA, an aperture of 120 μm, a working distance of 8.9 mm, and stepsizes of 1 μm in the carbonate clast and 2 μm in the volcaniclastic shear zone. EBSD was carried out on thin sections polished with colloidal silica and tilted at 70° to the electron beam at a stepsize of 1 μm in the clast shear zone and 0.7 μm in the volcaniclastic shear zone, a working distance of 13 μm, an accelerating voltage of 20 keV, a beam current of

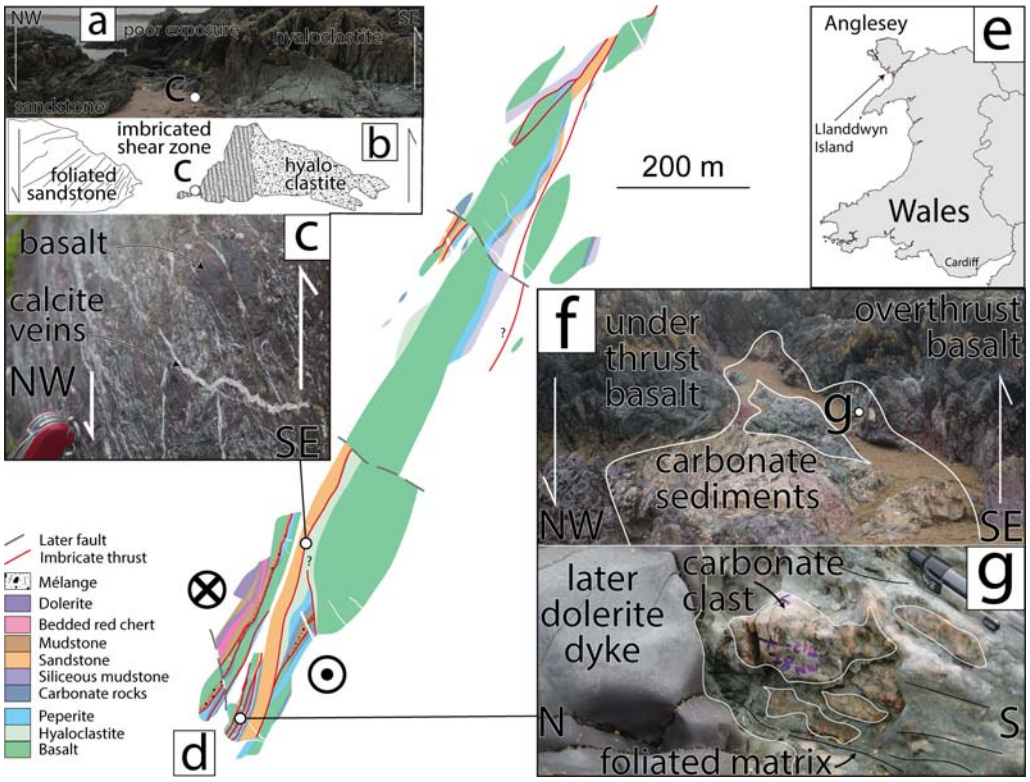

Figure 7.2: Map of Llanddwyn Island and outcrop-scale images with sketches of sampling locations used in the study of calcite deformation in this chapter. For further information on the imbricated shear zones see Chapter 6. Panels show (a) outcrop-scale image of the imbricated shear zone where the volcaniclastic shear zone was sampled, (b) a simple sketch of (a), (c) a sample-scale image of the sampled lithology. Map (d) shows imbricated thrust shear zones and lithological distribution, map (e) shows location of the study area Llanddwyn Island on Anglesey, Wales. Panel (f) shows outcrop-scale photo of shear zone where clast shear zone was sampled, (g) shows hand-scale photo of the sampled carbonate clast in a foliated matrix.

8.5 nA, and the same 120 μm aperture. Raw EBSD backscatter patterns were processed using Oxford Instruments Aztec software with a gain of 5 and 2x2 binning. EBSD data were then processed using the MTEX toolbox for Matlab (Bachmann *et al.*, 2010). Phyllosilicate grains were isolated in ImageJ (Schindelin *et al.*, 2012; Schneider *et al.*, 2012) using Mg kα EDS map data exported from Oxford Instruments Aztec software. The data were cropped to the vein area and a threshold was applied using the algorithm of Li and Tam (1998) and Li and Lee (1993), resulting

in a minimum value of 132 (from a range of 0-1778 counts). Grain shapes, areas, and best fit ellipse dimensions and orientations were then exported from ImageJ to Matlab. Grain size was calculated as the diameter of a circle (d) with the equivalent area to the grain, $d = 2 \times \sqrt{\frac{Area}{\pi}}$.

7.3.1 Deformation microstructures in the clast shear zone

On the SW end of Llanddwyn Island a series of closely-spaced imbricate shear zones encompass several repeated units of massive carbonates, pillow basalt, and hyaloclastites (Fig. 7.2). Within one of these imbricates a block-in-matrix texture comprises lenses of massive carbonate in a chlorite matrix. Carbonate lenses are up to 30 cm long and 20 cm wide and are elongate parallel to the sub-vertical bulk shear direction. A dolerite dyke associated with later NW-SE oriented extension and strike-slip deformation (Kirton and Donato, 1985) cuts across this unit immediately adjacent to the sampling locality. As the dyke is undeformed (Fig. 7.2g), it is not considered part of the Gwna subduction complex at Llanddwyn Island. There is no evidence of deformation associated with dyke emplacement, and the shear sense of deformation microstructures in the sample is consistent with the bulk sense within the shear zone, so it is therefore not discussed further here.

In thin section, a sample from a lenticular clast of massive carbonate shows it dominantly comprises calcite with a mottled greyish appearance and high relief (Fig. 7.3a). The shear zone considered here dips to the SE and is partially localised within a low relief calcite vein. The shear zone continues up-dip from the deformed vein, where it hosts en-echelon extensional fractures, < 50 μm chlorite grains, < 5 μm clays, and another, smaller calcite vein 20-30 μm thick. A NW-dipping calcite vein is offset by ~ 400 μm with a reverse sense across a 90 ± 10 μm wide shear zone, consistent with a shear strain of 4 to 5 (Fig. 7.3a).

Where the shear zone has localised in the offset vein, grains form distinct areas of fine equant and elongate grains (Fig. 7.3d). $30 - 300$ μm calcite grains with aspect ratios < 8 are elongate parallel to the apparent slip vector between continuous horizons of fine calcite grains (< 20 μm, Fig. 7.3d). The orientations and shapes of some elongate grains match across horizons of finer grains, suggesting they were

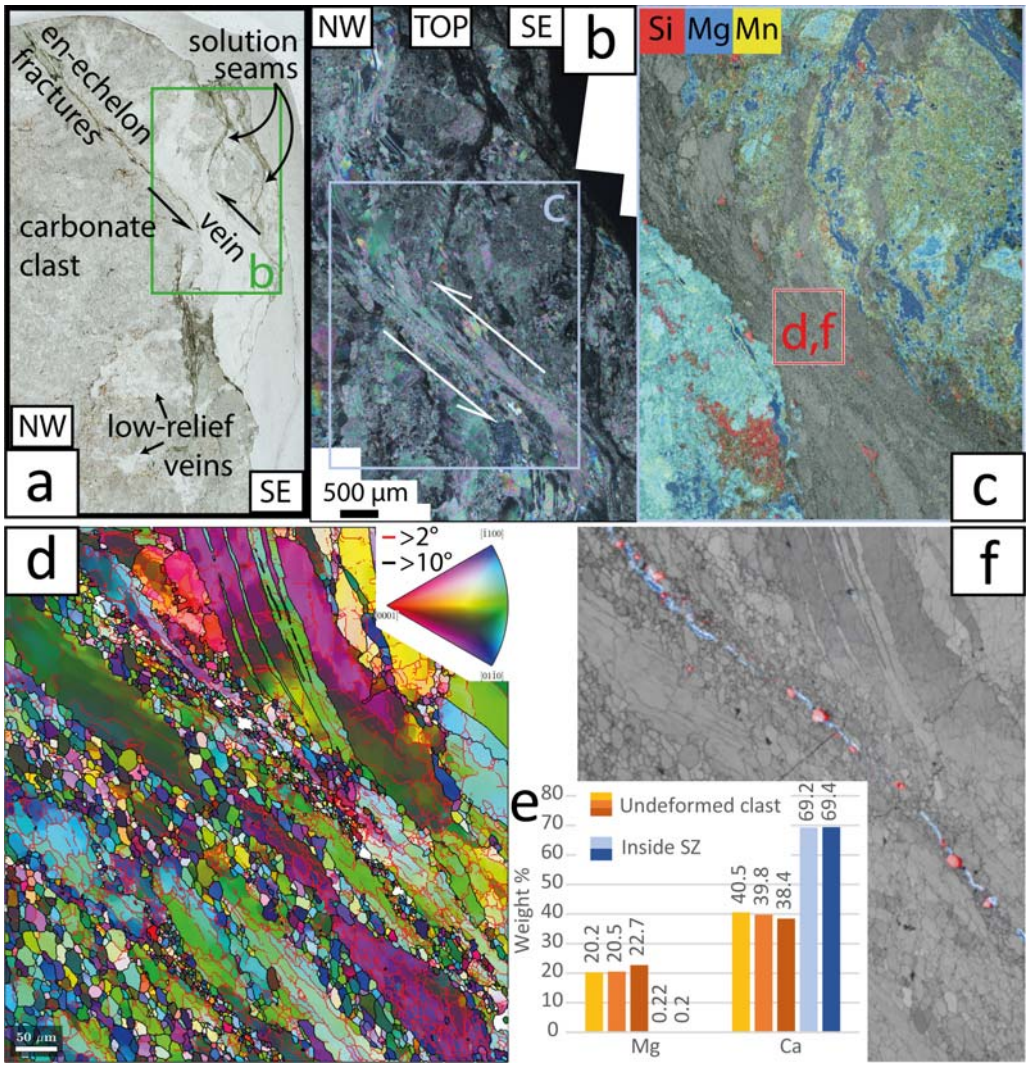

Figure 7.3: Microstructures in the clast shear zone. All panels show a vertical plane striking NW-SE (left-right) perpendicular to the strike of the shear zone. Panels show (a) annotated plane-polarised image of structures near the margin of the clast, location of (b) shown by green rectangle, (b) cross-polarised image of the calcite shear zone, blue rectangle indicates location of panel (c). Panel (c) shows the distribution of Mg, Mn, and Si in and around the shear zone, note the lack of impurities in the shear zone itself, (d) shows EBSD map coloured by pixel orientation aligned with slip vector, key in top right indicates colouring, (e) shows EDS data for Mg and Si which highlight yellow chorite and blue quartz strung out along the shear zone in a fine-grained band. Bar chart (f) shows the relative concentrations of Mg and Ca in calcite inside and outside the shear zone.

offset by deformation there (Fig. 7.3d). Finer grains are most commonly 5-15 μm in size, equant, and have relatively straight grain boundaries with common triple junctions. Subgrains of similar size and shape are common within larger elongate grains (Fig. 7.3d). In the upper third of the shear zone, grain sizes are much smaller where a series of quartz and chlorite grains form a through-going horizon (Fig. 7.3e). EDS maps show high-relief mottled calcite in the rest of the clast contains around 20 wt% magnesium, whereas calcite inside the shear zone has little to no magnesium (Fig. 7.3c).

EBSD mapping shows considerable scatter in average grain orientations outside the shear zone. A few grains align the slip directions of known slip systems (f, r, and c) in calcite with the shear zone slip vector (De Bresser and Spiers, 1997) but most do not (Fig. 7.4a). Towards the margins of the shear zone, orientations within several grains progressively rotate to align basal c slip in the $< a >$ direction with the slip vector (Fig. 7.4b-e). Within the shear zone basal c slip in the $< a >$ direction is most commonly aligned with the slip vector, followed by orientations consistent with e^+ slip in the $< 40\bar{4}1 >$ direction. Orientations consistent with slip on the f and r systems within the shear zone are rare (Fig. 7.4a).

7.3.2 Deformation microstructures in the volcaniclastic shear zone

A shear zone on the north side of Llanddwyn Island separates a volcaniclastic hanging wall to the SE from a siliciclastic footwall to the NW (Fig. 7.2). The volcaniclastic hanging wall contains steeply SE-dipping foliation-parallel shear zones localised in veins containing fine-grained recrystallised calcite (Fig. 7.5a, b, & e-g). These vein-localised shear zones cross-cut the chlorite-rich matrix and offset altered basalt clasts with a reverse shear sense (SE-up; Fig. 7.5a-c). Non-recrystallised calcite is also present within and between altered basalt clasts outside of shear zones in the sample (Fig. 7.5f). Altered basalt within the volcaniclastics dominantly comprises albite and fine-grained clays in lenticular laths, surrounded by a foliated Mg-rich chlorite matrix (Fig. 7.5a-c). Fine grains (<20 μm) of albite, clay, and chlorite are

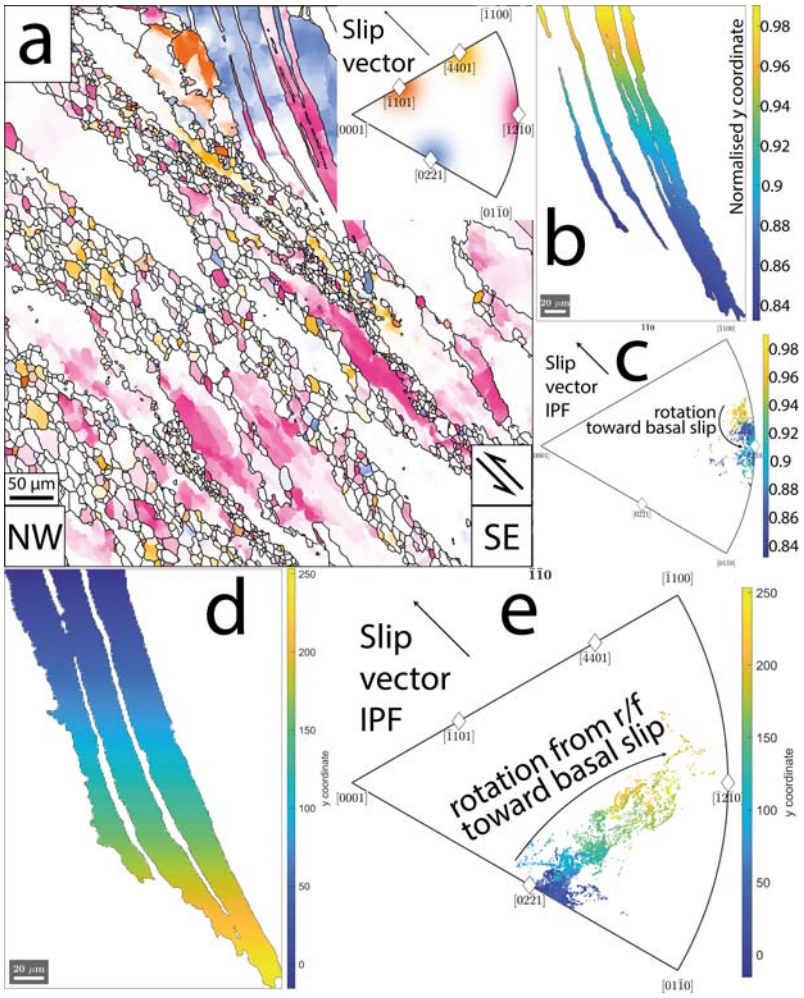

Figure 7.4: Crystallographic orientations and slip system alignment in grains within and adjacent to the clast shear zone. Panel (a) shows a vertical plane striking NW-SE (left-right) perpendicular to the strike of the shear zone. EBSD map (a) is coloured by slip vector alignment with slip system, key and major slip systems are shown in upper right. The remaining panels (b-e) are coloured by xy coordinate, panel (b) and (d) show the grain geometries and panels (c) and (e) show pixel orientations on the corresponding inverse pole figures.

smeared along horizons between offset altered basalt clasts bordering the fine-grained calcite shear zones. Clear shear-offset of clasts across shear zones with continuous marker horizons between them show they have been deformed to shear strains of ≥ 5 (Fig. 7.5c-e). Aside from the albite, clay, and chlorite inclusions, shear zones are comprised of fine-grained recrystallised calcite (<20 μm) with minor quartz.

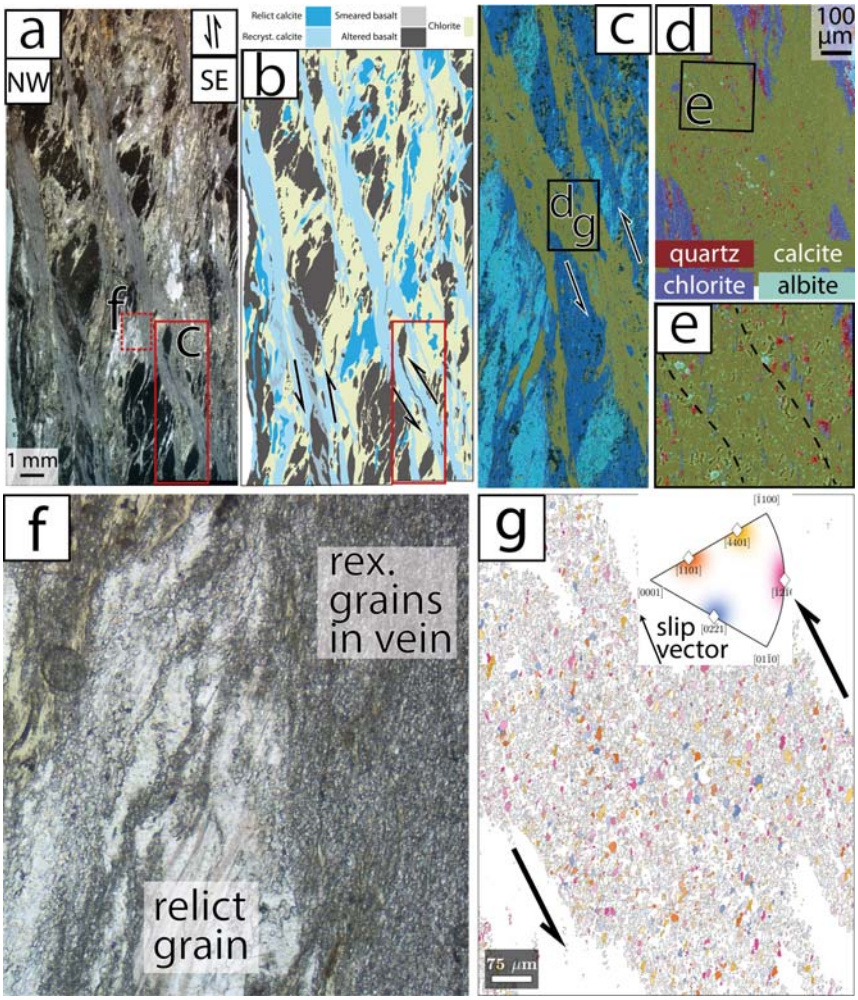

Figure 7.5: Microstructural summary of the volcaniclastic shear zone. All panels show a vertical plane striking NW-SE (left-right) perpendicular to the strike of the shear zone. Panels show (a) plane polarised image of foliation-parallel calcite veins throughout the hyaloclastite, (b) summary sketch of (a), (c) EDS map showing the distribution of Na, Mg, and Ca, (d) detailed EDS map showing chemistries consistent with quartz, chlorite, and albite grains within the calcite vein, (e) grain-scale EDS map showing a nearly pure calcite lath bounded by fine-grained quartz, chlorite, and albite inclusions in horizons (dashed lines), (f) plane polarised image (location shown in (a)) showing fine recrystallised grains in the vein adjacent to coarse relict grains outside of through-going volume, (g) EBSD orientation map (location approx. that of (d)) coloured by parallelism between the slip vector and known slip systems (see key in lower left).

Within the shear zone, recrystallised calcite varies in shape and orientation depending on its proximity to horizons of albite and chlorite inclusions (Fig. 7.6a-c); calcite bordering albite and chlorite is more commonly fine-grained (<20 μm) and has aspect ratios < 2.5 (Fig. 7.6a-d) whereas calcite grains between these horizons are coarser (long axis > 20 μm) and commonly have aspect ratios up to 6 (Fig. 7.6). The long axes of larger grains dip steeply towards the NW, at a low angle to both the shear zone boundary ($\sim 25^\circ$ clockwise when facing NE, Fig. 7.6d & e), and the bulk chlorite foliation outside the vein (5-15° counter-clockwise when facing NE, Fig. 7.6a-f). Finer grains have a wider distribution of orientations, though the majority also have steeply NW-plunging long axes, subparallel to the coarser grains (Fig. 7.6d & e).

Phyllosilicate grains within the shear zone are chemically and optically consistent with the surrounding chlorite matrix (Fig. 7.5a-f). Fine chlorite grains (< 7 μm) are most common but some large chlorite laths up to $\sim$ 500 μm long are also present (Fig. 7.7a). Chlorite grains < 7 μm generally have aspect ratios ≤ 2. Larger chlorite grains have greater aspect ratios, reaching > 6 where grains are > 10 μm in size (Fig. 7.7b). Fine chlorite grains also have a wider distribution of best-fit ellipse long axis orientations, $\pm 75^\circ$ from the foliation trace orientation (Fig. 7.7c). With increasing grain size the spread of long axis orientations decreases (Fig. 7.7c). Coarse grains (> 20 μm) are almost exclusively sub-vertical, within an arc extending from the bulk foliation to $\leq 30^\circ$ counter-clockwise from the bulk foliation (facing NE, Fig. 7.7c). Coarse chlorite grains with aspect ratios > 2 occur throughout most of the vein and form a continuous foliation consistent with the strain field determined from offset clast fragments (Figs. 7.5a-e & 7.7a). Adjacent to coarse calcite grains, chlorite grains are generally fine ($\leq$ 10 μm) and have low aspect ratios ($\leq$ 2, Fig. 7.7a).

7.3.3 Grain-scale mechanisms of viscous calcite deformation

The microstructures presented here are exposed $\sim$ 500 m apart in imbricated shear zones either side of several lenticular slices of ocean plate stratigraphy totalling approximately 100 m thickness (Fig. 7.2). Both examples show deformation to $\gamma \geq 5$ but microstructures in each sample are consistent with contrasting deforma-

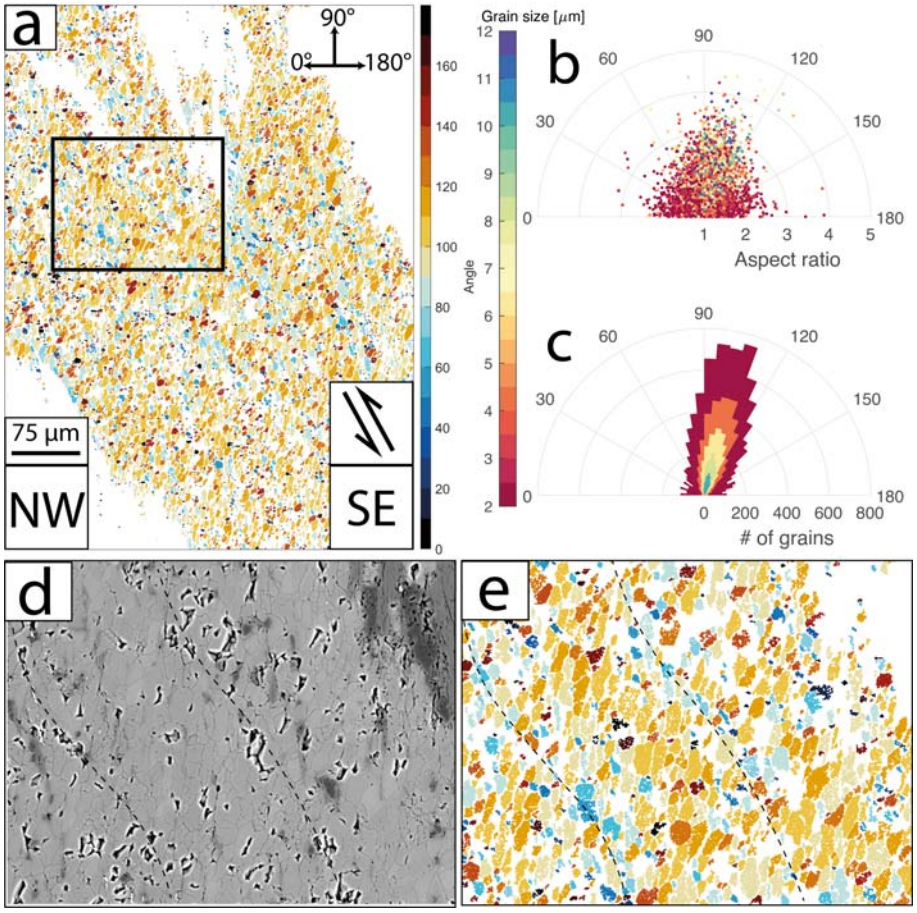

Figure 7.6: Summary of calcite grain shape and orientations in the volcaniclastic shear zone. Panels (a, d, & e) show a vertical plane striking NW-SE (left-right) perpendicular to the strike of the shear zone. Panels show (a) EBSD map showing reconstructed calcite grains coloured by the long axis angle of a best-fit ellipse, location of (d) and (e) shown as black rectangle, (b) ellipse aspect ratio plotted against grain angle and coloured by grain size (see colour bar) for grains (> 2 μm), (c) angular histogram of grain long axis orientations thresholded at incrementally greater grain size (2, 4, 6, 8, & 10 μm), colours of bars correspond to colour bar on left, (d) BSE image showing elongate secondary phases present along horizons (dashed lines), (e) detailed view of (a) showing larger, elongate foliation-parallel grains within the nearly-pure calcite lath and smaller, more equant, grains associated with secondary phases on the margins of the lath.

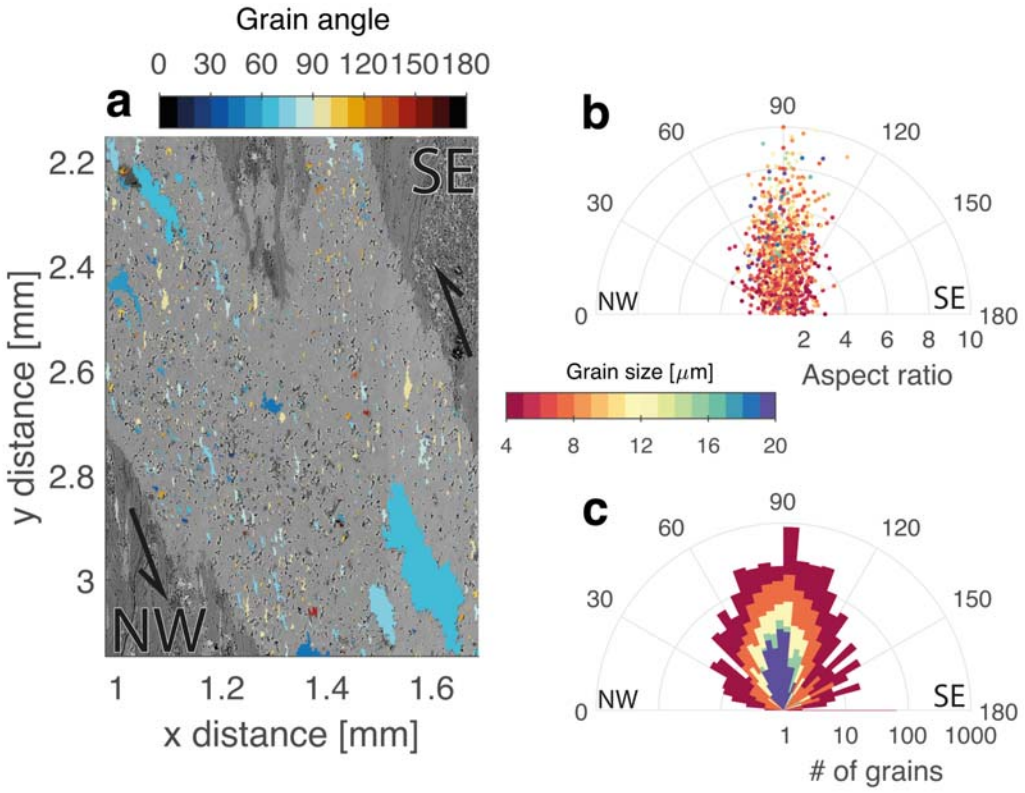

Figure 7.7: Included chlorite grain shapes and orientations in the volcaniclastic shear zone. Panel (a) shows a vertical plane striking NW-SE (left-right) perpendicular to the strike of the shear zone. Panels show (a) reconstructed chlorite grains coloured by best-fit ellipse long axis angle clockwise from horizontal in degrees, map area is same as Fig. 7.6a, (b) ellipse aspect ratio plotted against grain angle and coloured by grain size (see colour bar) for grains (> 4 μm), (c) angular histogram of grain long axis orientations thresholded at incrementally greater grain size (4, 8, 12, 16, & 20 μm), colours of histograms correspond to colour bar.

tion mechanisms. The variety in microstructures shows how variable deformation mechanisms can occur in calcite aggregates due to inherited local heterogeneity.

Both the volcaniclastic shear zone and clast shear zone localised within earlier-formed calcite veins. Both veins formed along surfaces of pre-existing weakness consistent with deformation at shallow depths (a fracture and the chlorite foliation; Figs. 7.3a & 7.5a). Calcite solubility is inversely related to temperature (Plummer and Busenberg, 1982), meaning calcite veins are more likely to form during, or prior

to, subduction at shallow levels where solubility is rapidly reducing with increasing temperature and fractures can form at lower confining pressures (Sibson, 1998). Individual veins containing mixed mineralogies such as calcite and quartz likely form by precipitation after supersaturation driven by a pressure drop (Meneghini and Moore, 2007; Raimbourg *et al.*, 2021), the degree of supersaturation and the concentration of solute sourced from the nearby dissolution of calcite would be controlled by calcite solubility. The exact temperature at which calcite solubility becomes negligible is difficult to estimate, but it is likely that calcite becomes effectively insoluble at elevated temperatures, possibly near the up-dip end of the seismogenic zone around 150 °C (Chapter 3). The inheritance of structures formed during earlier, shallower, deformation is therefore shown by these examples to exhibit a strong control on deformation mechanism and rheology.

Both shear zones show microstructures consistent with simple shear deformation localised within pre-existing veins (Figs. 7.3 & 7.5). Similarly, coarse relict grains in both shear zones contain subgrains with similar size and low internal orientation spread to adjacent recrystallised grains (Figs. 7.3d & 7.5f-g), consistent with subgrain rotation recrystallisation (Rutter, 1995). Whereas elongate relict calcite grains are present within the clast shear zone (Fig. 7.3d), grains within the volcaniclastic shear zone are entirely recrystallised where the calcite vein forms a throughgoing volume (Fig. 7.5a,b, & f). Some coarse relict grains within the clast shear zone match in crystallographic orientation and shape across grain-width strings of recrystallised grains (Fig. 7.3d), resembling twins of an original parent grain. Exclusive recrystallisation of twins suggests there may be an orientation control on recrystallisation. Like the mobility of slip systems in single crystals (De Bresser and Spiers, 1997), this orientation control is likely dependent on crystallographic orientation relative to the applied stress. The distribution of recrystallised grains within partially-recrystallised calcite aggregates may therefore be a function of the parent grain orientation.

Within the clast shear zone, patchy internal orientation variations within coarse relict grains (> 20 μm) suggest they deformed by intracrystalline deformation. Orientations within these grains align the $< a >$ axis with the slip vector (Fig. 7.4),

suggesting intracrystalline slip occurred by basal glide in that direction within the shear zone. This alignment is more common in coarse grains suggesting they deform more easily by this mechanism than fine grains, consistent with the Hall-Petch relationship proposed for dislocation creep of calcite by Renner *et al.* (2002). The rotation of crystallographic orientations at the shear zone margin, within coarse grains marginal to the shear zone towards those consistent with basal glide, shows this deformation is spatially associated with deformation within the shear zone (Fig. 7.4b-e). Similar results were described for intracrystalline deformation of calcite at < 150 °C by Bauer *et al.* (2018), who inferred basal glide with recovery by cross-slip. These data suggest basal glide may not be solely a high temperature mechanism as previously reported (De Bresser and Spiers, 1997), but could also occur to low strains at low temperature.

Dislocation migration is required to form subgrains, recrystallisation by subgrain rotation is consequently limited by the onset of dislocation creep (Rutter, 1995). Within the clast shear zone, dislocation creep appears active within coarser grains (Fig. 7.4a). Deformation is localised within the shear zone, suggesting the Mg-rich chemistry outside the shear zone may limit deformation there (Fig. 7.3c & f). Mg content has been experimentally observed to increase the strength of carbonates undergoing dislocation creep (Xu *et al.*, 2009). The higher Mg content outside the shear zone therefore inhibited dislocation creep, recrystallisation, and consequent rheological weakening and grain size-sensitive creep.

No evidence of intracrystalline deformation is observed in the volcaniclastic shear zone, attested to by the lack of clear alignment of known slip systems with the slip vector (Fig. 7.5g). This could be because fine grains inhibit dislocation creep, via the Hall-Petch relation, and are inhibited from growth by secondary chlorite throughout the vein. Herwegh and Jenni (2001) and Herwegh and Berger (2004) described phyllosilicate-bearing carbonate mylonites from the Doldenhorn nappe, which were deformed at temperatures of 340-400 °C. The calcite matrix there was thought to simultaneously deform by GBS, intracrystalline plasticity and stress-driven solution transfer, forming prismatic grains 18-50 μm long. Rather than simple rotation of pre-existing phyllosilicate grains, Herwegh and Jenni (2001) interpreted the phyl-

losilicate grains to have nucleated by diffusive mass transfer into voids formed by GBS in the calcite aggregate before rotating and growing to become subparallel to foliation. Deformation of the volcaniclastic shear zone presented here likely occurred by a process similar to that described by Herwegh and Jenni (2001) but those aggregates are coarser grained, have a higher average aspect ratio, and have a thicker deformed volume than the volcaniclastic shear zone described here. The higher temperatures associated with deformation of those aggregates would allow increased intracrystalline deformation, possibly leading to grain growth parallel to the slip direction (De Bresser *et al.*, 2001; Herwegh and Jenni, 2001; Renner *et al.*, 2002; Xu *et al.*, 2009). This could explain the larger grain size higher aspect ratios, and foliation-parallel orientations of those aggregates. Diffusive mass transfer is likely to be the dominant mechanism acting on coarser calcite grains within the volcaniclastic shear zone, consistent with lower deformation temperatures and grain growth oblique to the sliding surfaces but normal to the principal stress direction (Fig. 7.6; Rutter, 1976).

Similar to Herwegh and Jenni (2001), chlorite grains in the volcaniclastic shear zone may nucleate into voids formed by GBS (Paterson, 1995). After nucleation, they could rotate and grow by solid solution with solute sourced from solution of chlorite grain boundaries oriented oblique to the principal stress direction (Herwegh and Jenni, 2001; Rutter, 1976). Nucleation and rotation during chlorite grain growth is consistent with larger, higher aspect ratio chlorite grains oriented up to 30° counter-clockwise (when facing NE) from foliation, consistent with vorticity from offset basalt clast fragments (Fig. 7.7). The association of coarser chlorite with finer calcite grains suggests a combination of grain-parallel slip in fine chlorite grains (*sensu.* Okamoto *et al.*, 2019) and GBS of calcite occurred throughout much of the vein. Where coarse calcite grains occur, chlorite grains are smaller, have lower aspect ratios, and a wider spread of orientations (Fig. 7.7). These areas are interpreted to have lower shear strain due to the difficulty of coarse elongate calcite grains sliding past one another (Figs. 7.5g & 7.6a-c).

The distribution of chlorite grains within the vein records intergranular voids opened and filled by precipitation of chlorite during deformation. The growth of

chlorite grains would also require adjacent void space. Elongate chlorite grains therefore likely record more continuous void opening during deformation than less elongate, coincident with higher shear strains from GBS. The size, shape, and distribution of chlorite therefore likely reflects the shear strain distribution within the volcaniclastic shear zone where voids have not been filled with calcite.

The offset of the chlorite matrix across the volcaniclastic shear zone suggests the calcite shear zone deformed faster than the chlorite matrix during the phase of deformation recorded in the microstructures (Fig. 7.5a-c). Deformation of fine-grained aggregates containing interconnected and aligned chlorite are expected to be weaker than pure calcite (Collettini *et al.*, 2009; Okamoto *et al.*, 2019), but the weakness relative to the surrounding chlorite matrix is surprising. Fine-grained polyphase mixtures deforming by grain size sensitive creep have been found to be weaker than interconnected phyllosilicate networks by Stenvall *et al.* (2019), suggesting a similar fabric-driven rheological evolution may be present here.

GBS is more efficient at finer grain sizes so grain size reduction by recrystallisation has often been associated with rheological weakening, though it is likely a competition between grain size reduction and growth by recrystallisation and dislocation creep, respectively (De Bresser *et al.*, 2001). Both shear zones have secondary phases which would pin grain boundaries, inhibiting growth (Figs. 7.3, 7.5, & 7.8). If grain growth is a necessary product of dislocation creep in calcite, as the Hall-Petch relation (Renner *et al.*, 2002) and field-boundary hypothesis (De Bresser *et al.*, 2001) imply, common distributed secondary phases throughout the volcanic-hosted calcite vein may inhibit dislocation creep there, explaining the lack of CPO (Figs. 7.5 & 7.8). Alternatively, the vein may deform by GBS and sliding on aligned chlorite grains at stresses below those required to activate dislocation creep (Figs. 7.7 & 7.8; Herwegh and Jenni, 2001; Okamoto *et al.*, 2019). Either way, deformation and rheology within the volcaniclastic shear zone occurred by mechanisms controlled by secondary included phases.

In contrast, deformation of the clast-hosted vein was more strongly controlled by the evolution of calcite grain size within the Mg-poor shear zone (Fig. 7.3). Shear offsets are larger across finer-grained horizons, consistent with rheological weakening

due to secondary phases pinning grain boundaries. Away from secondary phases, grain sizes are larger and the competition between dislocation creep accompanied by grain growth and recrystallisation resulting in grain size sensitive flow is more apparent (Figs. 7.4 & 7.8). The field boundary hypothesis (*sensu.* De Bresser *et al.*, 2001) therefore appears to explain the deformation and evolution of more pure calcite aggregates, but the almost ubiquitous presence of secondary phases in deforming calcite aggregates means grain growth by dislocation creep is limited and the real-world applicability of the hypothesis is questionable.

7.3.4 The role of inheritance in subduction deformation of carbonates

Where calcareous sediments are included in the deforming megathrust at shallow levels, deformation is likely frictional due to low effective normal stress (Sibson, 1998). Frictional deformation of calcareous sediments may be accompanied by grain-scale pressure solution of calcite due to its high solubility at low temperatures, increasing the amount of dissolved carbonate (Bos, 2002; Plummer and Busenberg, 1982). Deformation would be dominated at shallow levels by slip on aligned phyllosilicates in the sediments, forming dilatant areas with lower cohesion and lower normal stress than the adjacent material (Bos, 2002; Niemeijer and Spiers, 2005). Where pore-fluid pressures become elevated, veins are likely to form along these low-cohesion horizons (see Chapter 6; Sibson, 1998). Fragments of phyllosilicate matrix, formed during fracturing, are likely to be incorporated into the veins during precipitation of minerals there. Low temperatures mean diffusion or dislocation creep and dynamic recrystallisation would require very high stresses to be active (Herwegh *et al.*, 2003; Renner *et al.*, 2002; Rutter, 1995), and the stresses in the veins are unlikely to be high enough unless they form a barrier to shear deformation (Beall *et al.*, 2019). Oceanic crust has been shown to contain common calcite veins at shallow depths (Alt and Teagle, 1999; Gillis and Coogan, 2011; Wallace *et al.*, 2019). Calcite in the oceanic crust may remain in place or act, alongside calcareous sediments, as sources of carbonate solute which is precipitated in veins at shallow levels (Fig. 7.1a & b;

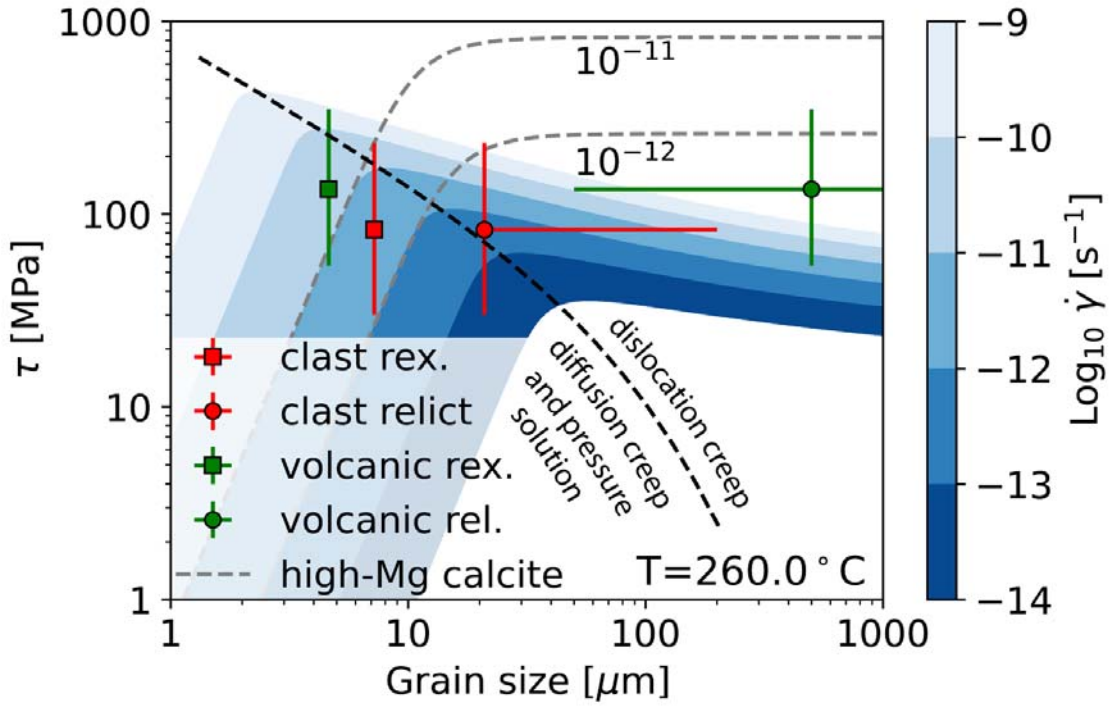

Figure 7.8: A summary of various weakening effects on deformation mechanisms shown in the examples. Blue-filled areas correspond to strain rate contours (see colour bar) calculated using composite strain rates from the dislocation creep flow law of Renner *et al.* (2002) and the diffusion creep flow law of Herwegh *et al.* (2003). Dashed black line corresponds to approximate field boundary between the two regimes (*sensu.* De Bresser *et al.*, 2001). Grey dashed lines are strain rate contours constructed using the Mgcc-80 dislocation creep flow law from Xu *et al.* (2009) combined with diffusion creep flow law from Herwegh *et al.* (2003). Green gradient fill is approximate grain-size distribution of parent grains bordering volcaniclastic shear zone (Fig. 7.5a & b), green-filled square is recrystallised calcite grain size and corresponding stress from Platt and De Bresser (2017) for the volcaniclastic shear zone. Red-filled circle is average parent grain size in clast-hosted calcite vein, red-filled square is recrystallised (rex) grain size in clast-hosted calcite vein. Both are plotted against stress from the piezometer of Platt and De Bresser (2017) for the mean recrystallised grain size. Error bars are 95% confidence limits for stress and grain size, grain size error bars for recrystallised grains are smaller than symbol size.

Wallace, 2020a). Once formed, calcite-dominated veins likely act as rigid volumes within the plate interface undergoing small amounts of solution at their margins.

The shear zones presented here localised within these earlier-formed, calcite-filled, veins. Later viscous deformation was limited to calcite within the veins, meaning shear zone geometry was controlled by brittle precursors (*sensu.* Mancktelow and Pennacchioni, 2005). Small-scale shear zones ($<$ 1 m wide) deformed at amphibolite-grade conditions in the Neves, Sierra Nevada, and Adamello areas have been recorded to similarly form at locations predetermined by brittle precursors (Pennacchioni and Mancktelow, 2018). The lengths and widths of such shear zones do not vary systematically with displacement, but result from the initial precursor geometry subject to shear stress. In the case of the volcaniclastic shear zone, the calcite-filled precursory vein is $\geq$ 10 cm long parallel to the foliation and slip direction (Fig. 7.5a & b). This allowed deformation to occur in a continuous volume along the precursory calcite vein. The clast shear zone, on the other hand, localised within a precursory calcite vein which was not oriented parallel to the slip direction, meaning slip outside the precursory vein must have occurred by deformation on chlorite-bearing en-echelon fractures (Fig. 7.3a). With increased temperature and pressure, long-term slip rates from deformation by frictional or brittle mechanisms are likely to be overtaken by those from viscous mechanisms (Fig. 7.1d). Strain within shear zones under prograde conditions would therefore progressively localise in volumes deforming by viscous mechanisms. The dimensions of shear zones localised within brittle precursors containing heterogeneous materials is therefore likely to evolve with deformation mechanisms active under changing P-T conditions.

As temperatures increase with depth, and calcite solubility decreases, the mobility of calcite from solution decreases (Plummer and Busenberg, 1982). Long-term normal stress on the megathrust (aside from episodic fluid pulses, Saffer and Tobin, 2011) also increases, requiring higher shear stresses for slip on phyllosilicate foliae (Imber *et al.*, 2008). Though no temperature-dependence of dynamic recrystallisation of calcite has been determined (Platt and De Bresser, 2017), a minimum activation temperature or strain is required to activate dynamic recrystallisation

(Rutter, 1995). The condition required to begin recrystallisation is not clear but may coincide with the onset of low-temperature crystal plasticity, around 125-200 °C (Bauer *et al.*, 2018). Once this condition is reached, earlier calcite veins begin to recrystallise and weakening by grain size reduction occurs. As shown by the two examples presented here, this recrystallisation may be localised by variations in calcite chemistry (Fig. 7.3); this may be considered the onset of the frictional-viscous transition in calcite.

7.4 The role of carbonates in creep, slow slip, and earthquakes

Grain-scale heterogeneity within the presented examples has promoted viscous mechanisms at temperatures below those they would normally occur at (Section 7.2) and such heterogeneities are likely widespread in lithologies hosting carbonate veins, such as oceanic volcanics or calcareous sediments (Section 7.3.4). This weakening may serve to allow deformation of carbonate veins at stresses below those required to nucleate seismic slip (Fig. 7.8). As carbonates generally appear in the lowest part of the sedimentary section or top of the oceanic crust (Table C.1; Alt and Teagle, 1999; Gillis and Coogan, 2011), they are likely to be under-thrust near the plate interface (Barnes *et al.*, 2020; Meneghini *et al.*, 2009) and affect deformation style where they deform at relatively high geological strain rates ($\geq 10^{-12}$ s^{-1}) at the frictional-viscous transition (200-300 °C). The shear zones presented here show that local heterogeneity likely promotes viscous deformation of calcite near the plate interface and exaggerates this effect, possibly decreasing the likelihood of rapid slip.

7.5 Conclusions

- Two examples of carbonate deformation are presented from the Gwna subduction complex where deformation occurred at subgreenschist conditions, around 260 °C.

- One example is a clast of Mg-rich calcite with deformation localised within a Mg-poor calcite vein. High Mg content outside the clast inhibited dislocation creep, preventing the dynamic recrystallisation and weakening which occurred within the vein.

- The other example is an altered volcaniclastic lithology with deformation localised within a recrystallised foliation-parallel calcite vein. Recrystallised grain boundaries in the foliation-parallel vein were pinned by abundant secondary phases, leading to grain size sensitive creep accompanied by sliding and diffusive mass transfer of chlorite within the vein.

- Both examples show that calcite deformation to high strains can occur by dislocation and grain size sensitive creep at temperatures colder than typically expected for the frictional-viscous transition in calcite.

- Deformation by dislocation and grain size sensitive creep in the frictional-viscous transition appears to be aided by the presence of grain-scale heterogeneity.

- Heterogeneous carbonates therefore appear to reduce the temperature of the frictional-viscous transition in the seismogenic zone plate interface, possibly reducing the likelihood for rapid (e.g. seismic) slip.

Part III

Synthesis and conclusions

Chapter 8

Synthesis

This thesis uses a broad variety of methods to investigate plate interface deformation in subduction zones. The studies of modern (Part I) and ancient (Part II) subduction systems have been considered in isolation up to this point, but are here synthesised alongside published literature in relation to the main research questions posed earlier.

How do subduction zone input lithologies control deformation and resultant mechanical evolution?

Given the deformation of oceanic volcaniclastics within plate interface shear zones presented in Chapter 6, and inferred for the Hikurangi margin by Barnes *et al.* (2020), subduction zone input lithologies are considered here to comprise the entire thickness of sediments in the trench and the upper part of the subducting oceanic crust. Sedimentary subduction zone inputs range in thickness from < 1 km up to several km (Heuret *et al.*, 2012) and are formed of sediments accumulated atop the oceanic crust during transport from a mid-ocean ridge (e.g. Matsuda and Isozaki, 1991). Pelagic sediments commonly dominate the lower part of sedimentary input sequences (Fig. 3.1d; Underwood, 2007) and contain a variable calcareous component alongside fine clays and other siliciclastic grains (Figs. 2.2b & 3.5a & b; Table C.1). As sediments near the trench, mass transport from the forearc wedge commonly leads to accumulation of siliciclastic-dominated turbidites in the upper part of the incoming sedimentary sequence (Fig. 2.2b; Festa *et al.*, 2018; Wakabayashi,

2015). The oceanic crust portion of the incoming sequence is less frequently sampled, but is likely dominated by volcaniclastic or other basaltic materials (Herath *et al.*, 2020; Shibuya *et al.*, 2013; Underwood, 2007; Villinger *et al.*, 2002). Volcaniclastics, basalts, and other eruptive materials are likely fractured, altered, or intermingled, especially where seamounts or evidence of seafloor volcanic activity are present (Underwood and Pickering, 2018; Wallace *et al.*, 2019).

For sediment on the subducting plate to be deformed at the plate interface it must be initially under-thrust at the megathrust toe (Fig. 3.11). Under-thrusting of sediment is more likely at the toe of the subduction megathrust if a thick sedimentary sequence is present (Meneghini *et al.*, 2009) or if the sediment is at the base of the sedimentary sequence (Fig. 2.2c). Sediments which are not under-thrust are accreted to the forearc wedge at the thrust toe. Basaltic lithologies comprising the lower plate are initially under-thrust as they are typically denser and more consolidated than sediments in the forearc wedge, and lie at the base of the input sequence. Lithologies likely to be of interest to study of shallow plate interface deformation ($<$ 20 km depth), therefore, are volcanics in the upper part of the subducting plate, pelagic sediments near the base of the sedimentary input section, and shallower sediments if the thickness of the sedimentary input section is large.

Deformation at the thrust toe is thought to occur over a poorly-bounded width by a mixture of brittle and ductile deformation in siliciclastic sediments that were deposited near the top of the incoming sedimentary sequence (Fagereng *et al.*, 2019; Kinoshita *et al.*, 2009; Tobin *et al.*, 2001). This is likely characteristic of shallow deformation down to several km depth, where thermally-driven mineral transformations occur and pelagic sediments lower in the incoming sequence may be in contact with the plate interface (Fig. 2.2c; Pytte and Reynolds, 1989; van de Kamp, 2008). Within calcareous pelagic sediments seaward of the Hikurangi margin, mixed brittle and viscous deformation is characterised by brittle faults localising within stylolites enriched in weak clays by earlier viscous pressure solution at the cm-scale (Section 3.6.2). Pressure solution is likely to be less active at low temperatures in less soluble siliciclastic sediments (Rutter, 1976), but shear deformation is still likely to localise onto weak through-going horizons (Gardner *et al.*, 2017). This may mean

slip at these shallow depths will likely occur within depositional clay-rich layers. Where more soluble lithologies meet the plate interface (e.g. calcareous sediments; Plummer and Busenberg, 1982) vertical shortening by pressure solution is likely to have exaggerated initial depositional layering (Gratier *et al.*, 2015), meaning clay-rich volumes are likely to have increased thickness compared to their undeformed pre-subduction equivalent. The presence of calcareous inputs at the plate interface shear zone, therefore, is more likely to result in localised slip in locations weakened by viscous pre-subduction deformation (e.g. Fig. 3.11).

The abundance of weak phyllosilicates and fluids in sediments deforming at shallow depths means that slip is likely to occur by granular flow and, with increasing depth and normal stress, frictional sliding on aligned clays within localised shear zones (den Hartog *et al.*, 2012; Fagereng *et al.*, 2019). Drilling studies directly sampling the shallow megathrust toe have shown that whereas the over-consolidated upper plate hanging wall is likely to undergo localised brittle deformation, the plate interface shear zone and lower plate footwall deform by both macroscopically ductile flow and later, overprinting, brittle deformation (Fagereng *et al.*, 2019; Tobin *et al.*, 2001). Fagereng *et al.* (2019) attributed this to varied slip speeds at different times, dictated by the sensitivity of frictional stability to stress perturbations controlled by variations in loading rate or fluid pressure (e.g. Leeman *et al.*, 2016). Mixed brittle and ductile deformation is likely to lead to contrasting clast-rich and clast-poor fabrics within different volumes of shallow subduction megathrust shear zones (Fagereng *et al.*, 2019; Tobin *et al.*, 2001). This shallow slip rate-dependent fabric may represent initial formation of the mélange texture described in many subduction complexes (Chapter 6; Fagereng, 2011b; Festa *et al.*, 2018; Mittempergher *et al.*, 2018; Rowe *et al.*, 2011; Wakabayashi, 2015). Shear strength within clast-bearing volumes is strongly controlled by the clast proportion (Beall *et al.*, 2019), and likely occurs by a combination of frictional sliding, dilatation, pressure solution, and phyllosilicate plasticity (*sensu.* Bos, 2002; Niemeijer and Spiers, 2005). Pressure solution occurs more rapidly where clasts are composed of more soluble material (Rutter, 1976), meaning calcareous clast-bearing mélanges are able to redistribute interacting clast material more effectively than their siliceous counterparts. This

would allow clasts to move past one another more effectively during deformation and reduce the frequency of 'locking up' (e.g. Beall *et al.*, 2019), and resultant transient (possibly seismic) slip. On the other hand, carbonates are velocity-weakening at low temperatures (Ikari *et al.*, 2013; Kurzawski *et al.*, 2016). This may mean that transient periods of elevated slip rate in carbonate-bearing shear zones are less frequent than in phyllosilicates during frictional-viscous slip, but are more likely to be seismic when they do occur.

Lithologies deformed in the Gwna Complex in Anglesey, UK, clearly illustrate that the plate interface shear zone at seismogenic depths ($\sim$ 17 km depth; Figure 6.7) is likely to inherit its materials and their textures from input lithologies subject to earlier, shallower, deformation (Sections 6.5 & 7.3.4). Shear zone textures will result from the mechanisms and rates of earlier deformation (i.e. slip Rowe *et al.*, 2011), meaning shallow slip patterns on the plate interface likely control later, deeper, deformation.

Shallow slow slip and earthquakes have both been associated with fluid release and vein formation in plate interface shear zones (Section 6.6.2; Fagereng, 2011b; Meneghini and Moore, 2007; Raimbourg *et al.*, 2021; Shaddox and Schwartz, 2019; Ujiie *et al.*, 2018). Veins that form during these slip events are likely to reflect the fluid composition present during the pressure drop and resultant supersaturation which led to vein-fill precipitation (Section 7.3.4; Meneghini and Moore, 2007). This means that veins deforming at seismogenic zone depths may have formed at shallow levels, possibly from solute sourced from fluid-assisted diffusive mass transfer in the surrounding rocks or far-travelled fluids from elsewhere in the subduction zone (Cerchiari *et al.*, 2020; Nishiyama *et al.*, 2020). Calcite-dominated veins in the Gwna Complex localised deformation by viscous mechanisms at seismogenic depths due to incorporated grain-scale heterogeneities (Chapter 7). Quartz-rich veins from the same complex, however, did not deform to appreciable strains by viscous mechanisms (Fig. 6.5). The combined effect of calcareous inputs on plate interface deformation can therefore be thought to be both (1) localisation due to strain weakening by shallow viscous deformation (Chapter 3) and (2) alteration of the bulk rheology of the plate interface relative to a quart-dominated lithology (chapters 6 & 7).

It therefore becomes apparent that as shallow deformation localises in weak materials, perhaps weakened further by pre-subduction deformation (Chapter 3), input lithologies control initial grain-scale strain localisation and therefore the rheology of the shallow plate interface. Most lithologies will deform by mixed brittle and ductile deformation on the shallow plate interface. Again, the distribution of this deformation is lithologically-controlled. Deformation during stable creep or transient slip events will produce structures (e.g. veins and fabrics) in the plate interface shear zone dependent on the dominant deformation mechanisms at the conditions of slip. These structures are likely inherited in later deformation. This means that the composition of input lithologies, alongside fluid pressure and P-T conditions (Chapter 6), controls deformation mechanisms within the plate interface and, therefore, slip rate. A wider variety of lithologies is likely to lead to a wider variety of deformation mechanisms, more complex responses to variable fluid pressures and temperatures, and therefore a greater propensity for complex slip behaviours such as slow slip.

Do elevated fluid pressures influence deformation at shallow ($<$ 20 km) depth in subduction plate interface shear zones?

Elevated pore fluid pressures are often reported to occur near shallow subduction plate interface shear zones and are associated with both slow slip and earthquakes (Bassett *et al.*, 2014; Kodaira *et al.*, 2004; Shaddox and Schwartz, 2019). Fluids in subduction zones are often thought to be sourced from compaction of underthrust sediment and dehydration of minerals which become unstable with increasing temperature and depth (Ellis *et al.*, 2015; Saffer and Tobin, 2011). Seismic data presented here are consistent with variably-altered fluid-rich volcaniclastics, sampled seaward of the trench during IODP Exp. 375, underlying the plate interface at seismogenic depths in the northern Hikurangi margin (Fig. 4.18). Porosities in volcaniclastics can be high, and low-temperature alteration products likely to form on the seafloor include smectite clays with high intracrystalline water content which are likely to dehydrate at shallow depths ($<$ 15 km) during subduction (Seyfried and Mottl, 1982; van de Kamp, 2008; Wallace *et al.*, 2019). In addition to underthrust sediments, altered volcanic-derived lithologies may therefore be an important

source of fluids where significant volumes of altered oceanic crust are subducting (e.g. Hikurangi, Mariana, Costa Rica; Clarke *et al.*, 2018; Davy and Wood, 1994; Salimullah, 1992).

Under-thrust sediments are likely to produce the largest volume of fluids during shallow subduction (Ellis *et al.*, 2015). The plate interface may direct fluids released from under-thrust sediments seaward along a relatively high-permeability interface (Ellis *et al.*, 2015; Moore and Vrolijk, 1990). In the plate interface shear zone, fluids are likely irregularly distributed along channels and throughout the damage zone (Saffer and Tobin, 2011). Elevated fluid pressures therefore result from the relative rates of fluid production and flow, focused in under-thrust material and the plate interface, respectively. Where outflow rates are lower than those of fluid production, pore fluid pressures will increase above hydrostatic ($\lambda > 0.4$).

Pore fluids at pressures between lithostatic and hydrostatic ($0.4 > \lambda > 1$) are consistent with shear veins and frictional slip on localised sliding surfaces (Sibson, 1998). Limited evidence was found for widespread localised sliding surfaces or shear veins in the Gwna Complex (Chapter 6). Shear displacement was generally distributed and veins commonly had a hybrid extensional-shear mode (Fig. 6.5), though localised slip surfaces may have been destroyed by later deformation. At the grain-scale, minor localised slip was recognised at the margins of clasts (Fig. 6.5), suggesting mixed materials with a mélange texture may promote the localisation of slip. Stresses required for frictional sliding on localised slip surfaces will weaken with increasing pore fluid pressures (Amontons, 1699), but depends on the host rock composition (Kurzawski *et al.*, 2018). Mixed materials in a mélange are likely to respond differently to deformation than monomineralic shear zones (Fagereng and Sibson, 2010; Handy, 1990), and modelling of shear zones in the Gwna Complex showed this behaviour is magnified at elevated fluid pressures (Section 6.7.5). Deformation observed within altered volcaniclastics likely required elevated fluid pressures to occur (Fig. 6.11), and the same may be true for volcaniclastics currently subducting beneath a plate interface hosting slow slip events at the Hikurangi margin (Chapter 2). Slow slip events have been temporally associated with earthquake clusters thought to result from fluid release (Shaddox and Schwartz, 2019), but the plate interface

itself may be deforming at elevated rates due to rheological weakening or broadening of the deforming shear zone width at fluid pressures greater than hydrostatic but less than lithostatic.

At pore fluid pressures greater than lithostatic, extensional or hybrid extensional-shear cracks can form (Sibson, 1998). Hybrid extensional-shear veins are present in the Gwna complex and contain minerals consistent with filling by supersaturation during pressure drops (Fig. 6.5; Meneghini and Moore, 2007). Pressure drops driving precipitation in hybrid extensional-shear veins are consistent with transient elevated fluid pressures (Chapter 6). This evidence suggests fluid escape from under-thrust materials happens briefly and rapidly, and is channelled onto weak surfaces (Section 6.7.6). Dehydration and compaction are driven by heating and loading, respectively, and are therefore likely constantly occurring at a low rate during interseismic deformation (French and Morgan, 2020; Saffer and Tobin, 2011). The disparity between the rates of fluid production and release may account for the varied slip behaviours which are ascribed to the effect of transient fluid pulses at various margins (Henry, 2000; Shaddox and Schwartz, 2019; Thorwart *et al.*, 2014).

As cracks are filled to become veins, the proportion of weak material on a plate interface will reduce (Section 6.6.2). This could be an arrest mechanism for a single episode of fluid-induced slip (e.g. Sample, 1990), but is also likely to influence the long-term rheology of the plate interface. Examples from calcite-dominated veins in the Gwna Complex show that veins, which likely formed during subduction at shallower depths, can host deformation to significant shear strains by viscous mechanisms during later, deeper, subduction (Chapter 7).

The effect of fluid pressure on shallow (< 20 km) subduction deformation might, therefore, be best viewed in terms of the time scales of different processes within the plate interface shear zone. These processes are likely at different stages in different volumes of the plate interface shear zone, leading to the complex and varied vein patterns observed in both the Gwna mélange (Chapter 6), and elsewhere (Fagereng *et al.*, 2010; Meneghini and Moore, 2007). Short term (seconds to days), transient pulses of elevated fluid pressure (between hydrostatic and lithostatic) are likely to weaken areas (Fig. 6.10) and promote slip episodes by enabling higher rates of

deformation within broader volumes of the plate interface (Fig. 6.11). Deformation in these volumes might occur by mechanisms requiring too high shear stress to occur at hydrostatic fluid pressures (e.g. frictional sliding; Fig. 6.9e & f). Medium term (days to years), cementation of veins formed during brief periods of elevated fluid pressures is likely to result in increased cohesion and strengthening of the plate interface after fluid pressures have returned to long-term values (Section 6.6.2).

Long term (years to decades) shear of veins formed during periods of elevated fluid pressure is likely to occur where their geometry means they are unlikely to deform by brittle mechanisms (e.g. Fig. 6.4). Foliation-parallel veins are likely to persist (Fig. 6.5), and some veins may deform by mechanisms enabled by local heterogeneities incorporated during precipitation of vein-filling materials (Chapter 7). The interaction between processes associated with these different timescales may lead to (a) the complex rheological behaviours observed in modern subduction zones, and (b) structures observed within exhumed plate interface shear zones in subduction complexes.

How could subduction plate interface shear zone geometry influence deformation style?

Observations of subduction plate interface shear zone geometries reported in this thesis vary in scale from a km-scale interface at depth (Chapter 4) to mm-scale shear zones preserved within 20 m thick deformed zones during ancient subduction (Chapters 6 & 7). At both sites (the Gwna Complex and the Hikurangi margin), volcanics appear involved in deformation at the plate interface (Figs. 2.1 & 6.1). Whereas subducting topography at the Hikurangi margin is clearly imaged in seismic and bathymetric data (Barnes *et al.*, 2020), the role of subducting topography in the Gwna Complex can only be interpreted from the rock record. At a km-scale, shear zones throughout the Gwna Complex vary about a general NE-SW strike (Fig. 5.3). Though not observable continuously across the study area, lithological contacts between imbricated lenticular slices of ocean plate stratigraphy in the complex define a relatively rough palaeo-subduction plate interface which undulates 10s of metres over several hundred metres and locally varies in thickness (Fig. 6.6). At the

Hikurangi margin, the plate interface mapped from receiver functions beneath the NZ3D array is also interpreted to be rough, possibly associated with its soling intersection with the Gable End fault, but has a locally-stepped geometry varying over several km about a general dip towards the NW (Fig. 4.17). Both margins are associated with subducted volcaniclastic materials near the plate interface, suggesting that plate interface shear zones where volcaniclastics bound the shear zone volume may be rougher than sediment-dominated shear zones over a variety of scales. This could be due to a geometrically-rough topography, variable alteration of volcaniclastics (e.g. Barnes *et al.*, 2020; Wallace *et al.*, 2019), or an irregular distribution of weaker volcaniclastics in the lower plate (Clarke *et al.*, 2018; Davy and Wood, 1994; Salimullah, 1992). It seems at the Hikurangi margin that the roughness is related to the subducting topography imaged offshore (Fig. 2.1), though the imbricated material at Llanddwyn Island suggests that at large shear strains the distribution of altered volcanics becomes increasingly important (Section 6.5). Roughness on the plate interface would lead to surface asperities, possibly creeping at high-stress or fracturing during periods of elevated fluid pressure (Shaddox and Schwartz, 2019; Wang and Bilek, 2014). Roughness increases the complexity of shear zone, locally-varying stress magnitudes, and limiting seismic ruptures (Bonnet *et al.*, 2019; Wang and Bilek, 2014). Variably-altered and distributed volcaniclastics may therefore be an additional factor to topographic roughness, inducing variable stresses and complex deformation styles where seamounts are subducted.

The shallow subduction plate interface ($<$ 20 km depth) is commonly thought to form broad shear zones, 100 m to 1 km, wide containing several deforming strands 1-100 m thick, though several shear zones within duplexes and imbricated lenses were assumed to be contemporaneous in this analysis (Rowe *et al.*, 2013). Individual shear zones in the Gwna Complex are $<$ 20 m wide and are spaced up to $\sim$ 400 m apart (Figs. 5.3 & 6.2). If contemporaneous, these dimensions are consistent with generalised models for the subduction plate interface. It is impossible to interpret from the data presented here whether shear zones in the Gwna Complex were contemporaneous, but their anastomosing structure is consistent with growth by addition of 1-100 m wide shear zones during deformation (Rowe *et al.*, 2013).

Imbricated shear zones in the Gwna Complex are localised on weaker horizons in the lower oceanic plate, requiring not just deformation of sediments atop the lower plate and in the forearc wedge, but also deformation of volcaniclastics that form the lower surface of imbricate lenticular slices (Fig. 6.6). This deformation may be complicated by the intersection of soling splay faults with the plate interface (Fig. 6.6), which could increase the variation of materials on the plate interface by creating additional complexity in the deforming volume. The entrainment of more varied materials on the plate interface varies the materials available to deform, and consequently the rheology and slip behaviour on shear zones there.

Individual shear zones in the Gwna Complex are up to 20 m wide, with deformation localised within an approximately tabular mélange-bearing volume (Fig. 6.2). The mélange-bearing volumes encompass the contact between mudstones and hyaloclastites from the structurally-higher and -lower lenticular slices of ocean plate stratigraphy. Outside the mudstones and hyaloclastites, the shear zone is constrained between more coherent pillow basalts in the hanging wall and sandstones in the footwall (Fig. 6.2). During deformation, the coherent units either side of the shear zone likely limited its growth by migration of slip to a new yield surface (*sensu.* Moore and Byrne, 1987; Rowe *et al.*, 2013). Limited shear zone growth during deformation likely led to the formation of a relatively thin volume of mélange in the shear zone where mixed continuous-discontinuous deformation in the matrix and clasts occurred (Figs. 3.11, 6.5 & 6.4; Fagereng, 2013). Mélange fabrics have been associated with complex deformation and slip behaviours, possibly during slow slip or earthquakes (Beall *et al.*, 2019; Fagereng and Sibson, 2010). Illitic and chloritic mélange likely formed from turbidites and volcaniclastics, respectively (Sections 3.8 & 6.3.2). Illite and chlorite in the matrix of these mélanges each have distinctive frictional characteristics and responses to fluid pressure (Fig. 6.9; den Hartog *et al.*, 2012; Okamoto *et al.*, 2019; Phillips *et al.*, 2020). The matrix materials, and their frictional response within the shear zone, are therefore the result of lithologies incorporated by the imbricated geometry. Imbricated lenticular slices of ocean plate stratigraphy created a geometry which limited the width of the deforming zone, forming a thin mélange-bearing volume with a characteristic deformation

style resulting from the mélange-forming lithologies.

The scale of observations presented in Chapter 6 is limited due to the outcrop of the Gwna Complex (Fig. 6.1a), though scaling-up m-scale observations to km-scale subduction-related shear zones raises the issue of representativeness. The idealised shear zone presented in Fig. 6.3 is based on observations of shear zones over several km of exposure. Interpretation and modelling of these shear zones, while limited in comparison to shear zones with similar materials, is based on the processes operating rather than the specific geometry. Similar to the shear zones presented in Chapter 7, the process-oriented approach taken in the thesis allows scaling-up of observations reported here.

Though fluid flow is likely commonplace within rocks in the subsurface, veins are a clear indication of fluid flow associated with deformation (Bons *et al.*, 2012; Fagereng *et al.*, 2018). Veining within mélanges in the Gwna Complex show that fluid flow during deformation was focused within shear zones (Figs. 6.5 & 6.4). High fluid through-put in narrow shear zones resulted in abundant veining in varied lithologies (Figs. 6.4, 6.5, & 7.3). Vein composition led to varied deformation styles (Section 6.6.2), but the foliation-parallel geometry of many of the veins led to the development of localised shear on some of these veins (Chapter 7). Foliation-parallel shear veins are common in subduction complexes due to the stress regime on the plate interface (Fagereng *et al.*, 2010; Hashimoto and Yamano, 2014; Vannucchi *et al.*, 2008). Where deformation is localised by vein compositions or fine grain size with incorporated secondary phases, deformation is likely to be more viscous than in the surrounding mélange fabric (Chapter 7). Large-scale geometries on the shallow plate interface therefore appear to control fluid pathways during deformation, dictating where weakening occurs with increased fluid pressure, strengthening occurs by vein cementation, or deformation localises into veins.

Which factors control shallow slow slip and how might they be better constrained?

Slow slip events (SSEs) are widespread and have relatively uniform moment-duration relationships (Gomberg *et al.*, 2016; Peng and Gomberg, 2010), suggesting they may

have similar physical mechanisms throughout subduction zones. SSEs recur at relatively short intervals (years to decades), with low stress drops and slow propagation velocities (Ando *et al.*, 2012; Gomberg *et al.*, 2016). Mechanisms of slow slip must therefore be transient and cyclical within the deforming zone, with relatively rapid healing times and a strong sensitivity to applied stress.

Fluids have been associated with slow slip at many margins (Saffer and Wallace, 2015), and are commonly invoked in nucleating instabilities due to their poorly-constrained, transient nature (Saffer and Tobin, 2011). The main physical mechanism by which fluids are thought to cause slow slip is by: (a) decreasing the effective normal stress, which influences the critical stiffness of the fault and leads to conditional fault stability (Kodaira *et al.*, 2004), or (b) reducing effective normal stress where materials have rate and state friction parameters $(a - b)$ approximating 0, leading to transitional stability (Ikari *et al.*, 2020; Scholz, 1998). Within a shear zone, these mechanisms require that sliding occurs frictionally on a discrete surface. Discrete slip surfaces are uncommon in the exhumed shear zones studied in this thesis, and where they do occur they tend to be too small to host critical nucleation lengths estimated for slow slip (Fig. 6.5; Uenishi and Rice, 2003). Elsewhere, localised slip has been suggested to occur in shear zone mélange-hosted phacoids at length-scales consistent with low-frequency earthquakes (Kotowski and Behr, 2019; Phillips *et al.*, 2020), but how this slip propagates over the large areas where slow slip occurs in inversions of geodetic observations (100s km^2) remains unclear.

One explanation for why empirical rate-and-state frictional models may not predict shallow slow slip well in subduction zones is that the approach is too simplistic. Subduction plate interface shear zones are characterised by mélanges with varied lithologies, textures and geometries (Kimura *et al.*, 2012). Slow slip on the plate interface has been associated with varied subduction zone input materials at the Hikurangi margin (Chapter 3; Barnes *et al.*, 2020), but the prevalence of mélange fabrics in plate interface shear zones suggests this heterogeneity may be innate to all subduction zones (Rowe *et al.*, 2013). The occurrence of slow slip within mélange-bearing plate interface shear zones may therefore be related to mechanistic or geometric heterogeneity there.

Study of the deformation of mixed geologic materials has shown that complex interplays of different mechanisms occur spatially and temporally (Chapters 3, 6, 7; De Bresser *et al.*, 2001; Gratier *et al.*, 2013; Rowe *et al.*, 2011). Experimental work on the deformation of phyllosilicate-bearing mixtures under hydrothermal conditions has shown that deformation occurs by a combination of mechanisms (Bos, 2002; Bos and Spiers, 2001; den Hartog *et al.*, 2012; Den Hartog and Spiers, 2014; Niemeijer and Spiers, 2005). As the closest analogue to mélange fabrics frequently associated with subduction, these mechanisms are likely to control slip and stability in subduction interface shear zones (Fagereng and Den Hartog, 2017). Shear zones in the Gwna Complex show evidence for interplay between these processes, though the lithological diversity exhibited there exaggerates this mechanistic variation with changing fluid pressures (Section 6.7.5). This may be more broadly true of plate interface shear zones, where locally-variable weakening of different material-dependent mechanisms leads to the nucleation of slip transients. The exact mechanism of this weakening would be material and condition dependent, and further research into how deformation mechanisms vary with conditions in realistic shear zone mélange materials may yield insights into this. The relatively slow propagation of slow slip (Ando *et al.*, 2012) suggests either: (1) the triggering condition (e.g. elevated fluid pressure) propagates away from the nucleation site and continues to trigger slip, or (2) acceleration in the nucleation patch leads to stress loading of the surrounding interface and that leads to slip propagation. The triggering of slow slip by earthquakes nearby suggests the latter is more appropriate (Wallace *et al.*, 2017) and the interface is nearly critically-stressed (Dahlen, 1990; Hardebeck, 2015). From small, possibly fluid-induced, patches of weakened mechanisms within mélange shear zones, elevated slip velocities would stress the areas surrounding the patch and a limited acceleration of slip would propagate, consistent with models for slow slip (Ando *et al.*, 2012). How stress loading leads to the propagation of slow slip, without acceleration to earthquake slip speeds, is therefore a prominent question, and insights on this can be gleaned from studies of the geometric controls on deformation within subduction interface shear zones.

Increased stress in a mélange shear zone can activate varied deformation mecha-

nisms at strain rates of $> 1 \times 10^{-10}$ s^{-1}, relevant to slow slip (Section 6.7.3). Where there is more lithological heterogeneity near the plate interface, such as the Hikurangi margin (Chapters 3, 4 & 7; Barnes *et al.*, 2020), more deformation mechanisms and interplays between them are likely to become active. Deformation of the plate interface shear zone is likely to mix materials, leading to the movement of clasts and the possible formation of force chains of phacoids within the mélange (Beall *et al.*, 2019). Slip-driven stress loading propagating along the plate interface may lead to the breakage of force chains (or 'beams', Sammis *et al.*, 1987) in the mélange, leading to weakening from its locked state and propagation of slip. Strain hardening associated with slip may occur due to new force chain formation or other mechanisms associated with the reduced flow stresses accompanying sliding, leading to the arrest of slow slip.

Areas of the plate interface down-dip of those modelled from geodetic data to host shallow slow slip events at the northern Hikurangi margin have low interseismic coupling values (Wallace *et al.*, 2004). Low interseismic coupling values suggest steady creep dominates the plate interface shear zone at plate convergence rates (40-50 mm yr^{-1}; Beavan *et al.*, 2002), and factors controlling shallow slip transients exert less control on plate interface deformation there. Temperatures at the plate interface immediately down-dip of the region of shallow slow slip are estimated to be 250-260 °C (Antriasian *et al.*, 2018), consistent with estimated temperatures of viscous deformation which formed structures observed in carbonate shear zones in the Gwna Complex (Chapter 7). Carbonate veins and cements are common in the volcaniclastics atop the Hikurangi Plateau and there are also carbonate-rich layers in the pelagic sedimentary sequence (Wallace *et al.*, 2019). Receiver functions immediately down-dip of areas thought to host slow slip at the northern Hikurangi margin show that volcaniclastics may underlie the plate interface there (Fig. 4.19). Carbonate in volcaniclastics at or near the plate interface may therefore deform at temperatures of 250-260 °C by viscous mechanisms weakened by grain-scale heterogeneities, leading to steady creep on the plate interface, if the carbonate veins and cements form an interconnected framework that controls deformation. The down-dip extent of shallow slow slip at the northern Hikurangi margin may

therefore be controlled by the onset of efficient viscous deformation mechanisms, weakened by grain-scale heterogeneities (Chapter 7).

Overall, the main controls on shallow slow slip appear to be (1) mechanisms operating within the plate interface and (2) the geometry of the deforming zone. Both of these factors result from lithologically-controlled strain localisation in input lithologies that form heterogeneous mélange, which exhibits a complex response to applied stress under locally-variable fluid pressures. In the seismogenic zone, thermally-activated viscous deformation mechanisms may be weakened by grain-scale heterogeneities, controlling the down-dip extent of shallow slow slip. Better constraints on slow slip may be gained by study of the lithological controls on strain localisation and deformation in realistically-varied subduction input materials. These constraints include possible mechanisms of deformation and slip instability nucleation and mechanisms of slip propagation and arrest.

Chapter 9

Conclusions and future work

9.0.1 Conclusions

This thesis has investigated deformation on the shallow plate interface of subduction zones using a mixture of field geology, microstructures, and geophysical techniques at modern margins and ancient exhumed complexes. At the Hikurangi margin, a modern margin, deformation was characterised in sediments seaward of the thrust toe and receiver functions were used to image the megathrust between 12 and 15 km depth. In the ancient Gwna mélange, Anglesey, UK, field and microstructural analysis of collected samples were used to characterise the bulk rheology of idealised plate interface shear zones at $\sim$ 17 km depth. These were also modelled to characterise the effects of varying fluid pressures. Microstructural analysis of some calcite-dominated shear zones localised within veins in the complex was also carried out to characterise mineral-scale deformation mechanisms of carbonates at seismogenic zone depths. The main conclusions of this thesis are:

- Calcareous-pelagic sediments seaward of the Hikurangi margin host structures from mixed brittle and viscous deformation where shear is likely to localise and occur by frictional-viscous mechanisms with rheologies more sensitive to pressure solution than in their siliciclastic counterparts.

- Receiver functions from the NZ3D array image splay faults extending from the surface towards a geometrically rough, NW-dipping plate interface between

12 and 15 km depth which overlies a thick sequence of relatively low seismic velocity materials, possibly variably-altered, fluid-rich volcaniclastics.

- The Gwna Complex at Llanddwyn Island was deformed at 260 ± 10 °C and comprises a series of thin (< 15 m wide) imbricated mélange-bearing shear zones, with block-in matrix textures and several generations of variably-deformed veins cross-cutting one another within a foliated phyllosilicate matrix, consistent with transient cyclical episodes of supra-lithostatic fluid pressure during stable creep.

- Models of illitic and chloritic mélanges in the Gwna Complex suggest that slip at convergence or slow slip rates requires pore fluid pressures intermediate between hydrostatic and lithostatic pressure, and that slip at those rates would occur by deformation of both mélanges.

- Two examples of small calcite-dominated shear zones localised in veins in the Gwna Complex show microstructures consistent with viscous deformation to shear strains of 4-5 at temperatures of 260 ± 10 °C and stresses of ∼ 88 MPa, colder than the experimentally-constrained traditional frictional-viscous transition in calcite.

- Deformation of calcite veins occurred by recrystallisation and rheological weakening promoted by grain-scale heterogeneities, suggesting carbonates may viscously creep at the plate interface, decreasing the likelihood of seismic slip.

- Slip at the shallow plate interface is controlled by deformation mechanisms active shear zones which often localise within structures resulting from earlier deformation, either in input sediments or at shallower depths, under variable pore fluid pressures.

- As localisation on inherited structures controls shallow subduction interface shear zone rheology and its weakening at elevated pore fluid pressures, diverse lithological inputs and fluid pressures at shallow depths are likely to lead to complex slip behaviours.

9.0.2 Future work

Structures in calcareous-pelagic sediments seaward of the Hikurangi margin suggested deformation was controlled by a rate-dependent interplay of slow pressure solution and rapid brittle faulting. On the plate interface this might manifest in shear as frictional-viscous flow along strain-weakened, clay-rich horizons. A possible next step is to characterise how strain localises with the onset of shear in sediments which have deformation structures from previous compaction. This could be done experimentally using samples obtained from seafloor drilling (e.g. IODP Exp. 375), or other calcareous-pelagic lithologies sampled in the field. New advances in three-dimensional x-ray micro-tomography (e.g. Macente *et al.*, 2018), might aid in characterising porosity during the duration of the experiments.

Receiver functions from arrivals at NZ3D array stations provided reasonably good coverage of a limited volume directly beneath the array, allowing interpretation of the plate interface there. Away from the NZ3D array the plate interface is described by the model of Williams *et al.* (2013), which was shown to inadequately capture local surface roughness due to its regional extent. Contemporaneous with the onshore NZ3D array, instruments comprising the SHIRE (Seismogenesis at Hikurangi Integrated Research Experiment, Henrys *et al.*, 2018) array were deployed over a much larger area and would allow for construction of a continuous CCP volume both parallel and perpendicular to the margin from the thrust toe to $>$ 100 km depth. This would help constrain plate interface and lower plate geometry, and its variation, over a much larger area at the northern Hikurangi margin. This could help discern the deformation geometries of subducting seamounts (*sensu.* Wang and Bilek, 2014), or determine if features observed in the CCP volume beneath the NZ3D array (Fig. 4.15) are observed to continue more broadly across the shallow plate interface.

Deformation within the Gwna Complex encompasses varied lithologies and geometries and the data presented in Chapter 6 characterised this in terms of its typical structures and bulk rheology. Though detailed work on carbonate veins in Chapter 7 yielded insights into the deformation of calcite at seismogenic zone depths, questions remain about alteration and deformation mechanisms within other materials

in the complex. Chlorite-rich mélange fabrics within imbricated shear zones are constrained to having formed pre- or syn-deformation due to overprinting deformed veins, but the source of chlorite is still unclear. Geochemical or isotopic analysis of chlorite in hyaloclastites within and away from shear zones on Llanddwyn Island could help in discerning if the matrix chlorite formed due to intensive alteration on the seafloor or in shear zones. If alteration occurred during deformation in a shear zone, characterising the geochemistry and timescales of alteration would yield useful insights into how basalt alteration may weaken the plate interface of shear zones.

Fluid pressures have been shown to have a complex effect on the rheology of mixed-material shear zones (Section 6.7.5). Experimental work on phyllosilicate-bearing fault rocks showed several deformation mechanisms interact to control deformation (Bos, 2002; Niemeijer and Spiers, 2005). Characterising the effects of pore fluid pressure on mechanisms and bulk rheology in mixed-material shear zones could aid in the interpretation of structures and mechanics observed in similar natural faults, such as those in the Gwna Complex.

An investigation into carbonate deformation during shallow subduction showed that calcite may preferentially localise deformation over foliated chlorite within a subduction mélange, meaning it can deform at similar or lower stresses (Chapter 7). The experimental study of calcite aggregates has been investigated by a myriad of workers (de Bresser and Spiers, 1993; Rutter, 1974; Schmid *et al.*, 1980; Turner *et al.*, 1954; Walker *et al.*, 1990; Weiss and Turner, 2013, and others), but this behaviour is not clearly accounted for by deformation mechanisms observed in these experiments. Carbonate veins are common in subducting oceanic basalts and may provide a mechanism for an otherwise relatively strong rock to deform during shallow subduction (< 20 km). A good next step then, would be to study the deformation of carbonate veins within basalts deformed at a greater variety of temperatures (< 300 °C) to better understand the range of mechanisms by which carbonate veins may weaken strong oceanic crust subducting at shallow levels today.

References

Abers, G. A., Mackenzie, L. S., Rondenay, S., Zhang, Z., Wech, A. G., and Creager, K. C. (2009). Imaging the source region of Cascadia tremor and intermediate-depth earthquakes. *Geology*, *37*(12), 1119–1122.

Agard, P., Plunder, A., Angiboust, S., Bonnet, G., and Ruh, J. (2018). The subduction plate interface: rock record and mechanical coupling (from long to short timescales). *Lithos*, *320-321*, 537–566.

Aharonov, E. and Katsman, R. (2009). Interaction between pressure solution and clays in stylolite development: Insights from modeling. *American Journal of Science*, *309*(7), 607–632.

Akuhara, T., Bostock, M. G., Plourde, A. P., and Shinohara, M. (2019). Beyond Receiver Functions: Green's Function Estimation by Transdimensional Inversion and Its Application to OBS Data. *Journal of Geophysical Research: Solid Earth*, *124*(2), 1944–1961.

Akuhara, T., Tsuji, T., and Tonegawa, T. (2020). Overpressured Underthrust Sediment in the Nankai Trough Forearc Inferred From Transdimensional Inversion of HighFrequency Teleseismic Waveforms. *Geophysical Research Letters*, *47*(15).

Allott and Lomax (1988). Wylfa 'B' power station pre-application studies, report on civil engineering aspects, Vol 2, geotechnical report. Technical report.

Alt, J. C. and Teagle, D. A. (1999). The uptake of carbon during alteration of ocean crust. *Geochimica et Cosmochimica Acta*, *63*(10), 1527–1535.

Ammon, C. J., Randall, G. E., and Zandt, G. (1990). On the nonuniqueness of receiver function inversions. *Journal of Geophysical Research*, *95*(B10), 15303.

Amontons, G. (1699). De la resistance caus'ee dans les machines. Technical report, l'Académie Royale, Amsterdam.

Ando, R., Takeda, N., and Yamashita, T. (2012). Propagation dynamics of seismic and aseismic slip governed by fault heterogeneity and Newtonian rheology. *Journal of Geophysical Research: Solid Earth*, *117*(B11).

Andrews and Railsback (1997). Controls on Stylolite Development: Morphologic, Lithologic, and Temporal Evidence from Bedding-Parallel and Transverse Stylolites from the U.S. Appalachians. *The Journal of Geology*, *105*(1), 59.

Antriasian, A., Harris, R. N., Tréhu, A. M., Henrys, S. A., Phrampus, B. J., Lauer, R., Gorman, A. R., Pecher, I. A., and Barker, D. (2018). Thermal Regime of the Northern Hikurangi Margin, New Zealand. *Geophysical Journal International*, *216*(2), 1177–1190.

Arai, R., Kodaira, S., Henrys, S., Bangs, N., Obana, K., Fujie, G., Miura, S., Barker, D., Bassett, D., Bell, R., Mochizuki, K., Kellett, R., Stucker, V., and Fry, B. (2020). ThreeDimensional P Wave Velocity Structure of the Northern Hikurangi Margin From the NZ3D Experiment: Evidence for FaultBound Anisotropy. *Journal of Geophysical Research: Solid Earth*, *125*(12).

Asanuma, H., Fujisaki, W., Sato, T., Sakata, S., Sawaki, Y., Aoki, K., Okada, Y., Maruyama, S., Hirata, T., Itaya, T., and Windley, B. F. (2017). New isotopic age data constrain the depositional age and accretionary history of the Neoproterozoic-Ordovician Mona Complex (Anglesey-Lleyn, Wales). *Tectonophysics*, *706-707*, 164–195.

Ashby, M. and Verrall, R. (1973). Diffusion-accommodated flow and superplasticity. *Acta Metallurgica*, *21*(2), 149–163.

Audet, P. (2020). RfPy: Teleseismic receiver function calculation and post-processing.

Audet, P. and Kim, Y. (2016). Teleseismic constraints on the geological environment of deep episodic slow earthquakes in subduction zone forearcs: A review. *Tectonophysics*, *670*, 1–15.

Audet, P. and Schaeffer, A. J. (2018). Fluid pressure and shear zone development over the locked to slow slip region in Cascadia. *Science Advances*, *4*(3), eaar2982.

Bachmann, F., Hielscher, R., and Schaeben, H. (2010). Texture Analysis with MTEX Free and Open Source Software Toolbox. *Solid State Phenomena*, *160*, 63–68.

Bannister, S., Reyners, M., Stuart, G., and Savage, M. (2007). Imaging the Hikurangi subduction zone, New Zealand, using teleseismic receiver functions: crustal fluids above the forearc mantle wedge. *Geophysical Journal International*, *169*(2), 602–616.

Barker, D. H. N., Henrys, S., Caratori Tontini, F., Barnes, P. M., Bassett, D., Todd, E., and Wallace, L. (2018). Geophysical Constraints on the Relationship Between Seamount Subduction, Slow Slip, and Tremor at the North Hikurangi Subduction Zone, New Zealand. *Geophysical Research Letters*, *45*(23), 12,804–12,813.

Barker, D. H. N., Sutherland, R., Henrys, S., and Bannister, S. (2009). Geometry of the Hikurangi subduction thrust and upper plate, North Island, New Zealand. *Geochemistry, Geophysics, Geosystems*, *10*(2).

Barnes, P. M., Lamarche, G., Bialas, J., Henrys, S., Pecher, I., Netzeband, G. L., Greinert, J., Mountjoy, J. J., Pedley, K., and Crutchley, G. (2010). Tectonic and geological framework for gas hydrates and cold seeps on the Hikurangi subduction margin, New Zealand. *Marine Geology*, *272*(1-4), 26–48.

Barnes, P. M., Wallace, L. M., Saffer, D. M., Bell, R. E., Underwood, M. B., Fagereng, A., Meneghini, F., Savage, H. M., Rabinowitz, H. S., Morgan, J. K., Kitajima, H., Kutterolf, S., Hashimoto, Y., Engelmann de Oliveira, C. H., Noda, A., Crundwell, M. P., Shepherd, C. L., Woodhouse, A. D., Harris, R. N., Wang, M., Henrys, S., Barker, D. H., Petronotis, K. E., Bourlange, S. M., Clennell, M. B.,

Cook, A. E., Dugan, B. E., Elger, J., Fulton, P. M., Gamboa, D., Greve, A., Han, S., Hüpers, A., Ikari, M. J., Ito, Y., Kim, G. Y., Koge, H., Lee, H., Li, X., Luo, M., Malie, P. R., Moore, G. F., Mountjoy, J. J., McNamara, D. D., Paganoni, M., Screaton, E. J., Shankar, U., Shreedharan, S., Solomon, E. A., Wang, X., Wu, H.-Y., Pecher, I. A., and LeVay, L. J. (2020). Slow slip source characterized by lithological and geometric heterogeneity. *Science Advances*, *6*(13).

Bassett, D., Sutherland, R., and Henrys, S. (2014). Slow wavespeeds and fluid overpressure in a region of shallow geodetic locking and slow slip, Hikurangi subduction margin, New Zealand. *Earth and Planetary Science Letters*, *389*, 1–13.

Baud, P., Rolland, A., Heap, M., Xu, T., Nicolé, M., Ferrand, T., Reuschlé, T., Toussaint, R., and Conil, N. (2016). Impact of stylolites on the mechanical strength of limestone. *Tectonophysics*, *690*, 4–20.

Bauer, H., Rogowitz, A., Grasemann, B., and Decker, K. (2018). Intracrystalline deformation of calcite in the upper brittle crust. *Geology*, *46*(4), 375–378.

Beall, A., Fagereng, Å., and Ellis, S. (2019). Strength of Strained TwoPhase Mixtures: Application to Rapid Creep and Stress Amplification in Subduction Zone Mélange. *Geophysical Research Letters*, *46*(1), 169–178.

Beanland, S. and Haines, J. (1998). The kinematics of active deformation in the North Island, New Zealand, determined from geological strain rates. *New Zealand Journal of Geology and Geophysics*, *41*(4), 311–323.

Beavan, J., Tregoning, P., Bevis, M., Kato, T., and Meertens, C. (2002). Motion and rigidity of the Pacific Plate and implications for plate boundary deformation. *Journal of Geophysical Research: Solid Earth*, *107*(B10), ETG 19–1–ETG 19–15.

Behr, W. M. and Bürgmann, R. (2021). What's down there? The structures, materials and environment of deep-seated slow slip and tremor. *Philosophical Transactions of the Royal Society A: Mathematical, Physical and Engineering Sciences*, *379*(2193), 20200218.

Bekins, B. A. and Dreiss, S. J. (1992). A simplified analysis of parameters controlling dewatering in accretionary prisms. *Earth and Planetary Science Letters*, *109*(3-4), 275–287.

Bell, R., Fagereng, A., and Arai, R. (2018). New Zealand 3D Full Waveform Inversion (NZ3D-FWI) 2017 2018 Field Acquisition Report. Technical Report December 2019.

Bell, R., Sutherland, R., Barker, D. H. N., Henrys, S., Bannister, S., Wallace, L., and Beavan, J. (2010). Seismic reflection character of the Hikurangi subduction interface, New Zealand, in the region of repeated Gisborne slow slip events. *Geophysical Journal International*, *180*(1), 34–48.

Beroza, G. C. and Ide, S. (2011). Slow Earthquakes and Nonvolcanic Tremor. *Annual Review of Earth and Planetary Sciences*, *39*(1), 271–296.

Bestmann, M. and Prior, D. J. (2003). Intragranular dynamic recrystallization in naturally deformed calcite marble: diffusion accommodated grain boundary sliding as a result of subgrain rotation recrystallization. *Journal of Structural Geology*, *25*(10), 1597–1613.

Bettelli, G. and Vannucchi, P. (2003). Structural style of the offscraped Ligurian oceanic sequences of the Northern Apennines: new hypothesis concerning the development of mélange block-in-matrix fabric. *Journal of Structural Geology*, *25*(3), 371–388.

Beyreuther, M., Barsch, R., Krischer, L., Megies, T., Behr, Y., and Wassermann, J. (2010). ObsPy: A Python Toolbox for Seismology. *Seismological Research Letters*, *81*(3), 530–533.

Blenkinsop, T. G. (1991). Cataclasis and processes of particle size reduction. *Pure and Applied Geophysics*, *136*(1), 59–86.

Bletery, Q., Thomas, A. M., Rempel, A. W., and Hardebeck, J. L. (2017). Imaging Shear Strength Along Subduction Faults. *Geophysical Research Letters*, *44*(22), 11,329–11,339.

Bodin, T., Sambridge, M., Tkalčić, H., Arroucau, P., Gallagher, K., and Rawlinson, N. (2012). Transdimensional inversion of receiver functions and surface wave dispersion. *Journal of Geophysical Research: Solid Earth*, *117*(B2).

Bodin, T., Yuan, H., and Romanowicz, B. (2014). Inversion of receiver functions without deconvolutionapplication to the Indian craton. *Geophysical Journal International*, *196*(2), 1025–1033.

Bonnet, G., Agard, P., Angiboust, S., Fournier, M., and Omrani, J. (2019). No large earthquakes in fully exposed subducted seamount. *Geology*, *47*(5), 407–410.

Bons, P. D., Elburg, M. A., and Gomez-Rivas, E. (2012). A review of the formation of tectonic veins and their microstructures. *Journal of Structural Geology*, *43*, 33–62.

Borg, I. Y. and Heard, H. C. (1970). Experimental deformation of plagioclases. In *Experimental and Natural Rock Deformation/Experimentelle und natürliche Gesteinsverformung*, 375–403. Springer.

Bos, B. (2002). Frictional-viscous flow of phyllosilicate-bearing fault rock: Microphysical model and implications for crustal strength profiles. *Journal of Geophysical Research*, *107*(B2), 2028.

Bos, B., Peach, C. J., and Spiers, C. J. (2000). Slip behavior of simulated gouge-bearing faults under conditions favoring pressure solution. *Journal of Geophysical Research: Solid Earth*, *105*(B7), 16699–16717.

Bos, B. and Spiers, C. (2001). Experimental investigation into the microstructural and mechanical evolution of phyllosilicate-bearing fault rock under conditions favouring pressure solution. *Journal of Structural Geology*, *23*(8), 1187–1202.

Boulton, C., Moore, D. E., Lockner, D. A., Toy, V. G., Townend, J., and Sutherland, R. (2014). Frictional properties of exhumed fault gouges in DFDP-1 cores, Alpine Fault, New Zealand. *Geophysical Research Letters*, *41*(2), 356–362.

Boulton, C., Niemeijer, A. R., Hollis, C. J., Townend, J., Raven, M. D., Kulhanek, D. K., and Shepherd, C. L. (2019). Temperature-dependent frictional properties of heterogeneous Hikurangi Subduction Zone input sediments, ODP Site 1124. *Tectonophysics*, *757*, 123–139.

Bürgmann, R. (2018). The geophysics, geology and mechanics of slow fault slip. *Earth and Planetary Science Letters*, *495*, 112–134.

Buxton, T. M. and Sibley, D. F. (1981). Pressure solution features in a shallow buried limestone. *Journal of Sedimentary Petrology*, *51*(1), 19–26.

Byrne, T., Maltman, A., Stephenson, E., Wonn Soh, and Knipe, R. (1993). Deformation structures and fluid flow in the toe region of the Nankai accretionary prism. In *Proc., scientific results, ODP, Leg 131, Nankai Trough*, Volume 131, 83–101. Ocean Drilling Program.

Casey, M., Kunze, K., and Olgaard, D. L. (1998). Texture of Solnhofen limestone deformed to high strains in torsion. *Journal of Structural Geology*, *20*(2-3), 255–267.

Cassidy, J. F. (1992). Numerical experiments in broadband receiver function analysis. *Bulletin - Seismological Society of America*, *82*(3), 1453–1474.

Cathelineau, M. and Nieva, D. (1985). A chlorite solid solution geothermometer the Los Azufres (Mexico) geothermal system. *Contributions to Mineralogy and Petrology*, *91*(3), 235–244.

Cerchiari, A., Remitti, F., Mittempergher, S., Festa, A., Lugli, F., and Cipriani, A. (2020). Cyclical variations of fluid sources and stress state in a shallow megathrust-zone mélange. *Journal of the Geological Society*, *177*(3), 647–659.

Chang, C., McNeill, L. C., Moore, J. C., Lin, W., Conin, M., and Yamada, Y. (2010). In situ stress state in the Nankai accretionary wedge estimated from borehole wall failures. *Geochemistry, Geophysics, Geosystems*, *11*(12).

Chang, C. and Song, I. (2016). Present-day stress states underneath the Kumano basin to 2 km below seafloor based on borehole wall failures at IODP site C0002,

Nankai accretionary wedge. *Geochemistry, Geophysics, Geosystems*, *17*(11), 4289–4307.

Chen, J. and Niemeijer, A. R. (2017). Seismogenic Potential of a Gouge-filled Fault and the Criterion for Its Slip Stability: Constraints From a Microphysical Model. *Journal of Geophysical Research: Solid Earth*, *122*(12), 9658–9688.

Chen, J., Niemeijer, A. R., and Spiers, C. J. (2017). Microphysically Derived Expressions for Rate-and-State Friction Parameters, a , b , and D c. *Journal of Geophysical Research: Solid Earth*, *122*(12), 9627–9657.

Chen, J., Niemeijer, A. R., and Spiers, C. J. (2021). Microphysical Modeling of Carbonate Fault Friction at Slip Rates Spanning the Full Seismic Cycle. *Journal of Geophysical Research: Solid Earth*, *126*(3).

Chen, J. and Spiers, C. J. (2016). Rate and state frictional and healing behavior of carbonate fault gouge explained using microphysical model. *Journal of Geophysical Research: Solid Earth*, *121*(12), 8642–8665.

Chen, J., Verberne, B. A., and Niemeijer, A. R. (2020). FlowtoFriction Transition in Simulated Calcite Gouge: Experiments and Microphysical Modeling. *Journal of Geophysical Research: Solid Earth*, *125*(11), 1–25.

Chester, F. M. (1994). Effects of temperature on friction: Constitutive equations and experiments with quartz gouge. *Journal of Geophysical Research*, *99*(B4), 7247.

Chester, F. M., Rowe, C., Ujiie, K., Kirkpatrick, J., Regalla, C., Remitti, F., Moore, J. C., Toy, V., Wolfson-Schwehr, M., Bose, S., Kameda, J., Mori, J. J., Brodsky, E. E., Eguchi, N., and Toczko, S. (2013). Structure and Composition of the Plate-Boundary Slip Zone for the 2011 Tohoku-Oki Earthquake. *Science*, *342*(6163), 1208–1211.

Christensen, N. I. (1966). Elasticity of ultrabasic rocks. *Journal of Geophysical Research*, *71*(24), 5921–5931.

Clark, K., Howarth, J., Litchfield, N., Cochran, U., Turnbull, J., Dowling, L., Howell, A., Berryman, K., and Wolfe, F. (2019). Geological evidence for past large earthquakes and tsunamis along the Hikurangi subduction margin, New Zealand. *Marine Geology*, *412*, 139–172.

Clarke, A. P., Vannucchi, P., and Morgan, J. (2018). Seamount chain-subduction zone interactions: Implications for accretionary and erosive subduction zone behavior. *Geology*, *46*(4), 367–370.

Coble, R. L. (1963). A Model for Boundary Diffusion Controlled Creep in Polycrystalline Materials. *Journal of Applied Physics*, *34*(6), 1679–1682.

Collettini, C., Niemeijer, A., Viti, C., and Marone, C. (2009). Fault zone fabric and fault weakness. *Nature*, *462*(7275), 907–910.

Collins, A. S. and Buchan, C. (2004). Provenance and age constraints of the South Stack Group, Anglesey, UK: U-Pb SIMS detrital zircon data. *Journal of the Geological Society*, *161*(5), 743–746.

Cox, D. R. and Lewis, P. A. W. (1966). *The Statistical Analysis of Series of Events*. London: Chapman and Hall.

Cox, S. F. (2011). The Application of Failure Mode Diagrams for Exploring the Roles of Fluid Pressure and Stress States in Controlling Styles of Fracture-Controlled Permeability Enhancement in Faults and Shear Zones. In *Frontiers in Geofluids*, Volume 10, 217–233. Oxford, UK: Wiley-Blackwell.

Croizé, D., Renard, F., Bjørlykke, K., and Dysthe, D. K. (2010). Experimental calcite dissolution under stress: Evolution of grain contact microstructure during pressure solution creep. *Journal of Geophysical Research: Solid Earth*, *115*(9), B09207.

Cross, A. J., Prior, D. J., Stipp, M., and Kidder, S. (2017). The recrystallized grain size piezometer for quartz: An EBSD-based calibration. *Geophysical Research Letters*, *44*(13), 6667–6674.

Crotwell, H. P., Owens, T. J., and Ritsema, J. (1999). The TauP Toolkit: Flexible Seismic Travel-time and Ray-path Utilities. *Seismological Research Letters*, *70*(2), 154–160.

Dahlen, F. (1990). Critical Taper Model Of Fold-And-Thrust Belts And Accretionary Wedges. *Annual Review of Earth and Planetary Sciences*, *18*(1), 55–99.

Davis, D., Suppe, J., and Dahlen, F. A. (1984). Mechanics of Fold-and-Thrust Belts and Accretionary Wedges: Cohesive Coulomb Theory. *Journal of Geophysical Research*, *89*(B12), 10087–10101.

Davy, B., Hoernle, K., and Werner, R. (2008). Hikurangi Plateau: Crustal structure, rifted formation, and Gondwana subduction history. *Geochemistry, Geophysics, Geosystems*, *9*(7).

Davy, B. and Wood, R. (1994). Gravity and magnetic modelling of the Hikurangi Plateau. *Marine Geology*, *118*(1-2), 139–151.

De Bresser, J. H., Evans, B., and Renner, J. (2002). On estimating the strength of calcite rocks under natural conditions. *Geological Society Special Publication*, *200*(1), 309–329.

De Bresser, J. H. and Spiers, C. J. (1997). Strength characteristics of the r, f, and c slip systems in calcite. *Tectonophysics*, *272*(1), 1–23.

De Bresser, J. H., Ter Heege, J. H., and Spiers, C. J. (2001). Grain size reduction by dynamic recrystallization: Can it result in major rheological weakening? *International Journal of Earth Sciences*, *90*(1), 28–45.

De Bresser, J. H. P. (2002). On the mechanism of dislocation creep of calcite at high temperature: Inferences from experimentally measured pressure sensitivity and strain rate sensitivity of flow stress. *Journal of Geophysical Research: Solid Earth*, *107*(B12), ECV 4–1–ECV 4–16.

de Bresser, J. H. P. and Spiers, C. J. (1993). Slip systems in calcite single crystals deformed at 300-800řC. *Journal of Geophysical Research: Solid Earth*, *98*(B4), 6397–6409.

De Paola, N., Holdsworth, R. E., Viti, C., Collettini, C., and Bullock, R. (2015). Can grain size sensitive flow lubricate faults during the initial stages of earthquake propagation? *Earth and Planetary Science Letters*, *431*, 48–58.

Delahaye, E. J., Townend, J., Reyners, M. E., and Rogers, G. (2009). Microseismicity but no tremor accompanying slow slip in the Hikurangi subduction zone, New Zealand. *Earth and Planetary Science Letters*, *277*(1-2), 21–28.

Delle Piane, C., Clennell, M. B., Keller, J. V., Giwelli, A., and Luzin, V. (2017). Carbonate hosted fault rocks: A review of structural and microstructural characteristic with implications for seismicity in the upper crust. *Journal of Structural Geology*, *103*, 17–36.

Demurtas, M., Smith, S. A. F., Prior, D. J., Brenker, F. E., and Di Toro, G. (2019). Grain Size Sensitive Creep During Simulated Seismic Slip in Nanogranular Fault Gouges: Constraints From Transmission Kikuchi Diffraction (TKD). *Journal of Geophysical Research: Solid Earth*, *124*(10), 10197–10209.

den Hartog, S., Niemeijer, A., and Spiers, C. (2012). New constraints on megathrust slip stability under subduction zone P T conditions. *Earth and Planetary Science Letters*, *353-354*, 240–252.

Den Hartog, S. A., Saffer, D. M., and Spiers, C. J. (2014). The roles of quartz and water in controlling unstable slip in phyllosilicate-rich megathrust fault gouges. *Earth, Planets and Space*, *66*(1), 78.

Den Hartog, S. A. and Spiers, C. J. (2014). A microphysical model for fault gouge friction applied to subduction megathrusts. *Journal of Geophysical Research: Solid Earth*, *119*(2), 1510–1529.

Dewers, T. and Ortoleva, P. (1990). Differentiated structures arising from mechanochemical feedback in stressed rocks. *Earth Science Reviews*, *29*(1-4), 283–298.

Dieterich, J. H. (1979). Modeling of rock friction 1. Experimental results and constitutive equations. *Journal of Geophysical Research: Solid Earth*, *84*(B5), 2161–2168.

Dimitrova, L. L., Wallace, L. M., Haines, A. J., and Williams, C. A. (2016). High-resolution view of active tectonic deformation along the Hikurangi subduction margin and the Taupo Volcanic Zone, New Zealand. *New Zealand Journal of Geology and Geophysics*, *59*(1), 43–57.

Doser, D. I. and Webb, T. H. (2003). Source parameters of large historical (1917-1961) earthquakes, North Island, New Zealand. *Geophysical Journal International*, *152*(3), 795–832.

Dragert, H. (2001). A Silent Slip Event on the Deeper Cascadia Subduction Interface. *Science*, *292*(5521), 1525–1528.

Dueker, K. G. and Sheehan, A. F. (1997). Mantle discontinuity structure from midpoint stacks of converted P to S waves across the Yellowstone hotspot track. *Journal of Geophysical Research: Solid Earth*, *102*(B4), 8313–8327.

Durney, D. W. (1972). Solution-transfer, an Important Geological Deformation Mechanism. *Nature*, *235*(5337), 315–317.

Eberhart-Phillips, D. and Bannister, S. (2015). 3-D imaging of the northern Hikurangi subduction zone, New Zealand: variations in subducted sediment, slab fluids and slow slip. *Geophysical Journal International*, *201*(2), 838–855.

Eberhart-Phillips, D., Bannister, S., and Reyners, M. (2017). Deciphering the 3-D distribution of fluid along the shallow Hikurangi subduction zone using P- and S-wave attenuation. *Geophysical Journal International*, *211*(2), 1032–1045.

Eberhart-Phillips, D., Reyners, M., Bannister, S., Chadwick, M., and Ellis, S. (2010). Establishing a versatile 3-D seismic velocity model for New Zealand. *Seismological Research Letters*, *81*(6), 992–1000.

Ebner, M., Piazolo, S., Renard, F., and Koehn, D. (2010). Stylolite interfaces and surrounding matrix material: Nature and role of heterogeneities in roughness and microstructural development. *Journal of Structural Geology*, *32*(8), 1070–1084.

Edwards, J. H., Kluesner, J. W., Silver, E. A., Brodsky, E. E., Brothers, D. S., Bangs, N. L., Kirkpatrick, J. D., Wood, R., and Okamoto, K. (2018). Corrugated megathrust revealed offshore from Costa Rica. *Nature Geoscience*, *11*(3), 197–202.

Ellis, S., Fagereng, Å., Barker, D., Henrys, S., Saffer, D., Wallace, L., Williams, C., and Harris, R. (2015). Fluid budgets along the northern Hikurangi subduction margin, New Zealand: The effect of a subducting seamount on fluid pressure. *Geophysical Journal International*, *202*(1), 277–297.

Etheridge, M. A. and Wilkie, J. C. (1979). Grainsize reduction, grain boundary sliding and the flow strength of mylonites. *Tectonophysics*, *58*(1-2), 159–178.

Eulenfeld, T. (2020). rf: Receiver function calculation in seismology. *Journal of Open Source Software*, *5*(48), 1808.

Fagereng and Beall, A. (2021). Is complex fault zone behaviour a reflection of rheological heterogeneity? *Philosophical Transactions of the Royal Society A: Mathematical, Physical and Engineering Sciences*, *379*(2193).

Fagereng, Savage, H. M., Morgan, J. K., Wang, M., Meneghini, F., Barnes, P. M., Bell, R., Kitajima, H., McNamara, D. D., Saffer, D. M., Wallace, L. M., Petronotis, K., and LeVay, L. (2019). Mixed deformation styles observed on a shallow subduction thrust, Hikurangi margin, New Zealand. *Geology*, *47*(9), 872–876.

Fagereng, Å. (2011a). Fractal vein distributions within a fault-fracture mesh in an exhumed accretionary mélange, Chrystalls Beach Complex, New Zealand. *Journal of Structural Geology*, *33*(5), 918–927.

Fagereng, Å. (2011b). Geology of the seismogenic subduction thrust interface. *Geological Society, London, Special Publications*, *359*(1), 55–76.

Fagereng, A. (2011c). Wedge geometry, mechanical strength, and interseismic coupling of the Hikurangi subduction thrust, New Zealand. *Tectonophysics*, *507*(1-4), 26–30.

Fagereng, Å. (2013). On stress and strain in a continuous-discontinuous shear zone undergoing simple shear and volume loss. *Journal of Structural Geology*, *50*, 44–53.

Fagereng, Å. and Biggs, J. (2019). New perspectives on geological strain rates' calculated from both naturally deformed and actively deforming rocks. *Journal of Structural Geology*, *125*(October 2018), 100–110.

Fagereng, Å. and Den Hartog, S. A. (2017). Subduction megathrust creep governed by pressure solution and frictional-viscous flow. *Nature Geoscience*, *10*(1), 51–57.

Fagereng, A., Diener, J., Ellis, S., and Remitti, F. (2018). Fluid-related deformation processes at the up- and down-dip limits of the subduction thrust seismogenic zone : What do the rocks tell us ? In T. Byrne, D. Fisher, L. McNeill, D. Saffer, K. Ujiie, M. Underwood, and A. Yamaguchi (Eds.), *Geology and Tectonics of Subduction Zones: A Tribute to Gaku Kimura*, Volume Geological, 1–30.

Fagereng, A. and Ellis, S. (2009). On factors controlling the depth of interseismic coupling on the Hikurangi subduction interface, New Zealand. *Earth and Planetary Science Letters*, *278*(1-2), 120–130.

Fagereng, Å., Remitti, F., and Sibson, R. H. (2010). Shear veins observed within anisotropic fabric at high angles to the maximum compressive stress. *Nature Geoscience*, *3*(7), 482–485.

Fagereng, Å. and Sibson, R. H. (2010). Mélange rheology and seismic style. *Geology*, *38*(8), 751–754.

Falcioni, M. and Deem, M. W. (1999). A biased Monte Carlo scheme for zeolite structure solution. *Journal of Chemical Physics*, *110*(3), 1754–1766.

Ferrand, T. P., Hilairet, N., Incel, S., Deldicque, D., Labrousse, L., Gasc, J., Renner, J., Wang, Y., Green, H. W., and Schubnel, A. (2017). Dehydration-driven stress transfer triggers intermediate-depth earthquakes. *Nature Communications*, *8*(1), 15247.

Ferraro, F., Grieco, D. S., Agosta, F., and Prosser, G. (2018). Space-time evolution of cataclasis in carbonate fault zones. *Journal of Structural Geology*, *110*(June 2017), 45–64.

Festa, A., Dilek, Y., Mittempergher, S., Ogata, K., Pini, G. A., and Remitti, F. (2018). Does subduction of mass transport deposits (MTDs) control seismic behavior of shallowlevel megathrusts at convergent margins? *Gondwana Research*, *60*, 186–193.

Festa, A., Dilek, Y., Pini, G., Codegone, G., and Ogata, K. (2012). Mechanisms and processes of stratal disruption and mixing in the development of mélanges and broken formations: Redefining and classifying mélanges. *Tectonophysics*, *568-569*, 7–24.

Fisher, D. M. and Byrne, T. (1987). Structural evolution of underthrusted sediments. *Tectonics*, *6*(6), 775–793.

Fisher, D. M. and Byrne, T. (1992). Strain variations in an ancient accretionary complex: Implications for forearc evolution. *Tectonics*, *11*(2), 330–347.

Fletcher, R. C. and Pollard, D. D. (1981). Anticrack model for pressure solution surfaces. *Geology*, *9*(9), 419–424.

Frassetto, A., Zandt, G., Gilbert, H., Owens, T. J., and Jones, C. H. (2010). Improved imaging with phase-weighted common conversion point stacks of receiver functions. *Geophysical Journal International*, *182*(1), 368–374.

Frassetto, A. M., Zandt, G., Gilbert, H., Owens, T. J., and Jones, C. H. (2011). Structure of the Sierra Nevada from receiver functions and implications for lithospheric foundering. *Geosphere*, *7*(4), 898–921.

Frederiksen, A. W. and Bostock, M. G. (2000). Modelling teleseismic waves in dipping anisotropic structures. *Geophysical Journal International*, *141*(2), 401–412.

Frederiksen, A. W. and Delaney, C. (2015). Deriving crustal properties from the P Coda without deconvolution: the southwestern Superior Province, North America. *Geophysical Journal International*, *201*(3), 1491–1506.

Fredrich, J. T., Evans, B., and Wong, T. F. (1989). Micromechanics of the brittle to plastic transition in Carrara marble. *Journal of Geophysical Research: Solid Earth*, *94*(B4), 4129–4145.

French, M. E. and Condit, C. B. (2019). Slip partitioning along an idealized subduction plate boundary at deep slow slip conditions. *Earth and Planetary Science Letters*, *528*, 115828.

French, M. E. and Morgan, J. K. (2020). Pore Fluid Pressures and Strength Contrasts Maintain Frontal Fault Activity, Northern Hikurangi Margin, New Zealand. *Geophysical Research Letters*, *47*(21), e2020GL089209.

Fyfe, W., Price, N., and Thompson, A. (1978). *Fluids in the Earth's Crust*, Volume 1. Elsevier.

Gardner, R., Piazolo, S., Evans, L., and Daczko, N. (2017). Patterns of strain localization in heterogeneous, polycrystalline rocks a numerical perspective. *Earth and Planetary Science Letters*, *463*, 253–265.

Geyer, C. J. (1991). Markov Chain Monte Carlo Maximum Likelihood. In *Computing Science and Statistics: Proceedings of the 23rd Symposium on the Interface*, Number 1, 156–163.

Ghisetti, F. C., Barnes, P. M., Ellis, S., Plaza-Faverola, A. A., and Barker, D. H. (2016). The last 2 Myr of accretionary wedge construction in the central Hikurangi margin (North Island, New Zealand): Insights from structural modeling. *Geochemistry, Geophysics, Geosystems*, *17*(7), 2661–2686.

Gibbons, W. and Ball, M. J. (1991). A discussion of Monian Supergroup stratigraphy in northwest Wales. *Journal of the Geological Society*, *148*(1), 5–8.

Gibbons, W. and Horák, J. (1990). Contrasting metamorphic terranes in northwest Wales. *Geological Society, London, Special Publications*, *51*(1), 315–327.

Gilbert, H. J. (2004). Images of crustal variations in the intermountain west. *Journal of Geophysical Research*, *109*(B3), B03306.

Gilbert, H. J., Sheehan, A. F., Dueker, K. G., and Molnar, P. (2003). Receiver functions in the western United States, with implications for upper mantle structure and dynamics. *Journal of Geophysical Research: Solid Earth*, *108*(B5), 1–19.

Gillespie, P. A., Johnston, J. D., Loriga, M. A., McCaffrey, K. J., Walsh, J. J., and Watterson, J. (1999). Influence of layering on vein systematics in line samples. *Geological Society Special Publication*, *155*(1), 35–56.

Gillis, K. and Coogan, L. (2011). Secular variation in carbon uptake into the ocean crust. *Earth and Planetary Science Letters*, *302*(3-4), 385–392.

Gomberg, J., Wech, A., Creager, K., Obara, K., and Agnew, D. (2016). Reconsidering earthquake scaling. *Geophysical Research Letters*, *43*(12), 6243–6251.

Grant, J. A. (1986). The isocon diagram; a simple solution to Gresens' equation for metasomatic alteration. *Economic Geology*, *81*(8), 1976–1982.

Gratier, J. P., Dysthe, D. K., and Renard, F. (2013). The Role of Pressure Solution Creep in the Ductility of the Earth's Upper Crust. In *Advances in Geophysics*, Volume 54, 47–179.

Gratier, J. P., Noiriel, C., and Renard, F. (2015). Experimental evidence for rock layering development by pressure solution. *Geology*, *43*(10), 871–874.

Gratier, J. P., Renard, F., and Labaume, P. (1999). How pressure solution creep and fracturing processes interact in the upper crust to make it behave in both a brittle and viscous manner. *Journal of Structural Geology*, *21*(8-9), 1189–1197.

Gray, M., Bell, R. E., Morgan, J. V., Henrys, S., and Barker, D. H. N. (2019). Imaging the Shallow Subsurface Structure of the North Hikurangi Subduction Zone, New Zealand, Using 2D FullWaveform Inversion. *Journal of Geophysical Research: Solid Earth*, *124*(8), 9049–9074.

Green, P. J. (1995). Reversible jump Markov chain Monte Carlo computation and Bayesian model determination. *Biometrika*, *82*(4), 711–732.

Greene, G. W., Kristiansen, K., Meyer, E. E., Boles, J. R., and Israelachvili, J. N. (2009). Role of electrochemical reactions in pressure solution. *Geochimica et Cosmochimica Acta*, *73*(10), 2862–2874.

Greenly, E. (1919). The Geology of Anglesey (Volume 1).

Griggs, D. T., Turner, F. J., and Heard, H. C. (1960). Chapter 4: Deformation of Rocks at 500ř to 800ř C. In *Memoir of the Geological Society of America*, Volume 79, 39–104. Geological Society of America.

Gülyüz, N., Shipton, Z. K., Kusçu, l., Lord, R. A., Kaymakc, N., Gülyüz, E., and Gladwell, D. R. (2018). Repeated reactivation of clogged permeable pathways in epithermal gold deposits: Kestanelik epithermal vein system, NW Turkey. *Journal of the Geological Society*, *175*(3), 509–524.

Gundersen, E., Renard, F., Dysthe, D. K., Bjørlykke, K., and Jamtveit, B. (2002). Coupling between pressure solution creep and diffusive mass transport in porous rocks. *Journal of Geophysical Research: Solid Earth*, *107*(B11), ECV 19–1–ECV 19–19.

Hailwood, E. A., Maddock, R. H., Ting Fung, and Rutter, E. H. (1992). Palaeomagnetic analysis of fault gouge and dating fault movement, Anglesey, north Wales. *Journal - Geological Society (London)*, *149*(2), 273–284.

Hall, E. O. (1951). The deformation and ageing of mild steel: II Characteristics of the Lüders deformation. *Proceedings of the Physical Society. Section B*, *64*(9), 742–747.

Han, R., Hirose, T., and Shimamoto, T. (2010). Strong velocity weakening and powder lubrication of simulated carbonate faults at seismic slip rates. *Journal of Geophysical Research: Solid Earth*, *115*(3), B03412.

Han, R., Hirose, T., Shimamoto, T., Lee, Y., and Ando, J.-i. (2011). Granular nanoparticles lubricate faults during seismic slip. *Geology*, *39*(6), 599–602.

Han, S., Bangs, N. L., Carbotte, S. M., Saffer, D. M., and Gibson, J. C. (2017). Links between sediment consolidation and Cascadia megathrust slip behaviour. *Nature Geoscience*, *10*(12), 954–959.

Handy, M. R. (1990). The solid-state flow of polymineralic rocks. *Journal of Geophysical Research*, *95*(B6), 8647.

Hardebeck, J. L. (2015). Stress orientations in subduction zones and the strength of subduction megathrust faults. *Science*, *349*(6253), 1213–1216.

Harris, R., Sakaguchi, A., Petronotis, K., Baxter, A., Berg, R., Burkett, A., Charpentier, D., Choi, J., Diz Ferreiro, P., Hamahashi, M., Hashimoto, Y., Heydolph, K., Jovane, L., Kastner, M., Kurz, W., Kutterolf, S., Li, Y., Malinverno, A., Martin, K., Millan, C., Nascimento, D., Saito, S., Sandoval Gutierrez, M., Screaton, E., Smith-Duque, C., Solomon, E., Straub, S., Tanikawa, W., Torres, M., Uchimura, H., Vannucchi, P., Yamamoto, Y., Yan, Q., and Zhao, X. (2013). Expedition 344 summary. In *Proc. IODP Volume 344*, Volume 344, 2.

Harris, R. N., Spinelli, G. A., and Fisher, A. T. (2017). Hydrothermal circulation and the thermal structure of shallow subduction zones. *Geosphere*, *13*(5), 1425–1444.

Hashimoto, Y. and Yamano, N. (2014). Geological evidence for shallow ductile-brittle transition zones along subduction interfaces: Example from the Shimanto Belt, SW Japan. *Earth, Planets and Space*, *66*(1), 141.

Heald, M. T. (1955). Stylolites in Sandstones. *The Journal of Geology*, *63*(2), 101–114.

Healy, D., Jones, R. R., and Holdsworth, R. E. (2006). Three-dimensional brittle shear fracturing by tensile crack interaction. *Nature*, *439*(7072), 64–67.

Heap, M., Reuschlé, T., Baud, P., Renard, F., and Iezzi, G. (2018). The permeability of stylolite-bearing limestone. *Journal of Structural Geology*, *116*(May), 81–93.

Heilbronner, R. and Barrett, S. (2014). *Image analysis in earth sciences: Microstructures and textures of earth materials*. Berlin, Heidelberg: Springer Berlin Heidelberg.

Heise, W., Caldwell, T. G., Bannister, S., Bertrand, E. A., Ogawa, Y., Bennie, S. L., and Ichihara, H. (2017). Mapping subduction interface coupling using magnetotellurics: Hikurangi margin, New Zealand. *Geophysical Research Letters*, *44*(18), 9261–9266.

Heise, W., Caldwell, T. G., Hill, G. J., Bennie, S. L., Wallin, E., and Bertrand, E. A. (2012). Magnetotelluric imaging of fluid processes at the subduction interface of the Hikurangi margin, New Zealand. *Geophysical Research Letters*, *39*(4), 1–5.

Henry, P. (2000). Fluid flow at the toe of the Barbados accretionary wedge constrained by thermal, chemical, and hydrogeologic observations and models. *Journal of Geophysical Research*, *105*(B11), 25855–25872.

Henrys, S., Reyners, M., Pecher, I., Bannister, S., Nishimura, Y., and Maslen, G. (2006). Kinking of the subducting slab by escalator normal faulting beneath the North Island of New Zealand. *Geology*, *34*(9), 777.

Henrys, S. A., Jacobs, K., Okaya, D. A., Van Avendonk, H. J., Bangs, N. L., Kurashimo, E., Arai, R., Kodaira, S., Savage, M. K., Barker, D. H. N., and Others (2018). Along-strike variations in the Hikurangi Subduction zone: land-based seismic observations during the 2017-2018 SHIRE seismic onshore-offshore imaging project. In *AGU Fall Meeting Abstracts*, Volume 2018, T51I—-0284.

Herath, P., Stern, T. A., Savage, M. K., Bassett, D., Henrys, S., and Boulton, C. (2020). Hydration of the crust and upper mantle of the Hikurangi Plateau as it subducts at the southern Hikurangi margin. *Earth and Planetary Science Letters*, *541*, 116271.

Herwegh, M. and Berger, A. (2004). Deformation mechanisms in second-phase affected microstructures and their energy balance. *Journal of Structural Geology*, *26*(8), 1483–1498.

Herwegh, M. and Jenni, A. (2001). Granular flow in polymineralic rocks bearing sheet silicates: New evidence from natural examples. *Tectonophysics*, *332*(3), 309–320.

Herwegh, M., Xiao, X., and Evans, B. (2003). The effect of dissolved magnesium on diffusion creep in calcite. *Earth and Planetary Science Letters*, *212*(3-4), 457–470.

Heuret, A., Conrad, C. P., Funiciello, F., Lallemand, S., and Sandri, L. (2012). Relation between subduction megathrust earthquakes, trench sediment thickness and upper plate strain. *Geophysical Research Letters*, *39*(5).

Hickman, S., Sibson, R., and Bruhn, R. (1995). Introduction to Special Section: Mechanical Involvement of Fluids in Faulting. *Journal of Geophysical Research: Solid Earth*, *100*(B7), 12831–12840.

Hickman, S. H. and Evans, B. (1995). Kinetics of pressure solution at halite-silica interfaces and intergranular clay films. *Journal of Geophysical Research*, *100*(B7), 13113–13132.

Hochmuth, K., Gohl, K., Uenzelmann-Neben, G., and Werner, R. (2019). Multiphase magmatic and tectonic evolution of a large igneous province - Evidence from the crustal structure of the Manihiki Plateau, western Pacific. *Tectonophysics*, *750*(November 2018), 434–457.

Horák, J. M. and Evans, J. A. (2011). Early Neoproterozoic limestones from the Gwna Group, Anglesey. *Geological Magazine*, *148*(1), 78–88.

Hubbert, M. K. and Rubey, W. W. (1961). Role of fluid pressure in mechanics of overthrust faulting, I. Mechanics of fluid-filled porous solids and its application to overthrust faulting: Reply to discussion by Francis Birch. *Bulletin of the Geological Society of America*, *72*(9), 1445–1451.

Hull, J. (1988). Thickness-displacement relationships for deformation zones. *Journal of Structural Geology*, *10*(4), 431–435.

Humphris, S. E. and Thompson, G. (1978). Hydrothermal alteration of oceanic basalts by seawater. *Geochimica et Cosmochimica Acta*, *42*(1), 107–125.

Hüpers, A., Saffer, D., and Kopf, A. (2018). Lithostratigraphic controls on dewatering and fluid pressure in the western Nankai subduction zone: Implications for

the drainage behavior and consolidation state of the underthrust sequence. In *Geology and Tectonics of Subduction Zones: A Tribute to Gaku Kimura*, Volume 534, 51–68. Geological Society of America.

Hüpers, A., Torres, M. E., Owari, S., McNeill, L. C., Dugan, B., Henstock, T. J., Milliken, K. L., Petronotis, K. E., Backman, J., Bourlange, S., Chemale, F., Chen, W., Colson, T. A., Frederik, M. C., Guèrin, G., Hamahashi, M., House, B. M., Jeppson, T. N., Kachovich, S., Kenigsberg, A. R., Kuranaga, M., Kutterolf, S., Mitchison, F. L., Mukoyoshi, H., Nair, N., Pickering, K. T., Pouderoux, H. F., Shan, Y., Song, I., Vannucchi, P., Vrolijk, P. J., Yang, T., and Zhao, X. (2017). Release of mineral-bound water prior to subduction tied to shallow seismogenic slip off Sumatra. *Science*, *356*(6340), 841–844.

Husker, A., Ferrari, L., Arango-Galván, C., Corbo-Camargo, F., and Arzate-Flores, J. A. (2018). A geologic recipe for transient slip within the seismogenic zone: Insight from the Guerrero seismic gap, Mexico. *Geology*, *46*(1), 35–38.

Hyndman, R. D. and Wang, K. (1993). Thermal constraints on the zone of major thrust earthquake failure: the Cascadia Subduction Zone. *Journal of Geophysical Research*, *98*(B2), 2039–2060.

Hyndman, R. D., Yamano, M., and Oleskevich, D. A. (1997). The seismogenic zone of subduction thrust faults. *Island Arc*, *6*(3), 244–260.

Ikari, M. J., Niemeijer, A. R., Spiers, C. J., Kopf, A. J., and Saffer, D. M. (2013). Experimental evidence linking slip instability with seafloor lithology and topography at the Costa Rica convergent margin. *Geology*, *41*(8), 891–894.

Ikari, M. J. and Saffer, D. M. (2012). Permeability contrasts between sheared and normally consolidated sediments in the Nankai accretionary prism. *Marine Geology*, *295-298*, 1–13.

Ikari, M. J., Saffer, D. M., and Marone, C. (2009). Frictional and hydrologic properties of clay-rich fault gouge. *Journal of Geophysical Research: Solid Earth*, *114*(5), B05409.

Ikari, M. J., Wallace, L. M., Rabinowitz, H. S., Savage, H. M., Hamling, I. J., and Kopf, A. J. (2020). Observations of Laboratory and Natural Slow Slip Events: Hikurangi Subduction Zone, New Zealand. *Geochemistry, Geophysics, Geosystems*, *21*(2), 1–19.

Im, K., Saffer, D., Marone, C., and Avouac, J. P. (2020). Slip-rate-dependent friction as a universal mechanism for slow slip events. *Nature Geoscience*, *13*(10), 705–710.

Imber, J., Holdsworth, R. E., Smith, S. A., Jefferies, S. P., and Collettini, C. (2008). Frictional-viscous flow, seismicity and the geology of weak faults: A review and future directions. *Geological Society Special Publication*, *299*(1), 151–173.

Irwin, G. R. (1957). Analysis of Stresses and Strains Near the End of a Crack Traversing a Plate. *Journal of Applied Mechanics*, *24*(3), 361–364.

Ito, Y., Hino, R., Kido, M., Fujimoto, H., Osada, Y., Inazu, D., Ohta, Y., Iinuma, T., Ohzono, M., Miura, S., Mishina, M., Suzuki, K., Tsuji, T., and Ashi, J. (2013). Episodic slow slip events in the Japan subduction zone before the 2011 Tohoku-Oki earthquake. *Tectonophysics*, *600*, 14–26.

Kameda, J., Harris, R. N., Shimizu, M., Ujiie, K., Tsutsumi, A., Ikehara, M., Uno, M., Yamaguchi, A., Hamada, Y., Namiki, Y., and Kimura, G. (2015). Hydrogeological responses to incoming materials at the erosional subduction margin, offshore Osa Peninsula, Costa Rica. *Geochemistry, Geophysics, Geosystems*, *16*(8), 2725–2742.

Kameda, J., Inoue, S., Tanikawa, W., Yamaguchi, A., Hamada, Y., Hashimoto, Y., and Kimura, G. (2017). Alteration and dehydration of subducting oceanic crust within subduction zones: implications for décollement step-down and plate-boundary seismogenesis. *Earth, Planets and Space*, *69*(1), 52.

Karato, S. I. (2008). *Deformation of earth materials: An introduction to the rheology of solid earth*, Volume 9780521844. Cambridge: Cambridge University Press.

Kato, A., Iidaka, T., Ikuta, R., Yoshida, Y., Katsumata, K., Iwasaki, T., Sakai, S., Thurber, C., Tsumura, N., Yamaoka, K., Watanabe, T., Kunitomo, T., Yamazaki,

F., Okubo, M., Suzuki, S., and Hirata, N. (2010). Variations of fluid pressure within the subducting oceanic crust and slow earthquakes. *Geophysical Research Letters*, *37*(14).

Kato, A., Obara, K., Igarashi, T., Tsuruoka, H., Nakagawa, S., and Hirata, N. (2012). Propagation of slow slip leading up to the 2011 Mw 9.0 Tohoku-Oki earthquake. *Science*, *335*(6069), 705–708.

Kawabata, K., Tanaka, H., and Kimura, G. (2007). Mass transfer and pressure solution in deformed shale of accretionary complex: Examples from the Shimanto Belt, southwestern Japan. *Journal of Structural Geology*, *29*(4), 697–711.

Kawai, T., Windley, B. F., Terabayashi, M., Yamamoto, H., Isozaki, Y., and Maruyama, S. (2008). Neoproterozoic glaciation in the mid-oceanic realm: An example from hemi-pelagic mudstones on Llanddwyn Island, Anglesey, UK. *Gondwana Research*, *14*(1-2), 105–114.

Kawai, T., Windley, B. F., Terabayashi, M., Yamamoto, H., Maruyama, S., Omori, S., Shibuya, T., Sawaki, Y., and Isozaki, Y. (2007). Geotectonic framework of the Blueschist Unit on Anglesey-Lleyn, UK, and its role in the development of a Neoproterozoic accretionary orogen. *Precambrian Research*, *153*(1-2), 11–28.

Kennedy, L. A. and White, J. C. (2001). Low-temperature recrystallization in calcite: Mechanisms and consequences. *Geology*, *29*(11), 1027–1030.

Kennett, B. L., Engdahl, E. R., and Buland, R. (1995). Constraints on seismic velocities in the Earth from traveltimes. *Geophysical Journal International*, *122*(1), 108–124.

Kennett, B. L. N. (1991). Iaspei 1991 Seismological Tables. *Terra Nova*, *3*(2), 122–122.

Keulen, N., Heilbronner, R., Stünitz, H., Boullier, A. M., and Ito, H. (2007). Grain size distributions of fault rocks: A comparison between experimentally and naturally deformed granitoids. *Journal of Structural Geology*, *29*(8), 1282–1300.

Kikuchi, M. and Kanamori, H. (1991). Inversion of complex body waves - III. *Bulletin - Seismological Society of America*, *81*(6), 2335–2350.

Kim, S., Ree, J. H., Han, R., Kim, N., and Jung, H. (2018). Fabric transition with dislocation creep of a carbonate fault zone in the brittle regime. *Tectonophysics*, *723*(December 2017), 107–116.

Kim, Y., Miller, M. S., Pearce, F., and Clayton, R. W. (2012). Seismic imaging of the Cocos plate subduction zone system in central Mexico. *Geochemistry, Geophysics, Geosystems*, *13*(7).

Kimura, G. and Mukai, A. (1991). Underplated units in an accretionary complex: Melange of the Shimanto Belt of eastern Shikoku, southwest Japan. *Tectonics*, *10*(1), 31–50.

Kimura, G., Yamaguchi, A., Hojo, M., Kitamura, Y., Kameda, J., Ujiie, K., Hamada, Y., Hamahashi, M., and Hina, S. (2012). Tectonic mélange as fault rock of subduction plate boundary. *Tectonophysics*, *568-569*, 25–38.

Kimura, H., Kasahara, K., and Takeda, T. (2009). Subduction process of the Philippine Sea Plate off the Kanto district, central Japan, as revealed by plate structure and repeating earthquakes. *Tectonophysics*, *472*(1-4), 18–27.

Kinoshita, M., Tobin, H., Ashi, J., Kimura, G., Lallemant, S., Screaton, E., Curewitz, D., Masago, H., and Moe, K. (Eds.) (2009). *NanTroSEIZE Stage 1*, Volume 314/315/31 of *Proceedings of the IODP*. International Ocean Discovery Program.

Kirton, S. R. and Donato, J. A. (1985). Some buried Tertiary dykes of Britain and surrounding waters deduced by magnetic modelling and seismic reflection methods. *Journal of the Geological Society*, *142*(6), 1047–1057.

Kitajima, H., Saffer, D., Sone, H., Tobin, H., and Hirose, T. (2017). In Situ Stress and Pore Pressure in the Deep Interior of the Nankai Accretionary Prism, Integrated Ocean Drilling Program Site C0002. *Geophysical Research Letters*, *44*(19), 9644–9652.

Kobussen, A. F., Christensen, N. I., and Thybo, H. (2006). Constraints on seismic velocity anomalies beneath the Siberian craton from xenoliths and petrophysics. *Tectonophysics*, *425*(1-4), 123–135.

Kodaira, S., Iidaka, T., Kato, A., Park, J. O., Iwasaki, T., and Kaneda, Y. (2004). High pore fluid pressure may cause silent slip in the Nankai Trough. *Science*, *304*(5675), 1295–1298.

Kodaira, S., Takahashi, N., Park, J. O., Mochizuki, K., Shinohara, M., and Kimura, S. (2000). Western Nankai Trough seismogenic zone: Results from a wide-angle ocean bottom seismic survey. *Journal of Geophysical Research: Solid Earth*, *105*(B3), 5887–5905.

Koehn, D., Rood, M., Beaudoin, N., Chung, P., Bons, P., and Gomez-Rivas, E. (2016). A new stylolite classification scheme to estimate compaction and local permeability variations. *Sedimentary Geology*, *346*, 60–71.

Kotowski, A. J. and Behr, W. M. (2019). Length scales and types of heterogeneities along the deep subduction interface: Insights from exhumed rocks on Syros Island, Greece. *Geosphere*, *15*(4), 1038–1065.

Koulali, A., McClusky, S., Wallace, L., Allgeyer, S., Tregoning, P., D'Anastasio, E., and Benavente, R. (2017). Slow slip events and the 2016 Te Araroa Mw 7.1 earthquake interaction: Northern Hikurangi subduction, New Zealand. *Geophysical Research Letters*, *44*(16), 8336–8344.

Krischer, L., Megies, T., Barsch, R., Beyreuther, M., Lecocq, T., Caudron, C., and Wassermann, J. (2015). ObsPy: a bridge for seismology into the scientific Python ecosystem. *Computational Science & Discovery*, *8*(1), 014003.

Kronenberg, A. K., Kirby, S. H., and Pinkston, J. (1990). Basal slip and mechanical anisotropy of biotite. *Journal of Geophysical Research*, *95*(B12), 19257.

Kurzawski, R. M., Niemeijer, A. R., Stipp, M., Charpentier, D., Behrmann, J. H., and Spiers, C. J. (2018). Frictional Properties of Subduction Input Sediments

at an Erosive Convergent Continental Margin and Related Controls on Décollement Slip Modes: The Costa Rica Seismogenesis Project. *Journal of Geophysical Research: Solid Earth*, *123*(10), 8385–8408.

Kurzawski, R. M., Stipp, M., Niemeijer, A. R., Spiers, C. J., and Behrmann, J. H. (2016). Earthquake nucleation in weak subducted carbonates. *Nature Geoscience*, *9*(9), 717–722.

Kushnir, A. R., Kennedy, L. A., Misra, S., Benson, P., and White, J. C. (2015). The mechanical and microstructural behaviour of calcite-dolomite composites: An experimental investigation. *Journal of Structural Geology*, *70*, 200–216.

Lacroix, B., Tesei, T., Oliot, E., Lahfid, A., and Collettini, C. (2015). Early weakening processes inside thrust fault. *Tectonics*, *34*(7), 1396–1411.

Lamb, S. (2006). Shear stresses on megathrusts: Implications for mountain building behind subduction zones. *Journal of Geophysical Research*, *111*(B7), B07401.

Langston, C. A. (1979). Structure under Mount Rainier, Washington, inferred from teleseismic body waves. *Journal of Geophysical Research*, *84*(B9), 4749.

Laronne Ben-Itzhak, L., Aharonov, E., Karcz, Z., Kaduri, M., and Toussaint, R. (2014). Sedimentary stylolite networks and connectivity in limestone: Large-scale field observations and implications for structure evolution. *Journal of Structural Geology*, *63*, 106–123.

Laronne Ben-Itzhak, L., Aharonov, E., Toussaint, R., and Sagy, A. (2012). Upper bound on stylolite roughness as indicator for amount of dissolution. *Earth and Planetary Science Letters*, *337-338*, 186–196.

Larson, K. M., Lowry, A. R., Kostoglodov, V., Hutton, W., Sánchez, O., Hudnut, K., and Suárez, G. (2004). Crustal deformation measurements in Guerrero, Mexico. *Journal of Geophysical Research: Solid Earth*, *109*(4).

Lauer, R. M. and Saffer, D. M. (2012). Fluid budgets of subduction zone forearcs: The contribution of splay faults. *Geophysical Research Letters*, *39*(13).

Lawther, S. E., Dempster, T. J., Shipton, Z. K., and Boyce, A. J. (2016). Effective crustal permeability controls fault evolution: An integrated structural, mineralogical and isotopic study in granitic gneiss, Monte Rosa, northern Italy. *Tectonophysics*, *690*, 160–173.

Leah, H., Fondriest, M., Lucca, A., Storti, F., Balsamo, F., and Di Toro, G. (2018). Coseismic extension recorded within the damage zone of the Vado di Ferruccio Thrust Fault, Central Apennines, Italy. *Journal of Structural Geology*, *114*, 121–138.

Leeman, J. R., Saffer, D. M., Scuderi, M. M., and Marone, C. (2016). Laboratory observations of slow earthquakes and the spectrum of tectonic fault slip modes. *Nature Communications*, *7*, 11104.

Lehner, F. K. (1995). A model for intergranular pressure solution in open systems. *Tectonophysics*, *245*(3-4), 153–170.

Li, C. H. and Lee, C. K. (1993). Minimum cross entropy thresholding. *Pattern Recognition*, *26*(4), 617–625.

Li, C. H. and Tam, P. K. (1998). An iterative algorithm for minimum cross entropy thresholding. *Pattern Recognition Letters*, *19*(8), 771–776.

Li, J. C. and Chou, Y. T. (1970). The role of dislocations in the flow stress grain size relationships. *Metallurgical and Materials Transactions*, *1*(5), 1145–1159.

Ligorría, J. P. and Ammon, C. J. (1999). Iterative deconvolution and receiver-function estimation. *Bulletin of the Seismological Society of America*, *89*(5), 1395–1400.

Lin, W., Conin, M., Moore, J. C., Chester, F. M., Nakamura, Y., Mori, J. J., Anderson, L., Brodsky, E. E., Eguchi, N., Cook, B., Jeppson, T., Wolfson-Schwehr, M., Sanada, Y., Saito, S., Kido, Y., Hirose, T., Behrmann, J. H., Ikari, M., Ujiie, K., Rowe, C., Kirkpatrick, J., Bose, S., Regalla, C., Remitti, F., Toy, V., Fulton, P., Mishima, T., Yang, T., Sun, T., Ishikawa, T., Sample, J., Takai, K., Kameda, J., Toczko, S., Maeda, L., Kodaira, S., Hino, R., and Saffer, D. (2013).

Stress state in the largest displacement area of the 2011 Tohoku-Oki earthquake. *Science*, *339*(6120), 687–690.

Lind, I. (1993). Stylolites in Chalk from Leg 130, Ontong Java Plateau. In *Proceedings of the Ocean Drilling Program, 130 Scientific Results*, Volume 130, 445–451. Ocean Drilling Program.

Litchfield, N. J., Clark, K. C., Cochran, U. A., Mcfadgen, B. G., Berryman, K. R., and Steele, R. (2016). Gisborne seismic and tsunami hazard: constraints from marine terraces at Puatai Beach. Technical Report June, GNS Science Report 2016/21.

Litchfield, N. J., Van Dissen, R., Sutherland, R., Barnes, P. M., Cox, S. C., Norris, R., Beavan, R. J., Langridge, R., Villamor, P., Berryman, K., Stirling, M., Nicol, A., Nodder, S., Lamarche, G., Barrell, D. J., Pettinga, J. R., Little, T., Pondard, N., Mountjoy, J. J., and Clark, K. (2014). A model of active faulting in New Zealand. *New Zealand Journal of Geology and Geophysics*, *57*(1), 32–56.

Logan, J. M., Dengo, C. A., Higgs, N. G., and Wang, Z. Z. (1992). *Fabrics of experimental fault zones: Their development and relationship to mechanical behavior BT - Fault Mechanics and Transport Properties of Rocks*, Volume Internatio.

Lu, L. X. and Jiang, D. (2019). Quartz Flow Law Revisited: The Significance of Pressure Dependence of the Activation Enthalpy. *Journal of Geophysical Research: Solid Earth*, *124*(1), 241–256.

L'Vov, B. V. (2002). Mechanism and kinetics of thermal decomposition of carbonates. *Thermochimica Acta*, *386*(1), 1–16.

Lyakhovsky, V., Ben-Zion, Y., and Agnon, A. (1997). Distributed damage, faulting, and friction. *Journal of Geophysical Research: Solid Earth*, *102*(B12), 27635–27649.

Macente, A., Fusseis, F., Butler, I. B., Tudisco, E., Hall, S. A., and Andò, E. (2018). 4D porosity evolution during pressure-solution of NaCl in the presence of phyllosilicates. *Earth and Planetary Science Letters*, *502*, 115–125.

Maltman, A. J. (1998). Deformation structures from the toes of active accretionary prisms. *Journal of the Geological Society*, *155*(4), 639–650.

Mancktelow, N. S. and Pennacchioni, G. (2005). The control of precursor brittle fracture and fluid-rock interaction on the development of single and paired ductile shear zones. *Journal of Structural Geology*, *27*(4), 645–661.

Maruyama, S., Kawai, T., and Windley, B. F. (2010). Ocean plate stratigraphy and its imbrication in an accretionary orogen: The Mona Complex, Anglesey-Lleyn, Wales, UK. *Geological Society Special Publication*, *338*(1), 55–75.

Matsuda, T. and Isozaki, Y. (1991). Welldocumented travel history of Mesozoic pelagic chert in Japan: From remote ocean to subduction zone. *Tectonics*, *10*(2), 475–499.

Mazengarb, C. and Speden, I. G. (2000). *Geology of the Raukumara area*, Volume 6. Institute of Geological and Nuclear Sciences.

McClay, K. R. (1976). Pressure solution. *Nature*, *264*(5586), 511–512.

McClay, K. R. (1977). Pressure solution and Coble creep in rocks and minerals: A review. *Journal of the Geological Society*, *134*(1), 57–70.

McCrory, P. A., Blair, J. L., Waldhauser, F., and Oppenheimer, D. H. (2012). Juan de Fuca slab geometry and its relation to Wadati-Benioff zone seismicity. *Journal of Geophysical Research: Solid Earth*, *117*(B9), 1–24.

McKay, L., Lunn, R. J., Shipton, Z. K., Pytharouli, S., and Roberts, J. J. (2021). Do intraplate and plate boundary fault systems evolve in a similar way with repeated slip events? *Earth and Planetary Science Letters*, *559*, 116757.

McKay, L., Shipton, Z. K., Lunn, R. J., Andrews, B., Raub, T. D., and Boyce, A. J. (2020). Detailed internal structure and along-strike variability of the core of a plate boundary fault: the Highland Boundary fault, Scotland. *Journal of the Geological Society*, *177*(2), 283–296.

McKiernan, A. and Saffer, D. (2006). Data Report: Permeability and Consolidation Properties of Subducting Sediments off Costa Rica, ODP Leg 205. In *Proceedings of the Ocean Drilling Program, 199 Scientific Results*, Volume 205, 1–24. Ocean Drilling Program.

Meneghini, F., Marroni, M., Moore, J. C., Pandolfi, L., and Rowe, C. D. (2009). The processes of underthrusting and underplating in the geologic record: Structural diversity between the Franciscan Complex (California), the Kodiak Complex (Alaska) and the Internal Ligurian Units (Italy). *Geological Journal*, *44*(2), 126–152.

Meneghini, F. and Moore, J. C. (2007). Deformation and hydrofracture in a subduction thrust at seismogenic depths: The Rodeo Cove thrust zone, Marin Headlands, California. *Geological Society of America Bulletin*, *119*(1-2), 174–183.

Merino, E., Ortoleva, P., and Strickholm, P. (1983). Generation of evenly-spaced pressure-solution seams during (late) diagenesis: A kinetic theory. *Contributions to Mineralogy and Petrology*, *82*(4), 360–370.

Michibayashi, K., Mainprice, D., Fujii, A., Uehara, S., Shinkai, Y., Kondo, Y., Ohara, Y., Ishii, T., Fryer, P., Bloomer, S. H., Ishiwatari, A., Hawkins, J. W., and Ji, S. (2016). Natural olivine crystal-fabrics in the western Pacific convergence region: A new method to identify fabric type. *Earth and Planetary Science Letters*, *443*, 70–80.

Mitchell, T. M. and Faulkner, D. R. (2009). The nature and origin of off-fault damage surrounding strike-slip fault zones with a wide range of displacements: A field study from the Atacama fault system, northern Chile. *Journal of Structural Geology*, *31*(8), 802–816.

Mittempergher, S., Cerchiari, A., Remitti, F., and Festa, A. (2018). From soft sediment deformation to fluid assisted faulting in the shallow part of a subduction megathrust analogue: the Sestola Vidiciatico tectonic Unit (Northern Apennines, Italy). *Geological Magazine*, *155*(2), 438–450.

Moore, J. and Mascle, A. (Eds.) (1990). *Proceedings of the Ocean Drilling Program, 110 Scientific Results*, Volume 110 of *Proceedings of the Ocean Drilling Program*. Ocean Drilling Program.

Moore, J. C. and Byrne, T. (1987). Thickening of fault zones: A mechanism of melange formation in accreting sediments. *Geology*, *15*(11), 1040–1043.

Moore, J. C. and Saffer, D. (2001). Updip limit of the seismogenic zone beneath the accretionary prism of southwest Japan: An effect of diagenetic to low-grade metamorphic processes and increasing effective stress. *Geology*, *29*(2), 183.

Moore, J. C. and Vrolijk, P. J. (1990). Fluids in accretionary prisms. *Eos, Transactions American Geophysical Union*, *71*(5), 245.

Morris, J. D., Villinger, H., Klaus, A., Cardace, D., Chavagnac, V. M. C., Clift, P. D., Haeckel, M., Hisamitsu, T., Kastner, M., Pfender, M., Saffer, D. M., Santelli, C., Schramm, B., Screaton, E. J., Solomon, E. A., Strasser, M., Thu, K. M., and Vannucchi, P. (2006). *Proceedings of the Ocean Drilling Program, 205 Scientific Results*, Volume 205 of *Proceedings of the Ocean Drilling Program*. Ocean Drilling Program.

Morrow, C., Radney, B., and Byerlee, J. (1992). Frictional Strength and the Effective Pressure Law of Montmorillonite and lllite Clays. In B. Evans and T.-f. B. T. I. G. Wong (Eds.), *International Geophysics*, Volume 51, 69–88. Academic Press.

Mortimer, N. and Parkinson, D. (1996). Hikurangi Plateau: A Cretaceous large igneous province in the southwest Pacific Ocean. *Journal of Geophysical Research B: Solid Earth*, *101*(1), 687–696.

Mountjoy, J. J. and Barnes, P. M. (2011). Active upper plate thrust faulting in regions of low plate interface coupling, repeated slow slip events, and coastal uplift: Example from the Hikurangi Margin, New Zealand. *Geochemistry, Geophysics, Geosystems*, *12*(1).

Nakashima, S. (1995). Diffusivity of ions in pore water as a quantitative basis for rock deformation rate estimates. *Tectonophysics*, *245*(3-4), 185–203.

Nayar, K. G., Sharqawy, M. H., Banchik, L. D., and Lienhard, J. H. (2016). Thermophysical properties of seawater: A review and new correlations that include pressure dependence. *Desalination*, *390*, 1–24.

Nedimović, M. R., Hyndman, R. D., Ramachandran, K., and Spence, G. D. (2003). Reflection signature of seismic and aseismic slip on the northern Cascadia subduction interface. *Nature*, *424*(6947), 416–420.

Nicol, A., Mazengarb, C., Chanier, F., Rait, G., Uruski, C., and Wallace, L. (2007). Tectonic evolution of the active Hikurangi subduction margin, New Zealand, since the Oligocene. *Tectonics*, *26*(4).

Niemeijer, A. R. and Spiers, C. J. (2005). Influence of phyllosilicates on fault strength in the brittle-ductile transition: Insights from rock analogue experiments. *Geological Society Special Publication*, *245*(1), 303–327.

Niemeijer, A. R. and Spiers, C. J. (2007). A microphysical model for strong velocity weakening in phyllosilicate-bearing fault gouges. *Journal of Geophysical Research: Solid Earth*, *112*(10), B10405.

Niemeijer, A. R., Spiers, C. J., and Bos, B. (2002). Compaction creep of quartz sand at 400-600řC: Experimental evidence for dissolution-controlled pressure solution. *Earth and Planetary Science Letters*, *195*(3-4), 261–275.

Nishiyama, N., Sumino, H., and Ujiie, K. (2020). Fluid overpressure in subduction plate boundary caused by mantle-derived fluids. *Earth and Planetary Science Letters*, *538*, 116199.

Nye, J. F. (1953). The flow law of ice from measurements in glacier tunnels, laboratory experiments and the Jungfraufirn borehole experiment. *Proceedings of the Royal Society of London. Series A. Mathematical and Physical Sciences*, *219*(1139), 477–489.

Obara, K. (2002). Nonvolcanic deep tremor associated with subduction in southwest Japan. *Science*, *296*(5573), 1679–1681.

Obara, K., Hirose, H., Yamamizu, F., and Kasahara, K. (2004). Episodic slow slip events accompanied by non-volcanic tremors in southwest Japan subduction zone. *Geophysical Research Letters*, *31*(23), 1–4.

Obara, K. and Kato, A. (2016). Connecting slow earthquakes to huge earthquakes. *Science*, *353*(6296), 253–257.

Ogden, C. S., Bastow, I. D., Gilligan, A., and Rondenay, S. (2019). A reappraisal of the H-κ stacking technique: Implications for global crustal structure. *Geophysical Journal International*, *219*(3), 1491–1513.

Okamoto, A. S., Verberne, B. A., Niemeijer, A. R., Takahashi, M., Shimizu, I., Ueda, T., and Spiers, C. J. (2019). Frictional Properties of Simulated Chlorite Gouge at Hydrothermal Conditions: Implications for Subduction Megathrusts. *Journal of Geophysical Research: Solid Earth*, *124*(5), 4545–4565.

Oleskevich, D. A., Hyndman, R. D., and Wang, K. (1999). The updip and downdip limits to great subduction earthquakes: Thermal and structural models of Cascadia, south Alaska, SW Japan, and Chile. *Journal of Geophysical Research: Solid Earth*, *104*(B7), 14965–14991.

Onishi, C. T., Kimura, G., Hashimoto, Y., Ikehara-Ohmori, K., and Watanabe, T. (2001). Deformation history of tectonic melange and its relationship to the underplating process and relative plate motion: An example from the deeply buried Shimanto Belt, SW Japan. *Tectonics*, *20*(3), 376–393.

Otsu, N. (1979). A Threshold Selection Method from Gray-Level Histograms. *IEEE Transactions on Systems, Man, and Cybernetics*, *9*(1), 62–66.

Passchier, C. W. and Trouw, R. A. (2005). *Microtectonics*. Berlin/Heidelberg: Springer-Verlag.

Paterson, M. S. (1995). A theory for granular flow accommodated by material transfer via an intergranular fluid. *Tectonophysics*, *245*(3-4), 135–151.

Paterson, M. S. and Wong, T. F. (2005). *Experimental rock deformation - The brittle field* (Second, Co ed.). Berlin/Heidelberg: Springer-Verlag.

Peacock, D. C. and Azzam, I. N. (2006). Development and scaling relationships of a stylolite population. *Journal of Structural Geology*, *28*(10), 1883–1889.

Peacock, D. C. and Sanderson, D. J. (1995). Pull-aparts, shear fractures and pressure solution. *Tectonophysics*, *241*(1-2), 1–13.

Peacock, S. M. (1996). Thermal and petrologic structure of subduction zones. In *Geophysical Monograph Series*, Volume 96, 119–133. Blackwell Publishing Ltd.

Pedregosa, F., Michel, V., Varoquaux, G., Thirion, B., Dubourg, V., Passos, A., Perrot, M., Grisel, O., Blondel, M., Prettenhofer, P., Weiss, R., Vanderplas, J., Cournapeau, D., Pedregosa, F., Varoquaux, G., Gramfort, A., Thirion, B., Grisel, O., Dubourg, V., Passos, A., Brucher, M., Perrot andÉdouardand, M., and Duchesnay, É. (2011). Scikit-learn: Machine Learning in Python. *Journal of Machine Learning Research*, *12*(85), 2825–2830.

Peng, Z. and Gomberg, J. (2010). An integrated perspective of the continuum between earthquakes and slow-slip phenomena. *Nature Geoscience*, *3*(9), 599–607.

Pennacchioni, G. and Mancktelow, N. S. (2018). Small-scale ductile shear zones: Neither extending, nor thickening, nor narrowing. *Earth-Science Reviews*, *184*, 1–12.

Peterson, J. (1993). Observations and modelling of seismic background noise. Open-File Report 93-322. Technical Report 2.

Pfiffner, O. A. and Ramsay, J. G. (1982). Constraints on geological strain rates; arguments from finite strain states of naturally deformed rocks. *Journal of Geophysical Research*, *87*(B1), 311–321.

Phillips, K. and Clayton, R. W. (2014). Structure of the subduction transition region from seismic array data in southern Peru. *Geophysical Journal International*, *196*(3), 1889–1905.

Phillips, N. J., Belzer, B., French, M. E., Rowe, C. D., and Ujiie, K. (2020). Frictional Strengths of Subduction Thrust Rocks in the Region of Shallow Slow Earthquakes. *Journal of Geophysical Research: Solid Earth*, *125*(3), 1–20.

Phillips, N. J., Motohashi, G., Ujiie, K., and Rowe, C. D. (2020). Evidence of Localized Failure Along Altered Basaltic Blocks in Tectonic Mélange at the Updip Limit of the Seismogenic Zone: Implications for the Shallow Slow Earthquake Source. *Geochemistry, Geophysics, Geosystems*, *21*(7), 1–17.

Pieri, M., Kunze, K., Burlini, L., Stretton, I., Olgaard, D. L., Burg, J. P., and Wenk, H. R. (2001). Texture development of calcite by deformation and dynamic recrystallization at 1000 K during torsion experiments of marble to large strains. *Tectonophysics*, *330*(1-2), 119–140.

Plank, T. and Manning, C. E. (2019). Subducting carbon. *Nature*, *574*(7778), 343–352.

Platt, J. P. and De Bresser, J. H. (2017). Stress dependence of microstructures in experimentally deformed calcite. *Journal of Structural Geology*, *105*(November), 80–87.

Plaza-Faverola, A., Henrys, S., Pecher, I., Wallace, L., and Klaeschen, D. (2016). Splay fault branching from the Hikurangi subduction shear zone: Implications for slow slip and fluid flow. *Geochemistry, Geophysics, Geosystems*, *17*(12), 5009–5023.

Plummer, L. N. and Busenberg, E. (1982). The solubilities of calcite, aragonite and vaterite in CO2-H2O solutions between 0 and 90řC, and an evaluation of the aqueous model for the system CaCO3-CO2-H2O. *Geochimica et Cosmochimica Acta*, *46*(6), 1011–1040.

Pluymakers, A. M. and Spiers, C. J. (2015). Compaction creep of simulated anhydrite fault gouge by pressure solution: Theory v. experiments and implications for fault sealing. *Geological Society Special Publication*, *409*(1), 107–124.

Poirier, J.-P. (1985). *Creep of Crystals*. Cambridge Earth Science Series. Cambridge University Press.

Pouderoux, H., Proust, J.-N., and Lamarche, G. (2014). Submarine paleoseismology

of the northern Hikurangi subduction margin of New Zealand as deduced from Turbidite record since 16 ka. *Quaternary Science Reviews*, *84*, 116–131.

Pozzi, G., De Paola, N., Nielsen, S. B., Holdsworth, R. E., and Bowen, L. (2018). A new interpretation for the nature and significance of mirror-like surfaces in experimental carbonate-hosted seismic faults. *Geology*, *46*(7), 583–586.

Pytte, A. M. and Reynolds, R. C. (1989). The Thermal Transformation of Smectite to Illite. In N. D. Naeser and T. H. McCulloh (Eds.), *Thermal History of Sedimentary Basins*, 133–140. New York, NY: Springer New York.

Rabinowitz, H. S., Savage, H. M., Skarbek, R. M., Ikari, M. J., Carpenter, B. M., and Collettini, C. (2018). Frictional Behavior of Input Sediments to the Hikurangi Trench, New Zealand. *Geochemistry, Geophysics, Geosystems*, *19*(9), 2973–2990.

Railsback, L. B. (1993). Lithologic controls on morphology of pressure-dissolution surfaces (stylolites and dissolution seams) in Paleozoic carbonate rocks from the mideastern United States. *Journal of Sedimentary Petrology*, *63*(3), 513–522.

Railsback, L. B. (1998). Evaluation of spacing of stylolites and its implications for self-organization of pressure dissolution. *Journal of Sedimentary Research*, *68*(1), 2–7.

Raimbourg, H., Rajič, K., MorisMuttoni, B., Famin, V., Palazzin, G., Fisher, D. M., Morell, K., Erdmann, S., Di Carlo, I., and Montmartin, C. (2021). Quartz Vein Geochemistry Records Deformation Processes in Convergent Zones. *Geochemistry, Geophysics, Geosystems*, *22*(4).

Raj, R. (1982). Creep in polycrystalline aggregates by matter transport through a liquid phase. *Journal of Geophysical Research*, *87*(B6), 4731–4739.

Ramsay, J. G. (1980a). Shear zone geometry: A review. *Journal of Structural Geology*, *2*(1-2), 83–99.

Ramsay, J. G. (1980b). The crack-seal mechanism of rock deformation. *Nature*, *284*(5752), 135–139.

Rasmussen, C. E. and Williams, C. K. I. (2006). *Gaussian Processes for Machine Learning* (1st ed.). The MIT Press.

Ratschbacher, L., Wenk, H. R., and Sintubin, M. (1991). Calcite textures: examples from nappes with strain-path partitioning. *Journal of Structural Geology*, *13*(4), 369–384.

Reches, Z. and Lockner, D. A. (1994). Nucleation and growth of faults in brittle rocks. *Journal of Geophysical Research*, *99*(B9), 18159–18173.

Regalla, C. A., Rowe, C. D., Harrichhausen, N., Tarling, M. S., and Singh, J. (2018). Styles of underplating in the Marin Headlands terrane, Franciscan complex, California. In *Special Paper of the Geological Society of America*, Volume 534, 155–173. Geological Society of America.

Remitti, F., Vannucchi, P., Bettelli, G., Fantoni, L., Panini, F., and Vescovi, P. (2011). Tectonic and sedimentary evolution of the frontal part of an ancient subduction complex at the transition from accretion to erosion: The case of the Ligurian wedge of the Northern Apennines, Italy. *Bulletin of the Geological Society of America*, *123*(1-2), 51–70.

Renard, F., Gratier, J. P., and Jamtveit, B. (2000). Kinetics of crack-sealing, intergranular pressure solution, and compaction around active faults. *Journal of Structural Geology*, *22*(10), 1395–1407.

Renard, F., Ortoleva, P., and Gratier, J. P. (1997). Pressure solution in sandstones: Influence of clays and dependence on temperature and stress. *Tectonophysics*, *280*(3-4), 257–266.

Renner, J. and Evans, B. (2002). Do calcite rocks obey the power-law creep equation? *Geological Society, London, Special Publications*, *200*(1), 293–307.

Renner, J., Evans, B., and Siddiqi, G. (2002). Dislocation creep of calcite. *Journal of Geophysical Research: Solid Earth*, *107*(B12), ECV 6–1–ECV 6–16.

Reyners, M. (1998). Plate coupling and the hazard of large subduction thrust earthquakes at the Hikurangi subduction zone, New Zealand. *New Zealand Journal of Geology and Geophysics*, *41*(4), 343–354.

Rimstidt, J. D. and Barnes, H. L. (1980). The kinetics of silica-water reactions. *Geochimica et Cosmochimica Acta*, *44*(11), 1683–1699.

Rogers, G. and Dragert, H. (2003). Episodic tremor and slip on the Cascadia subduction zone: The chatter of silent slip. *Science*, *300*(5627), 1942–1943.

Rowe, C. D., Fagereng, Å., Miller, J. A., and Mapani, B. (2012). Signature of coseismic decarbonation in dolomitic fault rocks of the Naukluft Thrust, Namibia. *Earth and Planetary Science Letters*, *333-334*, 200–210.

Rowe, C. D., Meneghini, F., and Casey Moore, J. (2011). Textural record of the seismic cycle: Strain-rate variation in an ancient subduction thrust. *Geological Society Special Publication*, *359*(1), 77–95.

Rowe, C. D., Moore, J. C., and Remitti, F. (2013). The thickness of subduction plate boundary faults from the seafloor into the seismogenic zone. *Geology*, *41*(9), 991–994.

Ruff, L. J. (1989). Do Trench Sediments Affect Great Earthquake Occurrence in Subduction Zones? In *Subduction Zones Part II*, 263–282. Birkhäuser Basel.

Rutter, E. H. (1974). The influence of temperature, strain rate and interstitial water in the experimental deformation of calcite rocks. *Tectonophysics*, *22*(3-4), 311–334.

Rutter, E. H. (1976). The Kinetics of Rock Deformation by Pressure Solution [and Discussion]. *Philosophical Transactions of the Royal Society A: Mathematical, Physical and Engineering Sciences*, *283*(1312), 203–219.

Rutter, E. H. (1983). Pressure solution in nature, theory and experiment. *Journal of the Geological Society*, *140*(5), 725–740.

Rutter, E. H. (1995). Experimental study of the influence of stress, temperature, and strain on the dynamic recrystallization of Carrara marble. *Journal of Geophysical Research: Solid Earth*, *100*(B12), 24651–24663.

Rutter, E. H., Casey, M., and Burlini, L. (1994). Preferred crystallographic orientation development during the plastic and superplastic flow of calcite rocks. *Journal of Structural Geology*, *16*(10), 1431–1446.

Rutter, E. H., Hackston, A. J., Yeatman, E., Brodie, K. H., Mecklenburgh, J., and May, S. E. (2013). Reduction of friction on geological faults by weak-phase smearing. *Journal of Structural Geology*, *51*, 52–60.

Safaricz, M. and Davison, I. (2005). Pressure solution in chalk. *AAPG Bulletin*, *89*(3), 383–401.

Saffer, D. M. (2016). The permeability of active subduction plate boundary faults. In *Crustal Permeability*, 207–227. Chichester, UK: John Wiley & Sons, Ltd.

Saffer, D. M. and Marone, C. (2003). Comparison of smectite- and illite-rich gouge frictional properties: Application to the updip limit of the seismogenic zone along subduction megathrusts. *Earth and Planetary Science Letters*, *215*(1-2), 219–235.

Saffer, D. M. and McKiernan, A. W. (2009). Evaluation of in situ smectite dehydration as a pore water freshening mechanism in the nankai trough, offshore southwest Japan. *Geochemistry, Geophysics, Geosystems*, *10*(2), 1–24.

Saffer, D. M. and Tobin, H. J. (2011). Hydrogeology and mechanics of subduction zone forearcs: Fluid flow and pore pressure. *Annual Review of Earth and Planetary Sciences*, *39*(1), 157–186.

Saffer, D. M., Underwood, M. B., and Mckiernan, A. W. (2008). Evaluation of factors controlling smectite transformation and fluid production in subduction zones: Application to the Nankai Trough. *Island Arc*, *17*(2), 208–230.

Saffer, D. M. and Wallace, L. M. (2015). The frictional, hydrologic, metamorphic and thermal habitat of shallow slow earthquakes. *Nature Geoscience*, *8*(8), 594–600.

Saito, T., Ujiie, K., Tsutsumi, A., Kameda, J., and Shibazaki, B. (2013). Geological and frictional aspects of very-low-frequency earthquakes in an accretionary prism. *Geophysical Research Letters*, *40*(4), 703–708.

Saito, T., Uno, M., Sato, T., Fujisaki, W., Haraguchi, S., bing Li, Y., Sawaki, Y., Yamamoto, S., and Maruyama, S. (2014). Geochemistry of accreted metavolcanic rocks from the Neoproterozoic Gwna Group of Anglesey-Lleyn, NW Wales, U.K.: MORB and OIB in the Iapetus Ocean. *Tectonophysics*, *662*, 243–255.

Salimullah, A. R. (1992). Volcaniclastic facies and sequences, Leg 129. In *Proc., scientific results, ODP, Leg 129, old Pacific crust*, Volume 129, 153–167. Ocean Drilling Program.

Sambridge, M. (2013). A parallel tempering algorithm for probabilistic sampling and multimodal optimization. *Geophysical Journal International*, *196*(1), 357–374.

Sammis, C., King, G., and Biegel, R. (1987). The kinematics of gouge deformation. *Pure and Applied Geophysics*, *125*(5), 777–812.

Sammis, C. G. and Ben-Zion, Y. (2008). Mechanics of grain-size reduction in fault zones. *Journal of Geophysical Research: Solid Earth*, *113*(2), B02306.

Sample, J. C. (1990). The effect of carbonate cementation of underthrust sediments on deformation styles during underplating. *Journal of Geophysical Research*, *95*(B6), 9111–9121.

Schindelin, J., Arganda-Carreras, I., Frise, E., Kaynig, V., Longair, M., Pietzsch, T., Preibisch, S., Rueden, C., Saalfeld, S., Schmid, B., Tinevez, J. Y., White, D. J., Hartenstein, V., Eliceiri, K., Tomancak, P., and Cardona, A. (2012). Fiji: An open-source platform for biological-image analysis. *Nature Methods*, *9*(7), 676–682.

Schmalholz, S. M. and Maeder, X. (2012). Pinch-and-swell structure and shear zones in viscoplastic layers. *Journal of Structural Geology*, *37*, 75–88.

Schmid, S. M., Boland, J. N., and Paterson, M. S. (1977). Superplastic flow in finegrained limestone. *Tectonophysics*, *43*(3-4), 257–291.

Schmid, S. M., Casey, M., and Starkey, J. (1981). The microfabric of calcite tectonites from the Helvetic Nappes (Swiss Alps). *Geological Society Special Publication*, *9*(1), 151–158.

Schmid, S. M., Panozzo, R., and Bauer, S. (1987). Simple shear experiments on calcite rocks: rheology and microfabric. *Journal of Structural Geology*, *9*(5-6), 747–778.

Schmid, S. M., Paterson, M. S., and Boland, J. N. (1980). High temperature flow and dynamic recrystallization in carrara marble. *Tectonophysics*, *65*(3-4), 245–280.

Schneider, C. A., Rasband, W. S., and Eliceiri, K. W. (2012). NIH Image to ImageJ: 25 years of image analysis.

Schofield, D. I., Leslie, A. G., Wilby, P. R., Dartnall, R., Waldron, J. W., and Kendall, R. S. (2021). Tectonic evolution of anglesey and adjacent mainland north Wales. *Geological Society Special Publication*, *503*(1), 371–390.

Scholz, C. H. (1998). Earthquakes and friction laws. *Nature*, *391*(6662), 37–42.

Schumann, K., Behrmann, J. H., Stipp, M., Yamamoto, Y., Kitamura, Y., and Lempp, C. (2014). Geotechnical behavior of mudstones from the Shimanto and Boso accretionary complexes, and implications for the Nankai accretionary prism. *Earth, Planets and Space*, *66*(1), 129.

Schwartz, S. Y. and Rokosky, J. M. (2007). Slow slip events and seismic tremor at circum-Pacific subduction zones. *Reviews of Geophysics*, *45*(3).

Schwarz, S. and Stöckhert, B. (1996). Pressure solution in siliciclastic HP-LT metamorphic rocks - Constraints on the state of stress in deep levels of accretionary complexes. *Tectonophysics*, *255*(3-4 SPEC. ISS.), 203–209.

Secor, D. T. (1965). Role of fluid pressure in jointing.

Seebeck, H., Nicol, A., Giba, M., Pettinga, J., and Walsh, J. (2014). Geometry of the subducting Pacific plate since 20 Ma, Hikurangi margin, New Zealand. *Journal of the Geological Society*, *171*(1), 131–143.

Seyfried, W. E. and Mottl, M. J. (1982). Hydrothermal alteration of basalt by seawater under seawater-dominated conditions. *Geochimica et Cosmochimica Acta*, *46*(6), 985–1002.

Shaddox, H. R. and Schwartz, S. Y. (2019). Subducted seamount diverts shallow slow slip to the forearc of the northern Hikurangi subduction zone, New Zealand. *Geology*, *47*(5), 415–418.

Shi, D., Wu, Z., Klemperer, S. L., Zhao, W., Xue, G., and Su, H. (2015). Receiver function imaging of crustal suture, steep subduction, and mantle wedge in the eastern India-Tibet continental collision zone. *Earth and Planetary Science Letters*, *414*, 6–15.

Shibata, T., Orihashi, Y., Kimura, G., and Hashimoto, Y. (2008). Underplating of mélange evidenced by the depositional ages: U-Pb dating of zircons from the Shimanto accretionary complex, southwest Japan. *Island Arc*, *17*(3), 376–393.

Shibuya, T., Yoshizaki, M., Masaki, Y., Suzuki, K., Takai, K., and Russell, M. J. (2013). Reactions between basalt and CO2-rich seawater at 250 and 350řC, 500bars: Implications for the CO2 sequestration into the modern oceanic crust and the composition of hydrothermal vent fluid in the CO2-rich early ocean. *Chemical Geology*, *359*, 1–9.

Sibson, R. H. (1986). Earthquakes and Rock Deformation in Crustal Fault Zones. *Annual Review of Earth and Planetary Sciences*, *14*(1), 149–175.

Sibson, R. H. (1994). Crustal stress, faulting and fluid flow. *Geological Society, London, Special Publications*, *78*(1), 69–84.

Sibson, R. H. (1996). Structural permeability of fluid-driven fault-fracture meshes. *Journal of Structural Geology*, *18*(8), 1031–1042.

Sibson, R. H. (1998). Brittle failure mode plots for compressional and extensional tectonic regimes. *Journal of Structural Geology*, *20*(5), 655–660.

Sibson, R. H. (2017). Tensile overpressure compartments on low-angle thrust faults. *Earth, Planets and Space*, *69*(1), 113.

Simpson, J. (2009). Stylolite-Controlled Layering in an Homogeneous Limestone: Pseudo-Bedding Produced by Burial Diagenesis. *Carbonate Diagenesis*, 293–303.

Singh, A., Dash, S., Kamruddin, M., Ajikumar, P. K., Tyagi, A. K., Raghunathan, V. S., and Raj, B. (2002). Formation of nanocrystalline calcia by the decomposition of calcite. *Journal of the American Ceramic Society*, *85*(4), 927–932.

Skarbek, R. M. and Rempel, A. W. (2017). Heterogeneous Coulomb wedges: Influence of fluid pressure, porosity, and application to the Hikurangi subduction margin, New Zealand. *Journal of Geophysical Research: Solid Earth*, *122*(3), 1585–1613.

Skarbek, R. M. and Saffer, D. M. (2009). Pore pressure development beneath the décollement at the Nankai subduction zone: Implications for plate boundary fault strength and sediment dewatering. *Journal of Geophysical Research*, *114*(B7), B07401.

Smith, S. A., Nielsen, S., and Di Toro, G. (2015). Strain localization and the onset of dynamic weakening in calcite fault gouge. *Earth and Planetary Science Letters*, *413*, 25–36.

Spiers, C., Meer de, S., Niemeijer, A, R., and Zhang, X. (2004). Kinetics of rock deformation by pressure solution and the role of thin aqueous films. In S. Nakashima, C. J. Spiers, L. Mercury, P. A. Fenter, and M. F. Hochella Jr. (Eds.), *Physicochemistry of water in geological and biological systems*, Tokyo, Japan, 129–158. Universal Academy Press.

Spiers, C. J., Schutjens, P. M. T. M., Brzesowsky, R. H., Peach, C. J., Liezenberg, J. L., and Zwart, H. J. (1990). Experimental determination of constitutive parameters governing creep of rocksalt by pressure solution. *Geological Society, London, Special Publications*, *54*(1), 215–227.

Spinelli, G. A. and Saffer, D. M. (2004). Along-strike variations in underthrust sediment dewatering on the Nicoya margin, Costa Rica related to the updip limit of seismicity. *Geophysical Research Letters*, *31*(4), L04613.

Spinelli, G. A. and Underwood, M. B. (2004). Character of sediments entering the Costa Rica subduction zone: Implications for partitioning of water along the plate interface. *Island Arc*, *13*(3), 432–451.

Stenvall, C. A., Fagereng, Å., and Diener, J. F. A. (2019). Weaker Than Weakest: On the Strength of Shear Zones. *Geophysical Research Letters*, *46*(13), 7404–7413.

Stern, T., Lamb, S., Moore, J. D., Moore, J. D., Okaya, D., and Hochmuth, K. (2020). High mantle seismic P-wave speeds as a signature for gravitational spreading of superplumes. *Science Advances*, *6*(22).

Stern, T. A., Henrys, S. A., Okaya, D., Louie, J. N., Savage, M. K., Lamb, S., Sato, H., Sutherland, R., and Iwasaki, T. (2015). A seismic reflection image for the base of a tectonic plate. *Nature*, *518*(7537), 85–88.

Sun, T., Saffer, D., and Ellis, S. (2020). Mechanical and hydrological effects of seamount subduction on megathrust stress and slip. *Nature Geoscience*, *13*(3), 249–255.

Sun, T., Wang, K., Fujiwara, T., Kodaira, S., and He, J. (2017). Large fault slip peaking at trench in the 2011 Tohoku-oki earthquake. *Nature Communications*, *8*(1), 14044.

Syracuse, E. M., van Keken, P. E., and Abers, G. A. (2010). The global range of subduction zone thermal models. *Physics of the Earth and Planetary Interiors*, *183*(1-2), 73–90.

Tesei, T., Collettini, C., Barchi, M. R., Carpenter, B. M., and Di Stefano, G. (2014). Heterogeneous strength and fault zone complexity of carbonate-bearing thrusts with possible implications for seismicity. *Earth and Planetary Science Letters*, *408*, 307–318.

Thorpe, R. S. (1972). Ocean Floor Basalt Affinity of Precambrian Glaucophane Schist from Anglesey. *Nature Physical Science*, *240*(103), 164–166.

Thorpe, R. S. (1993). Geochemistry and eruptive environment of metavolcanic rocks from the Mona Complex of Anglesey, North Wales, U.K. *Geological Magazine*, *130*(1), 85–91.

Thorwart, M., Dzierma, Y., Rabbel, W., and Hensen, C. (2014). Seismic swarms, fluid flow and hydraulic conductivity in the forearc offshore North Costa Rica and Nicaragua. *International Journal of Earth Sciences*, *103*(7), 1789–1799.

Tobin, H., Vannucchi, P., and Meschede, M. (2001). Structure, inferred mechanical properties, and implications for fluid transport in the décollement zone, Costa Rica convergent margin. *Geology*, *29*(10), 907–910.

Todd, E. K. and Schwartz, S. Y. (2016). Tectonic tremor along the northern Hikurangi Margin, New Zealand, between 2010 and 2015. *Journal of Geophysical Research: Solid Earth*, *121*(12), 8706–8719.

Todd, E. K., Schwartz, S. Y., Mochizuki, K., Wallace, L. M., Sheehan, A. F., Webb, S. C., Williams, C. A., Nakai, J., Yarce, J., Fry, B., Henrys, S., and Ito, Y. (2018). Earthquakes and Tremor Linked to Seamount Subduction During Shallow Slow Slip at the Hikurangi Margin, New Zealand. *Journal of Geophysical Research: Solid Earth*, *123*(8), 6769–6783.

Tondi, E., Antonellini, M., Aydin, A., Marchegiani, L., and Cello, G. (2006). The role of deformation bands, stylolites and sheared stylolites in fault development in carbonate grainstones of Majella Mountain, Italy. *Journal of Structural Geology*, *28*(3), 376–391.

Tonegawa, T., Miura, S., Ishikawa, A., Sano, T., Suetsugu, D., Isse, T., Shiobara, H., Sugioka, H., Ito, A., Ishihara, Y., Tanaka, S., Obayashi, M., Yoshimitsu, J., and Kobayashi, T. (2019). Characterization of Crustal and Uppermost-Mantle Seismic Discontinuities in the Ontong Java Plateau. *Journal of Geophysical Research: Solid Earth*, *124*(7), 7155–7170.

Toussaint, R., Aharonov, E., Koehn, D., Gratier, J.-P., Ebner, M., Baud, P., Rol-

land, A., and Renard, F. (2018). Stylolites: A review. *Journal of Structural Geology*, *114*(May), 163–195.

Tulley, C. J., Fagereng, Å., and Ujiie, K. (2020). Hydrous oceanic crust hosts megathrust creep at low shear stresses. *Science Advances*, *6*(22), eaba1529.

Turcotte, D. L. (1992). Fractals and chaos in geology and geophysics. *Fractals and chaos in geology and geophysics*, *46*(5), 68–68.

Turner, F. J., Griggs, D. T., and Heard, H. (1954). Experimental deformation of calcite crystals. *Bulletin of the Geological Society of America*, *65*(9), 883–934.

Uenishi, K. and Rice, J. R. (2003). Universal nucleation length for slip-weakening rupture instability under nonuniform fault loading. *Journal of Geophysical Research: Solid Earth*, *108*(B1), 2042.

Ujiie, K. (2002). Evolution and kinematics of an ancient décollement zone, mélange in the Shimanto accretionary complex of Okinawa Island, Ryukyu Arc. *Journal of Structural Geology*, *24*(5), 937–952.

Ujiie, K., Saishu, H., Fagereng, Å., Nishiyama, N., Otsubo, M., Masuyama, H., and Kagi, H. (2018). An Explanation of Episodic Tremor and Slow Slip Constrained by Crack-Seal Veins and Viscous Shear in Subduction Mélange. *Geophysical Research Letters*, *45*(11), 5371–5379.

Underwood, M. B. (2007). 3. Sediment Inputs to Subduction Zones. In *The Seismogenic Zone of Subduction Thrust Faults*, 42–85. Columbia University Press.

Underwood, M. B. and Pickering, K. T. (2018). Facies architecture, detrital provenance, and tectonic modulation of sedimentation in the Shikoku Basin: Inputs to the Nankai Trough subduction zone. In *Special Paper of the Geological Society of America*, Volume 534, 1–34. Geological Society of America.

van de Kamp, P. C. (2008). Smectite-Illite-Muscovite Transformations, Quartz Dissolution, and Silica Release in Shales. *Clays and Clay Minerals*, *56*(1), 66–81.

van den Ende, M. P., Chen, J., Ampuero, J. P., and Niemeijer, A. R. (2018). A comparison between rate-and-state friction and microphysical models, based on numerical simulations of fault slip. *Tectonophysics*, *733*(December 2017), 273–295.

van den Ende, M. P., Chen, J., Niemeijer, A. R., and Ampuero, J. P. (2020). Rheological Transitions Facilitate Fault-Spanning Ruptures on Seismically Active and Creeping Faults. *Journal of Geophysical Research: Solid Earth*, *125*(8), 1–27.

van den Ende, M. P., Niemeijer, A. R., and Spiers, C. J. (2019). Influence of Grain Boundary Structural Evolution on Pressure Solution Creep Rates. *Journal of Geophysical Research: Solid Earth*, *124*(10), 10210–10230.

vanădenăEnde, M. P., Marketos, G., Niemeijer, A. R., and Spiers, C. J. (2018). Investigating Compaction by Intergranular Pressure Solution Using the Discrete Element Method. *Journal of Geophysical Research: Solid Earth*, *123*(1), 107–124.

Vannucchi, P., Remitti, F., and Bettelli, G. (2008). Geological record of fluid flow and seismogenesis along an erosive subducting plate boundary. *Nature*, *451*(7179), 699–703.

Vannucchi, P., Remitti, F., Phipps-Morgan, J., and Bettelli, G. (2009). Aseismic-seismic transition and fluid regime along subduction plate boundaries and a fossil example from the Northern Apennines of Italy. In *International Geophysics*, Volume 94, 37–68. Academic Press.

Verberne, B. A., de Bresser, J. H., Niemeijer, A. R., Spiers, C. J., de Winter, D. A., and Plümper, O. (2013). Nanocrystalline slip zones in calcite fault gouge show intense crystallographic preferred orientation: Crystal plasticity at subseismic slip rates at 18-150 řC. *Geology*, *41*(8), 863–866.

Verberne, B. A., Niemeijer, A. R., De Bresser, J. H., and Spiers, C. J. (2015). Mechanical behavior and microstructure of simulated calcite fault gouge sheared at 20-600řC: Implications for natural faults in limestones. *Journal of Geophysical Research: Solid Earth*, *120*(12), 8169–8196.

Verberne, B. A., Plümper, O., De Winter, D. A., and Spiers, C. J. (2014). Superplastic nanofibrous slip zones control seismogenic fault friction. *Science*, *346*(6215), 1342–1344.

Verberne, B. A. and Spiers, C. J. (2017). A quantitative microstructural investigation of depleted and undepleted reservoir sandstones. *51st US Rock Mechanics / Geomechanics Symposium 2017*, *5*, 3396–3405.

Verberne, B. A., Spiers, C. J., Niemeijer, A. R., De Bresser, J. H., De Winter, D. A., and Plümper, O. (2014). Frictional Properties and Microstructure of Calcite-Rich Fault Gouges Sheared at Sub-Seismic Sliding Velocities. *Pure and Applied Geophysics*, *171*(10), 2617–2640.

Villinger, H., Grevemeyer, I., Kaul, N., Hauschild, J., and Pfender, M. (2002). Hydrothermal heat flux through aged oceanic crust: Where does the heat escape? *Earth and Planetary Science Letters*, *202*(1), 159–170.

Viti, C., Collettini, C., and Tesei, T. (2014). Pressure solution seams in carbonatic fault rocks: Mineralogy, micro/nanostructures and deformation mechanism. *Contributions to Mineralogy and Petrology*, *167*(2), 1–15.

Wakabayashi, J. (2015). Anatomy of a subduction complex: Architecture of the Franciscan Complex, California, at multiple length and time scales. *International Geology Review*, *57*(5-8), 669–746.

Wakabayashi, J. and Rowe, C. D. (2015). Whither the megathrust? Localization of large-scale subduction slip along the contact of a mélange. *International Geology Review*, *57*(5-8), 854–870.

Walker, A. N., Rutter, E. H., and Brodie, K. H. (1990). Experimental study of grain-size sensitive flow of synthetic, hot-pressed calcite rocks. *Geological Society Special Publication*, *54*(1), 259–284.

Wallace, L. M. (2020a). Slow Slip Events in New Zealand. *Annual Review of Earth and Planetary Sciences*, *48*, 175–203.

Wallace, L. M. (2020b). Slow Slip Events in New Zealand. *Annual Review of Earth and Planetary Sciences*, *48*(1), 175–203.

Wallace, L. M. and Beavan, J. (2006). A large slow slip event on the central Hikurangi subduction interface beneath the Manawatu region, North Island, New Zealand. *Geophysical Research Letters*, *33*(11), 2006GL026009.

Wallace, L. M. and Beavan, J. (2010). Diverse slow slip behavior at the Hikurangi subduction margin, New Zealand. *Journal of Geophysical Research: Solid Earth*, *115*(12), B12402.

Wallace, L. M., Beavan, J., Bannister, S., and Williams, C. (2012). Simultaneous long-term and short-term slow slip events at the Hikurangi subduction margin, New Zealand: Implications for processes that control slow slip event occurrence, duration, and migration. *Journal of Geophysical Research B: Solid Earth*, *117*(11).

Wallace, L. M., Beavan, J., McCaffrey, R., and Darby, D. (2004). Subduction zone coupling and tectonic block rotations in the North Island, New Zealand. *Journal of Geophysical Research: Solid Earth*, *109*(12), 1–21.

Wallace, L. M., Cochran, U. A., Power, W. L., and Clark, K. J. (2014). Earthquake and tsunami potential of the Hikurangi subduction thrust, New Zealand: Insights from paleoseismology, GPS, and Tsunami modeling. *Oceanography*, *27*(2), 104–117.

Wallace, L. M., Kaneko, Y., Hreinsdóttir, S., Hamling, I., Peng, Z., Bartlow, N., D'Anastasio, E., and Fry, B. (2017). Large-scale dynamic triggering of shallow slow slip enhanced by overlying sedimentary wedge. *Nature Geoscience*, *10*(10), 765–770.

Wallace, L. M., Reyners, M., Cochran, U., Bannister, S., Barnes, P. M., Berryman, K., Downes, G., Eberhart-Phillips, D., Fagereng, A., Ellis, S., Nicol, A., McCaffrey, R., Beavan, R. J., Henrys, S., Sutherland, R., Barker, D. H., Litchfield, N., Townend, J., Robinson, R., Bell, R., Wilson, K., and Power, W. (2009). Char-

acterizing the seismogenic zone of a major plate boundary subduction thrust: Hikurangi Margin, New Zealand. *Geochemistry, Geophysics, Geosystems*, *10*(10).

Wallace, L. M., Saffer, D. M., Barnes, P. M., Pecher, I. A., Petronotis, K. E., LeVay, L., Scientists, and the Expedition 372/375 (2019). *Hikurangi Subduction Margion Coring, Logging, and Observatories* (375 ed.). College Station, TX: International Ocean Discovery Program.

Wang, K. (2021). If not brittle: Ductile, plastic, or viscous? *Seismological Research Letters*, *92*(2A), 1181–1184.

Wang, K. and Bilek, S. L. (2011). Do subducting seamounts generate or stop large earthquakes? *Geology*, *39*(9), 819–822.

Wang, K. and Bilek, S. L. (2014). Invited review paper: Fault creep caused by subduction of rough seafloor relief. *Tectonophysics*, *610*, 1–24.

Wang, K. and Hu, Y. (2006). Accretionary prisms in subduction earthquake cycles: The theory of dynamic Coulomb wedge. *Journal of Geophysical Research: Solid Earth*, *111*(6).

Watkinson, A. J. and Geraghty Ward, E. M. (2006). Reactivation of pressure-solution seams by a strike-slip fault-sequential, dilational jog formation and fluid flow. *American Association of Petroleum Geologists Bulletin*, *90*(8), 1187–1200.

Webber, S., Ellis, S., and Fagereng, Å. (2018). Virtual shear box experiments of stress and slip cycling within a subduction interface mélange. *Earth and Planetary Science Letters*, *488*, 27–35.

Weiss, L. E. and Turner, F. J. (2013). Some Observations on Translation Gliding and Kinking in Experimentally Deformed Calcite and Dolomite.

Willemse, E. J., Peacock, D. C., and Aydin, A. (1997). Nucleation and growth of strike-slip faults in limestones from Somerset, U.K. *Journal of Structural Geology*, *19*(12), 1461–1477.

Williams, C. A., Eberhart-Phillips, D., Bannister, S., Barker, D. H., Henrys, S., Reyners, M., and Sutherland, R. (2013). Revised interface geometry for the hikurangi subduction zone, New Zealand. *Seismological Research Letters*, *84*(6), 1066–1073.

Wintsch, R. P., Christoffersen, R., and Kronenberg, A. K. (1995). Fluid-rock reaction weakening of fault zones. *Journal of Geophysical Research: Solid Earth*, *100*(B7), 13021–13032.

Wood, M. (2012). The Historical Development of the Term Mélange' and Its Relevance to the Precambrian Geology of Anglesey and the Lleyn Peninsula in Wales, UK. *Journal of Geography (Chigaku Zasshi)*, *121*(1), 168–180.

Xu, L., Renner, J., Herwegh, M., and Evans, B. (2009). The effect of dissolved magnesium on creep of calcite II: transition from diffusion creep to dislocation creep. *Contributions to Mineralogy and Petrology*, *157*(3), 339–358.

Yabe, S., Ide, S., and Yoshioka, S. (2014). Along-strike variations in temperature and tectonic tremor activity along the hikurangi subduction zone, New Zealand. *Earth, Planets and Space*, *66*(1), 142.

Yamaguchi, A., Ujiie, K., Nakai, S., and Kimura, G. (2012). Sources and physicochemical characteristics of fluids along a subduction-zone megathrust: A geochemical approach using syn-tectonic mineral veins in the Mugi mélange, Shimanto accretionary complex. *Geochemistry, Geophysics, Geosystems*, *13*(1).

Yarce, J. (2020). *Microearthquake detection and seismic imaging using ocean bottom seismometers in the Hikurangi Margin, New Zealand*. Phd, University of Colorado.

Yarce, J., Sheehan, A. F., Nakai, J. S., Schwartz, S. Y., Mochizuki, K., Savage, M. K., Wallace, L. M., Henrys, S. A., Webb, S. C., Ito, Y., Abercrombie, R. E., Fry, B., Shaddox, H., and Todd, E. K. (2019). Seismicity at the Northern Hikurangi Margin, New Zealand, and Investigation of the Potential Spatial and Temporal Relationships With a Shallow Slow Slip Event. *Journal of Geophysical Research: Solid Earth*, *124*(5), 4751–4766.

Yasuhara, H. (2003). A mechanistic model for compaction of granular aggregates moderated by pressure solution. *Journal of Geophysical Research*, *108*(B11), 1–13.

Yasuhara, H., Marone, C., and Elsworth, D. (2005). Fault zone restrengthening and frictional healing: The role of pressure solution. *Journal of Geophysical Research: Solid Earth*, *110*(6), 1–11.

Zang, W. and Fyfe, W. S. (1995). Chloritization of the hydrothermally altered bedrock at the Igarapé Bahia gold deposit, Carajás, Brazil. *Mineralium Deposita*, *30*(1), 30–38.

Zhang, X., Salemans, J., Peach, C. J., and Spiers, C. J. (2002). Compaction experiments on wet calcite powder at room temperature: Evidence for operation of intergranular pressure solution. *Geological Society Special Publication*, *200*(1), 29–39.

Zhang, X. and Spiers, C. (2005). Compaction of granular calcite by pressure solution at room temperature and effects of pore fluid chemistry. *International Journal of Rock Mechanics and Mining Sciences*, *42*(7-8), 950–960.

Zhang, X., Spiers, C. J., and Peach, C. J. (2010). Compaction creep of wet granular calcite by pressure solution at 28řC to 150řC. *Journal of Geophysical Research: Solid Earth*, *115*(9), B09217.

Zhao, L., Zheng, T., Zhu, R., Wang, Q., Paul, A., Guillot, S., Aubert, C., Dumont, T., Schwartz, S., Solarino, S., Malusà, M. G., and Salimbeni, S. (2015). First seismic evidence for continental subduction beneath the Western Alps. *Geology*, *43*(9), 815–819.

Zhou, X. and Aydin, A. (2012). Mechanics of the formation of orthogonal sets of solution seams, and solution seams and veins and parallel solution seams and veins. *Tectonophysics*, *532*, 242–257.

Zubtsov, S., Renard, F., Gratier, J. P., Guiguet, R., Dysthe, D. K., and Traskine, V. (2004). Experimental pressure solution compaction of synthetic halite/calcite aggregates. *Tectonophysics*, *385*(1-4), 45–57.

Appendix A

Modelling pressure solution at site U1520

This appendix chapter details how P-T-t was constrained at Site U1520, the modelling methodology, and strains from models run at high pore fluid factor or with variable strain rate-mineralogy relationships. The full MATLAB code to run the models is available at github.com/HarryLeah/pressure-solution-modelling.

A.1 Constraining pressure, temperature, and calcite solubility through time

Following published constitutive models for diffusion-controlled pressure solution, differential stress and temperature-controlled solubility and diffusion coefficient limit the resulting strain rate (Nakashima, 1995; Plummer and Busenberg, 1982; Rutter, 1976; Spiers *et al.*, 2004, 1990; Zhang *et al.*, 2010). I used the age model described earlier and reported in Wallace *et al.* (2019) to calculate past sediment depth at a given time at each dated horizon in 0.1 Myr time steps (Figs. 9a & A.1a). I used this depth history to calculate the history of various conditions, including temperature and effective vertical stress, at a given depth and time. Temperature with time was calculated at constant sedimentary horizons corresponding to modern depths assuming a constant past geothermal gradient of 38 °C km^{-1} (Fig. 2c) from a

sea floor temperature of 0 °C. These temperatures (T) were then used to calculate calcite solubility in the same manner as Zhang *et al.* (2010); the square root of the dissolution coefficient (K_{sp}), itself calculated with time and depth using the equation of Plummer and Busenberg (1982):

$$LogK_{sp(t,z)} = -171.9065 - 0.077993T_{(t,z)} + 2839.319/T_{(t,z)} + 71.595T_{(t,z)}. \quad \text{(A.1)}$$

I avoided the problem of factoring in sea level change since the Cretaceous by directly calculating effective vertical stress (σ_v^{eff}) assuming hydrostatic stress throughout the sediment column using a typical constant sea water density (ρ_w) of 1024 kg m^{-3} (Nayar *et al.*, 2016). This means at the sea floor or in the water column (i.e. when sediment depth (z) ≤ 0):

$$\sigma_v^{eff} = (\rho_b - \rho_w)gz = 0 \quad \text{(A.2)}$$

where g is gravitational acceleration (9.81 ms^{-1}) and ρ_b is mean bulk sediment density between the seafloor and the depth considered (Fig. 3.1a). I then used this bulk sediment density data with the age model (Fig. 3.1d) to calculate effective vertical stress at each time step. I also explored the effect of near-lithostatic pore pressures (Fig. A.1) by incorporating a pore fluid factor ($\lambda = P_f/\sigma_v$) to give:

$$\sigma_v^{eff} = g\sum_{i=1}^{n}(\rho_{b(i)} - \lambda\rho_{b(i)})dz_{(i)} \quad \text{(A.3)}$$

where P_f is the pore fluid pressure and σ_v is the vertical stress. I explored an end-member of near-lithostatic $\lambda = 0.95$.

A.2 Modelling the history of pressure solution at Site U1520

The depth, temperature, solubility, and stress histories shown above were then used with a published diffusion-controlled pressure solution model, first derived by Rut-

ter (1976, 1983) and since adapted or experimentally calibrated by several authors (Gratier *et al.*, 2013; Spiers *et al.*, 2004, 1990; Zhang *et al.*, 2010). To calculate the rate of change in uniaxial strain from pressure solution at each modern depth with time, I used the equation:

$$\dot{\varepsilon}_{ps(t,z)} = A_d \frac{D_{(t,z)} S C_{(t,z)}}{d^3} \frac{\sigma_{n(t,z)} \Omega}{R T_{(t,z)}} f_d(\phi_{(z)}) \tag{A.4}$$

where A_d is a geometric constant equal to 100 (Pluymakers and Spiers, 2015), D is the diffusion coefficient, which follows an Arrhenius temperature dependency and has a typical value of $1 \times 10^{-10} \mathrm{m^2 s^{-1}}$ at 25 °C (Nakashima, 1995), S is the grain boundary fluid phase thickness of 1×10^{-9} m (Renard *et al.*, 1997), $C_{(t,z)}$ is the solubility of calcite at time t and depth z in $\mathrm{m^3\ m^{-3}}$ (Eq. A.1). Grain size (d), was varied from 10 to 150 μm to represent variability within the sampled sediments and test accordance with strains calculated from stylolite frequency, the value shown in plots is 100 μm as this shows the best agreement with independently calculated strains. Effective normal stress ($\sigma_{n(t,z)}$) was used at each time (t) and depth (z) in the model, assuming normal stress is equal to the vertical stress as stylolites are generally horizontal (Eq. A.3). Also used was the molar volume of calcite (Ω, 3.693×10^{-5} $\mathrm{m^3 mol^{-1}}$), universal gas constant (R, 8.31 J $\mathrm{mol^{-1}\ K^{-1}}$), and $f_d(\phi_{(z)})$. This final factor is a term accounting for grain contact area:

$$f_d(\phi_{(z)}) \approx 1/(q - 2\phi_{(z)})^2 \tag{A.5}$$

where $\phi_{(z)}$ is measured porosity at depth z (Fig. 6c) and q is a critical porosity (assumed to be equal to twice maximum porosity). This model assumes regular packing of spherical grains, with diffusion-controlled dissolution occurring at grain contact areas, itself controlled by porosity, strain, and stress (Pluymakers and Spiers, 2015). As calcite is the only mineral dissolving but not the only mineral in the sediment, strain rate from the model was then scaled by the relative volume of calcite within the core, determined from the weight percent (Fig. 6d) and density of calcite (2710 kg $\mathrm{m^3}$). In this way the physical and chemical properties of the sediment at each depth are represented in the strain rate model over the history of

dissolution within the sediment.

I then integrated modelled strain rate ($\dot{\varepsilon}$) with time (t) to get cumulative strain (ε) by applying the strain from each 0.1 Myr time step (ε^{step}) to an arbitrary length (L) at each modelled depth. The strain from each time step is calculated using ($\varepsilon^{step}_{(t)} = \dot{\varepsilon}_{(t)} t^{step}$). This was then applied to either the original length (when $t = 1$, $L_{(t)} = L_o + \varepsilon^{step}_{(t)} L_o$) or the strained length (when $t > 1$, $L_{(t)} = L_{(t-1)} + \varepsilon^{step}_{(t)} L_{(t-1)}$) and the strain compared to the original length was calculated ($\varepsilon_{(t)} = [L_{(t)} - L_o]/L_o$).

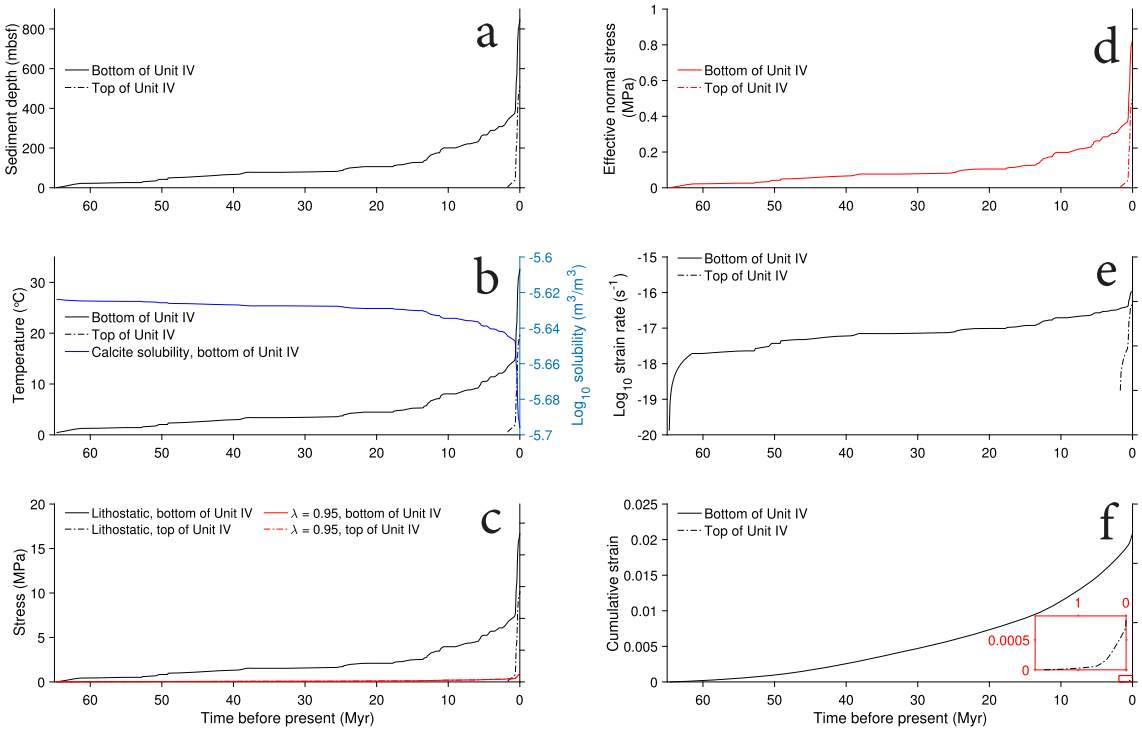

Figure A.1: Pressure solution model inputs and outputs with time at high pore fluid factor. Plots show (a) sediment depth, (b) temperature and solubility calculated from Plummer and Busenberg (1982), (c) lithostatic and near-lithostatic stress from high pore fluid pressures, (d) effective normal stress, (e) strain rate from diffusion controlled dissolution of calcite according to published models for pressure solution (Rutter, 1976, 1983), and (f) cumulative strain from diffusion controlled dissolution of calcite at the top and bottom of Unit IV with time. Inset in (f) is zoomed area showing cumulative strain at top of Unit IV. Most plots show results for the bottom (848.45 mbsf) and top (510.96 mbsf) of Unit IV. Plots of model results are for a grain size of 100 μm.

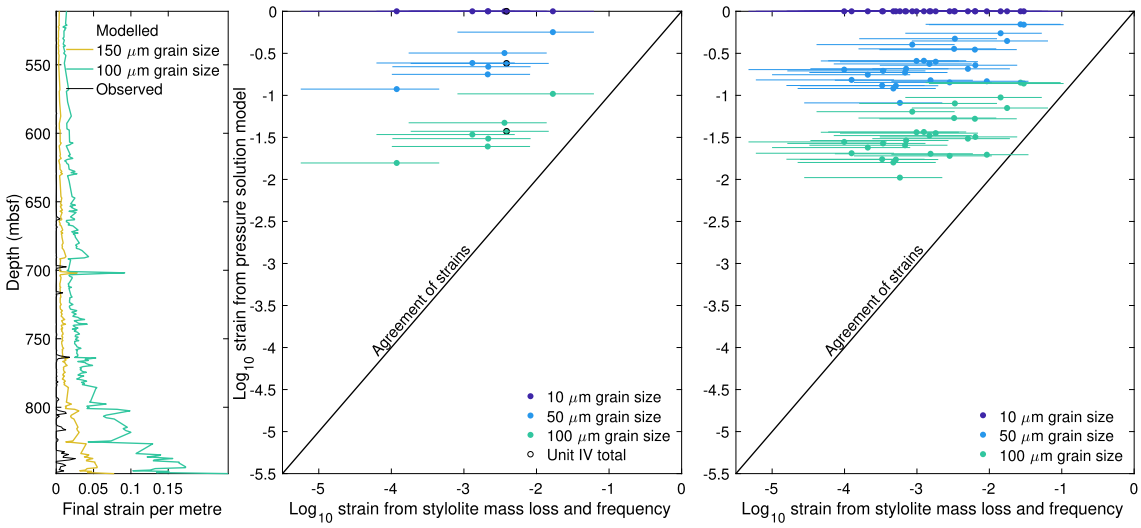

Figure A.2: Comparison of modelled and calculated strains for compaction by stylolites at hydrostatic fluid pressures within Unit IV using the scaling of Zubtsov *et al.* (2004). Plots show (left) final cumulative strain with depth per metre, (middle) strain within each lithology and all of Unit IV (outlined in black), and strain within each core section (right). Error bars show strain ranges for individual stylolite seams of strain 0.1 to 0.9 used in calculation of bulk strain. As I am dealing solely with shortening strains, they are shown as positive.

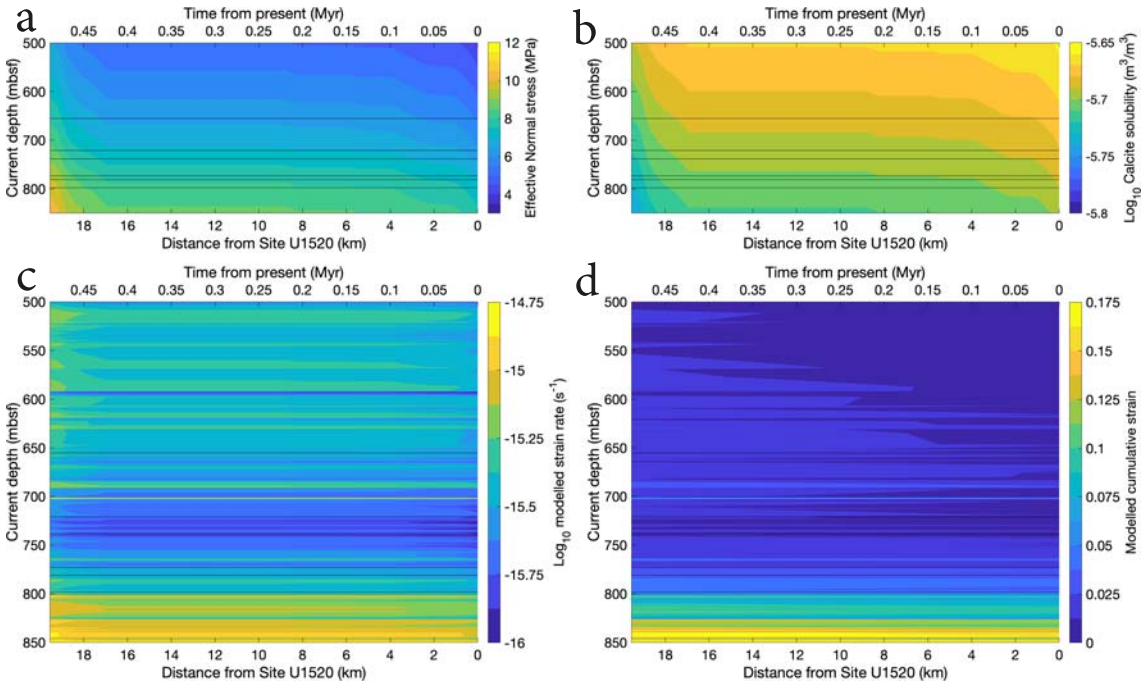

Figure A.3: Modelled effective normal stress (a), calcite solubility (b), strain rate from pressure solution (c), and resultant cumulative strain (d) from Site U1520 to the interface as a function of distance. Model is for 100 μm grain size. Conditions were calculated assuming a sediment load equal to that currently overlying Unit IV between Site U1520 and the toe of the décollement.

Appendix B

Receiver function processing methods

B.1 Receiver function deconvolution and Green's function inversion

The rf package (Eulenfeld, 2020), which makes use of Obspy (Beyreuther *et al.*, 2010; Krischer *et al.*, 2015), was used to download arrivals at the NZ3D stations from earthquakes with M_w between 5.5 and 7.5 that occurred at epicentral distances between 30° and 90° away (Fig. 4.5).

The iterative time-domain deconvolution of Ligorría and Ammon (1999) assumes the vertical component records the incident wavelet and uses a least squares method to minimise the difference between the R component trace and a convolution of the estimated receiver function with the Z component trace. The receiver function is constructed a series of positive and negative Gaussian spikes; the time of each spike is determined by the peak lag in a cross-correlation of the Z and R components and the amplitude is determined using the method of Kikuchi and Kanamori (1991). At the end of each iteration, after one spike has been added to the receiver function, the convolution of the receiver function and the Z component trace are subtracted from the R component trace and the misfit between the two is calculated. High amplitude spikes are added first, reducing in amplitude until the addition of further

spikes results in negligible change in the misfit. This method avoids many of the complications which result from frequency-domain estimation of receiver functions and provides less noisy receiver functions as the addition of noise peaks to the receiver function does not significantly reduce the misfit (Ligorría and Ammon, 1999). The width of the Gaussian pulse used to construct each spike can be varied with the method; typical values for Gaussian pulse width in receiver functions are around 2.5 (Ligorría and Ammon, 1999), creating a pulse that is 1 s wide. I applied this method to run until it reaches a maximum of 200 iterations(i.e. until there are 200 spikes), or the misfit reduction is less than 1×10^{-5}. An example of the resulting receiver function can be seen in Figure B.1.

Iterative time-domain estimation of receiver functions was a big step forward in estimating receiver functions in noisy environments and has been applied to various collisional settings (Kim *et al.*, 2012; Phillips and Clayton, 2014; Shi *et al.*, 2015; Zhao *et al.*, 2015), where high seismic noise is common. Despite its widespread adoption, the method is not without its drawbacks. The choice of Gaussian pulse width is important, for instance a width of 2.5 effectively filters out frequency content higher than 1.2 Hz (Ligorría and Ammon, 1999). While this may not be a problem for many applications, I aimed to estimate crustal structure at depths of less than 80 km with resolution around the plate interface below the NZ3D array at depths of 15-20 km (Williams *et al.*, 2013). This required higher frequency content and a smaller Gaussian pulse width (i.e. width > 2.5), though this introduces the potential for more noise to translate into the receiver functions. I retried the method with a Gaussian pulse width of 4 (Fig. B.2). This results in a pulse width of 0.75 s and an effective low-pass frequency of around 2 Hz. The resulting receiver functions were very similar to those deconvolved using a pulse width of 2.5 (Figs. B.1 & B.2). Higher frequency deconvolution methods were tried (up to a Gaussian pulse width of 10) but yielded poorer fits and less clear receiver functions.

As pointed out by Akuhara *et al.* (2019), the addition of pulses to the receiver function during iterative time-domain deconvolution is immutable; once a pulse has been added it cannot be removed, even if it increases the misfit. At high frequencies (or low Gaussian pulse widths) the addition of pulses commonly increases the misfit

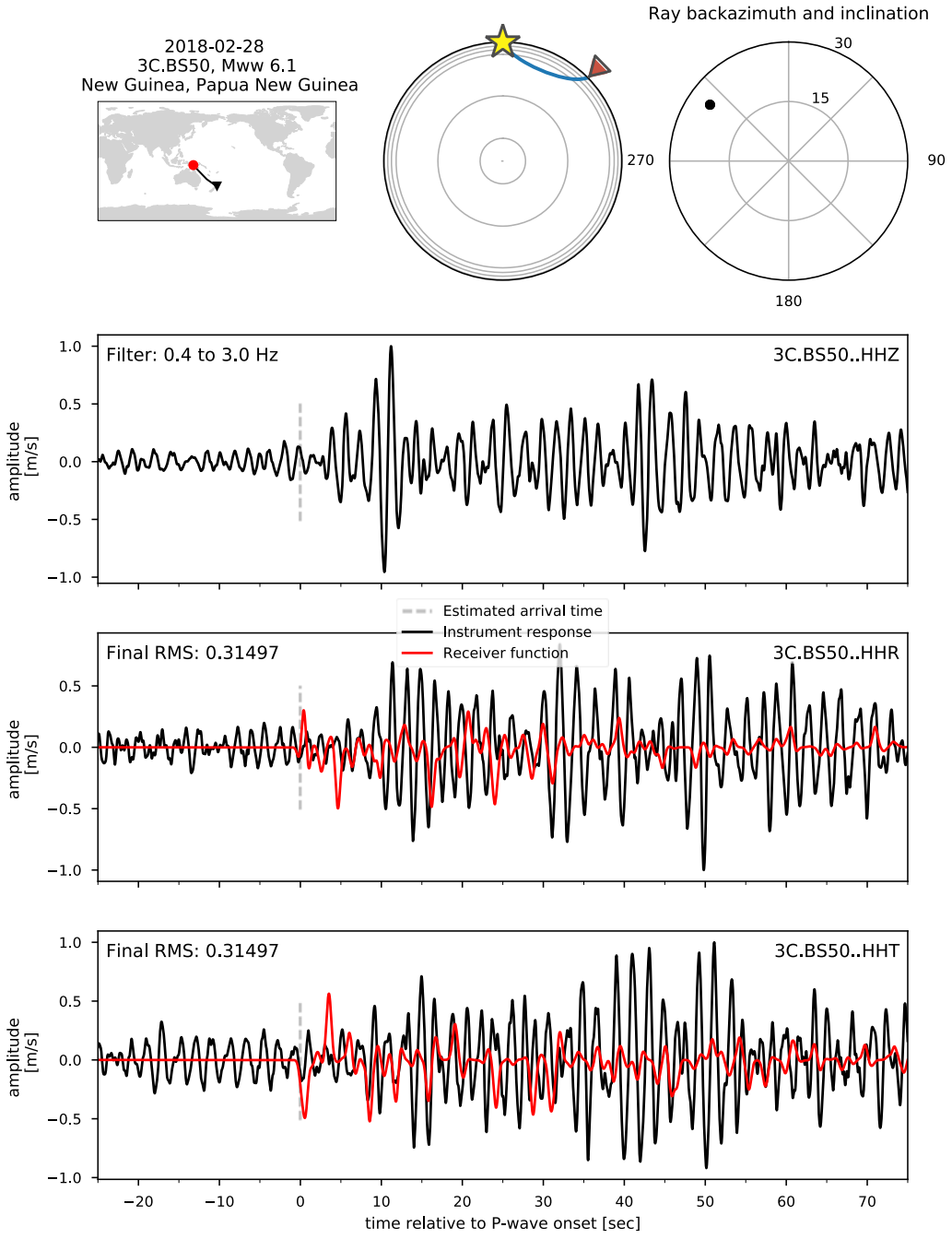

Figure B.1: A summary of an earthquake arrival and good receiver function estimated using the iterative time-domain deconvolution method of Ligorría and Ammon (1999) with a Gaussian pulse width of 2.5.

as the deconvolution is more sensitive to noise. Recently-published work on receiver function estimation using Bayesian statistics was developed for application to OBSs (Akuhara *et al.*, 2019), where noise is typically high. I therefore explored the use of this deconvolution method to provide more reliable receiver functions at higher frequency.

Recently, workers have made use of ever-growing computing power and advanced statistics to recover interface depths or velocities from teleseismic earthquake arrivals without deconvolution of receiver functions (Bodin *et al.*, 2012, 2014; Frederiksen and Delaney, 2015). These methods avoid deconvolution by defining misfit functions in terms of direct observations on the R and Z components in the time domain, where error can be assumed to be normally distributed and estimated using conventional statistics (Bodin *et al.*, 2014). The likelihood of other parameters can then be estimated using this error estimate and probability distributions of various parameters can be constructed. These works provided a new way of investigating receiver-side structure, though the inversion techniques described so far relied on laterally-continuous layers with reasonably consistent seismic properties (Bodin *et al.*, 2012, 2014; Frederiksen and Delaney, 2015). In areas such as the Hikurangi margin this poses a problem; the area is likely laterally heterogeneous with highly variable seismic properties where approaches such as these are unlikely to yield reasonable results. The recently published work of Akuhara *et al.* (2019) is a generalisation of the work of Bodin *et al.* (2014). Akuhara *et al.* (2019) estimate Green's functions of receiver-side perturbation for each ray rather than directly solving for subsurface structure, inherently allowing for complex 3-dimensional variation.

Green's functions are estimated using a trans-dimensional Bayesian inversion method where the number and value of model parameters are estimated during the inversion process (Akuhara *et al.*, 2019). To achieve this the inversion is posed as a multichannel deconvolution problem which is translated into a Bayesian framework. Multichannel deconvolution assumes that the observed three-component seismograms ($u_x(t)$ where x is component R, T, or Z at time t) is the result of the convolution of an incident wavelet ($s(t)$), a Green's function representing the perturbation of the wavelet due to the receiver-side structure ($g_x(t)$ where x is component

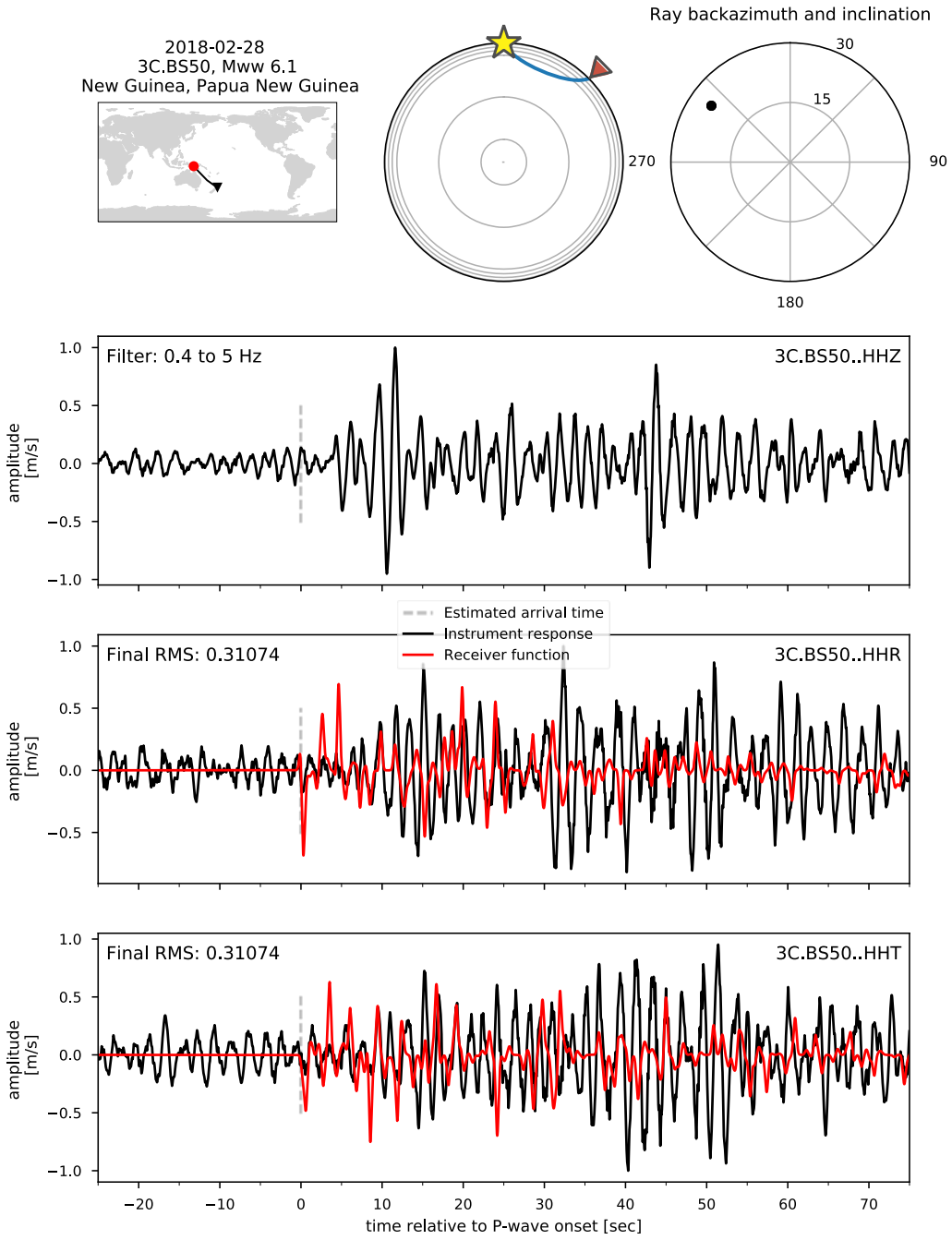

Figure B.2: A summary of an earthquake arrival and good receiver function estimated using the iterative time-domain deconvolution method of Ligorría and Ammon (1999) with a Gaussian pulse width of 4. Note the higher final RMS misfit than with a lower Gaussian pulse width.

R, T, or Z), and noise ($\epsilon_x(t)$ where x is component R, T, or Z):

$$\begin{aligned} u_r(t) &= s(t) * g_r(t) + \epsilon_r(t) \\ u_t(t) &= s(t) * g_t(t) + \epsilon_t(t) \\ u_z(t) &= s(t) * g_z(t) + \epsilon_z(t) \end{aligned} \tag{B.1}$$

where an asterisk denotes convolution. The effective incident wavelet ($s(t)$) is assumed to be consistent for all three components, meaning it can be cancelled when combining two components (typically R and Z). A composite noise term ($\epsilon(t) = \epsilon_r(t) * g_z(t) - \epsilon_z(t) * g_r(t)$) can be obtained via

$$u_r(t) * g_z(t) - u_z(t) * g_r(t) = \epsilon(t) \tag{B.2}$$

where the left hand side of Equation B.2 can be used as a misfit function:

$$\phi(t) = u_r(t) * g_z(t) - u_z(t) * g_r(t). \tag{B.3}$$

In this way common factors between the two components (R and Z in this case) are considered the incident wavelet rather than just the Z component directly (Langston, 1979).

Similar to the iterative time-domain deconvolution method of Ligorría and Ammon (1999), the Green's function is constructed of a series of Gaussian pulses (Akuhara *et al.*, 2019). A single isolated pulse of amplitude 1 is constrained to the P wave onset time ($t = 0$ s) on the Z component and further pulses are limited to at least 1 second after that time to separate the incident wavelet from the Green's function. The inversion solves for the number, timing, and amplitudes of pulses on the two components (typically R and Z) where $t > 1$ s. This is done by constructing posterior probability distributions assuming uniform prior probability between prior bounds (Green, 1995). Prior bounds are to be carefully selected as narrow bounds may not capture the real solution and wide bounds may not lead to a unique solution (Akuhara *et al.*, 2019). Initial inversions yield maximum posterior probabilities for the number of pulses at the default upper bound (200), so I increased this value

to 1001 to fully capture the pulse number. Aside from the number of pulses, I used the default bounds when running my inversion (Table B.2). Noise within the traces being inverted is assumed not to be temporally correlated (Akuhara *et al.*, 2019). This assumption is not true (temporally correlated noise is used in ambient seismic studies, for instance) and can lead to over-fitting of noise during the inversion, as will be shown later.

During the inversion sampling and construction of the posterior probability distributions is performed by a RJMCMC method (Green, 1995). Once per iteration the Markov chain Monte Carlo (MCMC) algorithm samples the input probabilities (Table B.2) and either: adds a pulse (a birth proposal), removes a pulse (a death proposal), moves the timing of a pulse (a move proposal), or perturbs the amplitude of a pulse (a perturbation proposal) on either of the two input components (typically R and Z Akuhara *et al.*, 2019). Birth proposals add a new dimension to the inversion by increasing the number of pulses, whereas death proposals reduce the dimensions of the inversion by reducing the number of pulses. The ability to add and remove pulses allows the inversion to test and undo unlimited combinations of pulses and their variables (e.g. amplitude, timing, component) during its exploration of trans-dimensional space (Green, 1995). This means the inversion is reversible and forms the basis for the reversible-jumping part of the RJMCMC algorithm (Akuhara *et al.*, 2019). Reversibility gives the trans-dimensional RJMCMC inversion a distinct advantage over the popular iterative time-domain receiver function deconvolution, where the addition of pulses is immutable even if it worsens fit (Ligorría and Ammon, 1999).

From a random seed (Akuhara *et al.*, 2019) the inversion is run for 1.2×10^6 iterations (N_{iter}; Table B.2). A short initial 'burn-in' period (where the model is not saved) runs for 2×10^5 iterations (N_{burn}; Table B.2) before the model is sampled every 200 iterations (N_{corr}) for the remaining 1×10^6 iterations ($N_{iter} - N_{burn}$). This means the inversion retrieves 5×10^3 models (N_{mod}), from which (ignoring t for simplicity) the marginal posterior probability (p) of low-pass filtered Green's

functions (g_r^{LPF} and g_z^{LPF}) are estimated using:

$$p(g_r^{LPF}) = \frac{1}{N_{mod}} \sum_{i=1}^{N_{mod}} \delta(g_r^{LPF} - f_{r,i}^{LPF})$$
$$p(g_z^{LPF}) = \frac{1}{N_{mod}} \sum_{i=1}^{N_{mod}} \delta(g_z^{LPF} - f_{z,i}^{LPF}) \tag{B.4}$$

where $f_{r,i}^{LPF}$ and $f_{z,i}^{LPF}$ are low-pass filtered Green's functions from the ith model.

The RJMCMC process is computationally expensive, and efficiencies are achieved by running 100 RJMCMC sampling chains in parallel (N_{chain}) with different 'temperatures' dictating their exploration range for each variable, a method known as 'parallel tempering' (Falcioni and Deem, 1999; Geyer, 1991). Of the 100 chains, 20 (N_{cool}) are kept at a temperature (T) of 1. Higher temperature chains are more likely to accept proposals, yet posterior probability is only evaluated using chains where $T = 1$ (Akuhara *et al.*, 2019). Parallel tempering allows chains to swap models during the inversion (Sambridge, 2013); higher temperature chains explore trans-dimensional space and when a probable model is found it is transferred to a low temperature chain and recorded as one of N_{mod}.

Code for running the Green's function inversion of Akuhara *et al.* (2019) is available on GitHub (https://github.com/akuhara/MC3deconv) and Zenodo (DOI: 10.5281/zenodo.1487600) and took around 2 minutes to run for each earthquake arrival. It was first done with a subset of arrivals with a $SNR > 3$ (around 2700 traces), before being expanded to all the arrivals (around 7000 arrivals). The inversion yields probabilities of each amplitude at each time for the Z and R components, and the resulting Green's function for each component follows the highest probability amplitude at each time (Fig. B.3). Posterior probability distributions for the number of pulses commonly show multiple peaks, reflecting the non-uniqueness of the solution. In some cases brief increases in seismic noise (e.g local earthquakes or passing traffic) have led to over-fitting and increases in amplitude where amplitudes would be expected to tail off (Fig. B.3).

Group	Notation	Description	Value
Prior	k_{min}	Minimum number of pulses	1
	k_{max}	Maximum number of pulses	1001
	τ_{min}	Minimum time of pulses (after P wave arrival)	1 s
	τ_{max}	Maximum time of pulses (after P wave arrival)	60 s
	r_{min}	Minimum pulse amplitude on R component	-0.8
	r_{max}	Maximum pulse amplitude on R component	0.8
	z_{min}	Minimum pulse amplitude on Z component	-0.8
	z_{max}	Maximum pulse amplitude on Z component	0.8
Proposal type	p_{birth}	Probability of birth proposal	0.35
	p_{death}	Probability of death proposal	0.35
	p_{move}	Probability of move proposal	0.05
	$p_{perturb}$	Probability of perturbation proposal	0.25
Proposal	σ_τ	Standard deviation for move proposal	0.1 s
	σ_r	Standard deviation for perturbation proposal on R component	0.05
	σ_z	Standard deviation for perturbation proposal on Z component	0.05
	$\sigma_{r,birth}$	Standard deviation for birth proposal on R component	0.4
	$\sigma_{z,birth}$	Standard deviation for birth proposal on Z component	0.4
Iteration	N_{iter}	Total number of iterations	1.2×10^6
	N_{burn}	Number of iterations in burn-in period	2×10^5
	N_{corr}	Iteration sampling interval	200
Low-pass filter	a	Parameter of Gaussian low-pass filter	8
Parallel tempering	N_{chain}	Number of MCMC chains running in parallel	100
	N_{cool}	Number of chains with low temperature ($T = 1$)	20
	T_{high}	Maximum temperature	100

Table B.2: Input parameters used for the inversion of Green's functions.

B.2 Velocity inversion

An extension of the RJMCMC algorithm has been developed for inversion of receiver functions for P and S wave velocity (Akuhara *et al.*, 2020). Given the wide array of solutions (V_p, V_s, and interface number and depth are all kept variable), the velocity inversion requires a starting velocity model to find a numerically stable solution. Similar to previous velocity inversion methods (Bodin *et al.*, 2012, 2014), this method assumes lateral homogeneity so that different traces arriving at the

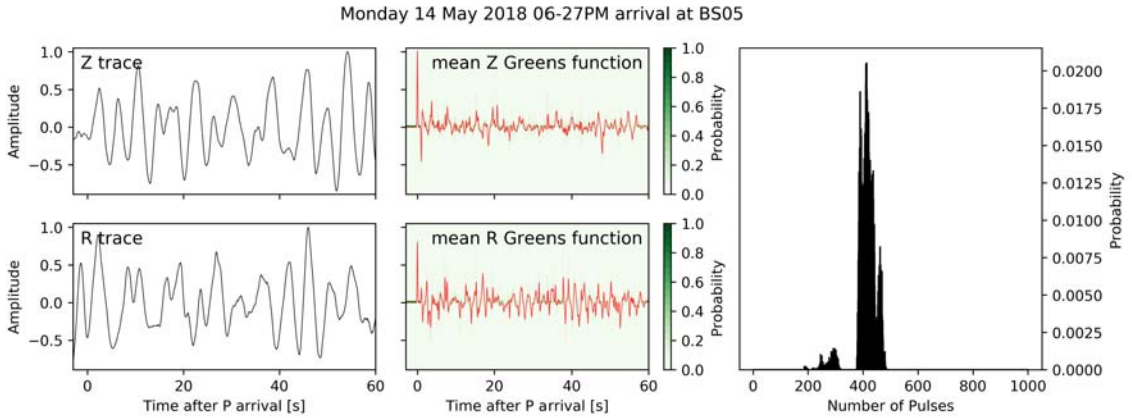

Figure B.3: An example of an earthquake arrival and resulting Green's function inverted using the method of Akuhara *et al.* (2019). Arrival traces (left) have been normalised to 1. Posterior probability distribution for number of pulses is shown on right. Note within both R and Z Green's functions the increased amplitude after 40 seconds where the inversion has over-fitted to noise.

same station sample the same velocities. For $Z < 20$ km this can be accounted-for by separating rays based on back-azimuth (Akuhara *et al.*, 2020), but deeper in the Hikurangi margin subduction zone, significant local variation and ray dispersion is likely to occur (Bassett *et al.*, 2014; Eberhart-Phillips *et al.*, 2017, 2010).

A velocity profile vertically beneath station BS05 was interpolated from a regional velocity model (Eberhart-Phillips *et al.*, 2010). All other values were kept at the defaults (Table B.4) suggested by Akuhara *et al.* (2020) and in the documentation associated with the inversion code (DOI: 10.5281/zenodo.3614105). The inversion yields Log-likelihood estimates at each iteration as well as posterior probability distributions for the number of interfaces, the amplitude of the receiver function at each time (for comparison to the input), and V_p, V_s, V_p/V_s and interface likelihood at each depth (Figs. B.5, B.6, B.7). Velocity inversions yield good fits to the first 10 s of receiver functions, with poorer fits after 10 s (Fig. B.4). The most likely inverted velocity model closely matches the input model. To test the sensitivity of the inversion to inputs, the velocity model was increased and decreased by 10% (Figs. B.6 & B.7). Outputs of these inversions also closely follow the input velocity models, suggesting the inversion would not yield reliable results if used here.

Group	Description	Value
Iteration	Number of burn-in iterations	2.5×10^5
	Number of sampling iterations	5×10^6
	Iteration sampling interval	100
Parallel tempering	Number of chains	120
	Number of cool chains	24
	Highest temperature	50
Input data	Time period for inversion	0-30 s
	Number of points in Fourier transform	2048
Prior	Minimum number of interfaces	1
	Maximum number of interfaces	200
	Minimum interface depth	0 km
	Maximum interface depth	100 km
	Minimum layer thickness	0.5 km
	Standard deviation for V_s perturbation	0.1
	Standard deviation for V_p perturbation	0.2
	Minimum Gaussian parameter for random noise	0.005
	Maximum Gaussian parameter for random noise	0.08
Proposal	Standard deviation for depth perturbation proposal	0.03
	Standard deviation for V_s perturbation proposal	0.02
	Standard deviation for V_p perturbation proposal	0.02
	Standard deviation for noise sigma perturbation proposal	0.005
Bounds	Minimum V_p	2 km s^{-1}
	Maximum V_p	10 km s^{-1}
	Minimum V_s	1 km s^{-1}
	Maximum V_s	7 km s^{-1}
	Minimum V_p/V_s	1
	Maximum V_p/V_s	3

Table B.4: Input parameters used for the inversion of V_p and V_s from Green's functions.

To test whether simultaneously inverting multiple receiver functions yielded more reliable results, 5 receiver functions from BS05 with similar back azimuths and inclinations were used as inputs. In contrast to the inversion of single receiver functions, inversion of multiple receiver functions yielded highly variable fits between peak posterior probabilities and input receiver functions (Fig. B.4). The inversion locally yielded good fits for early parts of the receiver functions ($t < 10$ s), but fits in the latter part of the receiver functions ($t > 10$ s) were generally poor (Fig. B.4). Inverted velocities offer only slight variations from the input velocity model, suggesting there was little use in exploring this inversion method further.

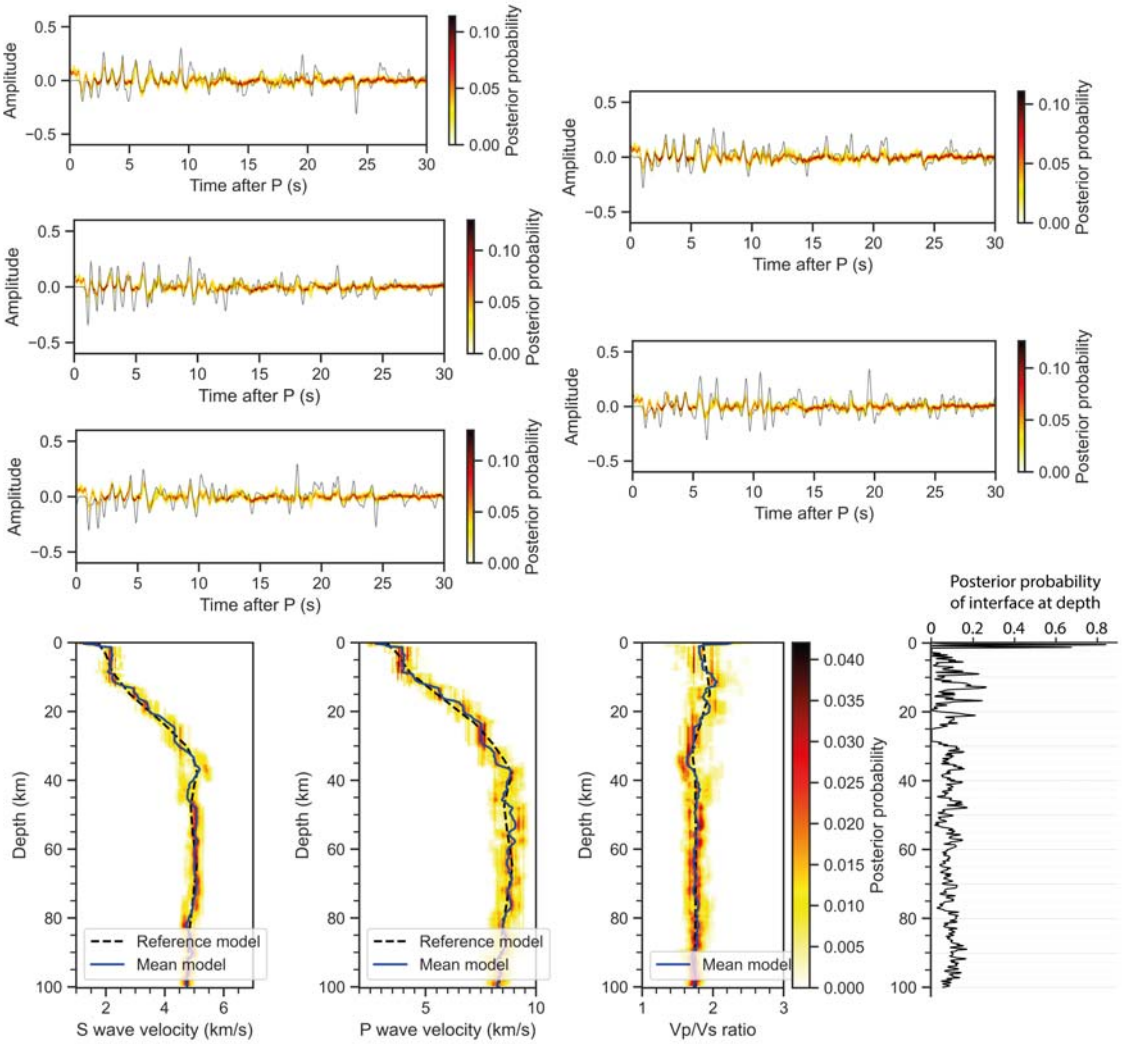

Figure B.4: Velocity inversion results for 5 R component receiver functions from station BS05 with interpolated input velocity model vertically below station BS05 from velocity model of Eberhart-Phillips *et al.* (2010).

B.3 Modelling major conversion horizons

During initial selection of time windows around earthquake arrivals, V_p and V_s from the iasp91 model were used to calculate the average ray parameter (also called slowness) for the path of the earthquake using the Taup toolbox (Crotwell *et al.*, 1999). This slowness can be used to calculate the theoretical arrival time of a P to S conversion using Equation 4.1. Multiples can also be calculated by adding the corresponding number of P wave velocities ($\sqrt{\frac{1}{V_p^2} - p^2}$) or S wave velocities

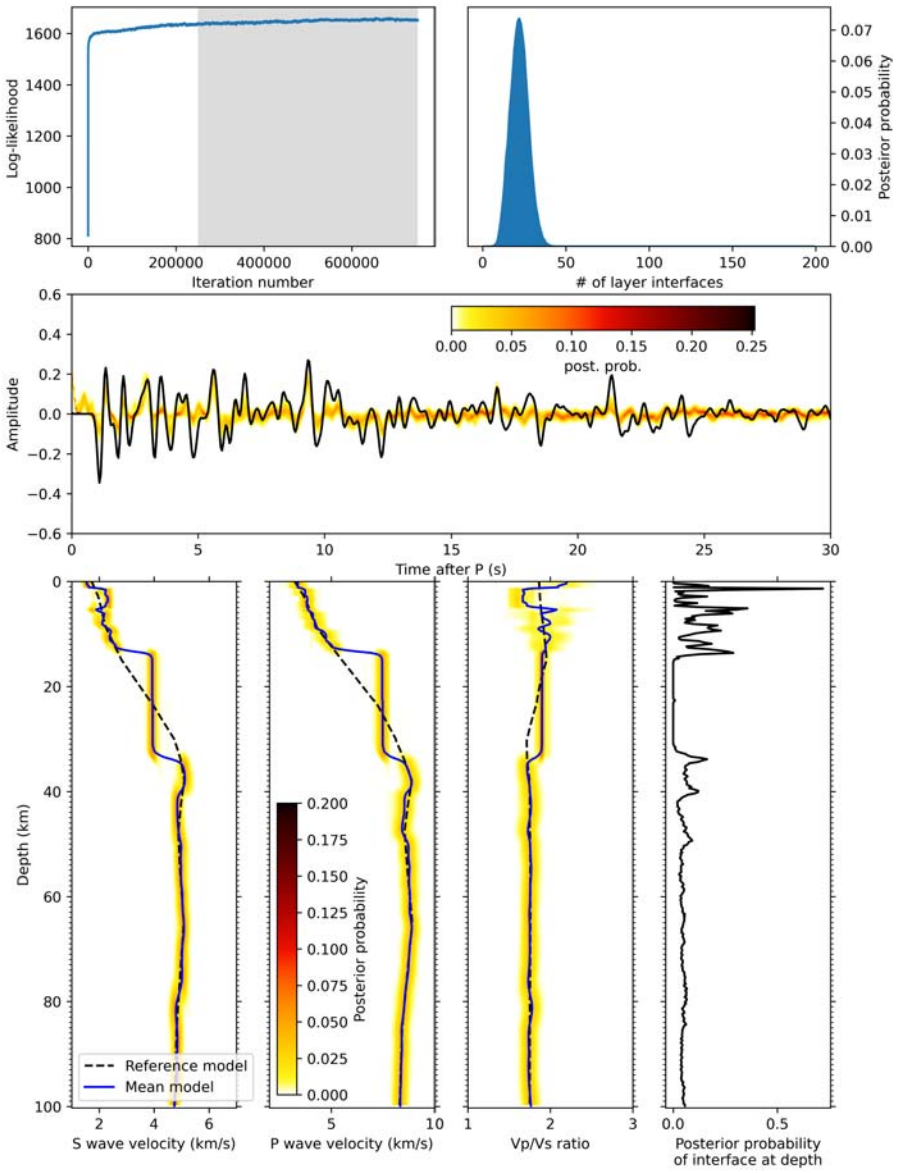

Figure B.5: Velocity inversion results for an R component Green's function from station BS05 with interpolated input velocity model vertically below station BS05 from velocity model of Eberhart-Phillips *et al.* (2010).

$(\sqrt{\frac{1}{V_s^2} - p^2})$ to the initial S wave velocity, for example:

$$t_{PpPs} = z * \left[\sqrt{\frac{1}{V_s^2} - p^2} + \sqrt{\frac{1}{V_p^2} - p^2}\right]$$
$$t_{PpSs,PsPs} = z * \left[2\sqrt{\frac{1}{V_s^2} - p^2}\right]. \tag{B.5}$$

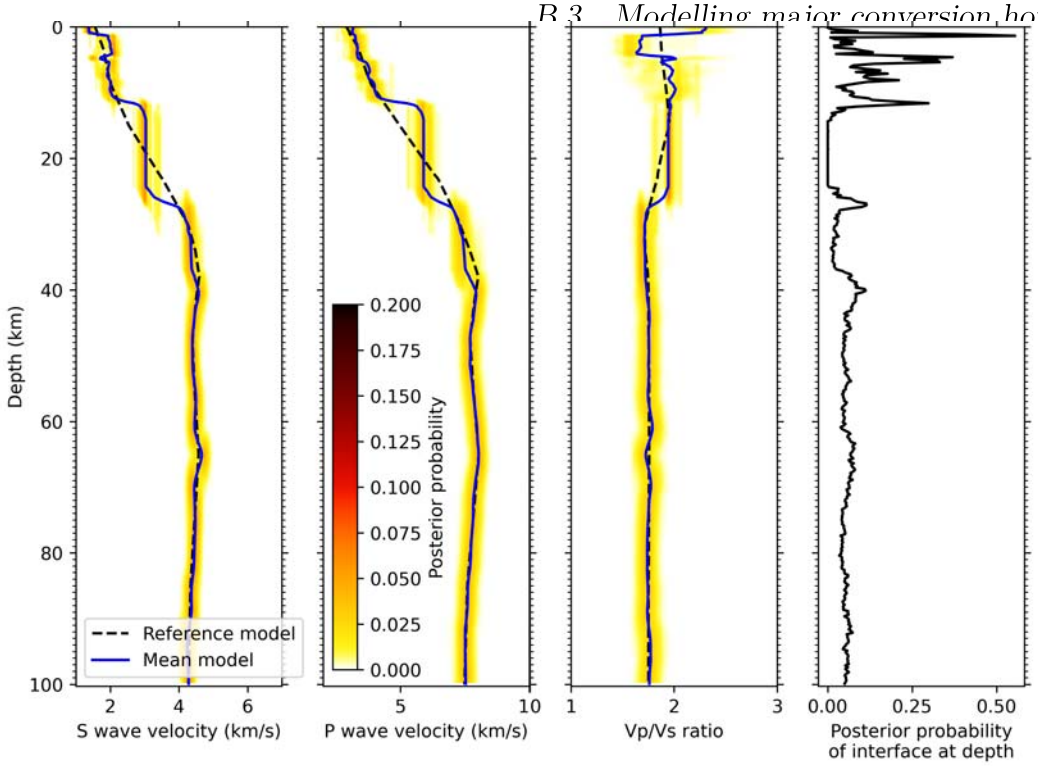

Figure B.6: Velocity inversion result with an input velocity model 10% lower than in Fig. B.5.

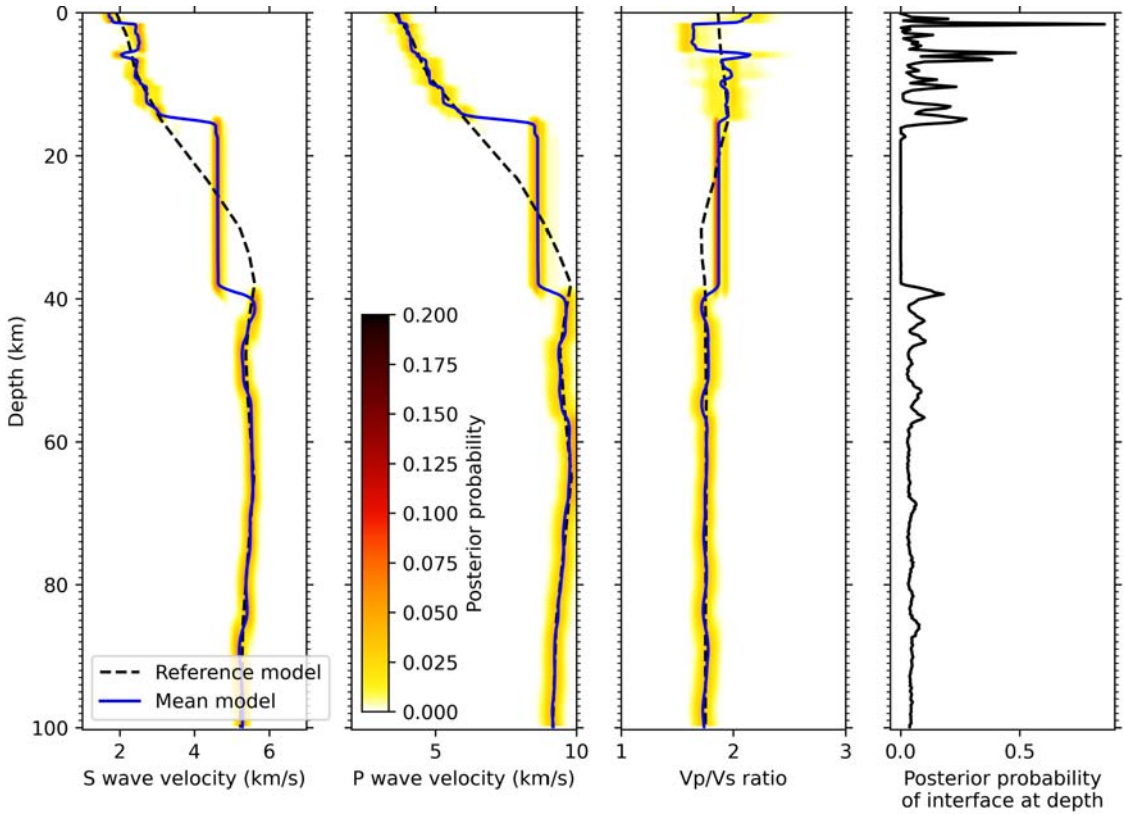

Figure B.7: Velocity inversion result with an input velocity model 10% higher than in Fig. B.5.

Velocity-depth profiles interpolated along each ray path from the regional model of Eberhart-Phillips *et al.* (2010) are smooth due to the low resolution of the regional model, and smooth velocity profiles do not produce receiver functions with clear peaks (Cassidy, 1992). To model an interface at a given depth while retaining the same travel times (and thus relative arrival times) an abrupt velocity change must be introduced to the interpolated velocity-depth profile whilst maintaining the same average velocities above the velocity change. This was done for each arrival at a station and the resulting velocity model was used as an input (along with the back azimuth and slowness of the arrival) for the RAYSUM program (Frederiksen and Bostock, 2000), used through the python interface PyRaysum (available on GitHub at https://github.com/paudetseis/PyRaysum). Three component arrivals were generated using RAYSUM before receiver functions were deconvolved from the R and Z components and the resulting waveform was low-pass filtered at 3 Hz to match the approximate frequency content of the real receiver functions.

To show how a possible conversion horizon model might manifest in a receiver function retrieved from the data Fig. B.8 shows a comparison between a real receiver function at station BS05 and a modelled receiver function using the velocity profile interpolated along the ray path from the New Zealand regional velocity model (Eberhart-Phillips *et al.*, 2010). The real receiver function was selected as it has the highest cross-correlation coefficient with the average receiver function for the station. The synthetic receiver function was modelled using the slowness and back azimuth of the real receiver function to have a single P-to-S conversion at a 14 km horizon (the approximate depth of the plate interface beneath BS05, Williams *et al.*, 2013, Fig. B.8). Peaks from P, Ps and PpPs arrivals are clearly recognisable in both the synthetic and real receiver functions, suggesting the arrival may have travelled through a conversion horizon at approximately 14 km depth and that these peaks can be taken to represent this conversion. PpSs and PsPs arrivals, which are clearly visible as a negative peak in the synthetic receiver function, are mostly masked in the real receiver function by later peaks arriving at the same time. A small negative deflection, visible in the positive peak of the real receiver function at 12.5 s, may reflect the convolution of these signals (Fig. B.8). Amplitudes of arrivals within the

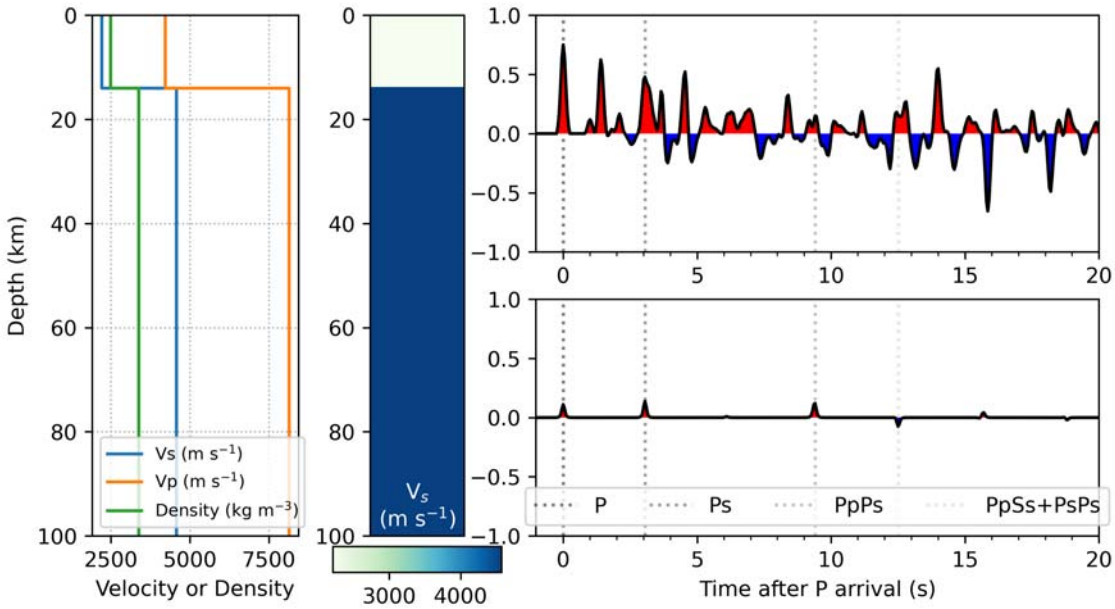

Figure B.8: Example of modelling a single interface to match peaks in a trace arriving at station BS05. Plots show V_p, V_s, and density with depth (left), layers coloured by their V_s (centre-left), real receiver function at BS05 (upper right), and synthetic receiver function modelled using the velocity and density profile on the left(lower right). Average velocities for each layer are the same over their depth range (< 100 km depth) as interpolated along the ray path from the regional velocity model of Eberhart-Phillips *et al.* (2010). Direct (P and Ps) and multiple (PpPs, PpSs, and PsPs) phase arrival times are highlighted on both traces.

real receiver function are much higher than those modelled in the synthetic receiver function suggesting the time, rather than the amplitude, of modelled conversions are more reliable.

B.4 Surface regression methodology

The coordinates corresponding to the peaks picked in the receiver functions (e.g. Fig. B.9) were selected for each of the areas of higher peak density shown in Fig. 4.12. This resulted in a three-dimensional scatter of 2000-3000 points associated with each major conversion horizon. To estimate the depth and 95% confidence

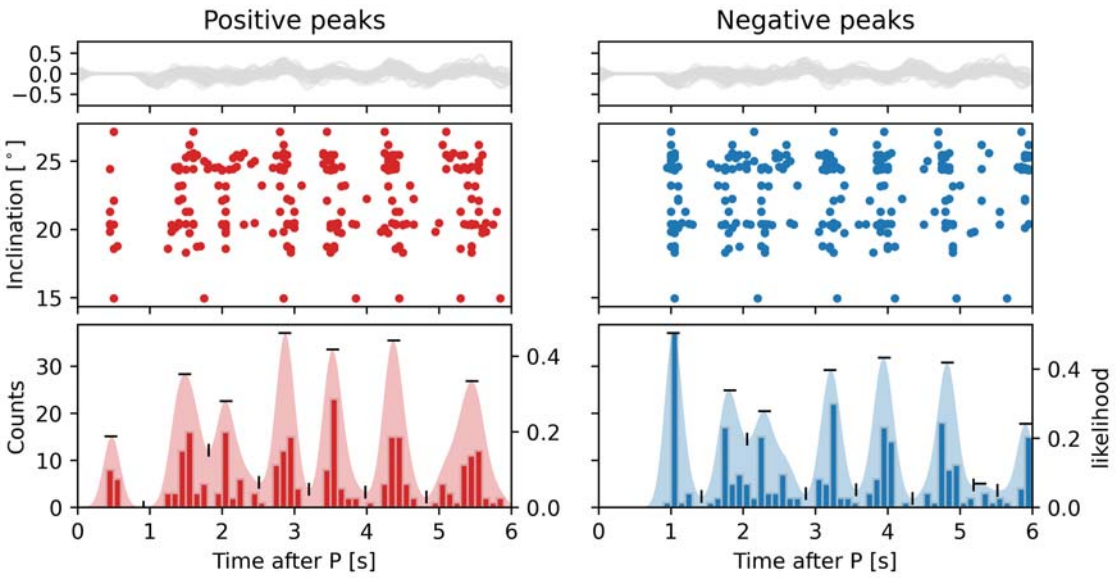

Figure B.9: Positive and negative peaks picked in the first 6 seconds of traces arriving at station BS05. Note the good agreement with peaks in Fig. 4.11.

limits for each horizon from a 3d scatter of conversion coordinates, two-dimensional (latitude, longitude, depth) Gaussian process regression was used via the *scikit-learn* Python package (Pedregosa *et al.*, 2011). An example longitudinal slice through a fitted surface is shown in Fig. B.10.

Three parameters were selected for simplicity and to minimise the number of assumptions. Conversion coordinates from peak fitting delineate gently dipping ($< 30°$) surfaces (Fig. B.10) so a linear trend was used as the initial basis for each surface. Local variations in conversion point depths were fitted using a radial basis function kernel, where the estimated depth depends on the distance from the nearest data points. Conversion coordinate depths show variation on the order of 1 km either side of the best-fit surface (Fig. B.10). This variation is attributed to noise in the data which was estimated using a white noise kernel. Parameters fitted were the slope of the linear surface, the length scale of the radial basis function kernel, and the noise level of the white noise kernel. The length-scale of roughness in seismically-imaged surfaces within subduction zones has been shown to be anisotropic (Edwards *et al.*, 2018), so radial basis function kernel length scale was allowed to vary in the

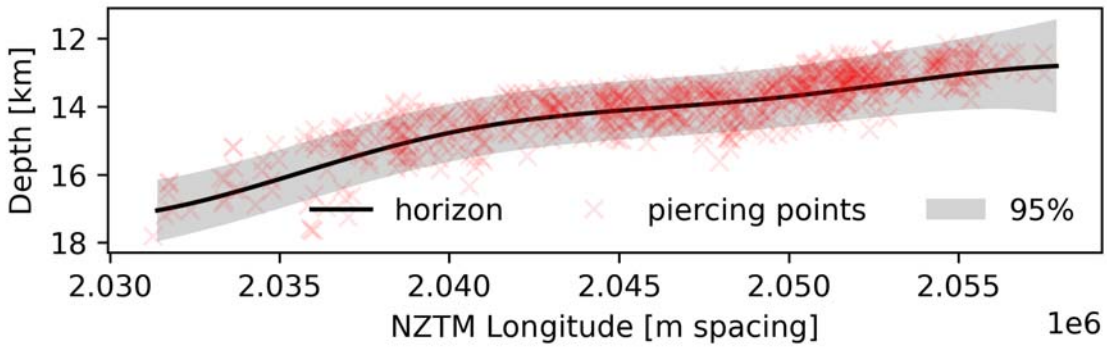

Figure B.10: An example of how Gaussian process regression was applied. Depth-converted Ps conversion points (red crosses) within highlighted period E on Fig. 4.12 delineate a sloping horizon across the study area. The linear slope of the fitted surface (black line) was used as a mean and the local variation of the line results from the radial basis function kernel. Conversion depths show 1-2 km of variation at similar locations, this variation was characterised using the white noise kernel and the 95% confidence limits are shown (grey fill).

north-south and east-west directions between prior bounds of 1 km and 100 km. The noise level ascribed to the data was allowed to vary between 100 m and 2 km.

Best-fit solutions are non-unique, depending on length scales and noise levels, so these bounds are selected to maintain realistic estimates for parameters so fitting realises a probable solution. Fitting for each horizon (A-I) was run 15 times with different initial starting length scales and noise levels (within the aforementioned bounds) to ensure the solution is the most probable. The resulting surface and standard error for each horizon was then estimated on a 100 m spaced grid within the latitudes and longitudes bounding arrivals within the corresponding time period (Fig. B.10).

B.5 common conversion point stacking

The code to achieve CCP stacking was heavily adapted from the *rfpy* toolbox (Audet, 2020). First, using the estimated conversion coordinates for the ray-tracing

described earlier (Section 4.7), travel times were estimated using Equations 4.1 and 4.1 for Ps, PpPs and PpSS + PsPs phases. receiver function time series were filtered at 4 Hz, 2 Hz, and 1.6 Hz for Ps, PpPs and PpSS + PsPs phases, respectively, to maintain similar horizon widths in the resulting image. This choice of parameters is an *a priori* choice, but the frequencies selected here are based on the frequency ratios used by Audet and Schaeffer (2018). Amplitudes at the estimated travel times were projected onto a section line oriented $\sim 121°$ starting at the Hikurangi margin trench (lat/lon -38.884/178.942). These projected amplitudes were then stacked into CCP bins for each phase, averaged, and smoothed parallel to the line direction (perpendicular to the trench) using a Gaussian filter with a width of 2.5 km (five CCP volumes). CCP bins used to construct the volume perpendicular to the trench are either 0.25 by 0.25 km or 0.5 by 0.5 km (distance parallel to line by depth). These trench-perpendicular lines are spaced 1 or 2 km apart (distance parallel to trench), depending on the lateral resolution required. The resulting stacks for each phase were then multiplied by a weight factor and phase weighted stacking was carried out, following the methodology of Frassetto *et al.* (2010). The weights used for stacking reflect the importance placed on the conversions highlighted by each phase. The depth range of interest here is up to 100 km, where direct Ps conversions from the same horizon show considerable spread (Fig. 4.12). Multiple arrivals from conversions in the upper 100 km are expected to be relatively strong (Fig. 4.11), so weights of 1, 3 and -3 were used for phases Ps, PpPs and PpSs + PsPs, respectively. Note that the weight for stacking of the PpSs + PsPs multiple is negative because its arrival amplitude is negative (Fig. 4.1). Before plotting a final smoothing parallel to the line direction was carried out with a 1.5 km wide Gaussian filter.

Some of the local variation seen in Fig. B.11 may reflect noise due to low ray coverage within 1 km (the lateral spacing) of that CCP volume slice. The counts per box for each volume-parallel slice are generally low (< 25) on the east side of the volume, or at depths > 60 km where the ray paths from arrivals disperse (Fig. B.13). Amplitudes are more sensitive to noise where fewer counts are registered per CCP cell but Gaussian filtering of the resulting CCP image helps remove lateral noise between cells (Fig. B.11).

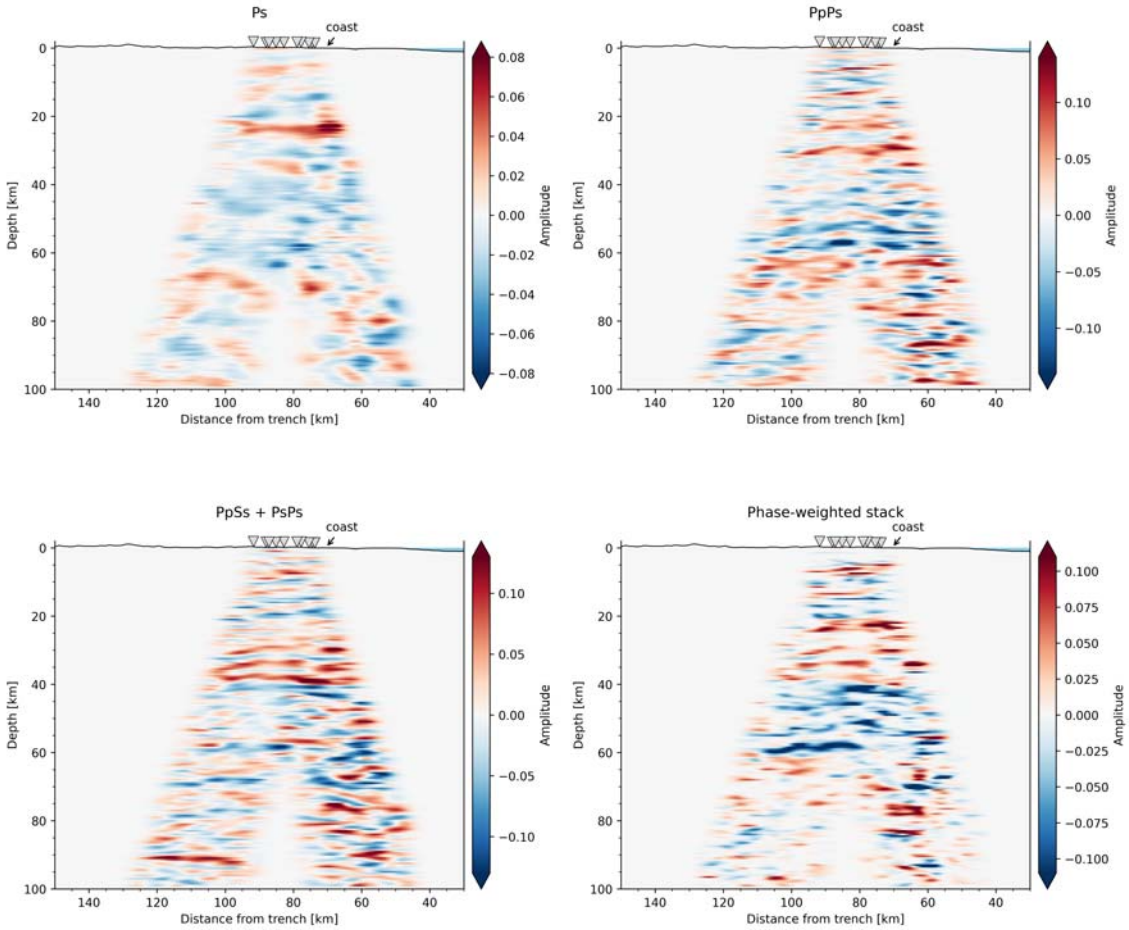

Figure B.11: Cross section through CCP stack volume for each of the phases and resulting phase-weighted stack. Cross section is constructed of 0.5 by 2 by 0.5 km bins on a bearing of 121° and plotted against distance from the trench at lat/lon -38.884/178.942.

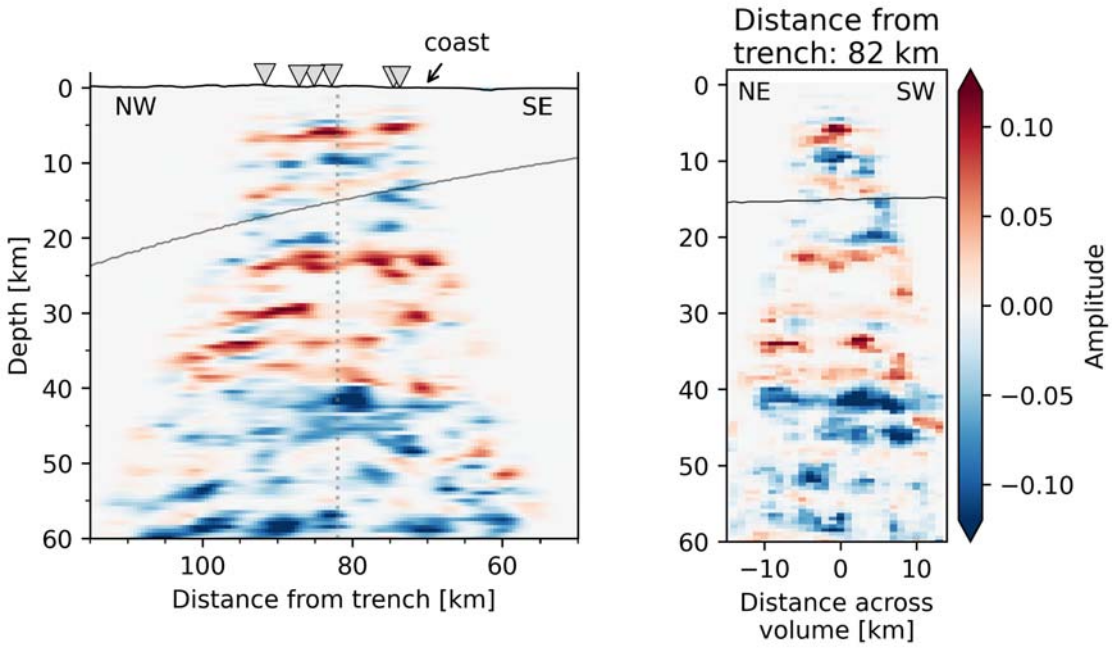

Figure B.12: Cross sections perpendicular to (left), and parallel to (right) the trench through a CCP volume. CCP volume has cell dimensions of 0.5 x 1 x 0.5 km (dx,dy,dz). Perpendicular cross section is constructed on a bearing of 121° and plotted against distance from the trench at lat/lon -38.884/178.942. Parallel cross section is plotted on a bearing of 61° and plotted against distance from the perpendicular section. Gray low-angle lines on both sections are the interpolated plate interface of Williams *et al.* (2013). Vertical grey line on perpendicular cross section (left) is location of parallel cross section (right)

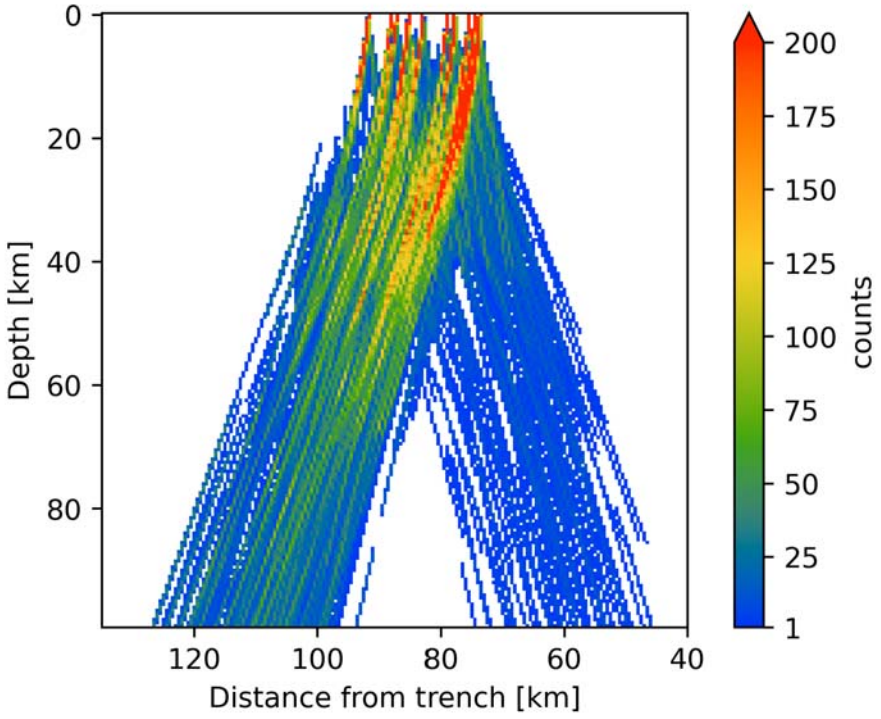

Figure B.13: Cross section through a CCP stack volume showing the counts per bin. Cross section is constructed of 0.5 by 2 by 0.5 km bins on a bearing of 121° and plotted against distance from the trench at lat/lon -38.884/178.942.

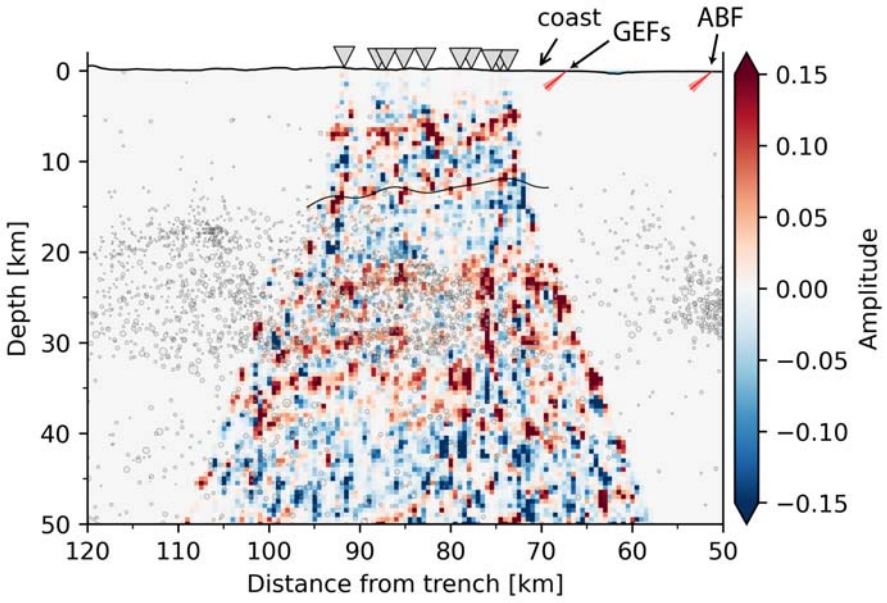

Figure B.14: Trench-perpendicular phase-weighted stack section through the centre of the 0.5 by 2 by 0.5 km CCP volume which has not been smoothed horizontally with a Gaussian filter. The black line shows regressed plate interface. Scattered points are the projected hypocentres of local earthquake which occurred within 10 km of the section line since 1970, earthquake hypocentral data was downloaded from GeoNet (https://www.geonet.org.nz/). Red lines and wedges are active faults projected 2 km down from the surface using their dip estimates as estimated by Litchfield *et al.* (2014). GEFs and ABF are the Gable End Fault south and the Ariel Bank Fault, respectively.

Appendix C

International drilling program sampling of calcareous sediments

Organisation	Expedition	Site	Water depth (m)	Top depth of carbonates (m)	Bottom depth of Carbonates (m)	Thickness of carbonates (m)	Unit	Latitude	Longitude
IODP	375	U1520	3520.1	509.82	848.45	338.63	IV	-38.96922	179.131853
ODP	114	701	4636.7	395.15	481.3	86.15	IIB III	-51.9846	-23.212267
IODP	383	U1543	4200	0	376.3	20	Lithofacies 4	-54.584333	-76.6765
ODP	202	1232	4072	133	134	1	Core section 13X-3	-39.890833	-75.901333
ODP	202	1237	3212	38.05	360.65	322.6	IB-IIB	-16.007017	-76.378083
ODP	201	1231	4824.9	55.5	119.1	63.6	Unit III	-12.020518	-81.903987
DSDP	34	321	4817	49	115	66	Unit 4	-12.0215	-81.904
DSDP	34	320	4483	73.5	155	81.5	Unit 2	-9.0067	-83.53
ODP	202	1238	2202.2	0	467.3	467.3	IA	-1.8718	-82.7823
ODP	202	1239	1414.7	0	557.5	557.5	I	-0.672	-82.0808
DSDP	69	505	3537	0	232	232	Units I-III	1.9133	-83.79
ODP	111	677	3472	0	308.5	308.5	Units II-III	1.2023	-83.737
DSDP	16	155	2752	0	521	521	Units 1-4	6.123	-81.0437
ODP	202	1242	1363.4	0	287.74	287.74	Units I-II	7.8559	-83.6067
IODP	344	U1381	2068.7	3.69	95.5	87.81	Units II IV	8.428583	-84.157817

Organisation	Expedition	Site	Water depth (m)	Top depth of carbonates (m)	Bottom depth of Carbonates (m)	Thickness of carbonates (m)	Unit	Latitude	Longitude
IODP	344	U1414	2458.6	0	336	336	Units I-III	8.50384	-84.225497
ODP	170	1039	4351.7	152.49	381	228.51	Units 2-3	9.6399	-86.2001
DSDP	67	495	4140	177	428	251	Units 2-4	12.4963	-91.0377
DSDP	63	473	3249	0	150	1		20.9653	-107.063
DSDP	66	487	4764	0	0	0		15.8535	-99.1753
ODP	167	1020	3041.6	220	260	40	Units II	41.009	-126.434
DSDP	18	174	2815	750	879	1	Unit II	44.8897	-126.347
ODP	146	888	2516.3	0	0	0		48.1668	-126.6632
ODP	139	855	2444.8	0	0	0		48.4427	-128.6378
DSDP	18	177	2006	190	451	100		50.4697	-130.205
IODP	341	U1418	3668.2	0	0	0		58.776825	-144.492962
IODP	341	U1417	4187.7	0	0	0		56.959993	-147.109975
ODP	145	887	3631.2	45	74	1		54.3654	-148.446
ODP	19	183	4708	238	249	11	Unit C	52.5717	-161.206
DSDP	4	27	5251	245	290	45	Units 3 4	15.8565	-56.8793

Organisation	Expedition	Site	Water depth (m)	Top depth of carbonates (m)	Bottom depth of Carbonates (m)	Thickness of carbonates (m)	Unit	Latitude	Longitude
ODP	110	672	4982.5	0	450	320	Units 1, 2 4-6	15.54	-58.641
ODP	145	886	5713.4	0	0	0		44.6897	168.24
DSDP	19	191	3854	520	529	9	Unit B	56.945	169.179
DSDP	19	192	3014	940	1044	104		53.0095	164.714
ODP	145	883	2407	597	818	221	Units III-IV	51.1983	167.7688
ODP	145	881	5531.1	0	363	1	all	47.1023	161.4915
DSDP	19	193	4811	0	0	0		45.8033	155.871
DSDP	86	580	5375	60	80	20	Unit 1B	41.6245	153.976
DSDP	56	436	5240	359.5	388.3	28.8	Unit 3	39.9327	145.558
ODP	185	1149	5817.6	282.3	408.2	125.9	Units IV-V	31.342	143.3513
DSDP	6	52	5744	0	0	0		27.7717	147.13
DSDP	60	452	5858	0	25	25	Unit 1	17.6698	148.629
DSDP	6	58	4503	10	145	20		9.235	144.418
DSDP	6	59	5554	0	0	0		11.78	147.582

Organisation	Expedition	Site	Water depth (m)	Top depth of carbonates (m)	Bottom depth of Carbonates (m)	Thickness of carbonates (m)	Unit	Latitude	Longitude
DSDP	6	56	2508	0	233.5	233.5	Entire thickness	8.3733	143.56
DSDP	6	55	2850	0	130.8	130.8	Entire thickness	9.3017	142.535
IODP	333	C0011	4049	0	0	0		32.82883	136.8815
IODP	332	C0010	2552	0	0	0		32.20997	136.68654
ODP	190	1173	4790.7	510	680	100	Unit III	32.2444	135.0251
ODP	190	1177	4844.3	520	680	20	Unit III	31.6525	134.0119
DSDP	31	297	4458	54	90	36	Unit 2	30.8727	134.165
DSDP	31	296	2920	0	453	453	Unit 1	29.3402	133.525
IODP	351	U1438	4700.2	0	0	0		27.38351333	134.3183667
DSDP	58	446	4952	14.2	628	256.3	Units II, III-IV	24.7007	132.775
DSDP	58	445	3377	0	760	760	Units I-Va	25.5227	133.208
DSDP	31	295	5808	0	0	0		22.5627	131.367
DSDP	31	292	2943	0	367.5	367.5	Unit 1	15.8185	124.651
DSDP	31	291	5217	61.5	101.8	40.3	Units 2-3	12.8072	127.831

Organisation	Expedition	Site	Water depth (m)	Top depth of carbonates (m)	Bottom depth of Carbonates (m)	Thickness of carbonates (m)	Unit	Latitude	Longitude
ODP	184	1145	3175.6	0	212.65	1	Layers in Unit I	19.584	117.6311
ODP	184	1148	3297.1	194.02	457.22	263.2	Units II-V	18.8361	116.5655
IODP	367	U1500	3801.7	1272.1	1310.98	38.88	Unit VB	18.30451167	116.2199183
IODP	349	U1431	4237.3	101.16	603.42	50	Units II-IV	15.37581833	117.000015
DSDP	22	217	3010	0	480	480	Units 1-2c	8.9262	90.5388
DSDP	22	218	2749	0	650	464	Units 1, 3, 5-7	8.007	86.2828
ODP	121	758	2923.6	0	367.3	367.3	Units I-II	5.3842	90.3612
IODP	362	U1480	4147.53	0	1415	41.59	Units I-V	3.0341	91.60580167
DSDP	22	213	5601	135	154	19	Units 3-4	-10.2118	93.8962
DSDP	22	211	5518	411.5	528.6	117.1	Unit 6	-9.7755	102.699
DSDP	27	260	5702	0	323	256.5	Units 1, 3 4	-16.1445	110.299
ODP	124	767	4905.6	0	420.9	32.7	Units IIB-IIC	4.7911	123.5034
DSDP	27	261	5667	19	532.5	228	Units 2 4	-12.9472	117.893
DSDP	27	262	2298	0	442	442	All units	-10.8698	123.846

Organisation	Expedition	Site	Water depth (m)	Top depth of carbonates (m)	Bottom depth of Carbonates (m)	Thickness of carbonates (m)	Unit	Latitude	Longitude
IODP	363	U1483	1732.93	0	293.37	293.37	Nannofossil ooze	-13.0873	121.804
DSDP	30	286	4465	83	197	114	Nannofossil ooze	-16.532	166.37
DSDP	21	204	5354	0	0	0		-24.9545	-174.111
IODP	330	U1372	1957.6	0	18.34	13.84	Foraminiferal ooze	-26.493362	-174.729177
IODP	330	U1373	1447	0	0	0		-28.564845	-173.280832
IODP	330	U1375	1269	0	8.5	8.5	Foraminiferal ooze	-33.698367	-171.448992
DSDP	23	222	3546	0	1300	238.6	Nanno ooze with clay	20.0915	61.5093
DSDP	23	223	3633	0	657	657	Nanno chalk	18.7497	60.1297
DSDP	42	374	4078	0	373	373	Nannofossil marl	35.8478	18.1963

Organisation	Expedition	Site	Water depth (m)	Top depth of carbonates (m)	Bottom depth of Carbonates (m)	Thickness of carbonates (m)	Unit	Latitude	Longitude
DSDP	13	131	3037	0	272	1	calcareous-rich pelagic clay	33.1065	28.5115

Table C.1: Carbonate sediment thicknesses (> 40% $CaCO_3$) drilled seaward of subduction zones from IODP, DSDP, and ODP databases. Note that thicknesses do not necessarily correspond to the difference between top and bottom depth due to discontinuous thicknesses calcareous sediments.